Theoretical investigation of scanning probe lithography in field-emission mode

Dissertation

Steve Lenk

Fachgebiet Mikro- und Nanoelektronische Systeme
Fakultät für Elektrotechnik und Informationstechnik

Technische Universität Ilmenau

Reviewer:

Prof. Dr.-Ing. habil. Ivo W. Rangelow
(Technische Universität Ilmenau)

Prof. Dr.-rer. nat. habil. Dirk Lützenkirchen-Hecht
(Bergische Universität Wuppertal)

Prof. em. PhD Timothy Groves
(University Albany)

Date of Submission: 08.01.2019
Date of Defense: 06.09.2019

urn:nbn:de:gbv:ilm1-2019000353

Abstract

The miniaturization of the smallest devices of silicon-based integrated circuits, namely transistors, using conventional optical lithography techniques reaches slowly their physical limitations and alternative patterning and pattern transfer methods are needed to further reduce the device size. One of such patterning alternatives is field-emission scanning probe lithography. This technique uses electrons to expose the resist layer. The electrons are emitted from an ultrasharp tip ($r \lesssim 10\,nm$) of a scanning probe due to a strong applied electric field. This scanning probe method was already successfully applied to fabricate single quantum-dot transistors working at room temperature and is capable of high-resolution lithography with critical dimensions in the sub-$10\,nm$ range. Nevertheless, a theoretical description was not available, which considers the influences of the resist layer on the electron emission from the nanotip and the interaction of the electrons within the resist. Furthermore, the optimal parameters for high-resolution patterning had to be determined experimentally, which is time-consuming, increases tip wear and the risk of tip crashes. Therefore, a theoretical model would be useful, which can predict the optimal parameters for a specific tip.

Here, a comprehensive numerical model of the field-emission scanning probe lithography is presented, which consists of the calculation of the electric field, the emission current density at the tip and the trajectories of the electrons as well as a Monte Carlo simulation to compute the scattering of electrons in the resist. The model is applicable for any cylinder symmetric tip (including also e. g., volcano-gated tips) and takes the influence of the resist layer into account. For predicting optimal parameters, describing the underlying physics and minimizing the computational resources an analytical model (for a typical tip geometry) was derived. It includes all calculation steps of the numerical model except the scattering in the resist. It allows studying the various dependencies arising from tip-related constants (e. g., tip radius and material) and from externally adjustable parameters (e. g., bias voltage). The analytical model was successfully applied to explain field-emission experiments and to estimate the system inherent drift velocity and the growth rate of experimentally observed structures at the sample, respectively. Furthermore, it could describe the experimentally obtained dependence of the line width on the exposure dose.

Therewith, a comprehensive theoretical model to describe field-emission scanning probe lithography was achieved, which considers all relevant parameters (under vacuum conditions). The analytical model can be used to predict the properties of patterns to be written, to adjust external parameters for optimal results and it can be also included in the software of an actual field-emission scanning probe lithography tool.

Kurzzusammenfassung

Die Miniaturisierung der kleinsten Bauelementen, d. h. der Transistoren, in integrierten Schaltungen auf Siliziumbasis nähert sich langsam den physikalischen Grenzen und alternative Strukturierungs- und Strukturübertragungsmethoden werden benötigt um zu noch kleineren Strukturen zu gelangen. Eine dieser alternativen Strukturierungsverfahren ist die feldemissionsbasierte Rastersondenlithographie. Diese Technologie beruht auf der Belichtung einer Resistschicht mittels Elektronen, welche aus der Rastersondenspitze aufgrund des angelegten elektrischen Feldes emittiert werden. Das Verfahren wurde schon erfolgreich zur Herstellung neuartiger Einzelquantenpunkttransistoren verwendet, welche bei Raumtemperatur arbeiten und kann Strukturgrößen von unter $10\,nm$ erzeugen. Nichtsdestotrotz mangelt es an einer theoretischen Beschreibung, welche insbesondere den Einfluss der Resistschicht auf das Emissionsverhalten der Elektronen aus der Spitze wie auch die Wechselwirkung der Elektronen mit den Molekülen der Resistschicht umfasst. Optimale Parameter zum Er-reichen der besten Auflösung mit einer bestimmten Emissionsspitze müssen zur Zeit in einem empirischen Versuch bestimmt werden. Das ist sowohl zeitaufwendig, nutzt die Spitze ab und birgt das Risiko einer Berührung der Spitze mit der Probe. Dadurch entsteht wiederum die Gefahr, dass die empirische Optimierung wiederholt werden muss. Um dies zu vermeiden, wäre ein theoretisches Modell wünschenswert, welches die optimalen Parameter vorhersagen kann.
In dieser Arbeit wird ein umfassendes numerisches Modell der Rastersondenlithographie vorgestellt, welches die Berechnung des elektrischen Feldes, der Emissionsstromdichte aus der Spitze und der Elektronentrajektorien beinhaltet sowie eine Monte Carlo Simulation zur Berechnung der elektronischen Wechselwirkungen in der Resistschicht einschließt. Dieses Modell ist für beliebige zylindersymmetrische Spitzen anwendbar (u. a. für Spitzen mit einer umschließender Elektrode) und berücksichtigt den Einfluss der Resistschicht in der gesamten Berechnung. Zur Verbesserung des Verständnisses der physikalischen Grundlagen, zur Vorhersage optimaler Parameter und zur Resourcenminimierung der Berechnung wurde ein analytisches Modell abgeleitet, welches, bis auf die Wechselwirkungen in der Resistschicht, alle Teile des numerischen Modells für eine typische Spitzenform beinhaltet. Damit konnte der Einfluss der durch die Spitze vorgegebenen Parameter (z. B. Spitzenradius) und der extern einstellbaren Parameter (z. B. Spannung, Schreibgeschwindigkeit) untersucht werden. Das analytische Modell wurde erfolgreich zur Analyse von Feldemissionsexperimenten genutzt und es konnte damit die systemeigene Driftgeschwindigkeit beziehungs-weise die Wachstumsrate der experimentell beobachteten Strukturen abgeschätzt werden. Weiterhin konnte es die experimentell beobachtete Abhängigkeit der Linienbreite von der Bestrahlungsdosis und der Spannung reproduzieren.
Somit steht erstmals ein vollständiges theoretisches Modell zur Beschreibung der feldemissionsbasierten Rastersondenlithographie zur Verfügung, welches alle relevanten Parametereinflüsse (im Vakuumbetrieb) beinhaltet. Der analytische Teil des Modells kann zur Vorhersage der zu schreibenden Strukturen und zur Parameteranpassung verwendet und in die Software des Lithographiesystems eingebaut werden.

Contents

Chapter 1

Introduction

Controllable fabrication of nanoscale structures is crucial for next generation nanoelectronics like for devices based on quantum mechanical effects, for nanophotonics, nanobiotechnology and nanoelectromechanical systems. Until now, optical lithography combined with pattern transfer techniques (like reactive ion etching) has been the leading method for fabrication of nanostructures and is the driving force of the growth rate in integrated circuits described by Moore's law [1].
Despite the success of Moore's law, optical lithography for nanometer patterning is not advisable in science and for industrial research and development because it requires the fabrication of masks and includes complex etching techniques using self-aligned double or quadruple patterning to produce nanometer-sized features in silicon. This procedure is time-consuming and cost-intensive, especially for the fabrication of single devices or prototypes.
Furthermore, a direct investigation and analysis of the fabricated device structures is favored, in particular when an understanding of the underlying mechanisms is of great concern. Unfortunately, most of the available (top-down[1]) techniques are not able to offer a combined solution for lithography and in-situ metrology within one tool since they are only able to interact (while imaging or patterning) with a single physical quantity (like heat, light or charged particles). To a certain extent, it is still possible to achieve lithography and metrology functionality using a single source of information by adjusting energy and exposure dose as it is done for the combination of scanning electron microscopy (SEM) and focused electron beam deposition (FEBID) or the combination of helium beam microscopy (HIM) and focused ion beam (FIB) lithography [2]. However, different mechanisms for patterning and imaging are more advantageous since the probability of modifying the written structures during imaging is almost completely excluded.
Scanning probe methods are prominent techniques, which are able to combine different mechanisms for structuring and investigation like a combination of thermal resist evaporation or thermally induced chemical modifications and contact-force measurement [3, 4].

[1] This thesis does not mention any bottom-up approaches since fabrication and investigation are normally separated.

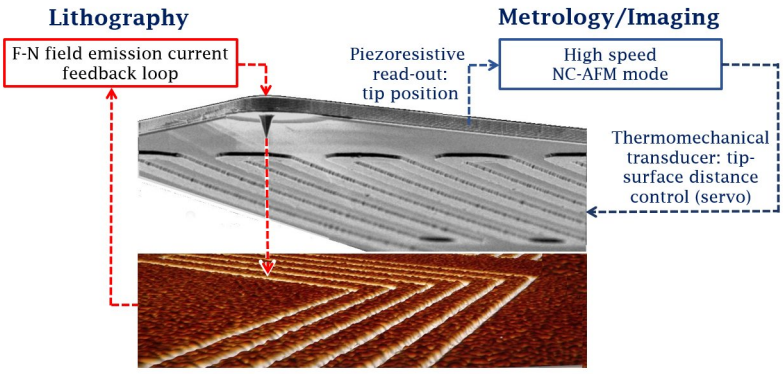

Figure 1.1: Schematic layout of the closed-loop SPL platform utilizing a thermally actuated, piezoresistive cantilever with an ultrasharp tip (taken from [14]).

The approach of our group is the combination of electron-induced resist modification [5–7] and tapping-mode atomic force microscopy (AFM) [8] using a field-emission scanning probe lithography (FE-SPL) tool [9–13], which is shown schematically in fig. 1.1.
The lithographic process is based on the field emission from a sharp nanotip, which generates an electron beam of low energy ($10 - 100\,eV$). Therefore, a bias voltage is applied between tip and sample. The generated electrons expose a resist layer and trigger resist modifications mainly due to inelastic scattering events. Imaging is typically achieved by atomic force microscopy but related techniques such as Kelvin probe could be used as well. Thus, two different physical mechanisms are used for patterning and imaging.
The technique offers several advantages like the ability to operate in ambient conditions, no need of complex laser systems or electron beam optics or blankers, and reduced proximity effects due to low-energy electrons and small tip-sample distances ($10 - 100\,nm$), in comparison with conventional electron beam lithography (EBL). Thus, it might be a cost-effective and easy-to-use alternative or a supplement to electron beam and extreme UV lithography for low-throughput applications [2, 13–15].
Our approach enabled the fabrication of single-electron transistors working at room temperatures [14, 16] using FE-SPL for pattern definition and a cryogenic reactive ion etching (RIE) step for transferring the patterns into silicon [17, 18].
Despite the experimental achievements, there are still many open questions regarding FE-SPL.
First, it is unknown if a resolution limit exists due to the emission process or the electronic interactions inside the resist layer.
Second, at the moment, optimal parameters for different types of tips, samples and resists have to be found experimentally, since there is no model to predict them. This procedure is time consuming and can lead to tip destruction entering an unstable lithographic regime. Furthermore, the influence of fabrication related tolerances of tip shape and resist layer properties is unknown.
Third, an understanding of the underlying processes is missing since it is unclear if the field emission process differs for the small tip-sample distances and

the curved tip shape compared to the typically analyzed large tip-sample distances using a plate-capacitor-like emission model.
A model describing the complete FE-SPL process could not only be used to answer these questions but could also be implemented in actual FE-SPL tools to enable on-the-fly optimization and determination of key parameters such as the tip-sample distance.
In this work such a theoretical model is developed, which includes the computation of the electrostatic field, the field emission probability, electron trajectories and interactions within the resist layer determined by a Monte Carlo approach [19–21]. Therewith, the dependencies of the tip parameters (e. g., tip material) and the external variables (e. g., bias voltage) on the emission process are studied as well as their effects on lithography.
The impact of resist layer properties like thickness, material and pre-defined structures is of major relevance and was only partly investigated before [6, 22, 23]. The underlying mechanisms for resist modifications during lithography with low-energy electrons influenced by the electric field, i. e., elastic and inelastic scattering events were mostly neglected and only preliminary attempts can be found in literature [6, 22, 23]. Due to its importance, electron scattering within the resist was considered in this thesis for a more realistic description of the lithographic process. The investigation is dedicated to ultrathin resist films (below $20\,nm$ layer thickness), which enables high-resolution patterning. However, it can also be applied to thicker resist films.
The theoretical results are compared to experimental field-emission data to verify the model and to analyze further influences not yet considered. Another important result of this thesis is the derivation of an analytical model for the FE-SPL process enabling a fast determination of optimal parameters for a certain tip, which might help to increase tip lifetime and to enhance writing reproducibility.
However, the thesis not only presents results important for the FE-SPL technique but also for the field emission process and for the scattering within an ultrathin adsorbate layer under the influence of an electric field.
The structure of the thesis is outlined in the following. At first, some basics of lithography and its theory will be presented, followed by an explanation of the used mathematical methods and implemented algorithms. Next, the results are summarized starting with a comparison of the different models, the derivation of an analytical expression from the numerical model before field-emission and lithographic results are presented. Additionally, a quantitative comparison between field-emission experiments and the analytical results is presented. At the end, the results are summarized and a brief outlook is given.

Part I

Fundamentals

Chapter 2

Fundamentals of field-emission scanning probe lithography experiments

In this chapter, standard lithographic technologies like optical and electron beam lithography are briefly discussed. Since the focus of this thesis is the field-emission scanning probe lithography (FE-SPL), it is introduced in section 2.2. In this chapter, the experimental achievements and technological implementations are considered whereas previous theoretical approaches are given in chapter 3.

2.1 Lithography in general

An important enabler for future nanodevices and nanosystems is the ability to fabricate features in the sub-10 nm regime in a reproducible manner [24]. Such feature sizes allow the use of quantum effects like quantized excitations, single-atom electron spin qubits in silicon, Coulomb blockade effects and single-electron tunneling [16]. It is expected by looking "beyond CMOS" that single electron transistors and other quantum devices become the building blocks for integrated circuits of the future. Thus, ultrahigh resolution and flexibility of fabrication technologies will become increasingly important [25].
So far, the dominating method for high-throughput fabrication of nanostructures is optical lithography, in combination with highly advanced pattern transfer techniques. However, for low-throughput fabrication of single experimental devices/prototypes and for the mask production process, which is necessary for optical or nanoimprint lithography [26], mask-less approaches are required, which are flexible, reproducible and offer high resolution. Bottom-up approaches like molecular self-assembly and self-organization are mostly not applicable since they are not adjustable and often require pre-defined guiding structures.
Mask-less lithography techniques can be divided into scanning beam lithography and scanning probe lithography (SPL) approaches. Scanning beam

techniques include ion beams, electron beams and laser beams. Scanning probe methods are classified by their energy source(s) used for triggering chemical or physical surface modifications on sample or resist layer. Most prominent energy sources are thermal energy (e. g., thermal SPL [27]), mechanical energy (e. g., static or dynamic ploughing [28, 29]), chemical energy (like local anodic oxidation [30]) and energy of electrons (scanning tunneling microscope (STM) lithography [31] and field-emission SPL [32] for example). A good overview of the different SPL approaches is given in ref. [33], in which combinations of interactions with different energy sources are also presented.
The focus of this work is field-emission scanning probe lithography (FE-SPL), which uses field-emitted electrons from the nanotip of a cantilever probe to pattern a resist layer. Electron beam lithography (EBL) and STM lithography are closely related and are thus briefly described. All three techniques, EBL, FE-SPL and STM lithography, use electrons as the energy transport medium to modify the surface using (more-or-less) sharp tips. In simplified terms, they can be classified by their tip-sample distance. In EBL, the tip-sample distance d tends to infinity whereas in STM lithography it approaches zero. In this sense, FE-SPL is an intermediate state of these two extremes.
The applied voltage, i. e., the kinetic energy of the electrons, might also be used as a classification criterion and the following different regimes can be distinguished for modifying resists [34]:

- Tunneling regime for kinetic energies of electrons (ϵ_{kin}) below the work function, i. e., $\epsilon_{kin} < \Phi$, studied by [31, 35–39],
- Near field emission for $\epsilon_{kin} \geq \Phi$,studied by [34, 40–44],
- Standard field emission for $\epsilon_{kin} > \Phi$, studied by [9–13, 16, 19, 20],
- Electron beam lithography for $\epsilon_{kin} \gg \Phi$, studied by [45–47].

Obviously, both criteria oversimplify the situation and, thus, EBL and STM lithography are considered separately.
EBL has its origins in scanning electron microscopy [48], in which the electrons are generated in a source by field emission (cold field emitter [49], Schottky field emitter [50]) or thermionic emission [51] or a mixture of both (thermal field emitters [52]) from an emitter tip. The electron beam is scanned over the sample using complex electric and/or magnetic focusing and deflection optics. Due to the large distance between source and sample ($\approx 50\,cm$ [53]), an ultrahigh vacuum is necessary to avoid electron scattering by gas molecules.
EBL has become an important R&D tool for micro- and nanoelectronics and for newer fields of micro- and nanoelectromechanics (MEMS/NEMS). The state-of-the-art EBL tools provides high intensity beams with energies up to $100\,keV$ and are capable of writing with a resolution of $8\,nm$ over $200\,nm$ wafer substrates [54].
Note that the normally used electron energies are in order of several keV and that focusing and acceleration are achieved far away from the sample. Therefore, the sample is not influenced by the high electric fields necessary for emission and focusing. Additionally, higher electron currents ($> 10\,pA$) are

used in regards to scanning probe techniques.
In scanning probe techniques, the "beam" is generated at the tip, located in close proximity to the sample. The tip itself is moved over the sample surface to generate lithographic patterns. The corresponding lithography techniques (scanning tunneling lithography and field-emission scanning probe lithography) stem from scanning tunneling microscopy [55] and atomic force microscopy [8, 56], respectively. Shortly after the invention of scanning tunneling microscopes, it was already used for lithographic applications [5, 6, 57]. Electron tunneling between the tip and sample causes the chemical bonds to break and, thus, lead to a lithographic reaction [31,38]. Since this method is strongly influenced by resist modifications and contaminations, vacuum conditions are necessary to achieve atomic resolution [39] with writing speeds up to $100\,nm/s$. State-of-the-art lithography using scanning tunneling [58] provides atomic resolution, such as the removal of single atoms in hydrogen depassivation lithography [38]. The involved bias voltages are relatively low (below $6\,V$).
In both competing methods (EBL and STM lithography), ultra-high vacuum is necessary, which increases costs and time for the patterning process. Furthermore, they use the same physical principle for imaging and patterning (EBL: electron scattering, STM lithography: electron tunneling), which might yield to issues like overexposure during imaging. The involved electron energies differ by a factor of 1000 and more (keV versus single eV) but the tip-sample distances vary by an even larger factor of 10^7 (cm versus Å).
In the next chapter, the FE-SPL technique is described and compared with the previously described methods (EBL and STM lithography). FE-SPL uses tens of eV as electron energy and tens to hundreds of nm as tip-sample distance, respectively.

2.2 Field-emission scanning probe lithography

In field-emission scanning probe lithography (FE-SPL), electrons are emitted from a nanotip (with radius r, opening angle γ and work function Φ) of a scanning probe, due to a high electric field ($E_{max} \gtrsim 1\,V/nm$) at the tip apex. These electrons propagate towards the sample and expose resist layers after an acceleration to energies up to $100\,eV$. Therefore, a bias voltage U is applied at the resist-covered sample whereas the tip is on ground, as shown in fig. 2.1. Some arbitrary electron trajectories are drawn in blue and the emission area, from which most electrons are emitted, is marked with green. Inside the resist layer (thickness d_l and dielectric constant ε), electrons scatter both elastically and inelastically. Some of the electrons may even be backscattered and leave the resist again, but due to the electric field, these will be attracted towards the sample and hit the resist surface again.
Since in air the tip-sample distances ($d \leq 100\,nm$) are below the electron mean free path under atmospheric pressure ($\lambda_e \approx 4\sqrt{2}\,\lambda_m \approx 350\,nm$[1] using a molecular mean free path of $\lambda_m \approx 66\,nm$ [59]), FE-SPL can be used either

[1] The factor $4\sqrt{2}$ is obtained from kinetic gas theory using the assumptions of hard spheres and negligible molecular velocity as shown in the appendix A.

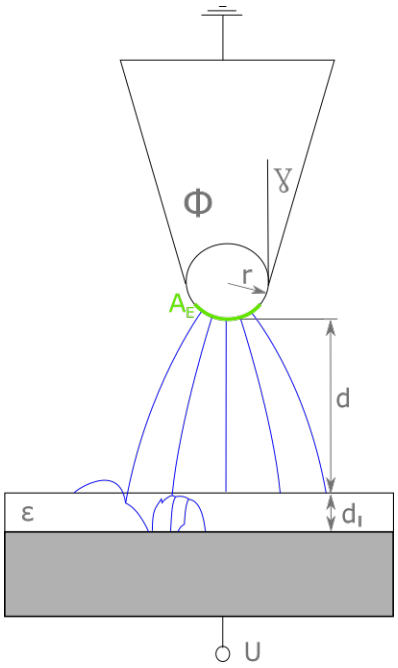

Figure 2.1: Scheme of the processes during field-emission scanning probe lithography and definition of parameters.

under ambient laboratory conditions or under vacuum conditions [60]. A complex electron-optics system including blankers, electronic and magnetic lenses is not necessary because the cantilever itself is scanned over the sample and it is in close proximity between the tip and sample. Our set-up (shown in fig. 2.2) does not rely on conventional optics or piezoelectric actuation or the optical read-out, because we use active cantilevers [61–68]. Therefore, a smaller construction size is enabled and adjustments of the optical laser system after cantilever exchange are unnecessary. The reduced construction size enables the inclusion of the FE-SPL tool in a conventional dual beam microscope, offering focused ion beam and scanning electron microscope functionality[2] [60, 61].
The energy of the exposing electrons is transferred to the resist molecules by inelastic scattering, which triggers bond breaking. The broken bonds lead to a decreased solubility of the resist due to subsequent cross-linking or to an increased solubility resulting in negative-tone and positive-tone lithographic patterns after resist development, respectively [70]. Additionally, a development-free, dry pattering process is available for several resist materials, in which the resist material is directly removed for a sufficiently intense electron dose under ambient conditions [13, 24, 70–73]. The experimentally used, so-called line exposure dose is equal to the ratio of the total current and the writing velocity v.
The kinetic energy of the electrons is determined by the applied voltage typically between 10 and 100 V. The electron energies are thus comparable to the molecular binding energies resulting in an increased interaction cross section

[2] This is crucial for the comparison between experimental and theoretical data presented in section 9.2.

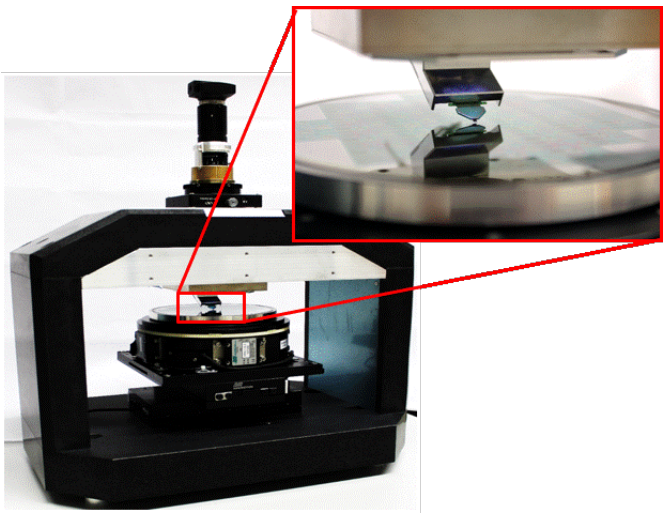

Figure 2.2: Field-emission scanning probe lithography tool combining top scanner and bottom coarse positioning stages for step-and-repeat functionality (taken from [69]).

compared to EBL. This yields to a decreased scattering depth, a reduced number of secondary electrons, and in this way to a strongly reduced proximity effect compared to EBL [32,74]. Besides the reduction of proximity effects, the small applied bias voltage ($U \leq 100\,V$) at the sample reduces also space charge effects causing problems in SEM and EBL, but introduces the requirement of using either conductive samples or conductive resist materials [69].
Since FE-SPL patterning uses a cold-emission process, undesirable effects like dopant spreading caused by local heating are avoided, which is assumed to be an issue for thermal SPL.
Our FE-SPL tool operates in the so-called constant-current mode, in which the current is kept constant during patterning by adjusting the tip-sample distance d continuously. This mode results in stable and reproducible lithography with low variations in the line width. Other groups used a constant-force mode, in which the cantilever deflection and, thus, the tip-sample distance was kept constant (the bias was unchanged during their experiment) [75, 76]. However, the patterning results showed large line width variations due to current fluctuations [75]. Nevertheless, due to tolerances in tip and probe geometry, and since contact between tip and sample, i. e., tip and sample modifications, needs to be avoided, the (absolute) tip-sample distance is hardly determinable experimentally.
Despite the successful experimental realization of even sub-$5\,nm$ line feature [10] and application of the FE-SPL technique for fabrication of devices, there are still open questions about the underlying physics, the optimal parameters for highest resolution patterning using a certain nanotip, and the minimal achievable feature size. These questions are addressed in this work.
The next chapter summarizes fundamental theoretical approaches used in this thesis.

Chapter 3

Basic theoretical approaches

In this chapter, fundamental theoretical approaches are briefly summarized and state-of-the-art models are presented.
The complete lithography process include the field emission of electrons from a sharp nanotip, propagation of these electrons to the resist layer on top of the sample and the interactions within the thin resist layer as visualized in fig. 2.1. The electric field around the tip apex is crucial for estimating the field emission probability and, thus, several analytical models are compared in section 3.1. The fundamental Fowler-Nordheim theory is the accepted basis of field emission from nanotips [75, 77], even if it was derived for field emission from flat surfaces. It will be introduced in section 3.2. In section 3.3, state-of-the-art descriptions for lithography based on field emission from sharp nanotips are discussed, which mostly include emission and propagation of the electrons. Only a few publications include first attempts of considering the electron interactions within the resist material. These are also included in section 3.3.

3.1 Electric field and field enhancement

The electric field can be calculated from the electrostatic potential ϕ by $E = -\nabla\phi$ for any geometrical form. The potential for a geometry consisting of a tip over a conductive sample is typically determined numerically using the finite-element method (FEM) [13,32,75,78,79] but image-charge methods [80,81] or finite differences [77] were also used.
In fig. 3.1, the electric field for a chosen parameter set is shown. A strong field enhancement effect at the tip apex, the so-called lightning rod effect [80, 82], can be seen. It describes the ratio between the magnitude of the maximal electric field E_{max} at the tip apex and the so-called macroscopic electric field E_0. The macroscopic electric field E_0 is estimated either by the electric field of a plate capacitor, or a conducting sphere over a biased plate. An enhancement factor is introduced, which takes the influence of the tip shape on the electric field into account.
If the tip is considered to be an altered sphere, the maximal electric field near

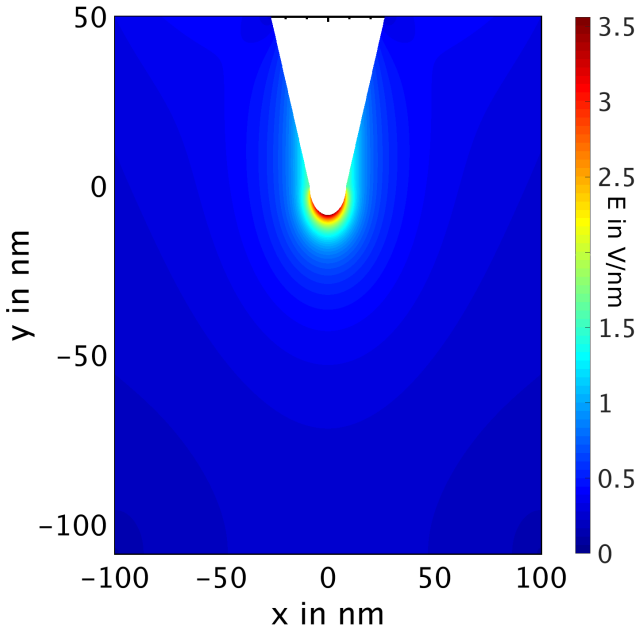

Figure 3.1: Color-coded electric field of a chosen parameter set (3D model: $d = 100\,nm, R = 8.5\,nm, \gamma = 20°, U = 30\,V$).

the tip can be described by

$$E_{max} = \frac{U}{k_s\, r}\,. \tag{3.1.1}$$

Here, the (spherical) macroscopic electric field $E_s = U/r$ was used, which depends on the applied voltage U and the tip (or sphere) radius r. The deviation of the tip shape from a spherical geometry is included in the spherical field correction factor k_s or the spherical field enhancement factor $\kappa_s = \frac{1}{k_s}$ [80].
If we treat the tip and the sample as a variation of a plate capacitor, the following definition for the maximal electric field can be used

$$E_{max} = \kappa_p\, \frac{U}{d}\,, \tag{3.1.2}$$

where the macroscopic electric field of a plate capacitor (without a tip) $E_p = U/d$ depends on the tip-sample distance d instead of the tip radius r in contrast to eq. (3.1.1). Here, κ_p is the respective field enhancement factor.
Different analytical expressions for the field enhancement factor can found in the literature [78, 80, 81, 83–90]. However, only a few [78, 80, 83, 84] are applicable to our case, which is defined by the ratio of tip-sample distance to tip length $\frac{d}{L} \in [0.001, 0.1]$, and the ratio of the tip radius to its length $\frac{r}{L} \in [0.0002, 0.02]$ (values taken from experimentally used tips).
For the plate capacitor model, two different distance definitions are typically used. Some authors define the field enhancement factor $\tilde{\kappa}_p$ by using the distance $D = d + L + r$ between sample and emitter plane. Thereby, they assume the tip as a small "protrusion" of an otherwise flat emitter plane [78, 81, 83–90].

Table 3.1: Overview of analytical models.

#	Reference	Eq.	Model	Conditions
1	Mesa et al. [80]	(3.1.5)	hyperboloid over plane	$\frac{r}{L} \in [0.01, 10]$
2	Miller [83]	(3.1.6)	floating sphere	$d \geq L$
3	Podenok et al. [78]	(3.1.7)	hemisphere on post	$\frac{d}{L} \in [0.01, 10]$

The second approach [83,91,92] uses κ_p (eq. (3.1.2)) defined by the distance d between sample and tip-apex. The relation between the enhancement factors $\kappa_p(d)$ and $\tilde{\kappa}_p(D)$ is trivially given by [78]

$$\kappa_p(d) = \frac{\tilde{\kappa}_p(D)}{1 + \frac{L}{d} + \frac{r}{d}} = \tilde{\kappa}_p \frac{d}{D} \tag{3.1.3}$$

and $\kappa_p(d)$ and the spherical correction factor k_s are obviously related by:

$$\kappa_p = \frac{d}{k_s\, r}\,. \tag{3.1.4}$$

However, other definitions (e. g., used by Dyke and Dolan [93]) can be found in literature as well.
Here, the analytical models will be given as κ_p to allow better comparability and their main properties are summarized in table 3.1. The different geometries are drawn in fig. 3.2, from which these analytical models were derived and the parameters are represented graphically. The analytical models are characterized in the following:

- Mesa et al. [80] (model 1) derived an analytical expression for a "hyperboloid in front of a plane" (fig 3.2 c)) by using the spherical correction factor:

$$\kappa_p = \frac{2\sqrt{d(d+r)}}{r \ln\left(\frac{1+\sqrt{\frac{d}{d+r}}}{1-\sqrt{\frac{d}{d+r}}}\right)}\,. \tag{3.1.5}$$

- Miller [83] (model 2) considered a "floated sphere at emitter potential" (fig. 3.2 a)). His field-enhancement relation for $d \geq L$ considers also the tip-sample distance d:

$$\kappa_p = \left(\frac{L}{r} + 3.5\right)\frac{d}{D} + \exp\left[-\frac{d}{L+r}\sqrt{\frac{L}{r} + 3.5}\right]\,. \tag{3.1.6}$$

- Podenok et al. [78] (model 3) simulated a "hemisphere on a post" model (fig. 3.2 b)) via FEM solver and fitted the results using a separation ansatz

$$\tilde{\kappa}_p(D) = f(L/r)\, g(L/d, d/r)\,.$$

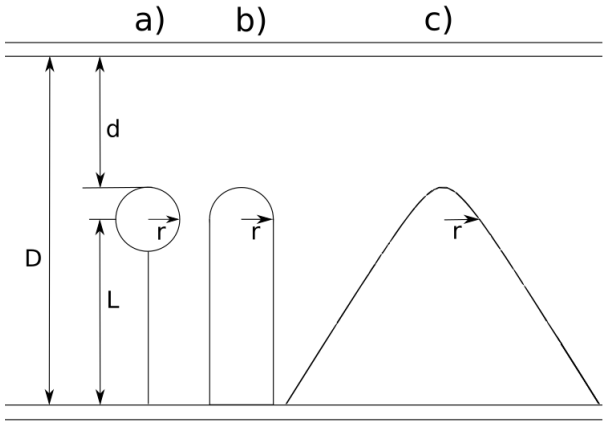

Figure 3.2: Scheme of different field enhancement models found in literature.

Their model for the field enhancement yielded

$$\kappa_p = \left[1.13\left(\frac{L}{r}\right)^{0.912} + 3\right] \times \left[1 + a_1\frac{L}{d}\right]\left[1 + a_2\frac{r}{d}\right]\left[1 + a_3\frac{r^2}{d^2}\right]\frac{d}{D}\,. \tag{3.1.7}$$

Here, the constants are given by $a_1 = 3.08 \times 10^{-3}$, $a_2 = 0.818$ and $a_3 = -9.18 \times 10^{-3}$ [78]. For very small tip-sample distances $d \approx r\sqrt{-a_3}$ the last factor of eq. (3.1.7) becomes negative. However, it is improbable that the assumed continuous classical theory is still applicable in this regime [78] since atomic and quantum effects need to be considered.

The models introduced here describe the dependence of the maximal field enhancement factor κ_p on the tip-sample distance d, the tip radius r, and the tip length L. Since small tip-sample distances ($d \leq 100\,nm$) are used in FE-SPL, $d \to 0$ is used to validate the analytical expressions (3.1.5−3.1.7). In the limit $d \to 0$, κ_p approaches 1 because for very small tip-sample distances the geometry approaches the plane-to-plane case for $d \ll r$. The same argument is valid for the limit $r \to \infty$. Only the models 1 and 2 yield the correct limit for $\frac{d}{r} \to 0$ and, therefore, model 3 will not be considered further.
An additional limit evolves from the fact that the tip length is much larger than the tip radius and tip-sample distance in reality, which leads to the assumption $L \to \infty$, which is used in the numerical simulation. To account for this assumption, κ_p of model 1 and 2 is used for the comparison with the FEM data in the limit $L \to \infty$. The analytical expression of model 1 is independent of L, the limit is simply given by (3.1.5). The limit for model 2 is equal to

$$\lim_{L\to\infty} \kappa_p = \frac{d}{r} + 1\,. \tag{3.1.8}$$

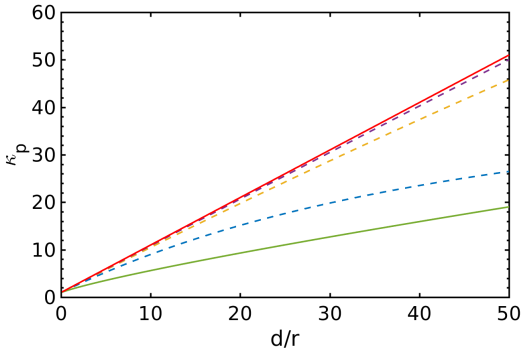

Figure 3.3: Maximal field enhancement factor κ_p as a function of tip-sample distance d over tip radius r for the models 1 (green) and 2 (red) taken from Mesa et al. [80] and Miller [83], respectively. The enhancement factors are plotted in the limit $L \to \infty$ (solid lines) whereas the broken lines represent the results of model 2 for tip lengths of $L = 0.1\,\mu m$ (blue), $1\,\mu m$ (yellow) and $10\,\mu m$ (purple).

In fig. 3.3, the field enhancement factor κ_p for models 1 and 2 are plotted in the limit $L \to \infty$ and in addition for three different values of the tip length L for model 2.
In section 8.1.1, the two analytical expressions (3.1.5) and (3.1.8) for $L \to \infty$ will be compared to the FEM data obtained for the FE-SPL case.
The maximal field enhancement κ_p enables the computation of the (maximal) electric field strength E_{max} by eq. (3.1.2), which determines the field-emission current density following the Fowler-Nordheim theory.

3.2 Fowler-Nordheim theory

The Fowler-Nordheim theory describes the tunneling of electrons from a flat metallic surface into vacuum by application of a sufficiently large electric field [94,95]. The main ingredients for the field emission current density

$$J(E,T) = \int_0^\infty d\epsilon_z \, j_{inc}(\epsilon_z, T)\, P(\epsilon_z, E) \tag{3.2.1}$$

are the tunneling probability P, and the incident current density j_{inc}, which describe how probable it is for the electrons to overcome the potential barrier, i. e., mainly the work function, and how many electrons are available, respectively. The tunneling probability can be simplified to the one dimensional (here in z direction) problem of one electron tunneling through a specific barrier by assuming a planar emission surface of infinite lateral extent [96] and the free-electron theory proposed by Sommerfeld [97]. The incident current density j_{inc} of the electrons within the metal can be expressed by the electron density D multiplied by the elementary charge e [96,98]. Since the theory stems from the late 1920s and several good books are available [96,98,99], this section will only give a brief overview of the derivation but not strictly follow the original derivation published by Fowler and Nordheim [94,95].

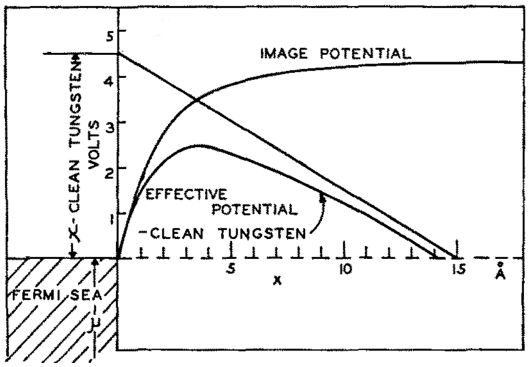

Figure 3.4: Electronic potential and energy diagram at a metal surface in the presence of an applied electric field including the image charge potential (adapted from [102]).

For the quantum mechanical derivation of the one-electron tunneling probability P in one dimension, it is assumed that there is no Coulomb interaction between two or more tunneling electrons. This is a good approximation for our FE-SPL case with currents in the pA range, i. e., the time between subsequent electrons is in the order of nanoseconds but the time of flight between tip and sample is in the femtosecond regime. Therefore, the electrons outside the metal tip only sense an averaged potential of the form

$$V(z) = \epsilon_F + \Phi - e\,E\,z - \frac{e^2}{16\pi\,\varepsilon_0\,z}\,,\ \text{for}\ z > 0 \tag{3.2.2}$$

including the electric field potential $V_e(z > 0) = -e\,E\,z$ and the image charge potential $V_{im}(z > 0) = -\frac{e^2}{16\pi\,\varepsilon_0\,z}$ (where ε_0 is the vacuum permittivity) [100, 101]. Inside the metal, there is a constant potential $V(z < 0) = 0$ (as shown in fig. 3.4). Here, Φ and ϵ_F represents the work function and the Fermi level of the metal, respectively. The potential maximum is equal to $V_{max}\epsilon_F+\Phi-\sqrt{\frac{e^3\,E}{4\pi\,\varepsilon_0}}$ and found at the position $z_{max} = \sqrt{\frac{e}{16\pi\,\varepsilon_0\,E}}$ [96]. Based on a generalized Wigner-Kramers-Brillouin (WKB) approach for slowly varying potential barriers from Miller and Good [103], the electron energy ϵ_z (in z direction) and electric field E dependent transmission probability, i. e., the ratio of transmitted and incident current density, can be calculated by

$$P(\epsilon_z, E) \equiv \frac{j_t}{j_{inc}} = \frac{1}{1 + \exp\left(Q(\epsilon_z, E)\right)}\,, \tag{3.2.3}$$

with

$$Q(\epsilon_z, E) = -2i \int_{z_1}^{z_2} \lambda(z, \epsilon_z, E) dz\,, \tag{3.2.4}$$

$$\lambda(z, \epsilon_z, E) = \sqrt{\frac{2m_e}{\hbar^2}\Big(\epsilon_z - V(z, E)\Big)}\,. \tag{3.2.5}$$

The integral boundaries z_1 and z_2 are the roots of the equation

$$\lambda^2(z, \epsilon_z, E) = \frac{2m_e}{\hbar^2}\left(\epsilon_z - \epsilon_F - \Phi + e\,E\,z + \frac{e^2}{16\pi\,\varepsilon_0\,z}\right) = 0\,. \tag{3.2.6}$$

Using the definition from Groves [96]

$$\rho(\epsilon_z, E) = \frac{2\,e\,E}{\epsilon_F + \Phi - \epsilon_z}\,z\,, \tag{3.2.7}$$

$$y(\epsilon_z, E) = \frac{2}{\epsilon_F + \Phi - \epsilon_z}\sqrt{\frac{e^3\,E}{16\pi\,\varepsilon_0}}\,, \tag{3.2.8}$$

the integral (3.2.4) can be transformed to

$$Q(\epsilon_z, E) = \frac{16\,m^2\,e^{\frac{5}{4}}}{3\,\hbar\,(16\pi\,\varepsilon_0)^{\frac{3}{4}}E^{\frac{1}{4}}\,y^{\frac{3}{2}}(\epsilon_z, E)}\,v\big(y(\epsilon_z, E)\big)\,, \tag{3.2.9}$$

$$v(y) = -\frac{3i}{4\sqrt{2}}\int_{1-\sqrt{1-y^2}}^{1+\sqrt{1-y^2}} d\rho\,\sqrt{\rho + \frac{y^2}{\rho} - 2}\,. \tag{3.2.10}$$

The function $v(y)$ can be expressed as elliptic integrals as found by Murphy and Good [104]. A more recent approach used a series expansion to estimate $v(y)$ [105]. Tabulated values of $v(y)$ can also be found in literature [98, 99]. Here, the expression from Spindt et al. [106] is used, giving $v(y) \approx 0.95 - y^2$. The one dimensional transmission probability $P(\epsilon_Z, E)$ for one electron is thus equal to

$$P(\epsilon_z, E) = \left[1 + \exp\left(\frac{16\,m^2\,e^{\frac{5}{4}}}{3\,\hbar\,(16\pi\,\varepsilon_0)^{\frac{3}{4}}E^{\frac{1}{4}}\,y^{\frac{3}{2}}}\,v(y)\right)\right]^{-1} \tag{3.2.11}$$

for $\epsilon_z < V_{max}$ and $P(\epsilon_z > V_{max}, E) \simeq 1$.
After derivation of the transmission probability, the incident current density j_{inc} of electrons impinging the surface from within the metal with a normal energy between ϵ_z and $\epsilon_z + d\epsilon_z$ needs to calculated. Therefore, the number of electrons per unit volume in the range $dp_x\,dp_y\,dp_z$ of momentum space is used, i. e., $N\,dp_x\,dp_y\,dp_z$, which is the number of cells in the phase space volume multiplied by the Fermi-Dirac distribution

$$N\,dp_x\,dp_y\,dp_z = \left(\frac{2}{h^3}\right)\left[1 + \exp\left(\frac{\epsilon - \epsilon_F}{k_B T}\right)\right]^{-1} dp_x\,dp_y\,dp_z\,. \tag{3.2.12}$$

In terms of velocities and after integration over the unrestricted components v_x and v_y, the distribution of electrons with normal velocities between v_z and $v_z + dv_z$ can be found [99] by

$$N\,dv_z = \frac{4\pi\,m_e^2\,k_B T}{h^3}\ln\left(1 + e^{-\frac{\epsilon_z - \epsilon_F}{k_B T}}\right)\,dv_z\,. \tag{3.2.13}$$

Multiplying eq. (3.2.13) by the elementary charge e and the velocity v_z, the incident current density for energies between ϵ_z and $\epsilon_z + d\epsilon_z$ is obtained by [96]

$$j_{inc} = e\, v_z\, N\, dv_z = \frac{4\pi\, m_e\, e\, k_B T}{h^3} \ln\left(1 + e^{-\frac{\epsilon_z - \epsilon_F}{k_B T}}\right) d\epsilon_z\,, \tag{3.2.14}$$

where $v_z\, dv_z = 1/m_e\, d\epsilon_z$ was used.
Therewith, the current density for the emitted electrons (eq. (3.2.1)) can be calculated by

$$\begin{aligned} J(E,T) &= \int_0^\infty d\epsilon_z\, j_{inc}(\epsilon_z, T)\, P(\epsilon_z, E) \\ &= \frac{e\, m_e\, k_B\, T}{2\pi^2\, \hbar^3} \left[\int_0^{V_{max}} d\epsilon_z\, \frac{\ln\left(1 + \exp\left(-\frac{\epsilon_z - \epsilon_F}{k_B\, T}\right)\right)}{1 + \exp\left(Q(\epsilon_z)\right)} \right. \\ &\quad \left. + \int_{V_{max}}^\infty d\epsilon_z\, \ln\left(1 + \exp\left(-\frac{\epsilon_z - \epsilon_F}{k_B\, T}\right)\right) \right] \end{aligned} \tag{3.2.15}$$

In the cold field emission case $T \to 0K$, the electron number $N(\epsilon_z, T) \propto \ln(1 + \exp(-(\epsilon_z - \epsilon_F)/k_B T))$ vanishes rapidly if the electron energy exceeds Fermi's energy ϵ_F, i. e., the second integral in eq. (3.2.15) is negligible. Additionally, for common metal barriers ($\Phi \approx 4.5\, eV$, $E \approx 1\, V/nm$) the transmission probability P reduces significantly for energies ϵ_z below ϵ_F. Thus, the first integrand of eq. (3.2.15) has only non-vanishing contributions near the Fermi level and the integration limits can be set to $\pm\infty$. Additionally, the function Q is much larger than 1, i. e., $1 + \exp Q \approx \exp Q$. Using these assumptions, the current density can be rewritten to

$$J(E,T) = \frac{e\, m_e\, k_B\, T}{2\pi^2\, \hbar^3} \int_{-\infty}^{+\infty} d\epsilon_z\, \ln\left(1 + e^{-\frac{\epsilon_z - \epsilon_F}{k_B\, T}}\right) e^{-Q(\epsilon_z)}\,. \tag{3.2.16}$$

Using only the first two terms of a Taylor expansion of Q around ϵ_F enables an analytical evaluation of the remaining integral. For very low temperatures the well-known Fowler-Nordheim equation [94, 95] is obtained [98]

$$J(E) = A'\, E^2\, \exp\left(-\frac{B'\, \Phi^{3/2}}{E}\right) \tag{3.2.17}$$

with the following parameter definitions:

$$\begin{aligned} A' &= \frac{e^3}{16\pi^2 \hbar\, \Phi\, t^2\,(y_0)}\,, \\ B' &= \frac{4}{3e}\sqrt{\frac{2m}{\hbar^2}}\, v\,(y_0)\,, \\ t(y) &= v(y) - \frac{2}{3}\, y\, \frac{dv(y)}{dy}\,, \\ y_0 &= 2\, \frac{\sqrt{e^3\, E}}{\sqrt{16\pi\, \varepsilon_0}\, \Phi}\,. \end{aligned}$$

However, two slightly different parameter definitions are used within this work. The first one was used by Spindt et al. [106]

$$\begin{aligned} A_S &= \frac{e^3}{16\pi^2\hbar} && \approx 1.54 \times 10^6 \, \frac{pA\, eV}{V^2}\,, \\ B_S &= \frac{4}{3e}\sqrt{\frac{2m}{\hbar^2}} && \approx 6.87 \, \frac{V}{nm\, eV^{3/2}}\,, \\ y_0 &= \frac{\sqrt{e^3\, E}}{\sqrt{4\pi\, \varepsilon_0}\, \Phi} && = \hat{y}_0 \, \frac{\sqrt{E}}{\Phi}\,, \\ \hat{y}_0 &= \frac{\sqrt{e^3}}{\sqrt{4\pi\, \varepsilon_0}} && \approx 3.79 \times 10^{-1/2} \, \frac{eV\, nm^{1/2}}{V^{1/2}}\,, \\ v(y_0) &\approx 0.95 - y_0^2\,, && t^2(y_0) \approx 1.1\,, \end{aligned}$$

which yields the following version of the Fowler-Nordheim equation

$$J(E) = A_S \, \frac{E^2}{\Phi\, t^2(y_0)} \, \exp\left(-B_S \frac{\Phi^{3/2}}{E} \, v(y_0) \right) . \tag{3.2.18}$$

The other one was taken from Mayer et al. [77] using

$$\begin{aligned} A &= \frac{A_S}{t^2(y_0)}\,, \\ B &= \hat{y}_0^2 \, B_S\,, \\ C &= 0.95 \, B_S \end{aligned} \tag{3.2.19}$$

leading to

$$J(E, \Phi) = A \, \frac{E^2}{\Phi} \, \exp\left(\frac{B}{\Phi^{1/2}} - \frac{C\, \Phi^{3/2}}{E} \right) . \tag{3.2.20}$$

The parameter values used for A, B and C can be found in tab. 8.1.
In section 9.2, the version of Spindt et al. [106] (eq. (3.2.18)) was used for comparing experiment and theory because it involves only two parameters A_S and B_S. However, eq. (3.2.20) from Mayer et al. [77] expresses the dependency on the electric field E and the work function Φ more clearly and is used otherwise.

In summary, based on the electric field strength E the field emission current density can be determined assuming a flat surface and low temperatures. In fig. 3.5, the emission current density J in dependence of the electric field strength E is plotted. The black dots represent listed values of the publication of Dolan [107] and the colored lines are results using eqs. (3.2.20) and (3.2.19). The Dolan obtained his data by considering different materials: tungsten with its averaged work function of $\Phi = 4.5\, eV$ and with $\Phi \approx 5\, eV$ for its (110) face as well as platinum ($\Phi \approx 6.3\, eV$) [107]. The lower work function values are said to be useful, e. g., for barium-coated tungsten cathodes [107].
In fig. 3.5, it is obvious that the maximal current density for electric field strengths from $1\, V/nm$ to $20\, V/nm$ is increased by more than 20 orders of

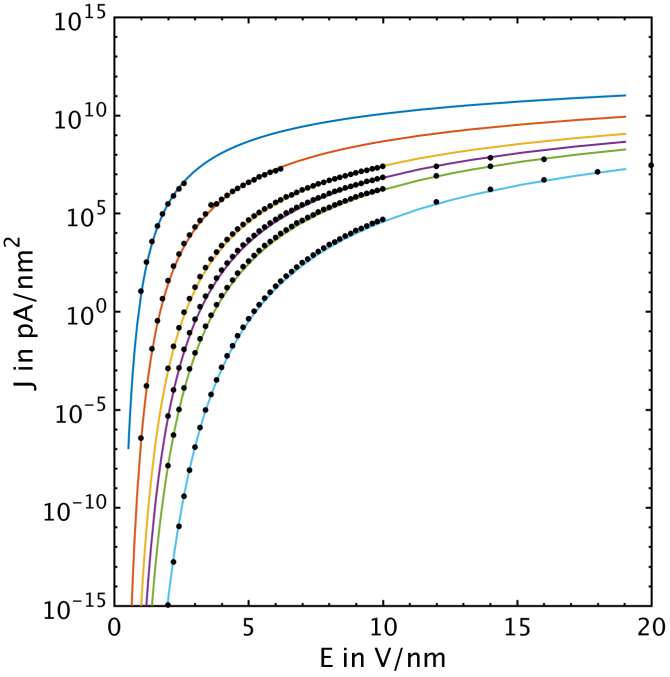

Figure 3.5: Field emission current density J over the electric field strength E (solid lines) together with the data published by Dolan [107] (black dots). The work function was set to $\Phi = 2\,eV$ (blue), $3\,eV$ (red), $4\,eV$ (yellow), $4.5\,eV$ (purple), $5\,eV$ (green) and $6.3\,eV$ (cyan), respectively.

magnitude. Thus, the numerical or analytical model for field-emission scanning probe lithography, described in this thesis, has to ensure a highly accurate estimation of the electric field[1] and so of the field enhancement (see previous chapter) to yield results comparable to experimental data.
Although the tip surface is not flat, most often one of the eqs. (3.2.17)-(3.2.20) is used to calculate the field emission [5, 106, 108] and, thus, the lithographic behavior of a system containing a sharp nanotip and a resist-covered sample [6, 22, 75, 77]. Thereby, the electric field is calculated for the respective nanotip. In these approaches, the geometry is only taken into account by the electric field calculation. Serena et al. [109] considered a similar approach but used a general formulation of eq. (3.2.15). However, some authors only used the (maximal) field enhancement factor as an estimate of the field emission [79, 80].
The influence of the tip geometry on the field emission process besides its effect on the electric field was studied by He et al. [110–112]. They studied the effect of the geometry on the image charge potential and the Fowler-Nordheim eq. (3.2.17) for tip radii below $10\,nm$. They found that the image charge potential had a smaller influence on the field emission than the electric field potential

[1] The electric field strength is estimated to vary between $0.1\,eV$ and $10\,eV$ in the FE-SPL case.

and that the third term of the Taylor expansion (proportional to $(\epsilon_z - \epsilon_F)^2$) leading to eq. (3.2.17) needs to be considered as well [110]. Unfortunately, they only considered the electric field along the tip axis and did not study the effect on the spatial distribution of the current density.
This was verified experimentally for ultrasharp tungsten field emitters ($r \approx 0.24\,nm$) leading to very large electric field strengths of about $30\,V/nm$ [113]. For larger tips and smaller field strengths, the original Fowler-Nordheim eq. (3.2.17) yielded good predictions as shown by He et al. [111]. Edgcombe and de Jonge derived a theory for emitters with spherical caps to determine parameters like work function and apex radius from experimentally obtained Fowler-Nordheim plots and energy distribution measurements of the same emitter [114]. Recently, Kyritsakis and Xanthakis published a generalized Fowler-Nordheim theory for nanoscopic tips [115, 116].
The influence of the geometry on the electron supply for nanotips with quantum-confined electron states was presented by Patterson and Akinwade [117].
Nevertheless, the Fowler-Nordheim equation (3.2.17) including the geometry-dependent electric field should give sufficient accurate results for conventionally etched emitter tips ($r_{tip} \gtrsim 10\,nm$) [111, 115]. Since the tips used in our FE-SPL belongs to this category, the standard Fowler-Nordheim equation in the form of (3.2.20) and (3.2.18) is used in this thesis to estimate the lithographic properties.
To expand the investigation to cover semiconductor tips, field emission from the valence and conduction band (including band bending at the surface) and surface state emission would need to be considered as mentioned by Gomer [99].

3.3 State-of-the-art theory for lithographic application

The first studies on field-emission based lithography from nanotips were published by McCord and Pease already in the late 1980s [5, 6], shortly after the invention of STM [55] and AFM [8, 56]. They used a setup consisting of a sphere and a plane, for which they calculated the field distribution by a series of point charges. From the electric field at the tip surface, they computed the current density distribution on the sphere based on a Fowler-Nordheim equation without image charge correction. Next, the current density at the sample was obtained using the ratio of the emission area and the exposed area. The exposed area was determined using the electron trajectories. The full-width half-maximum of the current density distribution was used as a measure of the electron beam radius on the sample. With this model, McCord and Pease found that the minimal beam diameter depends on the tip radius and an optimal value for the ratio of tip-sample distance and radius, which was identified for their configuration [5]. Additionally, they pointed out that the beam radius decreases if the electron energy is reduced [5]. My "nanolithography program" (see chapter 5) is inspired by the studies of McCord and Pease but uses different numerical algorithms and a more realistic geometric model, since they did not use a emission tip and completely neglected the resist layer. Additionally, a systematic analysis of the physical values is part of this thesis.

In their second paper, they performed a Monte Carlo simulation to investigate two kinds of backscattered electrons at the sample surface without a resist layer [6]. They called elastically backscattered electrons "reflected" electrons, which have the same energy as the "primary" electrons hitting the sample in the first place. The "secondary" electrons are the ones, which are inelastically backscattered with energies between 2 and $20\,eV$. They assumed certain backscattering rates and calculated the trajectories of the backscattered electrons to determine if a broadening of the current density occurs. Thereby, an assumption was made that approx. 30% of the primary electrons are reflected independent on the exposed material for primary energies below $100\,eV$ [6]. For the secondary electron emission coefficient, they expect a value below 1.2 for energies below $100\,eV$ and an energy distribution peak at around $2\,eV$ [6]. Both reflected and secondary electrons are assumed to have an angular emission distribution, which can be described as a cosine distribution [6]. They reported that an increase of the written pattern size might occur due to the backscattered electrons since for radial distances at the samples above $10\,nm$ from the maximum of the electron number density, the reflected electrons dominate the electron density distribution. This would cause a proximity effect as known from EBL. McCord and Pease found that a decrease of the radius increases the width of the electron density [6] using a constant-current mode. This was explained by the increased tip-sample distance and by an increased radial component of the electric field relative to the vertical one. So, they conclude that broader tips will increase the line width but decrease the proximity effect due to a reduced range of reflected electrons. The secondary electrons are found to be negligible since they have either insufficient energy to expose the resist or their number is not high enough to have an effect [6]. This work can be seen as the basis for the "Monte Carlo simulation" part of this thesis (see chapter 6) related to the resist interactions, which includes elastic and inelastic scattering events with variable scattering rates in the (ultra-thin) resist layer to investigate the lithographic process. Since McCord and Pease's study [6] only considered the effect of the two types of backscattered electrons without taking the scattering events inside a resist layer into account, the main interaction paths were not investigated so far.

After a gap of around ten years, three groups published further theoretical considerations on FE-SPL, which are Dobisz et al. [22, 23], Mayer et al. [77] and the group of Wilder and Quate [32, 75, 76, 118, 119].

Dobisz et al. [22, 23] used a finite-element type electron optics program to calculate the electric field distribution and the electron trajectories for a geometry consisting of a sphere over a sample. In their case, the sample was covered with a resist layer of different thickness. Additionally, they considered a $1\,nm$ thick water film on top of the resist layer, which was treated as an additional dielectric layer with a dielectric constant $\varepsilon = 81$. They reported that a $1\,nm$ water layer has no significant effect electrostatically [23]. Since they did not calculate the field emission probability in this part of their study, the electrons were considered to be emitted solely from the point of the tip apex with emission angles in the range of $\pm 80°$. They found that by increasing the resist

thickness, the electric field will be increased for a constant tip-sample distance and the electron energy at the resist surface will be decreased [23]. Additionally, they used a field emitter simulation code, which includes an analytical model for the electric field using a hyperbolic tip [22] . This electric field distribution was used for the determination of the current density distribution by a Fowler-Nordheim equation and a calculation of electron trajectories using a finite-difference approach. From their simulations, they concluded that a change of tip-resist distance has a larger effect than a tip radius change. They also expected that the line width will be controlled by the emission profile at the tip and the scattering inside the resist but could not prove it with their approach, which is part of my thesis.
The publication of Mayer et al. [77] includes a three dimensional electric field calculation (taking the spherical symmetry into account) using finite-differences, the determination of the current density distribution at the tip using the Fowler-Nordheim eq. (3.2.20) and at the sample by applying an electron trajectory code. The beam diameter was defined as 60% of the total current [77]. In their systematic analysis, they describe the dependence of the beam diameter on the bias voltage, tip-sample separation, work function and different tip geometries. The work of Mayer et al. [77] was extended here by considerations of a resist layer and by using an experimentally proposed approach to predict the line width using a threshold value of the electron density as explained in section 5.4.
Wilder et al. [32, 76, 118, 119] published mostly experimental results but also a theoretical investigation [75]. They performed a numerical two dimensional calculation for the electric field distribution using a finite-element method algorithm provided by the PDE toolbox of Matlab®. Beside the sphere-on-a-cone geometry, they even include a resist layer but use only two tip-resist distances, $1\,nm$ and $31\,nm$. They assume the smaller distance to be a representation of their contact-mode lithography, but since they use a set-up in ambient conditions, a water meniscus [120] should have been taken into account for tip-sample distances below $5\,nm$ [121] or they should consider to be already in the tunneling regime under vacuum conditions [122]. Based on the electric field distribution, they calculated the current density distribution at the tip and used the electric field lines as a measure for the electron trajectories. Unfortunately, in their work, they did not present current density distributions on the resist or sample surface. Their main theoretical result is that the tip should be held in close proximity of a sample covered with a thin resist layer to achieve good resolution [75].
To summarize, there are several different approaches to describe the lithographic process theoretically. All of them simulate the electric field electrostatically, which is mostly used to calculate the field emission current density at the tip and for the electron trajectory computation. However, not all of them include a resist layer in their study and only one publication presents a systematical investigation of the effects of different parameters like tip-sample distance d, tip radius r, bias voltage U and work function Φ on the beam diameter [77]. They used a definition commonly used for EBL, which does

not include a threshold value for the current density, which was found experimentally for our FE-SPL case. Only one group also considered the electron energy as an influence for the resist patterning [22,23]. Finally, the scattering approach of McCord and Pease [6] was not improved so far and the electron-resist interactions were not studied in more detail.
My study extends the previous investigations by (a) considering the influence of electron energy distribution inside the tip on the emission process; (b) calculating more realistic electron trajectories (compared to Wilder et al. [75]); (c) including a resist layer with various thickness, local changes in the dielectric constant and in the morphology; (d) including a Monte Carlo simulation calculating the trajectories and scattering processes inside the resist layer, which also considers the electric field inside the resist.
It was argued previously that electrons may lead to a high amount of secondary electrons and large interaction volumes to due a series of scattering events caused by the acceleration inside the resist layer [75]. However, this hypothesis was not yet studied.
A systematic investigation of the influence of the parameters (tip radius, opening angle, work function, voltage and tip-sample distance) was accomplished, which leads to an analytical description of the field-emission scanning probe lithography process. From these study, optimal parameter ranges can be defined. The comparison with field emission measurements enables a first evaluation of the theoretical model, which is presented in chapter 9.2.
The methodology and implementation are explained in the following part.

Part II

Mathematical methods and implementation

In this part, the implemented numerical model is described, consisting of two main parts, namely the nanolithography program (chapter 5) and the Monte Carlo simulation (chapter 6).
The nanolithography program includes all computational steps necessary for determining the current density distribution at the surface of the resist and sample, respectively. These are:

- *Calculation of the electric field:* Due to the bias voltage applied between tip and sample an electric field is generated, which is computed using a finite-element method approach for the electrostatic potential (see section 5.1).
- *Determination of the current density distribution at the tip surface:* The locally enhanced electric field at the tip apex enables field emission of electrons, which is modelled by the Fowler-Nordheim theory (see section 5.2).
- *Computation of electron trajectories from the tip to the sample surface:* The emitted electrons are accelerated towards the sample surface due to the electric field. The respective calculation is based on an one-step Leapfrog algorithm (see section 5.3).
- *Calculation of the current density distribution at the sample surface:* For the analysis the current or electron's density distribution is crucial, which is gained from the current density at the tip and the ratio of emission and exposure area (see section 5.4).

The main outcome of the nanolithography program is the electronic density distribution at the sample surface in dependence of the parameters of the tip (e. g., radius), external parameters (e. g., tip-sample distance) but also resist parameters (thickness, etc.). The electronic density distribution leads to beam diameter and line width for lithography. Furthermore, the energy distribution at resist and sample surface are calculated.
The Monte Carlo simulation includes elastic and inelastic scattering events (see sections 6.1 and 6.2, respectively) inside, and trajectories of interacting electrons inside and outside (backscattered electrons) the resist layer. The trajectories are calculated with an adapted version of the Leapfrog algorithm explained in section 5.3. The simulation procedure is explained in section 6.3 whereas the criteria for termination of the simulation is introduced in section 6.4. This simulation part leads to insights into the propagation of the electrons and their interaction with the resist molecules. Here, the interaction volume and the distribution of different scattering events are analyzed.
Before these parts of the computation are explained in detail, the geometrical model and the used assumptions are introduced in sections 4.1 and 4.2, respectively.

Chapter 4

Model description and assumptions

4.1 Geometrical models

The experimental set-up of the FE-SPL tool (shown in fig. 2.2) consists of a lot of components like piezoelectric actuators, electronics, field-programmable gate array, mechanical stage, etc. necessary for successful operation.
However, for the theoretical investigations presented here, the geometry consists of only a metallic tip and a metallic sample as shown in fig. 4.1. The parameters describing the geometry of the tip are the radius r, the opening angle γ and the tip length L. The geometric parameter adjustable during experiments is the tip-sample distance d. The geometry shown in fig. 4.1 is used for the field emission studies and for comparison with the field emission experiments. Additionally, it is used for investigations of field-emission lithography without including a resist layer.

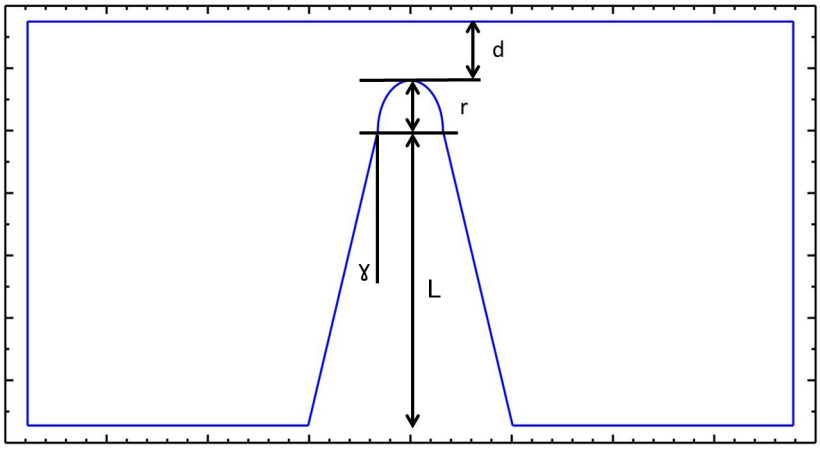

Figure 4.1: Tip geometry used for resist-less studies. The tip-sample distance d, the tip radius r, the opening angle γ and the length of the tip $L = 50\,nm$ are marked.

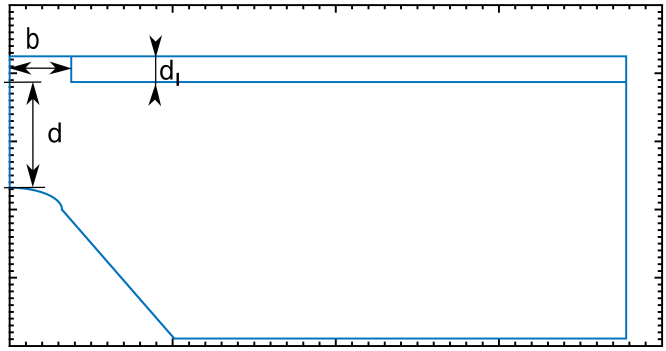

Figure 4.2: Tip geometry used for 3D simulations including a resist layer. The tip-resist distance d, the resist thickness d_l and the width b of the trench in the resist layer are marked. The height h of the trench is set to d_l in this example but was varied as well.

Beside the geometric parameters, the tip material is taken into account by the work function Φ and two adjustable external parameters, i. e., the bias voltage U applied at the sample and the writing speed v, are considered.
The model shown in fig. 4.2 was used to consider the influences of the resist layer. In addition to the already introduced parameters, the resist-layer thickness d_l, the width b and the height h of an existing trench are also taken into account. The definition of the parameter d is slightly changed since it defines the tip-resist distance rather than the tip-sample distance $D = d + d_l$ because it is more convenient for the discussions.
The resist layer is additionally characterized by its dielectric constant ε. Local modifications of the resist material are considered by the dielectric constant ε_2. A locally modified resist layer is assumed to be the result of a previous negative-tone lithography step, which yields to spatially defined cross-linking of resist molecules. Since there is nearly no swelling observed experimentally, a constant resist layer thickness d_l is assumed for this case, but different feature widths b are studied.
Besides the standard tips, two other tip types are tested in appendix B, which are presumed to increase the resolution and/or the throughput of FE-SPL.

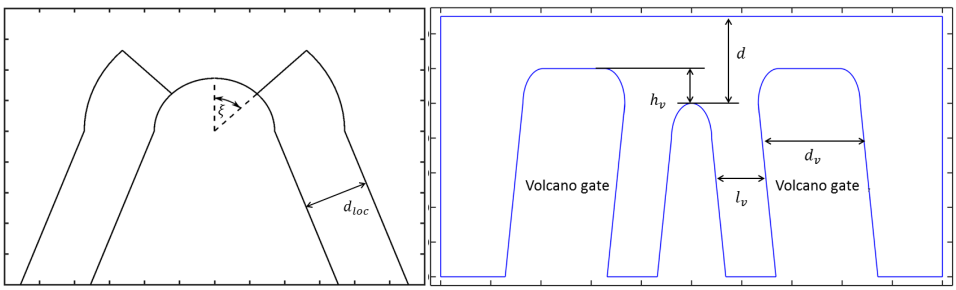

Figure 4.3: Tip geometry used for the investigations of the partially covered tips (*left*) and the volcano-gated tips (*right*).

Table 4.1: Standard parameter values and their variation ranges for computation.

Name	Explanation	Value	Range
	Internal tip parameters		
r_{tip}	Tip radius	$8.6\,nm$	$2\ldots20\,nm$
l_{tip}	Tip length (excl. r_{tip})	$50\,nm$	–
γ	Half opening angle of tip	$20°$	$5\ldots30°$
Φ	Work function of tip (tungsten)	$4.5\,eV$	$2\ldots6\,eV$
	External parameters		
d	Tip-sample (or tip-resist) distance	$10\,nm$	$10\ldots100\,nm$
U	Bias voltage between sample and tip	$50\,V$	$10\ldots100\,V$
v	Tip writing velocity	$1\,\frac{\mu m}{s}$	$1\ldots8\,\frac{\mu m}{s}$
τ	Exposure time in case of dot patterning mode	$1\,ms$	$1\ldots1000\,\mu s$
ν_{crit}	Threshold value for lithographic reaction	$100\frac{1}{nm^2}$	–
	Resist layer parameters		
d_l	Resist thickness	$10\,nm$	$10\ldots50\,nm$
ε	Dielectric constant of resist layer	3.7	$1\ldots10$
ε_2	Dielectric constant of feature in resist layer	6.6	$1\ldots10$
b	Trench width	$20\,nm$	$2\ldots100\,nm$
h	Trench height	d_l	$(0.2\ldots0.8)\cdot d_l$
ϵ_{co}	Cut-off energy for Monte Carlo simulation	$10\,eV$	$5\ldots15\,eV$
	Volcano-gated tip parameters		
d_v	thickness of volcano gate	$17\,nm$	–
h_v	gate-tip height difference (pos. value = buried tip)	$0\,nm$	$-20\ldots20\,nm$
l_v	tip-gate distance	$50\,nm$	–
Φ_v	work function of volcano gate	$4.8\,eV$	$2\ldots6\,eV$
	Partially covered tip parameters		
d_{loc}	Thickness of cover layer	$10\,nm$	$2\ldots10\,nm$
ξ	Half angle of the cover layer opening	$45°$	$5\ldots50°$
ε_{loc}	Dielectric constant of covering layer	3.9	$2\ldots10$

A covered tip is defined by the thickness d_{loc}, the opening angle ξ and the dielectric constant ε_{loc} of the covering layer (as shown on the left-hand side of fig. 4.3) whereas the volcano-gated tip is defined by the distance l_v, the height difference h_v between gate and tip, and the volcano gate thickness d_v (depicted on the right-hand side of fig. 4.3). The work function Φ_v and the bias voltage U_v between volcano gate and sample are considered as well.
In table 4.1, all used parameters are listed with their standard values together with the considered range of variations.

4.2 Assumptions

After introducing the geometry of the theoretical model and the used parameters, the assumptions are summarized in this section. The following boundary conditions and assumptions are used within the nanolithography and the Monte Carlo program:

- Modifications of sample and resist properties due to contaminations and imperfections are not considered, i. e., an isotropic resist material and flat sample and resist surface are used.

- We assume vacuum conditions and neglect the unavoidable water "film" on and partially in the resist layer in ambient conditions. The study of Dobisz et al. [23] includes a water film in their electrostatic calculation but found a negligible effect. However, a change of the water film shape is expected due to the electrostatic field, which leads to a water meniscus under certain conditions [33]. The accompanied charge and dipole re-allocations would influence the electrostatic calculation and chemical reactions would be enabled due to the presence of water affecting the presumed resist modifications.

- The assumption of low temperatures ($T \rightarrow 0$) and cold processes are used, thus, the standard Fowler-Nordheim equation [98] is applied and any heating effect due to electronic or other interactions is neglected. This might be justified by low emission currents and the difference between the thermal energy of room-temperature ($\epsilon_{th} \approx 0.03\,eV$) and expected electron energies ($\epsilon_{kin} \geq 10\,eV$). (Only the "advanced" 3D model in chapter 7 uses the temperature-dependent Fowler-Nordheim equation.)

- The effect of protrusions and contaminations of the tip and its crystal structure (due to spatially dependent work function of the tip) was neglected as well as any quantum confinement of electronic tip states [117] since the tip radii are $r \geq 2\,nm$. An adaption of the standard Fowler-Nordheim theory [115, 116] to account for the tip shape was not included.

- A ballistic transport of electrons between tip and sample is assumed since the tip-sample distance is in the range of tens of nanometer. The time of flight for an electron with $\epsilon_{kin} = 10\,eV$ is below $100\,fs$, which is much shorter than our estimation of the average time between two emitted electrons of about $7\,ns$. Additionally, the mean free-path in air (ambient conditions) is well above $100\,nm$ (see chapter 3). This also justifies the assumption of a (quasi-) steady state.

- Charge effects in the tip [123, 124], the resist and the sample were neglected due to the low currents.

- Dirichlet boundary conditions were applied at sample ($\phi = U$) and tip surface ($\phi = 0$) and von-Neumann boundary conditions at the bottom of the tip and at the sides of the simulation box [125].

- It is assumed that the inelastic scattering inside the resist is treatable as elastic electron-electron scattering [126].
- In the Monte Carlo simulation, a constant binding energy was assumed within the resist layer. Scattering of electrons with energies below the binding energy is taken to be negligible, i. e., these electrons move ballistically through the resist.
- No emission from dielectric layer covering the emission tip is taken into account in the respective investigation (section B.2).
- Classical corpuscles are used as representations of the electrons for the trajectory calculation since the de Broglie wavelength $\lambda = h/p = h/\sqrt{2m\,\epsilon_{kin}}$ [127] of electrons, even for $10\,eV$, is below $0.5\,nm$.
- Scattering mechanisms at the sample, the volcano gate and the tip are not included. Especially for the computation of volcano-gated tips, the trajectories of electrons hitting the gate were only computed up to the gate surface since the scattering at the gate is not included. The scattering at or in the sample was also neglected in the Monte Carlo simulation since the energy of the electron at the resist-sample interface is presumed to be below the binding energy.

Chapter 5

Nanolithography program

In this chapter, the nanolithography program consisting of the calculation of the electric field (section 5.1), the field emission current density (section 5.2), the trajectories of electrons (section 5.3) and the current density at sample and/or resist surface (section 5.4) is explained.

5.1 Electrostatic field calculation

The electric field is calculated from the electrostatic potential by $\vec{E} = -\nabla\varphi$. Thereby, φ is determined by solving the two dimensional Laplace's equation $\Delta\varphi = 0$ [128, 129] using the partial differential equation (PDE) toolbox from Matlab® [125]. This is a finite-element method calculation tool box for different kinds of PDE systems [125]. Thereby, the partial differential equation, in a general form, is given by

$$-\nabla\,(c\,\nabla u) + a\,u = f \tag{5.1.1}$$

using a two dimensional ∇-operator.
Here, two different models regarding the representation of the tip were applied. The first one is a straight-forward two dimensional model in Cartesian coordinates (x, z) for Laplace's equation [130]

$$\Delta\varphi = \left(\frac{\partial^2}{\partial x^2} + \frac{\partial^2}{\partial z^2}\right)\varphi = 0\,. \tag{5.1.2}$$

Such an approach was already published by Soh et al. [75] but the tip is actually modelled as a blade rather than a tip.
In the second more realistic approach, the rotational symmetry (i. e., $\varphi(r, z, \phi) = \varphi(r, z)$) of the tip is exploited. In this case, Laplace's equation in cylindrical coordinates (r, z) [130]

$$\Delta\varphi = \left(\frac{1}{r}\frac{\partial}{\partial r}\left(r\frac{\partial}{\partial r}\right) + \frac{\partial^2}{\partial z^2}\right)\varphi = 0 \tag{5.1.3}$$

was used. Mayer et al. published this approach in their work [77] but used a finite-difference rather than a finite-element method. The implementation of

eq. (5.1.3) with Matlab®'s PDE toolbox was done by setting the parameters of eq. (5.1.1) according to

$$c = \begin{pmatrix} -x & 0 \\ 0 & -x \end{pmatrix} \qquad a = 0 \qquad f = 0\,. \tag{5.1.4}$$

For all computations, the sample and the tip were set to a fixed bias voltage using Dirichlet boundary conditions. For the other boundaries, von-Neumann boundary conditions were used.
Regarding the computation of the electric field, one has to deal with two largely different length scales: the tip-sample distance is in the range of $d \in [10, 100]\,nm$, while the tip length L is typically 6 to $9\,\mu m$. Thus, the number of elements for a simulation covering the whole system with a spatial resolution capable of accurately representing the tip-sample distance would be huge. Fortunately, the highest electric field strength and so the highest field emission probability is obtained at the tip apex. Consequently, the complete tip does not need to be considered. A reduced tip length of $\tilde{L} = 50\,nm$ was used together with von-Neumann boundary conditions at the bottom of the nanotip, which simulates a tip length $L \to \infty$. Obviously, this reduces the simulation box dramatically and, thus, the computational effort and time.
A typical geometry was shown for the finite-element method calculation executed by the PDE toolbox of Matlab® for the resist-less case in fig. 4.1 and including a resist layer in fig. 4.2. The dielectric properties of the resist layer are included by using a modified c parameter given by

$$c = \begin{pmatrix} -\varepsilon x & 0 \\ 0 & -\varepsilon x \end{pmatrix} \tag{5.1.5}$$

inside the resist layer and the one given in eq. (5.1.4) otherwise. The parameter f and a remain unchanged since no electric charge movement is included.
The special cases of a covered tip, and a tip surrounded by a volcano gate are plotted in fig. 4.3. The layer partially covering the tip is approximated by a dielectric material and treated like a resist layer whereas the volcano gate is set to a potential ϕ_v using Dirichlet boundary conditions. The gate potential is applied to achieve either focusing or defocusing of the electron beam [20].
The electric field strength is calculated by $\vec{E} = -\nabla\varphi$, which is used for the solution of the Fowler-Nordheim equation [77,94,95] described in the following chapter.

5.2 Fowler-Nordheim emission

Based on the electric field strength $\vec{E}$ at the tip surface calculated by a finite-element method, the field emission current density can be determined.
The following two approaches are used. In the first, the Fowler-Nordheim equation (3.2.20) of Mayer et al. [77] is used

$$J(E, \Phi) = A\,\frac{E^2}{\Phi}\,\exp\left(\frac{B}{\Phi^{1/2}} - \frac{C\,\Phi^{3/2}}{E}\right)\,, \tag{5.2.1}$$

where A, B and C are constants taken from [77, 106]. The values can found in table 8.1. A derivation of eq. (5.2.1) can be found in section 3.2 explaining also the assumptions ($T \to 0$, etc.) used. Here, E and Φ are (the absolute value of) the electric field and the work function, respectively. In the case of a parallel-plate capacitor, i. e., a flat emitter surface (instead of an emitter tip), the electric field would be constant [77, 94, 95]. For the non-flat geometry of the tip, this is not valid. Thus, the current density $J(E(\vec{r}_{tip}), \Phi)$ has to be calculated for each point at the tip surface. Therefore, a non-uniform discretization at the tip surface is used, which is adapted to the strength of the field emission and thus the finest mesh is used for the tip apex. The grid points represent so-called emission spots, on which the current density is calculated based on the local electric field strength. The spot area A_{tip} around these emission spots is used to calculate the electron number and total current emitted from each emission spot. Since the electron number must not change between tip and sample (beside electrons leaving the simulation box), it can be used to calculate the current density at the sample surface.
In the second approach, the distribution of the initial velocities of electrons inside the nanotip is considered as well. Note, for a flat emission area, i. e., a constant electric field, the integration over the initial velocities lead to eq. (5.2.1) (see section 3.2). For the curved shape of the nanotip, the integration is only analytically achievable, if an analytical model exists describing the non-uniform electric field at the tip surface. Nevertheless, the emission current density can be given by

$$J = \frac{16\, e\, m_e \sqrt{\epsilon_{in}^3 \cos^2\theta\ (\Phi - \epsilon_F + \epsilon_{in}\cos^2\theta)}}{\hbar^3\,(\Phi + \epsilon_F)\left(1 + \exp\left(\frac{\epsilon_{in}-\epsilon_F}{k_B T}\right)\right)} \times \exp\left[-\frac{4\sqrt{2m_e\,(\Phi + \epsilon_F - \epsilon_{in}\cos^2\theta)^3}}{3e\hbar E}\, v(\epsilon_{in}, E, \Phi)\right] \cos\theta \sin\theta\, d\epsilon_{in}\, d\theta\, d\phi\,. \tag{5.2.2}$$

Here, ϵ_{in}, θ and ϕ are the initial electron energy, the polar, and the azimuthal angle, respectively. The physical constants are the electron charge e, Planck's constant $\hbar = \frac{h}{2\pi}$, the Fermi energy ϵ_F and Boltzmann's constant k_B. The temperature T was set to $300\,K$. By the help of this formula, the influence of the different angles and energy values around ϵ_F can be studied (see chapter 7).
Additionally, the image potential $v(\epsilon, E, \Phi)$ needs to be included. Here, two different approximations are compared. The first one was found in [99] where the following expression is used

$$v_G(\epsilon, E, \Phi) = \sqrt{1 - \hat{y_0}\,\frac{E^{1/2}}{\Phi + \epsilon_F - \epsilon_{in}\,\cos^2\theta}}\quad . \tag{5.2.3}$$

The second approximation for an image correction formula

$$v_S(\epsilon, E, \Phi) = 0.95 - \hat{y}_0^2 \left(\frac{E^{1/2}}{\Phi + \epsilon_F - \epsilon_{in} \cos^2 \theta} \right) \tag{5.2.4}$$

was published by Spindt et al. [106]. In both variants, the constant $\hat{y}_0 = \frac{\sqrt{e^3}}{\sqrt{4\pi\,\varepsilon_0}} \approx 1.2\,\frac{nm^{1/2}eV}{V^{1/2}}$ was used, which was introduced in section 3.2.
It is notable, that the definition of the electric field strength E for the Fowler-Nordheim theory is ambiguous, since the electric field is not constant, i. e., it changes within the tunneling distance influencing the actual tunneling barrier. However, this effect is neglected here since it is assumed that the deviation of the electric field is negligible.

5.3 Electron trajectory calculation

The next step after calculation of the density distribution of the emitted electrons at the tip is the computation of the electron trajectories to the sample to determine the electron density distribution at the sample surface. This calculation is based on a one-step Leapfrog algorithm, which is used to solve the equation of motion for electrons in the electric field, i. e., with an acceleration $\vec{a}(\vec{r}) = \frac{e\,\vec{E}(\vec{r})}{m}$:

$$\vec{x}(t) = \frac{\vec{a}(\vec{x}(t))}{2m}\,t^2 + \vec{v}_0(\vec{x}(t))\,t + \vec{x}_0(\vec{x}(t))\,. \tag{5.3.1}$$

To solve this non-linear equation, the time is discretized. The position and the velocity are calculated separately by

$$\begin{aligned} \vec{x}(t+\Delta t) &= \vec{x}(t) + \vec{v}(t)\,\Delta t + \frac{1}{2}\,\vec{a}(t))\,\Delta t^2\,, \\ \vec{v}(t+\Delta t) &= \vec{v}(t) + \frac{\vec{a}(t+\Delta t) + \vec{a}(t)}{2}\,\Delta t\,. \end{aligned} \tag{5.3.2}$$

The initial position for the trajectory calculation is the position, at which the electrons leave the tunneling barrier. Thereby, the width of the tunneling barrier varies for the different emission spots due to the non-uniform electric field. The trajectories are calculated until the sample surface is reached. The crossing of a trajectory and the sample or resist surface defines the respective exposure spot. From all exposure spots and the correlated exposure areas together with the current density distribution at the tip, the lithographically relevant values at the resist or sample surface can be obtained. These are the current density distribution at the sample surface, the electron beam diameter, and the line width. Their determination is described in the next section.

5.4 Current density at the sample surface and definitions of measures for lithography

Based on the current density at the tip surface and the trajectories of the electrons, the current density at the sample and resist surface can be obtained, respectively. Due to the conservation of the electron number, i. e., constant electric current, the current density distributions at the tip J_{tip} and at the sample J_{sam} are related by the following formula [5, 109]:

$$J_{tip}\, A_{tip} = J_{sam}\, A_{sam}\,, \tag{5.4.1}$$

where A_{tip} and A_{sam} are the emission spot area and the corresponding exposure area, respectively. The spot areas are defined by the discretization of the nanotip, i. e., by choice of the emission spots. The corresponding exposure areas are specified by the trajectories of the electrons as shown in fig. 5.1. The geometry of the tip defines the emission spot areas, which can be computed by

$$A_{tip} = \begin{cases} \pi\,(r_1 + r_2)\,\sqrt{(r_2 - r_1)^2 + h^2}\,\pi\,, \text{for cone} \\ 2\pi\, r_{tip}\, h\,, \text{for sphere} \end{cases} . \tag{5.4.2}$$

Here, sphere and cone represent the respective parts of the emission tip. h is the height of the section of the cone or the sphere, r_1, r_2 and r_{tip} are the smaller and the larger radius of the cone as well as the radius of the sphere, respectively.
The exposure area on the sample is given by

$$A_{sam} = \pi(R_2^2 - R_1^2)\,, \tag{5.4.3}$$

with the smaller (larger) radius R_1 (R_2) of the annulus at the sample.
The current density distribution at the sample (eq. (5.4.1)) can be used to analyze the expected width of the lithographic patterns. Different measures are typically used, which focus either on the electron beam or on the interaction with the resist. The first is termed beam diameter and the latter line width.
The beam diameter is defined by the position, at which the current density distribution is decreased to a certain value of the maximal value [5, 77]. Here, the following version is used:

$$d_b = 2\, r_{sam}\Big|_{J_{sam}/\max(J_{sam})=1/e} \tag{5.4.4}$$

The beam diameter definition (5.4.4) does not include the actual electron number or density or energy necessary to obtain resist modifications. To account for resist modifications, the line width is used. It is defined by a threshold for the density of electrons or for the electron energy density. It is assumed that the time scale used for the calculation of electron number and energy is to be larger than the relaxation times within the resist. Experiments by Kästner et al. [13, 131] lead to the assumption that a threshold value n_{crit} of the electron density exists. For electron densities below this threshold value no

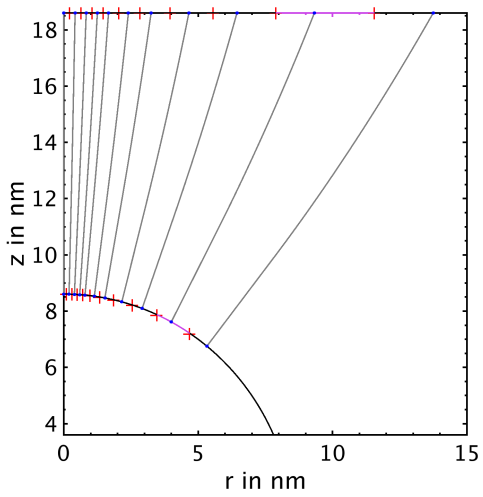

Figure 5.1: Schematics of the corresponding areas at the tip and the sample surface (an example is marked in magenta). Additionally, the trajectories (grey lines) which conects the areas are drawn. The trajectories start at the emission spots (blue dots on the tip) and end at the exposure points (blue spots on the sample). The boundaries of the areas are marked with red crosses.

modification of the resist layer occurs, which was not considered by the previous theoretical investigations [5, 6, 22, 23, 75, 77]. The minimal value would be one electron, which is able to inelastically scatter with the resist molecules and thus, trigger a lithographic reaction. For typical FE-SPL parameters and resists (thickness of about $10\,nm$), a surface electron density value of about 100 electrons per $1\,nm^2$ was estimated to be the threshold for direct ablation process [13, 131]. The value for negative-tone patterning is smaller due to the higher sensitivity for negative-tone patterning of the resist normally used [13]. For the theoretical investigations, the value of 100 electrons per nm^2 is used if not stated explicitly.
For the calculation of the electron density from the current density, a pixel exposure time t_{pix} is defined. The pixel size is obtained from the current density distribution since a continuous tip movement over the sample surface is assumed. The pixel size is defined by $2\,\sigma$ (standard deviation) assuming a Gaussian shape for the current density distribution [32]. By using the definition (5.4.4), the standard deviation is equal to the beam diameter, i. e., $\sigma = d_b$. The exposure path through the pixel leads to the pixel exposure time t_{pix} for a given tip and for a patterning velocity v:

$$t_{pix} = 2\,d_b/v\,. \tag{5.4.5}$$

The electron (number) density distribution n_e is obtained from the current

density distribution by

$$n_e = \frac{J_{sam}}{e}\, t_{pix}\,, \tag{5.4.6}$$

where e is the elementary charge. The line width w is determined by the intersection of the electron density distribution n_e and the threshold value n_{crit}:

$$w = 2\, r_{sam}\Big|_{n_e = n_{crit}}\,. \tag{5.4.7}$$

Both, the beam diameter d_b and the line width w are used as measures for the experimentally observed feature width (chapter 10). In the next chapter, the Monte Carlo simulation is explained, which uses the current density distribution as initial condition.

Chapter 6

Monte Carlo simulation

This chapter presents the implementation of the Monte Carlo simulation of electrons inside the ultra-thin resist layer with thickness values in the range of 2 to 50 nm, which also takes the electric field into account. These will be used to calculate the actual electron number density inside the resist layer, which can be modified due to secondary electron generation. Its average spread in the resist is used to estimate the line width during lithography experiments. The results will be shown in the section 10.4.5.
The initial condition for the Monte Carlo simulation is the electron density distribution calculated with the nanolithography model described in the previous chapter. Three basic physical interactions need to be taken into account: elastic scattering, inelastic scattering and boundary crossings, i. e., interactions near interfaces between two materials [132].
The elastic scattering describes interactions of incident electrons without an energy transfer whereas inelastic scattering results in an energy loss of the incident electrons. The incident electrons are also termed primary electrons. The implemented calculation for the elastic cross section and the elastic mean free path is explained in section 6.1.
Two different inelastic scattering mechanisms are taken into account in this thesis. In the first one, the incident electron transfers a part of its energy to excite but not ionize the resist. In the second mechanism, the incident electron ionize the resist by generation a a so-called secondary electron. Both cases differ in the energy transferred from the incident electron to the resist. If the "energy loss" ΔE of the incident electron exceeds the ionization energy, the resist atom or molecule is ionized (mechanism 2), otherwise it is only excited (mechanism 1). The approach for the inelastic mean free path is described in section 6.2.
Boundary interactions describe the physical processes at the interface of two materials. Here, we have two interfaces to consider: the air-resist and the resist-sample interface. Backscattering at the resist-air (vacuum) interface is not considered by using an extra boundary term but treated as elastic and inelastic scattering events since the transmission of low-energy electrons is usually higher than expected using layer-by-layer or continuum models [133]. At the resist-sample interface scattering is not included since the probability

of backscattering is assumed to be low for two reasons. First, the main energy loss will take place near the resist surface because the inelastic scattering mean free paths are less than $1\,nm$ in the considered energy range. Thus, the electrons crossing the resist-sample boundary typically have energies below the ionization energy. For these low energies, the probability of back-scattering is strongly reduced. Secondly, it is assumed that the probability to find an electron, which is backscattered at the sample and additionally decelerated by the electric field, having a higher energy than the binding energy (i. e., cut-off energy), is also low. Since the focus of the thesis is on the lithography, i. e., the resist modification, only the backscattered electrons, which have an energy above the cut-off energy are crucial since only these are allowed to scatter inelastically within the model. The conditional probability that an electron is backscattered and has enough energy to be scattered in the resist, is expected to be negligible in the FE-SPL case and, thus, backscattering of electrons from the sample is not included, i. e., the sample is treated as an ideal electron sink. Between scattering events, the electrons are assumed to move ballistically, influenced only by the electric field. Therefore, the algorithm of the electron trajectories, described in section 5.3, is adapted by the use of a limited step size and the inclusion of backscattering, i. e., calculation of the electron trajectory in air starting from the resist until it hits the resist again or leaves the simulation box.
The Monte Carlo simulation (s. section 6.3) is completed, when all electrons left the resist layer after several scattering events, i. e., they were absorbed at the sample surface or left the simulation box.
To achieve statistically relevant results, the Monte Carlo simulation is repeated until the termination criteria is fulfilled. This criteria is introduced in section 6.4.

6.1 Elastic scattering process

A wide variety of elastic scattering cross-section models are used in Monte Carlo simulations for energies above $100\,eV$ like Rutherford [134, 135] or Mott cross-sections [132, 136]. A fundamental change of the characteristics of elastic electron scattering takes place when the de Broglie wavelength of the electron exceeds the interatomic distances as well as the Mott mean free path [132]. The elastic scattering is changed from a particle-like scattering into Bloch wave-like scattering with an increased mean free path [137].
However, the inelastic mean free path exhibits a minimum for energies between 30 and $100\,eV$ whereas the elastic mean free path remains almost constant [132]. In the energy range relevant for FE-SPL, i. e., between 10 and $100\,eV$, inelastic scattering is assumed to be the dominant process. That means, only up to 3% difference should occur if the elastic scattering is completely neglected [133].
Compared to the large amount of studies for energies above $100\,eV$, there are only a few publications for electron energies below. Therefore, a fitting procedure was applied using various experimental and theoretical data sets

and a simple model based on a Wentzel-like potential (also called screened Coulomb or Yukawa potential). This simple analytical model [126] will be described first before explaining the fitting procedure.
Due to the low energy of the electrons of up to $100\,eV$, relativistic effects are negligible for this study. Based on the non-relativistic Schrödinger theory of electron scattering on a central potential $V(r)$ [126], the scattering amplitude f dependent on the scattering angle θ can be described by

$$f(\theta) = \frac{2\,m}{\hbar^2\,q}\int_0^\infty dr\,r\sin(qr)V(r)\,. \tag{6.1.1}$$

Here, $\hbar\vec{q}$ is the momentum lost/gained by the incident electron and m the free electron mass. By inserting the Wentzel-like potential

$$V(r) = -\frac{Z\,e^2}{r}\exp\left(-\frac{r}{a}\right)\,, \tag{6.1.2}$$

with the parameter $a = a_0/Z^{1/3}$, the scattering amplitude becomes to

$$f(\theta) = \frac{2m\,Z\,e^2}{\hbar^2\,q}\frac{q}{q^2+(1/a^2)}\,. \tag{6.1.3}$$

Here, Z is the atomic number of the resist, e is the electron charge and a_0 is the Bohr radius. Thus, the differential cross-section (ratio of particle flux per unit time scattered into the solid angle $d\Omega$ and incident flux) is given by

$$\frac{d\sigma_{el}}{d\Omega} = |f(\theta)|^2 = \frac{Z^2\,e^4}{4\epsilon^2}\frac{1}{(1-\cos\theta+\alpha)^2}\,, \tag{6.1.4}$$

with the screening parameter

$$\alpha = \frac{me^4\pi^2\,Z^{2/3}}{h^2\,\epsilon}\,. \tag{6.1.5}$$

Here, the relation between momentum $\hbar\vec{q}$ and the kinetic energy ϵ of the incident electron

$$\frac{\hbar^2\,q^2}{2m} = \epsilon(1-\cos\theta) \tag{6.1.6}$$

was used. By integration of the differential elastic cross section, the total elastic cross section can be obtained

$$\sigma_{el} = \frac{\pi\,Z^2e^4}{\epsilon^2\alpha(2+\alpha)} \tag{6.1.7}$$

and, thus the elastic mean free path

$$\lambda_{el} = \frac{1}{N\sigma_{el}} = \frac{\epsilon^2\alpha(2+\alpha)}{N\pi\,Z^2e^4}\,. \tag{6.1.8}$$

Here, N is the number of atoms per unit volume in the resist material. The derivation is well explained in several publications [126, 138].

The differential elastic cross section (eq. (6.1.4)) as well as the elastic mean free path (eq. (6.1.8)) are functions needed for the implementation of the Monte Carlo simulation, which will be explained in section 6.3.
Another approach for the elastic mean free path based on experimental and theoretical data. However, up to my knowledge, there are no studies based on calixarene resist ($C_{56}H_{72}O_{12}$), in which the elastic mean free path in the wanted energy range between 0 and $100\,eV$ are reported. Therefore, the approach proposed by Tan et al. [136] was used to determine the elastic cross-section. In this approach, the elastic scattering cross sections σ_i of the elements of the resist material and their stoichiometric fraction x_i are combined to obtain the total elastic cross section:

$$\sigma_{tot} = \sum_i x_i \, \sigma_i \, . \tag{6.1.9}$$

The elastic cross-sections of the elements were obtained from two dimensional fits to experimental and theoretical data for the elements hydrogen, oxygen and carbon in the respective energy range $\epsilon \in [0, 100]\,eV$ and the angular range $[0°, 180°]$.
The main source was the NIST electron elastic-scattering cross-section database [139–141]. The database includes theoretically obtained data sets from many different elements including the total and differential elastic scattering cross section. The energy range is from $50\,eV$ to $20\,keV$ and the angular range from 0° to 180°.
Since the elastic mean free path is also needed for energies below $50\,eV$, complementary experimental data were added. The experimental data were chosen to match the theoretical data and to avoid fitting artefacts, thus data from refs. [142–148] were not used. For hydrogen, data from the studies of Srivastava et al. [149] and from Callaway and Williams [150] were used. Callaway and Williams compare in their work experimental and theoretical data for atomic hydrogen. The paper of Shyn and Sharp [151] provided data for molecular oxygen from 2 to $200\,eV$, which were similar to the ones from the NIST database above $50\,eV$. The data set of Tanaka, Srivastava and Chutjian was used for carbon [152]. To obtain a complete data set of elastic mean free path λ_{el} and the differential elastic scattering cross section in the energy range $[10, 100]\,eV$ and the angular range $[0°, 180°]$ the above mentioned data were fitted by two dimensional polynomials up to the fifth degree.
As mentioned above the inelastic scattering process is assumed to be dominant compared to the elastic scattering. By comparing the results obtained by the two elastic scattering approaches (using a Wentzel-like potential and the fit procedure), the influence of the elastic scattering in this energy range can be estimated.

6.2 Inelastic scattering processes

Most data of electronic scattering cross-sections, stopping powers or mean free paths in literature deal with energy ranges above $100\,eV$ since they are mostly related to scanning electron microscopy and lithography. Phononic

scattering is the most important process for the low-energy electron models for metals or semiconductors/insulators. For amorphous materials phonon scattering might occur for energies below $1\,eV$ [153]. Furthermore, the acoustic and optical phonon energies are not known for our resist material. Thus, phononic interactions are not considered in this Monte Carlo approach.
For organic compounds, a universal curve for the inelastic mean free path λ_{inel} is suggested from empirical data analyzes [133, 154]. This can be explained by the fact that the electron scattering probability for low energies depends on the product of the electron density of the occupied states ($\propto \epsilon_n(\epsilon_F)$) and the unoccupied states ($\propto \epsilon_n(\epsilon_F)$). Since the inelastic mean free path is the inverse of the scattering probability, it will be proportional to $\lambda_{inel} \propto \epsilon^{-2}$ for electron scattering in the low-energy regime [133, 155]. The same dependence was derived by Quinn using a self-energy approach [156].
However for energies above $75\,eV$ a least squares analysis showed that the inelastic mean free path is described by $\sqrt{\epsilon}$ [133]. Therefore, the relation suggested by Seah and Dench is used

$$\lambda_{inel}(\epsilon) = \frac{A}{\epsilon^2} + B\sqrt{\epsilon}\,, \tag{6.2.1}$$

with the proposed parameters $A = 31\,nm\,eV$ and $B = 0.087\,nm\,\sqrt{eV}$ for organic compounds [133].

6.3 Monte Carlo implementation

Here, a modified version of a Monte Carlo simulation described by Dapor [126] was applied.
The flow chart of the Monte Carlo simulation is shown in fig. 6.1. The input parameters at the start of each Monte Carlo simulation are found by the nanolithography program (chapter 5) using the same tip parameters (radius, material and opening angle) and external parameters (tip-sample distance, bias voltage and writing velocity). The input parameters, i. e., distribution of the electron impact positions and velocities as well as of the current density at the resist surface, defines the start of the simulation. As shown in fig. 6.1, before the first Monte Carlo step begins, the first scattering position is determined based on the step length Δs and the calculated trajectories of the electrons. Based on the energy ϵ_0 of the electron at the time t_0 (before the Monte Carlo step), the elastic and inelastic mean free path, $\lambda_{el,0} = \lambda_{el}(\epsilon_0)$ (eq. (6.1.8)) and $\lambda_{inel,0} = \lambda_{inel}(\epsilon_0)$ (eq. (6.2.1)), are determined as described in sections 6.1 and 6.2, respectively. These are needed to calculate the probability of elastic and inelastic scattering. The probability of an inelastic scattering event is equal to

$$P_{inel} = \frac{\lambda_{inel,0}^{-1}}{\lambda_{el,0}^{-1} + \lambda_{inel,0}^{-1}} = \frac{\lambda_{el,0}}{\lambda_{el,0} + \lambda_{inel,0}}\,. \tag{6.3.1}$$

If a random number $z_1 \in [0, 1]$ drawn from an uniform distribution is less than or equal to P_{inel}, the collision will be inelastic otherwise elastic.

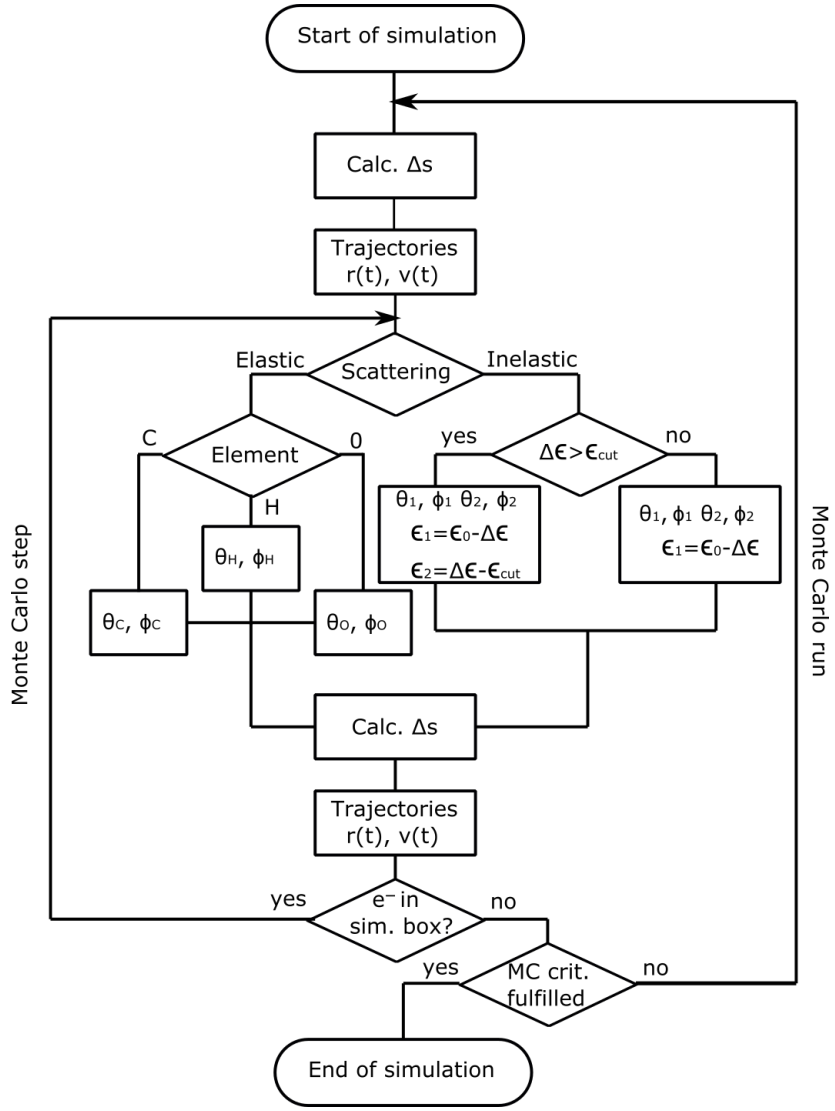

Figure 6.1: Flowchart of the Monte Carlo simulation.

For an elastic scattering event, the stoichiometric ratio of elements in a calixarene molecule determines the target element [136]. Therefore, another uniformly distributed random number $z_2 \in [0, 1]$ is used. Next, the scattering angles are determined. The azimuthal angle ϕ'_{el} is drawn from a uniform distribution between 0 to 2π. The selection of the polar angle θ'_{el} is based on the probability of the electron to be scattered elastically into a range from 0 to θ'_{el}

$$P(\theta'_{el}) = \frac{2\pi \int_0^{\theta'_{el}} \frac{d\sigma_{el}}{d\Omega} \sin(\vartheta) d\vartheta}{\sigma_{el}} \,. \tag{6.3.2}$$

By using tabulated values of $P(\theta'_{el})$, the polar angle θ'_{el} is obtained from an uniformly distributed random number $z_4 \in [0, 1]$ as proposed by Dapor [126].

Since the polar and azimuthal angles are given in natural coordinates of the electron trajectory, they have to be transformed into the global coordinate system, i. e., ϕ_{el} and θ_{el}[1]. The energy ϵ_0 is used to determine the velocity vector $\vec{v}_{el}$ after the elastic scattering event

$$\vec{v}_{el} = \sqrt{\frac{2\epsilon_0}{m_0}} \begin{pmatrix} \sin\theta_{el}\cos\phi_{el} \\ \sin\theta_{el}\sin\phi_{el} \\ \cos\theta_{el} \end{pmatrix} \tag{6.3.3}$$

in case of an elastic scattering event.
For an inelastic scattering process, the scattering angles and the kinetic energies are determined for both the primary and secondary electrons. Here, the inelastic electron-atom scattering is treated as an elastic electron-electron collision, in which the primary electron is scattered at a motionless electron [126]. Additionally, the binding energy of the motion-less electron is considered. Fulfilling momentum conservation, the azimuthal angles are given by $\phi_2' = 2\pi\, z_5$ and $\phi_1' = \phi_2' - \pi$ and the polar angles by $\theta_2' = z_6$ and $\sin\theta_1' = \cos\theta_2'$, with uniformly distributed random numbers z_5 and z_6 between 0 and 1. From energy conservation, the energy loss $\Delta\epsilon = \epsilon_0 \cos\theta_2'$ of the primary electron and the kinetic energy of the secondary electron $\epsilon_2 = \Delta\epsilon - \epsilon_{co}$ can be determined. Here, the cut-off energy ϵ_{co} is set to the estimated ionization energy of a calixarene molecule of $10\,eV$. If the energy transferred from the primary to the secondary electron does not exceed the cut-off energy (i. e., $\epsilon_2 < 0$), it is assumed that the secondary electron is only excited and not ionized. After transformation into global coordinates, the velocities of the primary and the secondary electron are given by

$$\vec{v}_1 = \sqrt{\frac{2(\epsilon_0 - \Delta\epsilon}{m_0}} \begin{pmatrix} \sin\theta_1\cos\phi_1 \\ \sin\theta_1\sin\phi_1 \\ \cos\theta_1 \end{pmatrix} \tag{6.3.4}$$

and

$$\vec{v}_2 = \sqrt{\frac{2(\Delta\epsilon - \epsilon_{co})}{m_0}} \begin{pmatrix} \sin\theta_2\cos\phi_2 \\ \sin\theta_2\sin\phi_2 \\ \cos\theta_2 \end{pmatrix} . \tag{6.3.5}$$

On the basis of the velocity after scattering and the location of the scattering event, trajectories of the primary electron and the potentially generated secondary electron are computed by a Leapfrog algorithm taking the electric field $\vec{E}$ into account (as described in section 5.3). At first, the step length Δs

$$\Delta s = -\lambda \ln(z_7) \tag{6.3.6}$$

is obtained from the total mean free path λ

$$\lambda^{-1} = \lambda_{el}^{-1} + \lambda_{inel}^{-1} . \tag{6.3.7}$$

Here, $z_7 \in [0, 1]$ is another random number drawn from a uniform distribution. The electron elastic and inelastic mean free paths, λ_{el} and λ_{inel}, are obtained

[1] In fig. 6.1, ϕ_{el} and θ_{el} are given as ϕ_x and θ_x with $x = C, H, O$ representing the element of the target.

using the energies after the scattering event. To account for the nonlinear shape of the trajectories due to the influence of the electric field strength $\vec{E}$, the step length Δs is divided in N steps. Thereby, the position vector for the next scattering step is given by $\vec{r}(t) = \vec{r}(t_0 + N\Delta t)$. Both, the primary and secondary electrons, are considered for subsequent scattering events.
If a scattered electron crosses the resist surface, i. e., if it is backscattered, the total mean free path outside the resist is assumed to be infinity. The trajectory of the backscattered electron is computed until the electron reaches the resist surface again or leaves the simulation box. Due to the electric field, backscattered electrons are accelerated towards the resist surface. When the backscattered electron reaches the resist surface, the next scattering event takes place after a propagation length Δs starting at the resist surface. This is the same procedure like for the first scattering event inside the resist layer. Since a single cantilever tip is considered, we do not use periodic boundary conditions to represent the experimental situation, i. e., if an electron hits the simulation box, it is not further considered.
As seen in fig. 6.1, the above described Monte Carlo step is repeated until all electrons (primary and secondary ones) are reached the sample or left the simulation box. This terminates a Monte Carlo run. Each Monte Carlo run of a Monte Carlo simulation starts using the same electron distribution at the resist surface obtained from the nanolithography program for a certain parameter set. After one Monte Carlo run is terminated, another run is computed to get a statistical average of the electron distribution at the resist layer and at the resist-sample interface (see fig. 6.1). The question for the Monte Carlo simulation, is how many runs n are necessary to obtain a good measure of the wanted distribution. To answer this question, one need to find a criterion for the termination, which is described in the following section. The outputs of the simulation are averaged distributions of the electron number, their positions and velocities, which are analyzed in section 10.4.5.

6.4 Termination criterion for the Monte Carlo simulation

The criterion, which terminates the Monte Carlo simulation is based on the deviation of the distribution obtained from the Monte Carlo simulation from the real one. Since the real distribution is not known, an estimator for the deviation has to be found. The physically relevant properties are mathematical probability density functions $f(r)$. However, the cumulative distribution function

$$F(r) = \int_0^r f(s)\, ds \tag{6.4.1}$$

is more advantageous since it converges, and it is bounded to the range between 0 and 1, if the probability density function is normalized [157]. To compute a measure for the error between the real value of the cumulative distribution function F and the estimator $\hat{F}$, standard stochastic methods for (statistical) data samples are applied. For a chosen value of the radius r and a specific data sample i, the expected value (or expectation or mean) for the estimator

is equal to [158]

$$E(\hat{F}_i(r)) = F(r)\,. \tag{6.4.2}$$

The expected value of the arithmetic mean of the estimator $\overline{F}_n = \frac{1}{n}\sum_{i=1}^{n} \hat{F}_i$ [158] is given by

$$E(\overline{F}_n(r)) = \frac{1}{n}\sum_{i=1}^{n} E(\hat{F}_i) = F(r)\,. \tag{6.4.3}$$

The variance of the arithmetic mean can be calculated by

$$\begin{aligned} \mathrm{Var}(\overline{\mathrm{F}}_\mathrm{n}(\mathrm{r})) &= \frac{1}{n}\,\mathrm{Var}\left(\hat{\mathrm{F}}_\mathrm{i}(\mathrm{r})\right) \\ &\approx \frac{1}{n}\,\frac{1}{n-1}\sum_{i=1}^{n}\left(\hat{F}_i(r) - \overline{F}_n(r)\right)^2 \\ &= \frac{1}{n} s_n^2(r))\,, \end{aligned} \tag{6.4.4}$$

with the (unbiased) sample variance $s_n^2 = \frac{1}{n-1}\sum_{i=1}^{n}\left(\hat{F}_i(r) - \overline{F}_n(r)\right)^2$. Therefore, for each value of the radius r, the real cumulative distribution function can be estimated by

$$F(r) = \overline{F}_n(r) \pm \frac{1}{\sqrt{n}}\, s_n(r)\,. \tag{6.4.5}$$

Since not only certain points of the cumulative distribution function shall be compared but rather the complete distribution, the L^2 norm is applied:

$$\|F(r)\|_2 = \sqrt{\int_0^\infty |F(r)|^2\, dr}\,. \tag{6.4.6}$$

The expected value of the squared L^2 norm is given by [157]:

$$\begin{aligned} E\|F - \overline{F}_n\|_2^2 &= E\int_0^\infty |F(r) - \overline{F}_n(r)|^2\, dr \\ &\approx E\sum_{k=1}^{N_r}\left(F(r_k) - \overline{F}_n(r_k)\right)^2 (r_k - r_{k-1}) \\ &= \sum_{k=1}^{N_r}\mathrm{Var}(\overline{\mathrm{F}}_\mathrm{n}(\mathrm{r}_\mathrm{k}))(\mathrm{r}_\mathrm{k} - \mathrm{r}_{\mathrm{k}-1}) \\ &\approx \frac{1}{n}\sum_{k=1}^{N_r} s_n^2(r_k)(r_k - r_{k-1}) \end{aligned} \tag{6.4.7}$$

and depends on the number n of the used data sets. The integral is approximated by a sum over N_r subintervals ($r_0 = 0 < r_1 < \cdots < r_{N_r} < \infty$) and the linearity of the expected value, the definition of the variance $\mathrm{Var(f)} = \mathrm{E(f - E(f))^2}$ as well as eqs. (6.4.3) and (6.4.4) are used.

The upper bound of the measure (6.4.7) can be estimated by setting $s_n^2(r_k) = 1$ ($s_n^2(r_k) \leq 1 \, \forall r_k$), which yields

$$E\|F - \overline{F}_n\|_2^2 \leq \frac{R}{n} \tag{6.4.8}$$

with $R = \sum_{k=1}^{N_r}(r_k - r_{k-1})$ [157]. The measure, defined in eq. (6.4.7), was used for the termination condition of the Monte Carlo simulation.
Since the the cumulative distribution function and so the value of eq. (6.4.7) depends on the used parameter sets, we used the following more general termination criterion:

$$\frac{E\|F - \overline{F}_n\|_2^2}{\max_{\forall j \leq n}(E\|F - \overline{F}_j\|_2^2)} \leq 0.2\,. \tag{6.4.9}$$

In the Monte Carlo simulation, the electron and energy distribution at the sample (i. e., as function of r_{sam}) are used as the probability density functions f_1 and f_2 (see eq. (6.4.1)), for which the termination criteria is calculated separately. The simulation is terminated, when the criterion (6.4.9) is fulfilled for both values.

Part III

Results

Chapter 7

Study of different numerical FE-SPL models

In this chapter, the different types of numerical models, described in chapter 5 will be compared. These models differ in their dimensionality, i. e., if a two dimensional or three dimensional computation is used. The dimensionality, thereby, is important for the electric field calculation in the finite-element method (FEM) approach and for the calculation of the field-emission current within the Fowler-Nordheim theory. Typically, only the first one is considered. Here, differences between a two dimensional model and two types of three dimensional models are discussed for field-emission scanning probe lithography. The two dimensional model for the electric field calculation work uses Laplace's equation in the form of eq. (5.1.2). A similar model was already used by Wilder et al. [75].
For the three dimensional FEM model, Laplace's equation (5.1.3) in cylindrical coordinates is used, in which the rotational symmetry of the nanotip was taken into account [77]. The differences between the 2D and 3D approach for the calculation of the electrostatic potential and electric field are presented in sec. 7.1. Thereby, the specific form of the electrostatic potential is investigated and explained.
In the section 7.2, two variants of the Fowler-Nordheim equation are compared within the three dimensional model. The first one was published by Fowler and Nordheim [94,95] for a flat emitter surface, which leads to the equation (3.2.20) as shown in section 3.2. It was previously used in the studies about lithography applications of nanotips using field-emitted electrons [5, 23, 75, 77]. The other approach takes the curved surface into account by using the Fowler-Nordheim equation (5.2.2), which was not reported so far for FE-SPL. It considers the velocity distribution of electrons inside the tip for the emission probability but also for the trajectory calculation. This model might help to investigate the effects of the incident angle of the electrons impinging the resist surface.
The differences of the models of the field emission are studied by comparing the current strength and the current density distributions at the sample. The relatively weak influences on the current density distribution by taking the intrinsic velocity distribution into account, were estimated using an analytical

expression. Additionally, the influence on the angle of incidence and the time of flight were investigated.

7.1 Electric field calculation in two and three dimensions

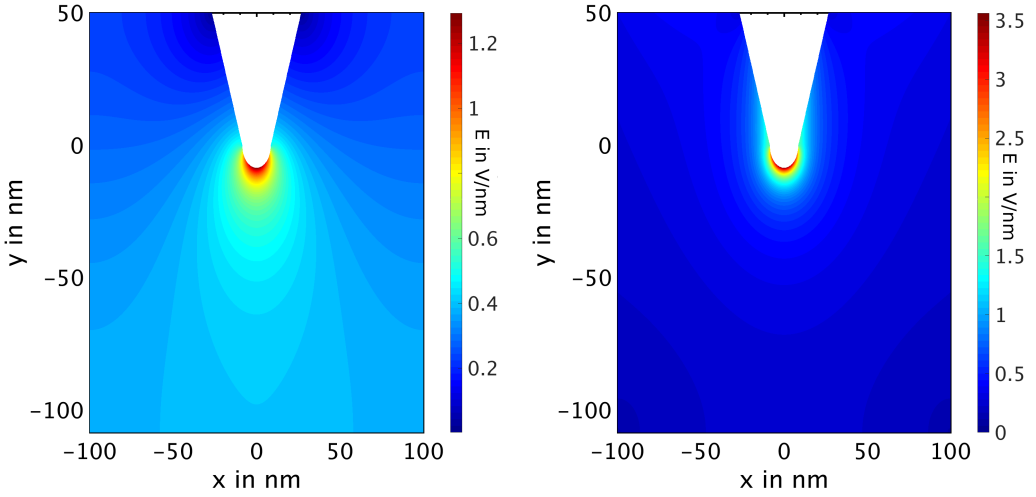

Figure 7.1: Color-coded electric field of a chosen parameter set for the two dimensional (*left*) and three dimensional FEM model (*right*) ($d = 100\,nm$, $U = 50\,V$, $R = 8.5\,nm$, $\gamma = 20°$).

The electric field distribution in proximity of the nanotip and the sample surface is shown for the two dimensional (left) and the three dimensional (right) FEM model in fig. 7.1. The lightning rod effect [82], i. e., the field enhancement at the tip apex, is clearly seen in both models. However, the enhancement of the electric field at the tip apex is more prominent in the 3D case and the maximal electric field strength is larger as well.
The representation of the tip geometry in two dimensions corresponds to a blade rather than a tip (if the third dimension is also considered). The different representations of the tip geometry for the 2D and 3D case determine the two variants of Laplace's equation, i. e., eqs. (5.1.2) and (5.1.3), respectively, and are the cause for deviations in the electric field E and the electrostatic potential φ.
The electric field strength E over $\frac{z}{d}$, i. e., for a scaled z axis[1], is plotted for different tip-sample distances d on the left-hand side of fig. 7.2. Here, the darker lines belong to the results of the 2D model and the brighter ones to the 3D model. In both cases, the enhancement of E is limited to the proximity of the tip apex and already for distances above $20\,nm$ from the tip apex, the electric field is almost constant. The maximum of the electric field is larger for the 3D case than for the 2D case. However, for large z values, the electric field

[1] The positions $z/d = 0$ and 1 correspond to tip apex and sample surface, respectively.

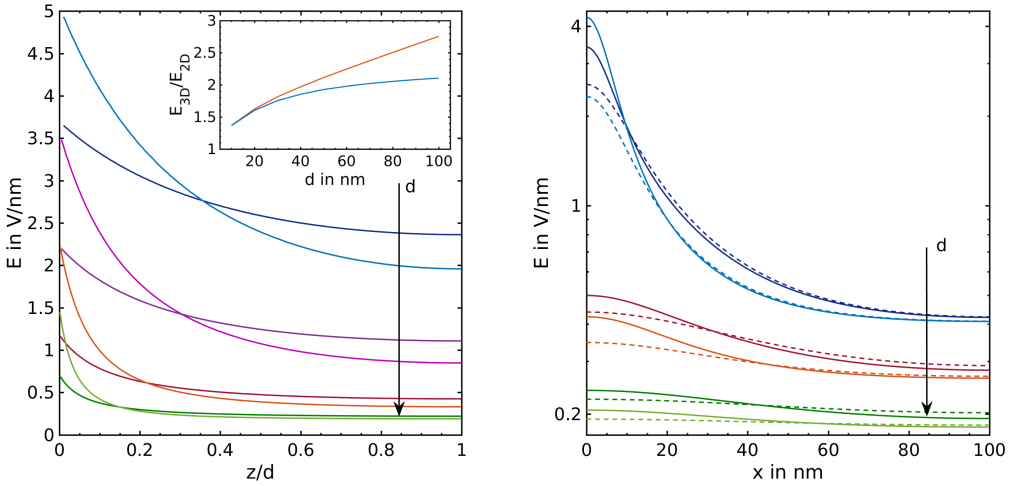

Figure 7.2: Plot of the electric field strength E along the z axis (*left*) and parallel to the sample surface (*right*) for the 2D (dark colors) and the 3D FEM calculation for $U = 10\,V$. Tip-sample distances of $d = 10\,nm$ (blue), $20\,nm$ (magenta, only (*left*)), $50\,nm$ (red) and $100\,nm$ (green) are plotted. (*Left*) The inset shows the ratio of the maximal electric field strength E of 3D model and 2D model for $U = 10\,V$ (blue) and $50\,V$ (red). (*Right*) Two sample distances relative to the tip-sample distance d are used: $\frac{z}{d} = \frac{1}{2}$ (lines) and $\frac{3}{4}$ (broken lines). Constant parameters are $r = 8.5\,nm$, $\gamma = 20°$ and $\Phi = 4.5\,eV$.

E of the 3D case is smaller than in the 2D case because the same bias voltage $U = \phi_{sam} - \phi_{tip}$ was applied in both cases. The difference for $E(z \to d)$ is more pronounced for small tip-sample distances whereas for larger distances d, the difference between the models nearly vanishes. The ratio $\frac{E_{3D}}{E_{2D}}$ of the maximal electric field strength, i. e., $E(z/d \to 0)$, is shown in the inset of fig. 7.2. This ratio approaches unity for decreasing tip-sample distance d because the field enhancement factor $\kappa_p \to 1$ regardless of the model dimension (and the bias voltage). Both models approach the plate-capacitor case for $d \to 0$, in which the electric field strength approaches infinity for $d \to 0$.
In other words, the two dimensional FEM calculation can be used to estimate the electric field strength close to the tip, i. e., E_{max}, only for very small tip-sample distances $d \to 0$ (as seen in the inset of fig. 7.2) whereas the electric field close to the sample could be estimated only for $d \to \infty$ (as seen on the left side of fig. 7.2). However, in most cases a 3D calculation is necessary and, thus, used in this thesis.
Additionally, the electric field strength parallel to the sample at a constant distance z is studied and plotted on the right-hand side of fig. 7.2 for the 2D and the 3D case. The relative distances $\frac{z}{d} = \frac{1}{2}$ and $\frac{3}{4}$ were used for $d = 10$, 50 and $100\,nm$ in fig. 7.2 (right). The distributions of the electric field seems to be describable by Gaussian distribution for $z \to d$ as shown in figs. 7.2 and 7.3, respectively. In fig. 7.3, the numerically calculated potential $\phi(r, z)$ for constant z values is shown together with a fit using a Gaussian function

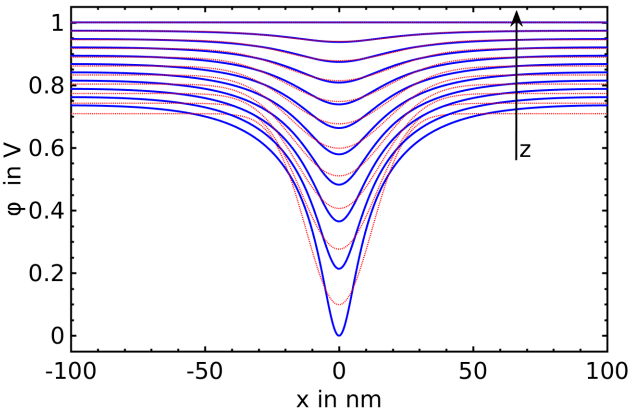

Figure 7.3: Axial symmetric electrostatic potential $\phi(r,z)$ over x for different ratios $\frac{z}{d} \in [0,1]$ for $d = 20\,nm$ for the three dimensional model (blue solid lines). The tip potential is set to 0 and the potential at the sample is $\phi(r, z = d) = 1\,V$. Gaussian fits $f_z(r) = a(z) \exp\left[-\frac{r^2}{2\,b(z)^2}\right] + c(z)$ are plotted as red dotted lines.

$f(r) = a \exp\left[-\frac{r^2}{2\,b^2}\right] + c$. The Gaussian function resembles the electrostatic potential esp. for $z/d \to 1$ as seen in fig. 7.3.
In fig. 7.4, the coefficients $|a(z)|$ and $b(z)$ are plotted for different tip-sample distances d. It can be seen that the magnitude of the amplitude a of the Gaussian decreases for $z \to d$ because the field lines impinge perpendicularly upon the sample surface, i. e., the curvature of the potential decreases. The standard deviation $\sigma = b$ increases for increasing z but seems to reach a saturation. An explanation for this behavior can be found by considering the following ansatz $\phi = h(z)\, g_z(x,y)$ for the electrostatic potential given by Laplace's equation in 3D Cartesian coordinates [130]. Here, the z coordinate corresponds to the tip axis and thus, the potential φ is mainly described by $h(z)$. For $g_z(x,y)$, the slowly varying envelope approximation is used, i. e., it is assumed that the profile of ϕ in the (x,y) plane is only slowly varying with z. Using this approximation Laplace's equation reads

$$\left(\frac{\partial^2}{\partial x^2} + \frac{\partial^2}{\partial y^2}\right) g_z + \frac{2}{h(z)} \frac{\partial h(z)}{\partial z} \frac{\partial g_z}{\partial z} = 0\,. \tag{7.1.1}$$

Since the electric field for $z \to d$ and large d is nearly constant as seen on the left of fig. 7.2, $h(z)$ can be approximated by a linear function $h(z) = A_z\,(z - z_0)$ with constants A_z and z_0. Using the approximation for $h(z)$ and the substitution $u = \frac{1}{4}(z - z_0)^2 - C$ (with a constant C), equation (7.1.1) can be written as

$$\left(\frac{\partial^2}{\partial x^2} + \frac{\partial^2}{\partial y^2}\right) g_u = -\frac{\partial}{\partial u}\, g_u\,. \tag{7.1.2}$$

Equation (7.1.2) represents a parabolic partial differential equation such as the heat equation, with the remarkable difference of the negative sign on the right

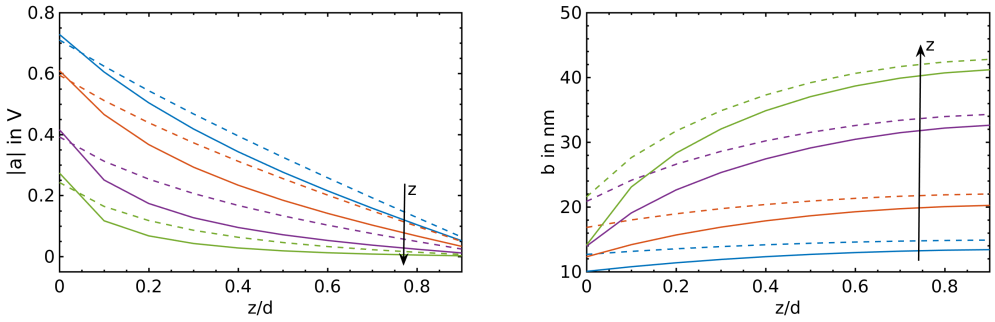

Figure 7.4: Coefficients $|a(z)|$ (*left*) and $b(z)$ (*right*) of the Gaussian fit $f_z(r)$ for tip-sample distances of $d = 10\,nm$ (blue), $20\,nm$ (red), $50\,nm$ (purple) and $100\,nm$ (green). The results of the two dimensional (broken lines) and three dimensional (solid lines) are plotted for the ratio $\frac{z}{d}$.

side. It can be solved by

$$g_u(x,y) = -\frac{g_0}{4\pi u}\,\exp\left[\frac{x^2+y^2}{4u}\right]. \tag{7.1.3}$$

Inserting $-u = C - \frac{1}{4}(z-z_0)^2$ yields

$$g_z(x,y) = \frac{g_0}{\pi\,(4\,C-(z-z_0)^2)}\,\exp\left[-\frac{x^2+y^2}{4\,C-(z-z_0)^2}\right]. \tag{7.1.4}$$

Here, the constant g_0 determines the value of g_z for $u = 0$, i. e., $z = \pm 2\sqrt{C}+z_0$, where g_z is localized in point $(x = 0, y = 0)$, i. e., described by an δ function. Since the amplitude of the Gaussian function should be positive, it is found that $4C > (z_0)^2$ for $z \in [0, z_0]$.

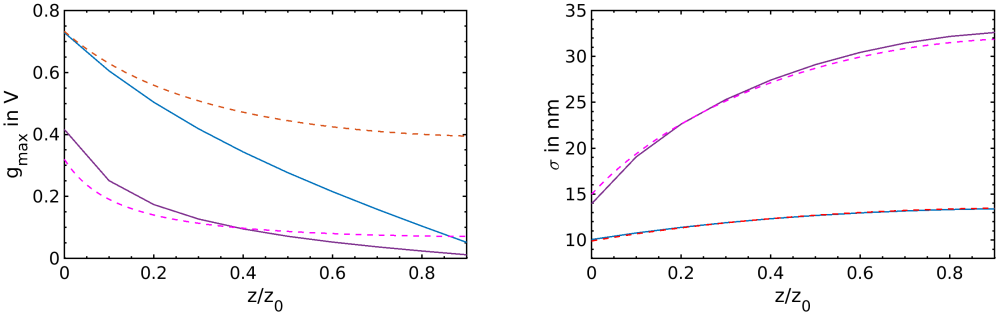

Figure 7.5: Amplitude g_{max} (*left*) and standard deviation σ (*right*) of $g_z(x,y)$ (broken lines) together with $|a(z)|$ and $b(z)$ of fit function $f_z(r)$ (solid lines) for $d = 10\,nm$ (blue and red) and $50\,nm$ (purple and magenta). The following parameter for $g(x,y)$ were used to match $b(z)$: $z_0 = 13\,nm$, $C \approx 91\,nm^2$ for $d = 10\,nm$ and $z_0 = 40\,nm$, $C \approx 512\,nm^2$ for $d = 50\,nm$. For both tip-sample distances, g_0 was set to $450\,V\,nm^2$.

In fig. 7.5, the standard deviation $\sigma(z) = \sqrt{2C - \frac{1}{2}(z - z_0)^2}$ and the amplitude $g_{max}(z) = \frac{g_0}{2\pi\sigma(z)}$ are plotted together with the fit coefficients $|a|$ and b of the three dimensional model for $d = 10\,nm$ and $50\,nm$. The parameters z_0 and C were chosen to obtain good agreement between σ and b. The offset values are $z_0 = 13\,nm$ and $40\,nm$, respectively. This is in good agreement with the respective tip-sample distances of the numerical 3D model. A fair agreement between g_{max} and $|a|$ was found. The deviations might be caused by the approximation of $h(z) \propto z$, which is a better approximation for large d than for small ones (as seen in figs. 7.2 and 7.5).
In summary, it was found that in most cases a 3D calculation of the electric field is necessary and a 2D model does not determine the electric field around nanotip. Additionally, it was shown that the origin of the Gaussian shape of the electrostatic potential φ in the (x, y) plane is a property of the solution of Laplace's equation in 2D or 3D under certain conditions. The requirements are that the solution needs be separable in a dominant part, which dependents only on one (main) direction and a part describing the properties in the other direction(s), which is slowly varying in the main direction.

7.2 Different approaches for field emission for lithography

In this section, the results using two variants of the Fowler-Nordheim equation within the three dimensional model are compared.
In the first one, the shape of the tip is neglected and a flat emitter surface is assumed, which leads to equation (3.2.20) (see section 3.2). Previous theoretical studies about field-emission scanning probe lithography used this approach [5, 23, 75, 77].

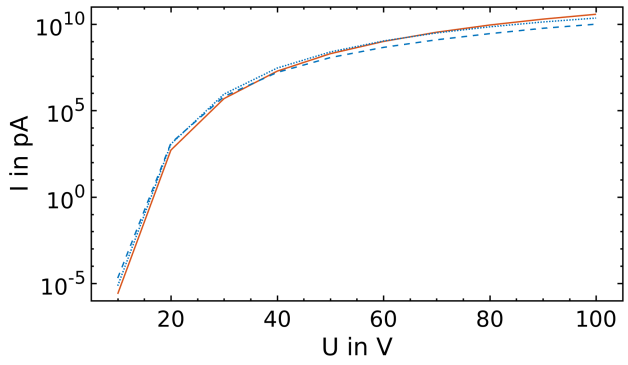

Figure 7.6: Dependence of the total current I on the applied bias voltage U for the 2D (green), 3D (red) and advanced 3D models with image charge correction of Spindt (blue dotted line) and Gomer (blue broken line) for $d = 10\,nm$. The radius was set to $r = 8.5\,nm$, the opening angle to $\gamma = 20°$ and the work function to $\Phi = 4.5\,eV$.

In the other variant (advanced 3D model) the curved surface of the tip is

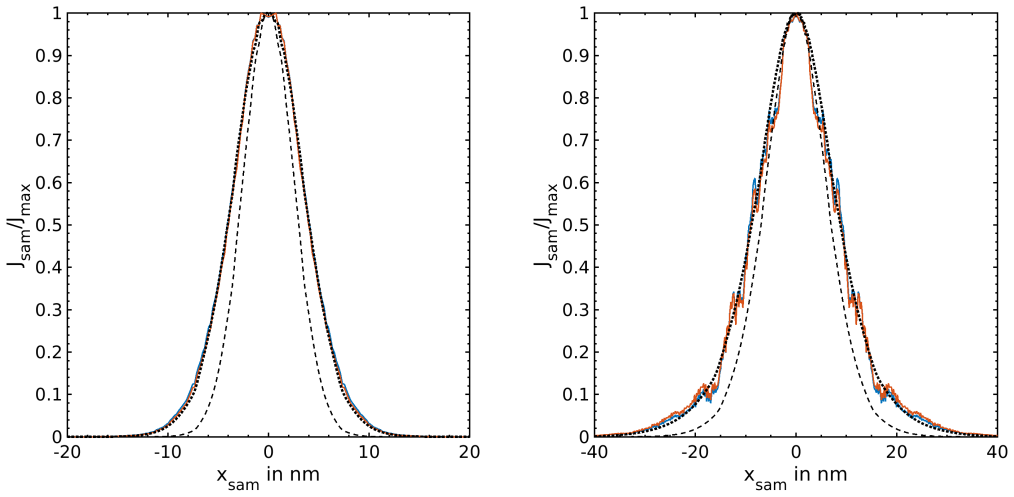

Figure 7.7: Scaled current density distribution for the 2D (broken black line), the 3D (dotted black line) and the advanced 3D model with the image charge correction proposed by Gomer [99] (blue line) and by Spindt et al. [106] (red line) for $U = 10\,V$ (*left*) and $100\,V$ (*right*) ($R = 8.5\,nm$, $\gamma = 20°$, $\Phi = 4.5\,eV$ and $d = 10\,nm$).

taken into account by using Fowler-Nordheim equation (5.2.2). Thereby, the velocity distribution of electrons inside the tip is considered for the emission probability and the trajectory calculation. The number of electron trajectories is increased by a factor depending on the number of energy values, polar and azimuthal angles of the incident electrons, which are taken into account. For the second model, two image charge potentials are considered in the Fowler-Nordheim equation (5.2.2) namely $v_G(y) = \sqrt{1-y}$ proposed by Gomer [99] and $v_S(y) = 1 - y^2$ from Spindt et al. [106] (see sec. 5.2 for more details). The first emission model includes the image charge model of Spindt et.al. [106].
The resulting dependence of the total current on the applied bias voltage is shown in fig. 7.6 for the different three dimensional models. Only for high bias voltages slight deviations between the 3D models can be seen.
Next, the current density distribution on the sample surface is considered since it will determine the line width and in this way the resolution of the FE-SPL. In fig. 7.7, the current density distributions for $U = 10\,V$ (left) and $100\,V$ (right) for the various 3D models are plotted. For better comparison, the current densities were scaled by their maximal value. The current density distribution using the flat-emitter assumption (2D model) is shown as well. On the left side of fig. 7.7 (for a small bias voltage), the variations between the different three dimensional models are hardly visible but the difference to the 2D model can be clearly seen. The differences between the 2D and 3D models can be explained by the differences of the electric field computation (see previous section). For the applied bias voltage of $100\,V$, the current density distributions are wider than for smaller voltages and the differences between the 3D models become more visible. The minor differences between the 3D flat-emitter approach and the advanced 3D model are due to the differences in

the current density distribution and the increased number of trajectories. The current density distributions for the different image charge correction factors, i e., the blue and the red line in fig. 7.7, almost overlap. The steps obtained for the advanced models arise from the adapted grid of the emission spots on the tips.
The influence of the incident velocity distribution was estimated by the following analytical approximation. The dominating factor of eq. (5.2.2) is the exponential function

$$J \propto \exp\left[-\frac{4\sqrt{2m_e\left(\Phi+\epsilon_F-\epsilon_{in}\cos^2\theta\right)^3}}{3e\hbar E}\,v(\theta,\epsilon_{in},E,\Phi)\right] = \exp\left[-\frac{D}{E}\,k(\theta)\right], \tag{7.2.1}$$

which includes the image charge correction $v(\theta,\epsilon_{in},E,\Phi)$. For the following analysis, the constants were summarized in parameter $D = \frac{4\sqrt{2m_e}}{3e\hbar}$ and the function $k(\theta)$ was introduced, using the image charge correction $v = v_S$ introduced in eq. (5.2.4)[2]. Thus, $k(\theta)$ is equal to

$$\begin{aligned} k(\theta) &= \left(\Phi+\epsilon_F-\epsilon_{in}\cos^2\theta\right)^{\frac{3}{2}}\left[c-\hat{y}_0^2\left(\frac{E^{\frac{1}{2}}}{\Phi+\epsilon_F-\epsilon_{in}\,\cos^2\theta}\right)^2\right] \\ &= \left(\Phi+\epsilon_F-\epsilon_{in}\cos^2\theta\right)^{-\frac{1}{2}}\left[c\left(\Phi+\epsilon_F-\epsilon_{in}\,\cos^2\theta\right)^2-\hat{y}_0^2\,E\right] \end{aligned} \tag{7.2.2}$$

It can be seen that for small polar angles $\theta \to 0$, function $k(\theta)$ decreases and so the current density J increases. Thus, a Taylor expansion for $\theta = 0$ up to the second order is used to find an estimation of function k

$$\begin{aligned} k \approx\ & \frac{c\left(\Phi+\epsilon_F-\epsilon_{in}\right)^2-\hat{y}_0^2\,E}{\left(\Phi+\epsilon_F-\epsilon_{in}\right)^{\frac{1}{2}}} \\ & + \frac{2\,\epsilon_{in}}{\Phi+\epsilon_F-\epsilon_{in}}\left[\frac{3\,c}{2}\left(\Phi+\epsilon_F-\epsilon_{in}\right)^{\frac{3}{2}}+\frac{\hat{y}_0^2\,E}{2}\left(\Phi+\epsilon_F-\epsilon_{in}\right)^{-\frac{1}{2}}\right]\frac{\theta^2}{2}. \end{aligned} \tag{7.2.3}$$

From the Fermi-Dirac distribution included in eq. (5.2.2) arises the criteria $\epsilon_{in} \approx \epsilon_F$ for the energy. This assumption leads to

$$k \approx \frac{c\,\Phi^2-\hat{y}_0^2\,E}{\Phi^{\frac{1}{2}}}+\frac{2\,\epsilon_F}{\Phi}\left[\frac{3\,c}{2}\,\Phi^{\frac{3}{2}}+\frac{\hat{y}_0^2\,E}{2\,\Phi^{\frac{1}{2}}}\right]\frac{\theta^2}{2} \tag{7.2.4}$$

and the current density J can be written as

$$J \propto A_0\,\exp\left[-\frac{D\,\epsilon_F}{E\,\Phi}\left[\frac{3\,c}{2}\,\Phi^{\frac{3}{2}}+\frac{\hat{y}_0^2\,E}{2\,\Phi^{\frac{1}{2}}}\right]\theta^2\right]. \tag{7.2.5}$$

The contribution for $\theta = 0$ is equal to

$$J(\theta=0) \propto A_0 = \exp\left[c\,\Phi^{\frac{3}{2}}-\hat{y}_0^2\,\frac{E}{\Phi^{\frac{1}{2}}}\right], \tag{7.2.6}$$

[2]Here, c is used for the constant value 0.95 of eq. (5.2.4).

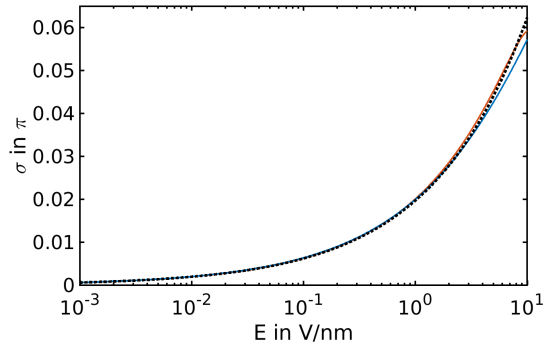

Figure 7.8: Standard deviation of $j(\theta)$ over the electric field strength for the case without (dotted black line), with Gomer's (red line) and Spindt's image charge correction (blue line) ($\Phi = 4.5\,eV$ [159] and $E_F = 6\,eV$ for tungsten [111] [160, 161]).

which corresponds to the Fowler-Nordheim equation (3.2.20) disregarding the incident velocity distribution. The derivation neglecting the image charge correction ($v(\theta) = 1$) or using $v = v_G$ proposed by Gomer can be done similarly.

The contribution of the polar angle θ is described by a Gaussian function (see (7.2.5)). The standard deviation of the Gaussian function

$$\sigma(E) = \sqrt{\frac{E\Phi}{2\,D\epsilon_F\left(\frac{3c}{2}\,\Phi^{\frac{3}{2}} + \frac{\hat{y}_0^2\,E}{2\,\Phi^{\frac{1}{2}}}\right)}} \tag{7.2.7}$$

determines the dependence of J on the incident polar angle θ, which is plotted in fig. 7.8 for all three different image charge corrections ($v = 1$, $v = v_G$ and v_S). It can be seen that σ does not reach $\frac{\pi}{10}$ in the range of interest for the FE-SPL case, i. e., for electric fields in the range of 0.1 to 10 $\frac{V}{nm}$. Thus, only for the highest field strengths, i. e., highest voltages and smallest tip-sample distances, and, thus, only for the emission spots in close proximity to the tip apex, a significant contribution of the Gaussian function (7.2.5) is obtained. In conclusion, the overall influence is assumed to be not crucial for FE-SPL in normal conditions and is neglected in the following chapters.
In the following, the distribution of the angle of incidence α on the tip sample (fig. 7.9) and electron time of flight between tip and sample (fig. 7.10) for all computed trajectories, are compared for the different models. On the left-hand side of fig. 7.9, α is shown for the advanced 3D model with the image correction suggested by Spindt et al. [106] for different bias voltages. The angle of incidence corresponds to a bias depending bending of the trajectories of the emitted electrons. A slight focusing effect is observable since the angle of incidence decreases for increasing bias voltage. However, an effect is only obtained for small bias voltages and there is hardly a difference between the distributions of α for $50\,V$ and $100\,V$ as seen in fig. 7.9. On the right side of this figure, the distributions of α for the different models are plotted. As expected, the 2D model differs from the advanced 3D models (which yield

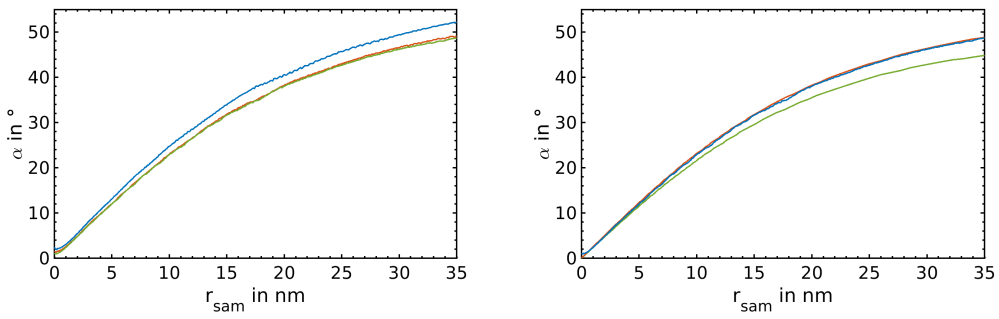

Figure 7.9: Distribution of angle of incidence α over the radial coordinate r_{sam} in the plane of the sample surface. (*Left*) $\alpha(r_{sam})$ is shown for the advanced 3D model with Spindt's image charge correction [106] for the applied bias voltage $U = 10\,V$ (blue), $50\,V$ (red) and $100\,V$ (green). (*Right*) Angle of incidence for the 2D model (green), the flat-emitter 3D (red) and the advanced 3D model with Spindt's image charge correction (blue) for $U = 100\,V$. The constant parameters were $r = 8.5\,nm$, $\gamma = 20°$, $\Phi = 4.5\,eV$ and $d = 10\,nm$.

nearly identical results, not distinguishable in this plot) and underestimates α esp. for higher values of r_{sam}. It is visible from fig. 7.9 that the differences of α for the different models starts to occur at $10\,nm$ which is consistent with the results of the current density distributions as shown in fig. 7.7. In other words, the differences in the electric field for 2D and 3D case cause differences in the trajectories, which can be observed in the distribution of the angle of incidence and in the current density distributions (see fig. 7.7).
The time of flight of the electrons from tip to sample is shown on the left side of fig. 7.10 for $U = 10\,V$ (blue), $50\,V$ (red) and $100\,V$ (green). The tip-sample distance was set to $10\,nm$. The results of the 2D model (broken lines) underestimates the time of flight t for $U = 10\,V$ whereas for higher voltages, it is overestimated. Only for the smallest bias voltage, a deviation between the three dimensional models can be observed, i. e., the "flat-surface" model yields a slightly higher t.
For all models, a decrease of t for increasing bias voltage U is visible as well as an increase of t for increased r_{sam} as expected from the electric field. To investigate the dependence on U and d, the time of flight $\langle t \rangle$ averaged over $r_{sam} \leq 20\,nm$ is plotted over the ratio $\frac{d}{\sqrt{U}}$ on the right side of fig. 7.10 for bias voltages $U \in [10, 100]\,V$. For all voltages, $\langle t \rangle$ is a linear function of $\frac{d}{\sqrt{U}}$ and for $U > 30\,V$, the variation for different U becomes negligible. For $U > 30\,V$, the averaged time of flight can be estimated by $\langle t \rangle = m\,\frac{d}{\sqrt{U}} + n$ with $m = 2.26\,\frac{fs\sqrt{V}}{nm}$ and $n = 0.32\,fs$. The analytical result for the time of flight is $t = \sqrt{\frac{2\,m_0}{e}}\,\frac{d}{\sqrt{U}}$, whereby a constant electric field $E = \frac{U}{d}$ (plate capacitor case) and zero incident velocity is assumed. This is shown in fig. 7.10 on the right-hand side by the broken black line. The smaller time of flight determined by the analytical results can be explained by the assumption of a constant electric field. However, the linear dependence on the ratio $\frac{d}{\sqrt{U}}$ is clearly observable.

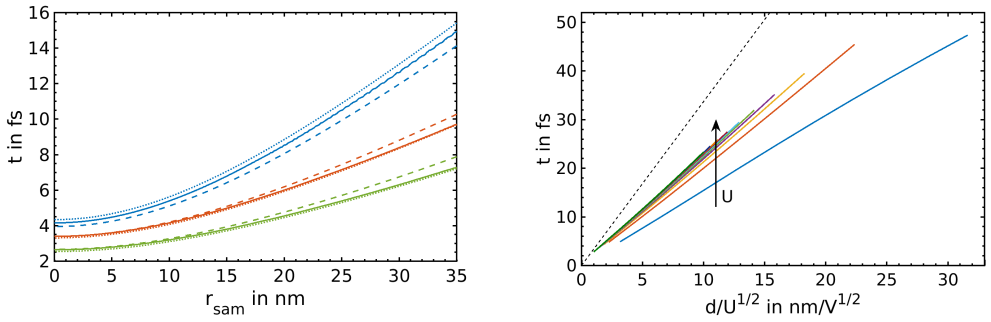

Figure 7.10: Distribution of the time of flight t at the sample for different applied voltages (*left*) and the average time of flight $\langle t \rangle$ over $\frac{d}{\sqrt{U}}$ (*right*). The graphs on the show the results of the 2D (broken lines), the 3D (dotted lines) and the advanced 3D model (solid lines) for applied voltages of $U = 10\,V$ (blue lines), $50\,V$ (red lines) and $100\,V$ (green lines). The parameters held constant were $r = 8.5\,nm$, $\gamma = 20°$, $\Phi = 4.5\,eV$ and $d = 10\,nm$.

To check the assumption to neglect electron-electron interactions in the air between tip and sample (or resist) surface, the time of flight is compared with the average time between the emission of two subsequent electrons from the tip which can be derived by the emission current. Typically, the maximal allowed current strengths in the experiments are in the nA range. Since large current strengths can yield to tip or sample damage. Note, this current limit restrict also the maximal bias voltage for a certain tip-sample distance, e. g., $U < 30\,V$ for $d = 10\,nm$ (see fig. 7.6). For maximal current strengths of about $100\,nA$, two subsequent electrons would be separated by an averaged time of about $\Delta t \approx \frac{e}{I} \approx 1.6\,ns$. From fig. 7.10 (right), it is obvious that the time of flight hardly exceeds $50\,fs$ in the parameter range of $d \in [10,\, 100]\,nm$ and $U \in [10,\, 100]\,V$. This verifies the assumption to neglect electron-electron interactions between the tip and the sample or resist surface.
In summary, results from different models were compared with regards to the application for FE-SPL. It was observed that the two dimensional calculation of the electric field is not appropriate to describe the FE-SPL case since the current strength (fig. 7.6), current density distribution (fig. 7.7), angle of incidence (fig. 7.9) and time of flight (fig. 7.10) deviate considerably. The results of the different three dimensional models show only small deviations, which were limited to highest electric field strengths and to the close proximity of the tip apex. In particular, the two different choices of the image correction yield nearly identical results. For most cases the 3D ("flat-emitter") model will be of appropriate accuracy, which reduce the computational effort drastically due to the reduced number of trajectories.
Consequently, in the remaining part of the thesis, the 3D flat-emitter model (5.2.1) will be used to calculate the current density distribution at the tip surface.
The next chapter deals with the analytical description of the numerical results to allow deeper physical insights and the opportunity for the use as real-time built-in function in the FE-SPL software.

Chapter 8

Analytical Model

The three dimensional numerical model ("flat emitter" case) allows the calculation of important values for the lithography application such as current density distribution and line width on the sample in dependence on internal tip parameters (radius, opening angle, work function) and external parameters (tip-sample distance, applied bias voltage, writing velocity). Nevertheless, finding optimal external parameters for a given tip or investigating global resolution limits with this model would be rather time and power consuming. For such purposes, it would be more favorable to have an analytical model, which predicts the most important influences of the various parameters onto the field-emission scanning probe lithography outcome.
In this chapter, the derivation of an analytical model is addressed, which consists of three parts:

- *the electric field distribution at the tip surface*: For the description of the electric field, the maximal field enhancement factor κ_p will be studied at first. It will be used to derive a model of the field enhancement κ of the complete tip surface.
- *the current density distribution at the tip surface:* The calculation of the emission current density is based on the well-known Fowler-Nordheim theory (eq. (3.2.20)) [77, 94, 95].
- *the current density distribution at the sample surface:* Based on a relation between the emission area at the tip and the respective exposed area at the sample, an analytical model for the conversion function between the current density distribution at the tip and at the sample is derived.

The analytical model is used to estimate the current density distribution J_{sam} on the sample considering external parameters (bias voltage and tip-sample distance) and internal parameters of the tip (work function radius and opening angle).
The current density distribution is applied for calculating the lithographic line width, which can be compared to experimental data. Furthermore, it allows the prediction of the optimal parameter set for a given tip but also of the resolution limits of the FE-SPL technique.

8.1 Electric field and field enhancement

8.1.1 Comparison of FEM data with analytical field enhancement models

The maximal electric field and, thus, the maximal field enhancement factor κ_p depend on the (smallest) tip-sample distance d, the tip radius r, the opening angle of the tip γ and the tip length L.

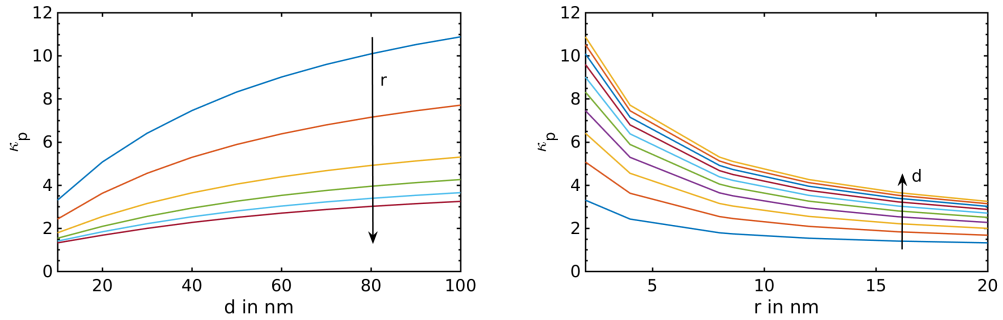

Figure 8.1: Field enhancement factor κ_p as a function of the tip-sample distance d (*left*) and the tip apex radius r (*right*) for different radii and distances, respectively. (*Left*) The tip radii are varied from $2\,nm$ (blue line) to $20\,nm$ (dark red line). (*Right*) κ_p is plotted for tip-sample distances from $d = 10\,nm$ (blue line) to $100\,nm$ (yellow line).

Besides the dependencies on the geometric values, the electric field is linear dependent on the applied bias voltage. In contrast, the field enhancement factor κ_p, as the ratio of the maximal electric field strength and the field strength of a plane capacitor, is independent of the bias voltage.
On the left side of figure 8.1, the maximal field enhancement factor κ_p is plotted as a function of the tip-sample distance d and on the right side as a function of the tip apex radius r. It could be assumed from fig. 8.1 that the field enhancement factor κ_p is proportional to d (left hand-side) and to $\frac{1}{r}$ (right hand-side) for different r and d, respectively. By plotting the field enhancement factor as a function of d/r (fig. 8.2), this assumption is proven since only slight deviations for $d \to 100\,nm$ are detectable for the respective radii r. These deviations seem to be negligible in the operational range of FE-SPL (see tab. 4.1). Therefore, the FEM results for all the different radii are treated like a single data set in the following part of this section.
In fig. 8.2, the numerically calculated field enhancement factor κ_p is also compared with the analytical models 1 (green line) and 2 (red line), which were introduced in the section 3.1. The model 1, reported by Mesa et al. [80], led to the eq. (3.1.5):

$$\kappa_p = \frac{2\sqrt{d(d+r)}}{r\,\ln\left(\frac{1+\sqrt{\frac{d}{d+r}}}{1-\sqrt{\frac{d}{d+r}}}\right)},$$

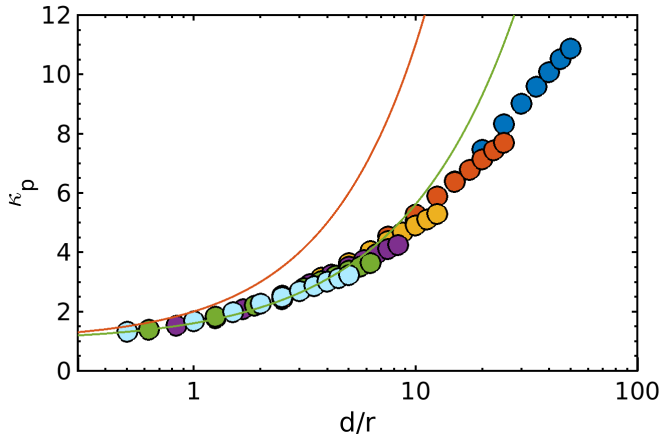

Figure 8.2: Field enhancement factor κ_p in dependence of $\frac{d}{r}$ for different tip radii r. The enhancement factors for different radii from $r = 2\,nm$ (blue dots) over $4\,nm$ (red dots), $8\,nm$ (yellow dots), $12\,nm$ (purple dots), $16\,nm$ (green dots) to $20\,nm$ (bright blue dots) are hardly distinguishable. The analytical models 1 (eq. (3.1.5)) and 2 (eq. (3.1.8)) are plotted as green and red line, respectively.

and model 2 from Miller [83] resulted in eq. (3.1.8) for $L \to \infty$:

$$\kappa_p = \frac{d}{r} + 1\,.$$

Model 1 of a hyperboloidic tip shows a fairly well overall agreement whereas model 2 resembles the FEM data only for small $\frac{d}{r}$ ratios as seen in fig. 8.2.
As expected for $d \ll r$, the numerical field enhancement factor κ_p, extracted from the FEM data, approaches 1 for $\frac{d}{r} \to 0$. For $\frac{d}{r} \to 0$, the curvature of the tip becomes negligible, i. e., the tip becomes more planar-like [83]. Therefore, the influence of the opening angle γ and the actual shape of the tip become negligible. This was shown by the study of Mesa et al. demonstrating that for the near-field case ($d < \frac{r}{2}$), the behavior resembles the sphere-plane system [80].

This behavior can also be seen in fig. 8.3, in which the influence of the opening angle γ on the field enhancement κ_p is plotted. Only, for larger $\frac{d}{r}$ ratios the influence of γ on κ_p becomes visible. For small ratios of $\frac{d}{r}$, the hyperboloidic model 1 underestimates the numerical values of κ_p. However, for constant r and increasing d, it changes since the hyperboloid (completely defined by r and d) becomes sharper, i. e., the opening angle γ decreases. This was already pointed out by Mesa et al. [80]. Therefore, a hyperboloidic model will predict the numerical or experimental data best if γ matches as well. For hemi-ellipsoidal tip models, a variation of d would not change γ, but the opening angle varies along the tip due to the ellipsoidal shape. This should influence κ_p esp. for large d.
So far only the maximal field enhancement κ_p was considered in the discussion.

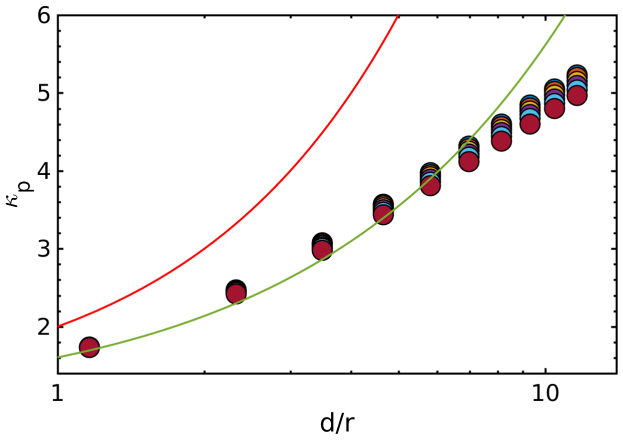

Figure 8.3: Field enhancement factor κ_p in dependence of the ratio of tip-sample distance d and radius r for different tip opening angles from $\gamma = 5°$ (blue dots) over 10° (red dots), 15° (yellow dots), 20° (purple dots), 25° (bright blue dots) to 30° (dark red dots). Models 1 (eq. (3.1.5)) and 2 (eq. (3.1.8)) are given as green and red line, respectively.

Nevertheless, the (spherical) field correction factor k_s might be used to extract the tip radius r from experimentally obtained data by plotting the applied voltage U as a function of $\frac{d}{r}$. This procedure was introduced by Young et al. [162] and refined by Mesa et al. [80] for hyperboloidic tips. For a constant-current field emission process, k_s is proportional to U since the maximal field strength $E_{max} = \frac{U}{k_s\, r}$ has to be constant (see eq. (3.1.1)). For large tip-sample distances $d \gg r$ of hyperboloidic tips, k_s was assumed by Gomer [99] to be

$$k_s \approx \frac{1}{2} \ln\left(\frac{4\,d}{r}\right) . \tag{8.1.1}$$

The extrapolated root of $k_s(d_0) = 0$ using eq. (8.1.1) yield to an estimation of the constant tip radius $r = 4\,d_0$. Thus, if d would be large enough for eq. (8.1.1) to become valid, a linear fit to k_s would enable the estimation of the tip radius. In the experimental constant-current field emission case, it could be done by measuring U as function of d.
In fig. 8.4, the spherical field correction factor k_s is plotted as a function of $\frac{d}{r}$ (on a logarithmic scale) for different radii together with the model 1 (green line) of Mesa et al. [80]. A linear regime of k_s for $d \to \infty$ is not obtained for the experimentally used tip-sample distances of our FE-SPL tool (see tab. 4.1). Additionally, the numerical field correction factor k_s (colored symbols in fig. 8.4) is nearly independent on the radius (varying from 2 to 20 nm). Therefore, the above mentioned procedure does not seem to be applicable to determine the tip radius in our case.
In summary, the numerical results of the field enhancement factor can be described only fairly well by the hyperboloidic model from Mesa et al. [80] in the range of distance-to-radius ratios of the FE-SPL experiments. The deviations

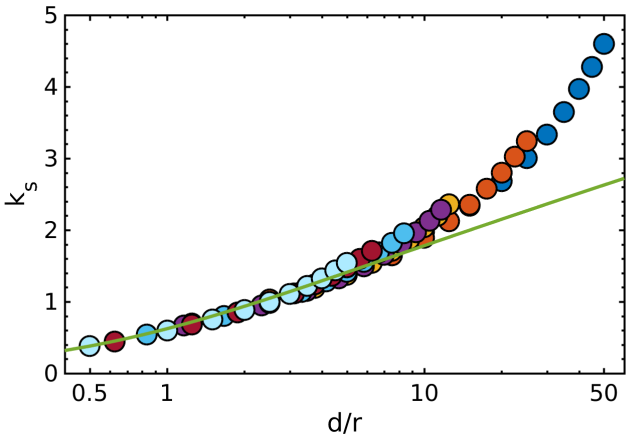

Figure 8.4: Spherical field correction factor k_s as a function of $\frac{d}{r}$ for the different tip radii from $r = 2\,nm$ (blue) to $20\,nm$ (bright blue). Additionally, the results of the analytical models 1 are shown as green line.

from the FEM data occur especially for large ratios of $\frac{d}{r}$. Thus, an analytical model is needed, which predicts the behavior of κ_p for the whole range of d/r used in FE-SPL.
A procedure to estimate the tip radius from experimentally obtained spherical field correction factor k_s data was discussed, which seems to be not applicable in the FE-SPL case since d is not large enough ($d \leq 100\,nm$).

8.1.2 Derivation of an analytical model for the FE-SPL case

To predict field emission current densities and lithographic results for a given tip shape, the estimate of the field enhancement factor κ_p has to be very accurate since the emission current density (eq. (3.2.18)) depends exponentially on the electric field strength. As shown in the previous section, the current analytical models do not fulfil this requirement for the whole parameter range. To derive an analytical expression, the limits for $r \to \infty$ and $d \to 0$ were considered, i. e., $\lim_{\frac{d}{r}\to 0} = 1$. This leads immediately to an expression of the form

$$\kappa_p\left(\frac{d}{r}\right) = 1 + \mathcal{A}_1 \left(\frac{d}{r}\right)^{\mathcal{B}_1}, \tag{8.1.2}$$

which might be expected from figs. 8.1 and 8.2. The best obtained fit of this function to the numerical data agreed reasonably well and the relative error was below 16% over the whole d/r range.
Unfortunately, the relative error is still too large for a sufficient agreement for the current density distribution based on the Fowler-Nordheim theory. As can be seen from fig. 8.2, the dependency of κ_p differs slightly with r. Thus, the

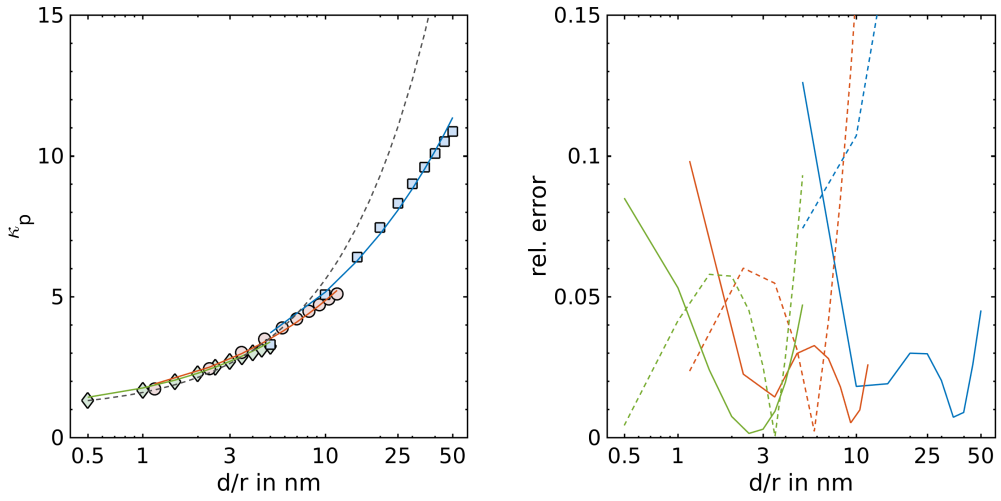

Figure 8.5: Field enhancement $\kappa_p(\frac{d}{r})$ (*left*) and relative error (*right*) obtained from the numerical simulation (symbols) and the model (8.1.4) for the tip radii $r = 2\,nm$ (□ and blue), $8.6\,nm$ (◯ and red) and $20\,nm$ (♢ and green). Results of the analytical model 1 of Mesa et al. [80] are drawn for comparison as broken lines (*left* in grey and *right* in the respective color).

power law was slightly refined and the magnitude of the expression was used:

$$\kappa_p(r,d) = \left| 1 + \mathcal{A}_2 \left(\frac{d}{r^{\mathcal{B}_2}} \right)^{\mathcal{C}_2} \right| . \tag{8.1.3}$$

The parameter $\mathcal{C}_2$ was found to be close to $\frac{1}{2}$. Thus, the equation for κ_p is found by

$$\kappa_p(d,r) = \sqrt{1 + \mathcal{A} \left(\frac{d}{r^{\mathcal{B}}} \right)} \tag{8.1.4}$$

with

$$\mathcal{A} \approx 2.72\, nm^{\mathcal{B}-1} , \qquad \mathcal{B} \approx 1.09 . \tag{8.1.5}$$

Expression (8.1.4) yields the theoretical limit of 1 for $d \to 0$ and $r \to \infty$. For the limits $d \to \infty$ and $r \to 0$, κ_p approaches ∞ as expected.
In fig. 8.5, the fit of the model (8.1.4) for the field enhancement factor κ_p to the numerical data is shown for three different radii $r = 2\,nm$ (□), $8.6\,nm$ (◯) and $20\,nm$ (♢). On the right side of fig. 8.5, the relative error values (between model and measurement data) are plotted for the three chosen radii as a function of $\frac{d}{r}$. The relative errors are lower than 5% for all ratios $\frac{d}{r}$ except for the smallest ratio (for each given radius). This is much smaller than the error values obtained for model 1 (fig. 8.5 (right)). The largest difference between the models is obtained for the smallest radius $r = 2\,nm$. Therefore, model (8.1.4) for $\kappa_p(\frac{d}{r}, r)$ will be used to derive an analytical expression of the FE-SPL process in the following.

8.1.3 Derivation of an expression for the electric field distribution at the tip surface

In the literature, the field enhancement factor κ_p at the tip apex, which corresponds to the maximal field enhancement, is often only considered in field emission related studies [22, 23, 79, 80, 83, 85, 86, 89, 90]. However, the electrons are not solely emitted from the tip apex but from a larger area of the tip, the so-called emission area due to the enhanced electric field in this region (see fig. 3.1). Some studies already described the enhanced electric field along the tip surface [78, 87, 163–166]. In this area of the tip, a measureable contribution of the field emission occurs due to the enhanced electric field strength, which was implicitly considered in some investigations [75, 77]. However, these publications do not include the concept of a field enhancement factor and used only numerical calculations of the electric field. Therefore, it is necessary to determine the electric field E_{tip} on the tip surface for the complete emission area to enable the computation of a realistic field-emission current density distribution J_{tip}.
To address this, a distribution κ of the field enhancement along the tip surface is used in analogy to the (maximal) field enhancement factor κ_p. The electric field E_{tip} at the tip surface can be written as

$$E_{tip}(\xi) = \kappa(\xi)\, E_p = \kappa(\xi)\, \frac{U}{d}\,. \tag{8.1.6}$$

in analogy to equation (3.1.2) for the (maximal) field enhancement factor κ_p. Here, ξ is the polar angle between the tip axis (z axis) and the discretization points at the tip surface[1]. Due to the rotational symmetry and the geometry of the tip, ξ is defined between between 0 and $\pi/2$.
Different formulas for the electric field on the tip surface were previously derived [78, 87, 164–166], which describe the angular dependency of the electric field directly rather than using a distribution of the field enhancement. For better comparability, these are rewritten as a distribution $\kappa(\xi)$.
Edgcombe and Valdrè [87] presented the analytical function

$$\kappa(\xi) = \kappa_p \cos\left(\frac{\xi}{2}\right)\,. \tag{8.1.7}$$

Podenok et al. [78] obtained

$$\kappa(\xi) = \kappa_p + h\left(\frac{L}{r}, \frac{d}{r}\right)\xi^2 \tag{8.1.8}$$

for their model of a "hemisphere on a post" (see fig. 3.2 b). The parameterized function h was set equal to

$$h\left(\frac{r}{L}, \frac{r}{d}\right) = \left(C_0 + C_1\,\frac{r}{L}\right)\left(1 + C_2\,\frac{r}{d} + C_3\,\frac{r^2}{d^2}\right)\,, \tag{8.1.9}$$

[1] The origin of the coordinate system is in the center of the sphere of the nanotip.

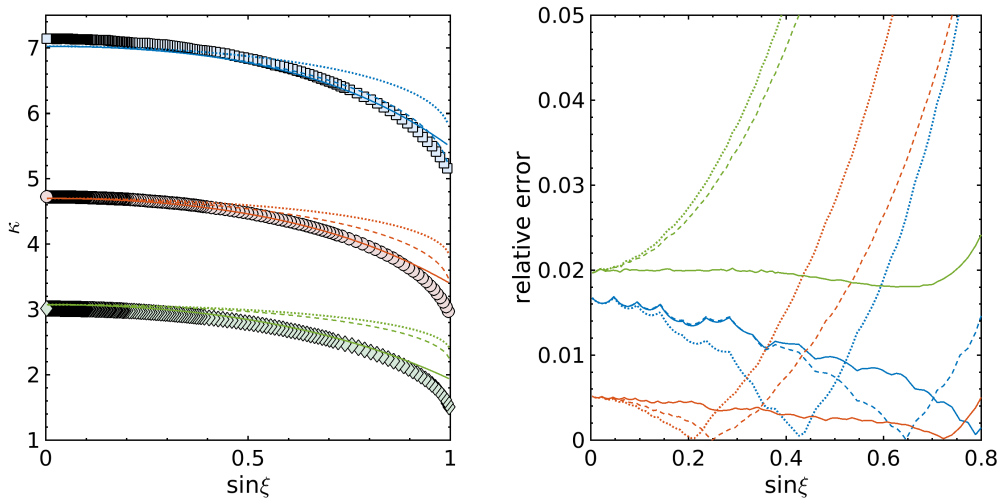

Figure 8.6: Field enhancement distribution κ along the tip surface, i. e., the normalized coordinate $\sin\xi = r_{tip}/r$, (*left*) and relative errors between numerical and analytical results (*right*) for tip radii $r = 4\,nm$ (blue), $8.6\,nm$ (red) and $20\,nm$ (green). The colored lines are the solutions $\kappa(\xi, \frac{d}{r}, r)$ of the analytical equation (8.1.12) (solid lines) and from models of Edgcombe and Valdre [87] (broken lines) and Podenok et al. [78] (dotted lines). (*Left*) The FEM data are marked by respective colored symbols. The tip-sample distance was set to $80\,nm$.

with parameters

$$C_0 = -7.71 \times 10^{-2}\,, \qquad C_1 = -0.659\,,$$
$$C_2 = 0.232\,, \qquad C_3 = 2.81\,. \tag{8.1.10}$$

Several studies used a "hyperboloidic tip" [164–166] schematically shown in fig. 3.2 d) based on the coordinate definition used by Pan et al. [167] for the analytical derivation of the electric field distribution. In this context, Zuber et al. [166] obtained the following distribution

$$\kappa(\xi) = \frac{2\sqrt{\frac{d}{r}}}{\ln\left(\frac{1+\sqrt{\frac{d}{d+r}}}{1-\sqrt{\frac{d}{d+r}}}\right)\sqrt{\xi^2 - \frac{d}{d+r}}}\,. \tag{8.1.11}$$

A comparison of FEM data with the models (8.1.7) and (8.1.9) is shown in fig. 8.6. Thereby, the field enhancement κ and so the electric field strength E_{tip} are relatively constant for angles below 50°, which is in agreement with the results published by McCord and Pease for tip radii r smaller than the tip-sample distance d [5]. The results of eq. (8.1.11) [166] are not shown because mostly relative errors above 10% were obtained for this model. It is obviously that the models (8.1.7) and (8.1.9) agree well with the FEM data for $\sin\xi < 0.5$ but not above.

Therefore, another model for $\kappa(\xi)$ is proposed here. By using a fit to the FEM data, the following field enhancement distribution at the tip surface was found to be

$$\kappa\left(\xi, d, r\right) = \kappa_p\left(d, r\right)\,\left(1 - \alpha\,\sin^4\xi\right) - \beta\,\sin^2\xi \tag{8.1.12}$$

with the parameter values

$$\alpha = \frac{1}{10}\,, \qquad\qquad \beta = \frac{5}{6}\,. \tag{8.1.13}$$

Here, the value $\kappa_p\left(d, r\right)$ is the maximal field enhancement factor derived in section 8.1.1. This expression of κ includes a term independent on κ_p (i. e., independent on the tip geometry and its distance to the sample) dominating κ for small ξ and a term depending on κ_p for larger ξ. A comparison between the field enhancement distribution κ_{num} obtained from FEM simulations and $\kappa(\xi, d, r)$ from the analytical equation (8.1.12) and the oe from the analytical models from Edgcombe and Valdrè [87] and Podenok et al. [78] are shown in fig. 8.6 (left). On the right side, the relative error $\frac{|\kappa_{num}-\kappa|}{\kappa_{num}}$ for the analytical expression (8.1.12) as well as for the models of Edgcombe and Valdrè [87] and Podenok et al. [78] are plotted. For all models shown in fig. 8.6, κ_p given by eq. (8.1.4) was used. It can be seen that the results of κ obtained from eq. (8.1.4) differ less than 3% from the FEM data for $\sin\xi$ up to 0.8. Additionally, the relative error remains almost constant over the whole range of $\sin\xi \in [0, 0.8]$. Thereby, the relative error originates mainly from the relative error of the maximal field enhancement κ_p at $\sin\xi = 0$. Thus, correctly estimating the maximal field enhancement factor κ_p over the whole parameter range of r and d is the most crucial part in predicting the enhancement distribution $\kappa(\xi, d, r)$. The results of eq. (8.1.12) agree better than the ones obtained from the other models [78, 87, 166] as seen on the right-hand side of fig. 8.6. Therefore, the electric field E_{tip} at the tip surface is obtainable using eq. (8.1.6) with $\kappa(\xi, d, r)$ defined by eq. (8.1.12).
Summarizing this section, an analytical expression for the electric field strength (eq. (8.1.6)) at the tip surface was derived, which is valid for the close proximity of tip and sample (FE-SPL case, see tab. 4.1). The model consists of the maximal field enhancement factor $\kappa_p\left(d, r\right)$ (eq. (8.1.4)) and the field enhancement distribution $\kappa\left(\xi, d, r\right)$ (eq. (8.1.12)) along the tip. It includes the dependencies on the tip radius r, the tip-sample distance d as well as the position at the tip using the polar angle ξ. It was found that the precise estimation of the (maximal) field enhancement factor $\kappa_p\left(d, r\right)$ is the most crucial part for the calculation of the current density to describe the FE-SPL process. The opening angle γ has only a minor influence on the field enhancement distribution and was, thus, neglected in the analytical expression of κ. Nevertheless, it was taken into account in the numerical simulation.

8.2 Derivation of an expression describing the current density distribution at the sample

To calculate the current density J_{sam} at the sample, it is necessary to calculate the current density J_{tip} at the tip surface and the ratio R between the emission area A_{tip} at the tip and the exposure area A_{sam} at the sample [5, 109]:

$$J_{sam}(\vec{r}_{sam}) = J_{tip}(\vec{r}_{tip}) \frac{A_{tip}(\vec{r}_{tip})}{A_{sam}(\vec{r}_{sam})} = J_{tip}(\vec{r}_{tip})\, R(\vec{r}_{tip}, \vec{r}_{sam})\,. \tag{8.2.1}$$

The field emission current density distribution J_{tip} along the tip surface is calculated by the Fowler-Nordheim equation (3.2.20) [77,106]. An example of J_{tip} is depicted in fig. 8.7. The current density is shown as scaled arrows and it is clearly visible that the emission is generated from an area equal to nearly half of the spherical area of the tip and not only from the tip apex.

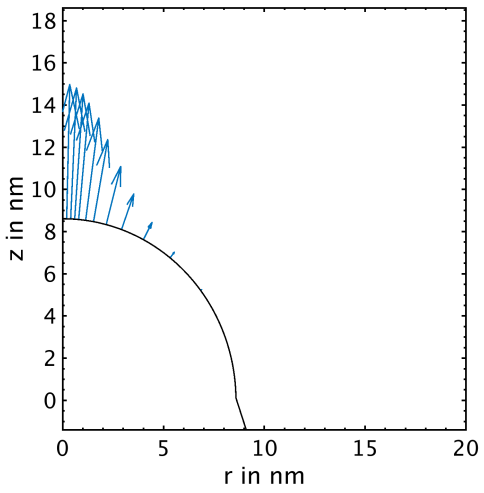

Figure 8.7: (Scaled) current density J_{tip} at tip surface (blue arrows). The current density is only shown for a few emission spots illustrating the adapted discretization.

Nevertheless, most part of J_{tip} is generated in close proximity of the tip apex and only this part will be considered for the derivation of the analytical ratio R_{an} of the emission and exposure area, i. e., the conical part of the tip is neglected. During the numerical computation the ratio $R_{num} = \frac{A_{tip}}{A_{sam}}$ is obtained from the trajectory calculation or by $R_{num} = \frac{J_{tip}}{J_{sam}}$ afterwards.
To find an analytical expression for the current density distribution at the sample, a model for the ratio of the areas is needed according to eq. (8.2.1). In other words, an estimate for the electron trajectories is needed. Here, the electric field lines and the so-called rays are used as estimates for the trajectories. In fig. 8.8, the field lines are plotted as blue lines, the rays as red lines and the calculated trajectories as grey broken lines. The rays are simply straight

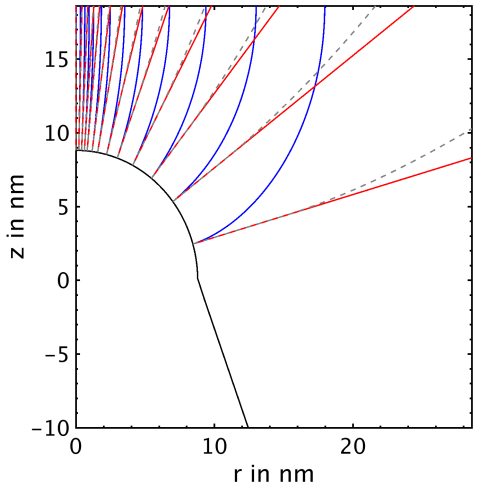

Figure 8.8: Electron trajectories (grey broken line), electric field lines (blue line) and rays (straight lines in red) between tip and sample.

extensions of the radius from the center of the circle through the emission spots towards the sample.
Estimation of the electron's trajectories from the electric field lines would be advantageous, since the electric field was already calculated for J_{tip}. By the use of elliptical coordinates, the electric field lines are given by the elliptical coordinate ν and the equipotential lines by the hyperboloidic coordinate μ. The relations to Cartesian coordinates are

$$\begin{aligned} x &= a \sinh\mu \sin\nu \\ z &= a \cosh\mu \cos\nu \,. \end{aligned} \tag{8.2.2}$$

Here, $a = r + d$ is the linear eccentricity of the hyperbola.
For the use of the elliptical coordinates, the tip geometry is transformed into an hyperboloidic tip with parameters similar to the ones used in the simulation, i. e., tip radius r and tip-sample spacing d. The geometry of the tip is given by the corresponding value of ν_{tip}, which can be obtained using the relation

$$\frac{x^2}{\sin^2\nu} + \frac{z^2}{\cos^2\nu} = a^2 \tag{8.2.3}$$

for the value of the smallest tip-sample distance, i. e., $z = d$ at $x = 0$:

$$\cos\nu_{tip} = \frac{d}{a} = \frac{d}{d+r} \,. \tag{8.2.4}$$

In this approach, the respective emission and exposure area are related by the same values of the μ coordinate. The emission area A_{tip} can be calculated by

rotating the tip around the z axis and using the respective equation

$$A_{tip} = 2\pi \int x(\mu) \sqrt{\left(\frac{dx}{d\mu}\right)^2 + \left(\frac{dz}{d\mu}\right)^2}\, d\mu\,. \tag{8.2.5}$$

The corresponding differential tip area is determined by

$$\frac{dA_{tip}}{d\mu} = 2\pi\, a^2\, \sinh\mu\, \sin\nu_{tip} \sqrt{\cosh^2(\mu)\, \sin^2(\nu_{tip}) + \sinh^2(\mu)\, \cos^2(\nu_{tip})}\,. \tag{8.2.6}$$

The differential sample area A_{sam} can be found using the definition of the area of a circle with the radius $x(\mu)$

$$\frac{dA_{sam}}{d\mu} = \frac{d(\pi\, x^2)}{d\mu} = 2\pi\, a^2\, \sinh\mu\, \cosh\mu\,. \tag{8.2.7}$$

Therefore, the ratio of both areas for the estimation of the electron trajectories by electric field lines is equal to

$$R_1 = \frac{A_{tip}}{A_{sam}} = \frac{dA_{tip}/d\mu}{dA_{sam}/d\mu} = \sin\nu_{tip} \sqrt{\sin^2(\nu_{tip}) + \tanh^2(\mu)\cos^2(\nu_{tip})}\,. \tag{8.2.8}$$

The second model uses rays to estimate the trajectories. Thereby, the polar angle ξ of a certain emission spot (already used in section 8.1.3) and $\Delta\xi$ as the angle between two adjacent emission spots (assuming equidistant emission spots) are used. The tip area is derived from the basic formula of a spherical segment

$$\begin{aligned} A_{tip}(r, \xi, \Delta\xi) &= 2\pi\, r\, h \\ &= 4\pi r^2\, \sin\left(\frac{\Delta\xi}{2}\right) \sin(\xi)\ . \end{aligned} \tag{8.2.9}$$

The corresponding sample area can be determined from

$$A_{sam}(r, d, \xi, \Delta\xi) = \pi\,(r+d)^2\, \frac{\sin\Delta\xi\, \sin(2\xi)}{\cos^2\left(\xi - \frac{\Delta\xi}{2}\right) \cos^2\left(\xi + \frac{\Delta\xi}{2}\right)}\,. \tag{8.2.10}$$

To obtain an expression independent of the actual choice of the emission spot grid spacing $\Delta\xi$, equations (8.2.9) and (8.2.10) are expanded using a Taylor series for $\Delta\xi \to 0$. Therefore, the tip area can be approximated by

$$A_{tip} \approx 2\pi\, r^2\, \Delta\xi\, \sin\xi \tag{8.2.11}$$

and the sample area by

$$A_{sam} \approx \frac{\pi\,(r+d)^2\, \Delta\xi\, \sin 2\xi}{\cos^4(\xi)}\,. \tag{8.2.12}$$

The ratio R_2 of A_{tip} and A_{sam} for small emission spot distances is thus given by

$$R_2 = \frac{A_{tip}}{A_{sam}} \approx \frac{r^2}{(r+d)^2}\, \cos^3(\xi)\,. \tag{8.2.13}$$

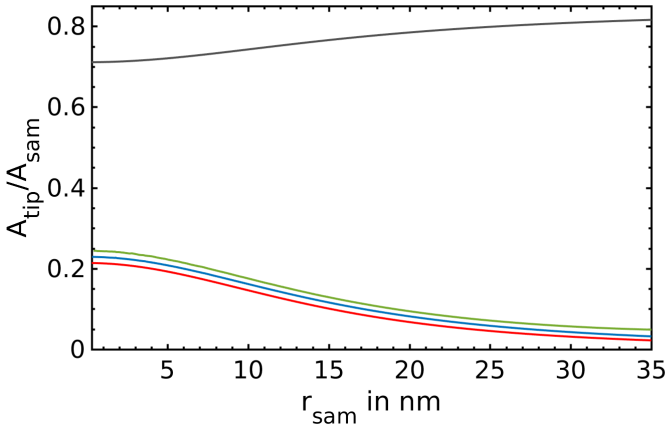

Figure 8.9: Ratio of tip to sample area for the FEM data (i. e., ratio of the current density at the tip and at the sample surface) for bias voltages $U = 10\,V$ (blue line) and $100\,V$ (green line) together with the two different analytical models. These models use either the electric field lines (grey line) or the "rays" (red line) to estimate tip and sample area.

In fig. 8.9, ratio $R_{num} = \frac{A_{tip}}{A_{sam}}$ of the numerical FEM data for bias voltages of $U = 10\,V$ (blue) and $100\,V$ (green) are drawn together with the analytical solutions R_1 for the field line models (grey) and R_2 for the ray model (red). It is obvious that the simple ray model describes the behavior of R_{num} and, thus, the trajectories better than the field line model. This can be understood, if one takes a look at the forces determining the trajectories. The field lines represent the force from the electric field on the electrons. The trajectories are given by the second derivative of the force. Thus, these are much less curved than the field lines. Additionally, the inhomogeneous electric field, i. e., the force, is enhanced near the tip apex surface and its strength weakens strongly for increasing distance to the tip apex, decreasing its influence on the trajectories. Thus, the electric field has only limited effect on the trajectories. This contradicts the use of field lines to estimate the trajectories from tip emitters as done in refs. [13, 22, 75]. Therefore, the straight rays are a better estimate for the electron trajectories.
In the following, the ray model is used for the calculation of the ratio of the areas, i. e., $R_{an} = R_2$.

8.2.1 Weighting function for the area ratio

Since the analytical expression of the ratio R_{an} of emission and exposure area is only an approximation of the area ratio R (see fig. 8.9), a weighting function f of the form

$$R(\xi, U, r, d) = f(\xi, U, r, d)\, R_{an}(\xi, r, d) \tag{8.2.14}$$

is necessary. Here, R_{an} is the analytical expression (8.2.13) of the ray trajectory model.
Before deriving the weighting function, some general aspects of the ratio R are considered. For small applied voltages $U \to 0$, the bending of trajectories becomes negligible and the ratio R approaches the ratio R_{an} of the ray model

$$\lim_{U\to 0} f(U,\dots) = 1\,. \tag{8.2.15}$$

The same value is expected for $d \to \infty$, since the electric field is proportional to the ratio $\frac{U}{d}$.
For large tip radii $r \to \infty$, the ratio of the areas will approach unity (plate-capacitor case). Thus, the weighting factor becomes

$$\lim_{r\to\infty} f(r,\dots) = \frac{1}{R_{an}(r\to\infty)} = \frac{1}{\cos^3(\xi)}\,. \tag{8.2.16}$$

However, for infinite tip radius, only the angle $\xi = 0$ is crucial leading to $\lim_{r\to\infty} f(r,\dots)|_{\xi=0} = 1$. The same argument can be used for the case $d \to 0$. By studying the different dependencies separately (by keeping the other parameters constant and not considering the limits), the following dependencies were found

$$\begin{aligned} &f(\xi,\dots) \propto \cosh(\text{const}\,\xi) + \text{const}\,, && f(r,\dots) \propto \frac{1}{r^{\text{const}}}\,. \\ &f(d,\dots) \propto d^{\text{const}}\,, && f(U,\dots) \propto \exp(-\text{const}\,U)\,. \end{aligned} \tag{8.2.17}$$

Combining these dependencies into one model yields

$$\begin{aligned} f(\xi,r,d,U) = f_1 \frac{d^{f_2}}{r^{f_3}} \left(1 - \exp\left(-f_4 \frac{U}{d}\right)\right) \cosh(f_5\,\xi) \\ + f_6 \frac{d^{f_7}}{r^{f_8}} \left(1 - \exp\left(-f_9 \frac{U}{d}\right)\right) + 1\,. \end{aligned} \tag{8.2.18}$$

The resulting values of the fit parameters allowed to decrease the number of fit parameters. Thus, the weighting functions is found to be

$$f(\xi,r,d,U) = f_1 \frac{d^{f_2}}{r^{f_3}} \left(1 - \exp\left[-f_4 \frac{U}{d}\right]\right) \Big(\cosh(4\,\xi) + 3\Big) + 1\,. \tag{8.2.19}$$

The remaining four parameter values were found to be

$$\begin{aligned} &f_1 \approx 0.01\,nm^{f3-f2}\,, && f_2 \approx 0.83\,, \\ &f_3 \approx 0.36\,, && f_4 \approx 3.98\,\frac{nm}{V}\,. \end{aligned} \tag{8.2.20}$$

Expression (8.2.19) yields the above mentioned limits for $U \to 0$ and $d \to \infty$ but also for $r \to \infty$ and $d \to 0$ by considering $\xi = 0$.
In fig. 8.10, the numerical (symbols) and analytical (colored lines) ratios R are drawn for a tip-sample distance $d = 80\,nm$ and a tip radius $r = 8.6\,nm$. The model (8.2.14) agrees well with the numerical simulation data for radii

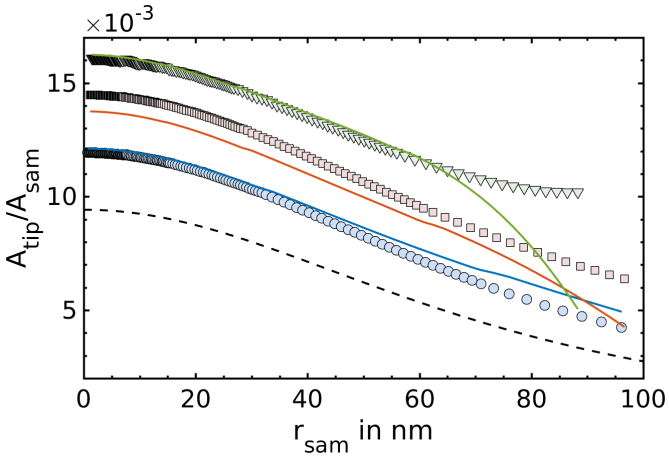

Figure 8.10: Ratio R of tip and sample area derived from the simulation data (symbols) and the ratio R_{an} of the analytical model multiplied by the weighting function $f(\xi, U, r, d)$ (colored lines) for voltages $U = 10\,V$ (blue ◯ and line), $20\,V$ (red □ and line) and $100\,V$ (green ▽ and line), tip-sample distance $d = 80\,nm$ and tip radius $r = 8.6\,nm$.

up to $r_{sam} = 60\,nm$ at the sample surface regardless of the value of the bias voltage. Thus, the most crucial region with the highest current density values is modelled sufficiently.

8.3 Summary of analytical model

In this section, the complete analytical model is summarized.
The analytical model for the current density J_{sam} at the sample is equal to

$$J_{sam}(\xi, r, d, U, \Phi) = J_{tip}(\xi, r, d, U, \Phi)\; R_{an}(\xi, r, d)\; f(\xi, r, d, U)\,, \tag{8.3.1}$$

where J_{tip} is the current density distribution at the tip surface, R_{an} the ratio of tip and the related sample area using the ray model and f the weighting function for R_{an}. The analytical model consists of the following parts:

- Maximal field enhancement factor (eq. (8.1.4))

$$\kappa_p(r, d) = \sqrt{1 + \mathcal{A}\,\frac{d}{r^{\mathcal{B}}}}\,, \tag{8.3.2}$$

- Field enhancement distribution along the tip surface (eq. (8.1.12))

$$\kappa(\xi, r, d) = \kappa_p(r, d)\,\left(1 - \alpha\,\sin^4(\xi)\right) - \beta\,\sin^2(\xi)\,, \tag{8.3.3}$$

- Electric field calculation (eq. (8.1.6))

$$E_{tip}(\xi, r, d, U) = \kappa(\xi, r, d)\,\frac{U}{d}\,, \tag{8.3.4}$$

Table 8.1: Parameter sets for analytical model.

eq.				
(8.3.2)	$\mathcal{A}$	$2.72\,nm^{\mathcal{B}-1}$	$\mathcal{B}$	1.09
(8.3.3)	α	1/10	β	5/6
(8.3.5)	A	$1.40\times10^{-6}\,\frac{eV\,A}{V^2}$	B	$9.87\,eV^{1/2}$
	C	$6.53\,\frac{V}{nm\,eV^{3/2}}$		
(8.3.6)	f_1	$0.01\,nm^{f_3-f_2}$	f_2	0.83
	f_3	0.36	f_4	$3.98\,\frac{nm}{V}$

- Fowler-Nordheim equation (eq. (3.2.20))

$$J_{tip}\left(\xi,r,d,U,\Phi\right)=\frac{A\,E_{tip}^{2}\left(\xi,r,d,U\right)}{\Phi}\times\exp\left(\frac{B}{\Phi^{\frac{1}{2}}}-\frac{C\Phi^{\frac{3}{2}}}{E_{tip}\left(\xi,r,d,U\right)}\right), \tag{8.3.5}$$

- Ratio of tip to sample area (eq. (8.2.13))

$$R_{an}\left(r,d,\xi\right)=\frac{A_{tip}\left(r,\xi\right)}{A_{sam}\left(r,d,\xi\right)}=\frac{r^2}{(r+d)^2}\cos^3(\xi)\,, \tag{8.3.6}$$

  and

- Weighting function (eq. (8.2.19))

$$f(\xi,r,d,U)=f_1\,\frac{d^{f_2}}{r^{f_3}}\left(1-\exp\left[-f_4\,\frac{U}{d}\right]\right)\Big(\cosh(4\,\xi)+3\Big)+1\,. \tag{8.3.7}$$

With these six equations (8.3.2)-(8.3.7) and 8 fit parameters[2], the current density at the sample can be computed for a "sphere on a cone" shaped tip. It takes into account the influences of the tip radius r and work function Φ, the tip-sample distance d, the applied bias U as well as the (polar) angles of the emission spots ξ. The opening angle of the tip is neglected in the analytical models because its influence was found to be negligible (as seen in fig. 8.3). The parameter values for eqs. (8.3.2)-(8.3.7) are listed in tab. 8.1.
A comparison of the numerically and analytically calculated current density distributions J_{sam} at the sample is shown in fig. 8.11 for different bias voltages U and a tip radius $r=8.6\,nm$ and tip-sample distance of $d=40\,nm$. As can be seen, the numerical and analytical results agree well. Small deviations from the numerical results occur, which can be mostly related to the estimation of the maximal enhancement factor κ_p. Nevertheless, the agreement is sufficient to predict relevant values for field-emission scanning probe lithography.

[2] A, B and C are parameters based on fundamental constants (see (3.2.19)).

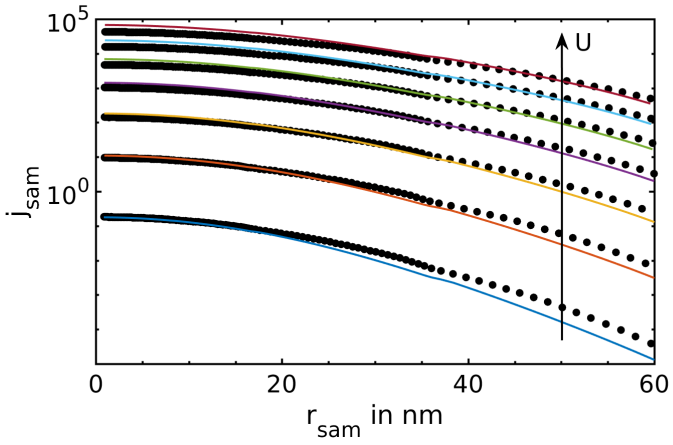

Figure 8.11: Analytical (colored lines) and numerical (black dots) current density distributions J_{sam} at the sample surface for applied bias voltages $U = 40\,V$ (blue line) to $100\,V$ (cyan line) ($\Delta U = 10\,V$), tip sample distance $d = 40\,nm$ and tip radius $r = 8.6\,nm$.

In the following chapters, the results obtained by the simulation and the analytical model will be compared in more detail and the dependence on the relevant parameters will be discussed. The discussion will be divided between relevant values for the field emission process (electric field and emission current) and important values for lithographic applications (current density distribution and line width).

Chapter 9

Results for field emission and comparison with experimental data

In this chapter, the results describing the field-emission characteristics are presented, which are important for applications like field-emission displays, etc. Thereby, the total field emission current I, an analysis of the Fowler-Nordheim plot and the emission area A_E on the tip surface will be discussed. The results are the basis for the chapter presenting the theoretical field-emission scanning probe lithography results of chapter 10. Additionally, the theoretical results are compared to experimentally obtained data in chapter 9.2.

9.1 Theoretical results for field emission

Since in the experiment, the current strength I is measured and not the current density distribution J, the derivation of the current strength will be done first. The total emission current I is equal to the surface integral over the current density. This is done numerically by the sum over the current density distribution J_{tip} of the various emission spots along the tip surface multiplied by the respective emission areas A_{tip}, i. e., $I_{num} = \sum_i J_{tip,i} A_{tip,i}$. For the analytical model, the total emission current I is derived using the analytical expression (8.3.5) of the emission current density J_{tip}. Note, the current density J_{sam} (8.3.2) at the sample could be used as well due to charge conservation. As mentioned before, the tip is modeled by a half sphere on top of a cone but, here, only the spherical part is considered like for the analytical model (see chapter 8). Thus, the use of spherical coordinates is advantageous for the derivation of the total current, which is given by

$$I = \iint J_{tip}\, dA_{tip} = \int_0^{2\pi} \int_0^{\pi/2} J_{tip}\, r^2 \sin\xi \, d\xi \, d\varphi \,. \tag{9.1.1}$$

The current density J_{tip} is independent of the azimuthal angle φ because of the rotational symmetry of the tip. This yields

$$I = 2\pi A \frac{r^2}{\Phi} \exp\left(\frac{B}{\sqrt{\Phi}}\right) \int_0^{\pi/2} E_{tip}^2(\xi) \exp\left(-\frac{C\,\Phi^{3/2}}{E_{tip}(\xi)}\right) \sin\xi\, d\xi\,, \qquad (9.1.2)$$

where the Fowler-Nordheim equation (8.3.5) was used. The electric field E_{tip} is given by eqs. (8.3.3) and (8.3.4)

$$E_{tip}(\xi) = \kappa(\xi) E_0 = \left(\kappa_p\,(1 - \alpha \sin^4\xi) - \beta \sin^2\xi\right) E_0 \qquad (9.1.3)$$

with the maximal field enhancement factor κ_p and the macroscopic electric field $E_0 = \frac{U}{d}$ of a plate capacitor. Neglecting the constants, the total current is proportional to

$$I \propto \int_0^{\pi/2} d\xi \left(\kappa_p - \alpha\kappa_p \sin^4\xi - \beta \sin^2\xi\right)^2 \sin\xi \times \exp\left(\frac{-1}{\kappa_p - \alpha\kappa_p \sin^4\xi - \beta \sin^2\xi}\right). \qquad (9.1.4)$$

To solve the integral, the exponent is approximated by

$$\exp\left(\frac{-1}{\kappa_p - \alpha\kappa_p \sin^4\xi - \beta \sin^2\xi}\right) \approx \exp\left(-\frac{1}{\kappa_p} - \frac{\beta}{\kappa_p^2}\xi^2\right) \qquad (9.1.5)$$

and the prefactor by

$$\left(\kappa_p - \alpha\kappa_p \sin^4\xi - \beta \sin^2\xi\right)^2 \sin\xi \approx \kappa_p^2\,\xi \qquad (9.1.6)$$

using Taylor expansions for $\xi = 0$ up to 2^{nd} degree. The remaining integral has the form $\int x \exp(-cx^2)\, dx = \frac{1}{2c} \exp(-cx^2)$ and the total current can, thus, be approximated by

$$I \approx \frac{\pi A}{\beta C} \frac{r^2 \kappa_p^4 E_0^3}{\Phi^{5/2}} \exp\left(\frac{B}{\sqrt{\Phi}} - \frac{C\Phi^{3/2}}{\kappa_p E_0}\right). \qquad (9.1.7)$$

Here, the contribution from the upper integration limit is negligible.
In fig. 9.1, the results of eq. (9.1.7) (solid lines) are compared with the numerical data (symbols) and the numerically integrated analytical current density given by (8.3.5) (broken lines). The numerical and analytical results of the total current agree well. The minor deviations between these results are caused by the approximations used for the analytical integration. Furthermore, eq. (9.1.7) describes the total current obtained numerically well in the parameter range of the FE-SPL experiments and will be used in the remaining part of the chapter.
To study a system based on field emission, measurements are often plotted in so-called Fowler-Nordheim plots, i. e., plotting $\ln(I/U^2)$ vs $1/U$. It is based on the assumption that the field-emission current I follows a similar equation

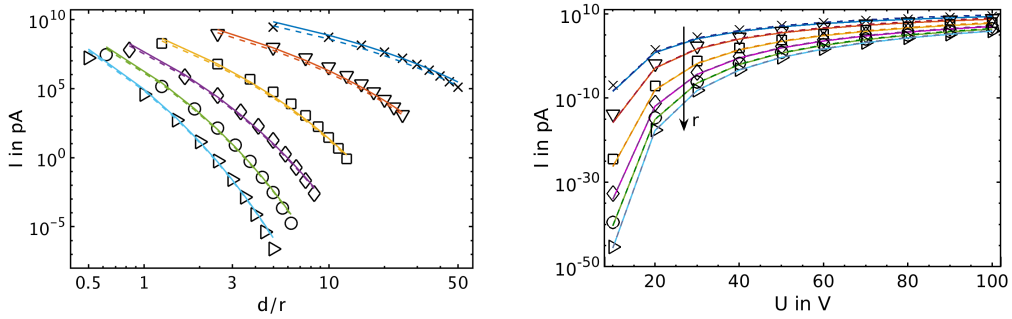

Figure 9.1: Numerical (symbols) and analytical results (lines) of the total current I as a function of the ratio $\frac{d}{r}$ (for $U = 50\,V$) (*left*) and of the bias voltage U (for $d = 50\,nm$) (*right*). The radius was $r = 2\,nm$ (X and blue), $4\,nm$ ($\triangledown$ and red), $8\,nm$ ($\square$ and yellow), $12\,nm$ ($\diamondsuit$ and purple), $16\,nm$ ($\bigcirc$ and green) and $20\,nm$ ($\triangleright$ and cyan), and the distance was varied from $10\,nm$ to $100\,nm$. The analytical results of eq. (9.1.7) are shown as solid line. The broken lines represent the analytical data using a numerical integration routine.

like the Fowler-Nordheim eq. (8.3.5) valid for J_{tip}. Thus, plotting $\ln(I/U^2)$ vs $1/U$ would yield to a linear function

$$\ln\left(\frac{I}{U^2}\right) \propto m(\Phi)\,\frac{1}{U} + n\,, \tag{9.1.8}$$

if $E_{tip} \propto \frac{U}{d}$ is used. Here, the slope m could be used to calculate the work function of the tip material Φ from experimentally obtained data. However, considering equation (9.1.7), a Fowler-Nordheim plot with $\ln(I/U^2)$ vs. $1/U$ would not give a linear function, since $\ln(I/U^2)$ would be given by two U-dependent terms. This hinders the determination of the work function. Fortunately, the adaption of the Fowler-Nordheim plot by using $\ln(I/U^3)$ leads to

$$\ln\left(\frac{I}{U^3}\right) = -\frac{C\Phi^{3/2}d}{\kappa_p}\,\frac{1}{U} + \ln\left(\frac{\pi A}{\beta C}\,\frac{r^2\kappa_p^3}{\Phi^{5/2}d^3}\right) + \frac{B}{\sqrt{\Phi}}\,. \tag{9.1.9}$$

Here, the slope

$$m = -\frac{Cd\Phi^{3/2}}{\kappa_p(r,d)} \tag{9.1.10}$$

can be used to estimate the work function since only one term dependents on the bias voltage U. Note, that in both cases (conventional Fowler-Nordheim plot (9.1.8) and adapted one (9.1.10)), the determination of the work function is only possible if the field enhancement factor κ_p is known, which in turn depends on tip-sample distance d and tip radius r. Eq. (9.1.10) for m is equal to the one obtained using the conventional Fowler-Nordheim plot.
In fig. 9.2, the conventional and the adapted Fowler-Nordheim plots are shown for the analytical model of the total current I determined by eq. (9.1.7). It is obvious that they deviate in both, the slope and the offset. By using a linear fit to the graphs of fig. 9.2 (left), the work function Φ is obtained. The resulting

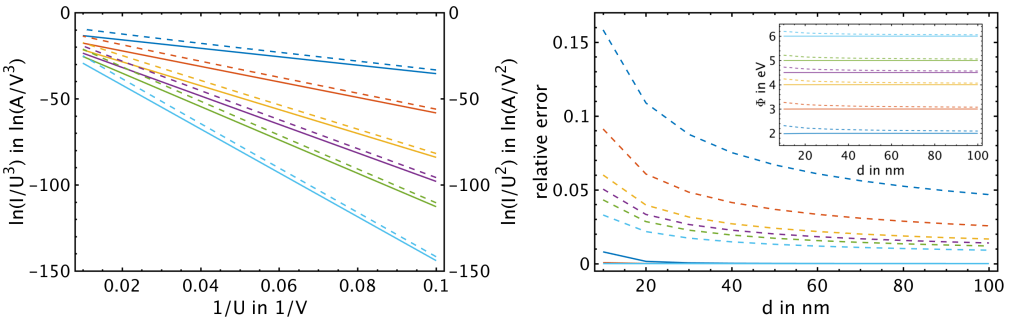

Figure 9.2: (*Left*) Fowler-Nordheim (broken lines) and adapted Fowler-Nordheim plots (solid lines) of the analytical model (9.1.7). (*Right*) Relative error of the computed work function Φ based on the conventional Fowler-Nordheim (broken lines) and the adapted Fowler-Nordheim plots (solid lines) for $\Phi = 2\,eV$ (blue), $\Phi = 3\,eV$ (red), ,$\Phi = 4\,eV$ (yellow), $\Phi = 4.5\,eV$ (purple) ,$\Phi = 5\,eV$ (green) and $\Phi = 6\,eV$ (cyan). The inset shows the corresponding values of the work function Φ. On both side, the tip radius was set to $8.6\,nm$ and the tip-sample distance to $d = 50\,nm$.

Φ values and the corresponding relative error of these values are plotted on the right side of fig. 9.2. As can be seen, the extraction of Φ from the conventional Fowler-Nordheim plots results in larger relative errors than the adapted ones. However, by taking the measurement tolerances into account, the values of Φ determined from experimental data might differ only slightly between both variants esp. for large tip-sample distances d. Another important value for field emitters is the emission area on the tip surface. It describes the surface area of the emitter tip, from which the main part of the current is emitted. For the field emission area A_E, an adapted definition of the one published by Zuber et al. [166] is used. A_E is determined by the position of the emission spot in the numerical case and by the angle ξ_A in the analytical case, for which the requirement

$$\frac{J_{sam}(\vec{r})}{\max(J_{sam})} = 0.01 \tag{9.1.11}$$

is fulfilled.

The spot area A_{tip} used in the previous chapter is the area of each emission spot, whereas the field emission area A_E is the sum of A_{tip}, for which the requirement (9.1.11) is fulfilled.

On the left-hand side of fig. 9.3, the dependence of the field emission area A_E on the tip radius r is shown. It is expected that A_E decreases for decreasing r since the tip surface decreases with r as can be seen from eq. (8.2.11) for the single emission spot areas A_{tip}. The solid lines in fig. 9.3 represent the results from the analytical model of chapter 8, while the symbols denote the results from the nanolithography simulations (see chapter 5). A remarkable agreement is observed considering that the focus of the derivation of the analytical model was on the area close to the tip apex. This agreement between numerical and analytical model can also be seen on the right side of fig. 9.3 showing the

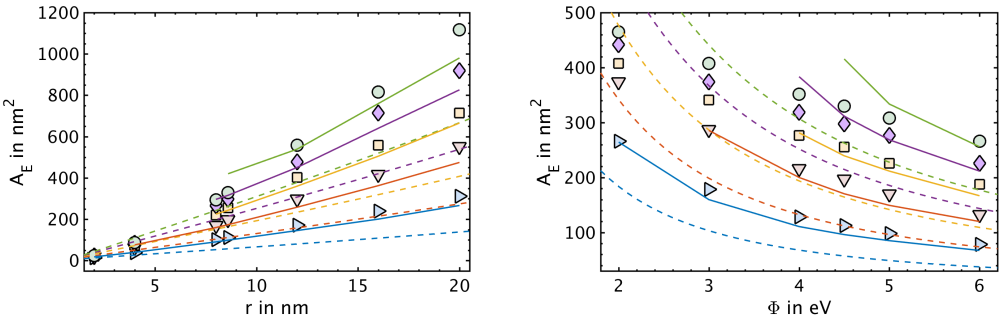

Figure 9.3: Emission area A_E plotted as a function of the tip radius r (*left*) and of the work function Φ (*right*) for the simulation (black symbols) and the analytical model (colored lines). $A_E(r)$ is shown for the bias voltages $U = 20\,V$ (X and blue line), $40\,V$ ($\triangledown$ and red), $60\,V$ ($\square$ and yellow), $80\,V$ ($\diamondsuit$ and purple) as well as $100\,V$ ($\bigcirc$ and green). The broken lines corresponds to the results of eq. (9.1.13). The distance between tip and sample was kept to $50\,nm$.

influence of the work function on A_E. The work function alters not only the strength of the current density but also its distribution and, in this way, the emission area.
To estimate the width of J_{tip} and, thus, A_E, the same approach is used for the analytical expression of the current density distribution (8.3.5) like for the derivation of the current strength, i. e., the Taylor expansion of the exponent (see eq. (9.1.5)). The resulting standard deviation equals

$$\sigma = \frac{\kappa_p}{2}\sqrt{\frac{E_0}{\beta C\,\Phi^{3/2}}} \tag{9.1.12}$$

and the emission area is then calculated by

$$A_E \approx 2\pi r^2\left[1 - \cos\left(-2\sigma^2 \ln 0.01\right)\right] \tag{9.1.13}$$

using the same requirement (eq. (9.1.11)). The results of this simple approach are shown by the broken lines in fig. 9.3. Again even by using a Taylor expansion around the tip apex, i. e., $\xi = 0$, the dependencies on r and Φ are represented fairly well by eq. (9.1.13). However, the emission area is underestimated by this simple approach. Surprisingly high values of the emission area are obtained, which refer to angles at the tip surface equal to $\xi_A = \sqrt{-2\sigma^2 \ln 0.01} = 60° \ldots 80°$. These high values of the emission area are in agreement with Dobisz et al. [22]. Nevertheless, they contradict the (unsaid) assumption that the electric field distribution for the field emission can be solely described by the maximal field enhancement κ_p [80, 83–85, 89].
On the left side of fig. 9.4, the emission area A_E is plotted against the tip-sample distance d for the numerical and analytical model in comparison. The numerically obtained emission area (black symbols) slightly decrease with increasing tip-sample distance d. The decrease of A_E is describable roughly by eq. (9.1.13) as seen by the broken lines in fig. 9.4. However, the dependence

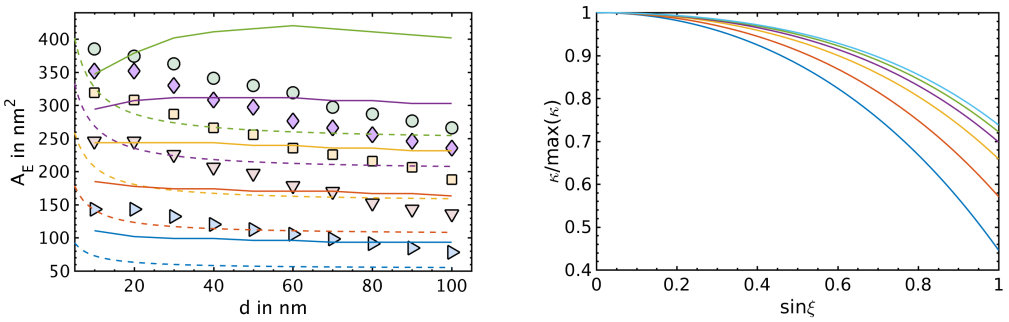

Figure 9.4: Numerically (black symbols) and analytically (colored lines) calculated field emission area A_E as a function of the tip-sample distance d (*left*) together with the scaled field enhancement distribution along the tip surface (*right*). (*Left*) $A_E(d)$ is shown for the bias voltages $U = 20\,V$ (X and blue line), $40\,V$ ($\triangledown$ and red), $60\,V$ ($\square$ and yellow), $80\,V$ ($\diamondsuit$ and purple) as well as $100\,V$ ($\bigcirc$ and green). The broken lines corresponds to the results of eq. (9.1.13). (*Right*) The scaled enhancement distribution is given for $d = 10\,nm$ (blue), $20\,nm$ (red), $40\,nm$ (yellow), $60\,nm$ (purple), $80\,nm$ (green) and $100\,nm$ (cyan). The radius was set to $8.6\,nm$.

of A_E on d changes for the smallest d values, i. e., a maximal emission area is observed for $d = 20\,nm$. The increase of A_E for the smallest distances can be explained by the field enhancement at the tip surface shown on the right side of fig. 9.4. There, it can be seen that the decrease of the (scaled) κ_p (for increased ξ) is reduced for increasing tip-sample distance d. In other words, the electric field strength remains nearly constant over a larger tip surface (for increased d), which yields to an increase of the emission area. For larger distances and larger bias voltages, the small decrease can also be described by eq. (9.1.13). While the analytical model (8.3.2) (solid lines) agrees mainly with the numerical results of A_E, it underestimates the influence of the tip-sample distance for small d and does not include the above mentioned increase of A_E. This is mainly due to the focus on the tip apex for the derivation of the analytical model.
On both sides of fig. 9.3 and on the left side of fig. 9.4, the increase of A_E for increased bias voltages can be seen, which is included in eq. (9.1.13).
It is seen, that the influence of U on A_E exceeds the effects of the other parameters r, d and Φ.
In summary, an analytical model for the total current strength was derived and compared with respective results from the numerical model and from the analytical model using a numerical integration procedure. Therewith, a method for fast and simple estimation of the total current strength in FE-SPL was achieved by the analytical model. Based on the derived analytical expression, the analysis of the Fowler-Nordheim plot was presented, which leads to an adapted Fowler-Nordheim plot. This adaption allows the determination of the work function Φ of the tip material with high accuracy, if the field enhancement factor $\kappa_p(d, r)$ is known. Using the conventional Fowler-Nordheim plot a

relative error of up to 15% were obtained.
The emission area (defined by 1% of the maximal current density at the tip surface [166]) encompasses the majority of the spherical part of the studied tips (for $r \geq 20\,nm$). Due to the strong effect of the bias voltage on field emission and so on the emission area, it is the most important dependence to express analytically and yield the largest differences between numerical and analytical results (as seen in figs. 9.3 and 9.4). Nevertheless, the behavior could be described correctly in most cases and a simple approach using a Taylor expansion of the current density resembles the dependencies well but underestimates the emission area.
In the next section, the theoretically determined current strength I will be compared to experimentally obtained data.

9.2 Comparison between experimental and theoretical field-emission results

To experimentally verify the previously described models, measurements of the field emission current and tip-sample distance have to be done (nearly) simultaneously. The functionality of FE-SPL but also AFM and STM does not rely on the knowledge of the absolute distance between tip and sample but on the interaction between them, i. e., the relative tip-sample distance. Thus, in these systems, the absolute tip-sample distance is normally not available or only measurable by additional equipment. However, the tip-sample distance is of great importance, since a verification of the analytical model can only be successful, if most of the parameters are known. Otherwise different sets of parameters might be found for a certain experimental data set. One proposed possibility to define the absolute value of the tip-sample distance would be to approach the tip into scanning tunneling microscope operation ($d < 5\,nm$) by applying only a small bias voltage [79]. If the feedback control is not carefully adjusted, tip and sample might be brought into mechanical or electrical contact. This could yield to modifications of tip shape and sample, which prevent a reliable comparison with the theory due to a modified tip shape. Additionally, this approach can only be done under vacuum conditions, since otherwise local oxidation would occur caused by a water meniscus between tip and sample [120]. This would alter the behavior and increase the error of the zero point determination.
After a significant amount of technological and engineering work of our group (mainly done by M. Holz, I. Atanasov, C. Reuter, Dr E. Guljiev, Dr A. Ahmad and A. Reum), measurements of the current strength I as function of the applied bias voltage U together with (nearly) simultaneous measurements of tip-sample distance d and tip radius r_{tip} were achieved. It was also possible to obtain the dependency of the field emission current on the (relative) tip-sample distance d_{rel} and to check the tip for modifications before and after each measurement.
For this measurements, a basic atomic force microscope with integrated scan-

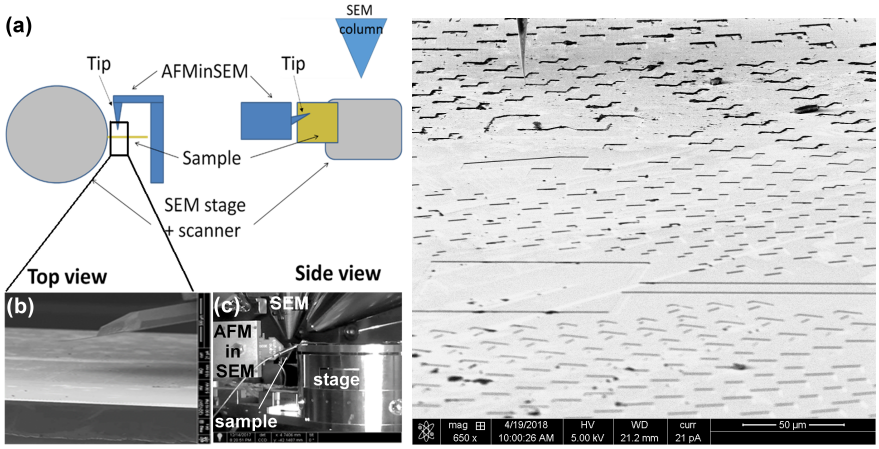

Figure 9.5: (*Left*) Scheme of the modified AFMinSEM set-up [60,61] for the field emission experiments (a). SEM image of the cantilever and the sample (b). Optical image of the experimental set-up inside the dual beam (electron and ion beam) vacuum chamber (c). The nanotip and the electron gun (above tip and sample in the image) are mounted perpendicular to each other to allow measurement of tip-sample distance and tip radius. (Figure taken from [169].) (*Right*) Scanning electron image with low resolution ($50\,\mu m$) for an overview of the silicon sample, which was covered with a $5\,nm$ thick chromium layer (adhesion layer) and $30\,nm$ thick gold top layer.

ning probe lithography functionality using active cantilevers [11,68] was adjusted to vacuum conditions. This includes an increased sensitivity of the control feedback because a main damping mechanism of the cantilever oscillation is friction in air [168]. Additionally, the system was adapted to the limited space inside the vacuum chamber of a scanning electron microscope. Typically, AFM systems incorporated into SEM are mounted in a way that tip and electron gun are oriented in the same direction to enable SEM imaging and corresponding AFM topography imaging to yield nanometer precise lateral (via SEM) and vertical information (via AFM) of the surface [60] or to enable overlay alignment for mix-and-match capabilities by combining electron beam and scanning probe lithography. In contrast, for measurements of the tip-sample distance d, tip and sample have to be mounted perpendicular to the electron gun to enable a sideview of tip and sample as shown on the left side of fig. 9.5. After these mechanical, electronical, controlling and software adaptions, Dr Claudia Lenk was able to achieve the experimental measurements presented in the following, which could be compared to results from the analytical expression (9.1.7).
On the left-hand side of fig. 9.5, the experimental set-up is explained. The adapted AFMinSEM set-up [60, 61] within the vacuum chamber of a dual-beam tool[1] is shown by an optical image (fig. 9.5 (c)). The cantilever, which is mounted on a printed circuit board, and the gold covered sample are seen in the SEM image (fig. 9.5 (b)). On the right side of fig. 9.5, a low-resolution image (scale: $50\,\mu m$) of the gold covered silicon sample is shown. Pre-patterned

[1] A tool combining SEM and focused ion beam (FIB) functionality.

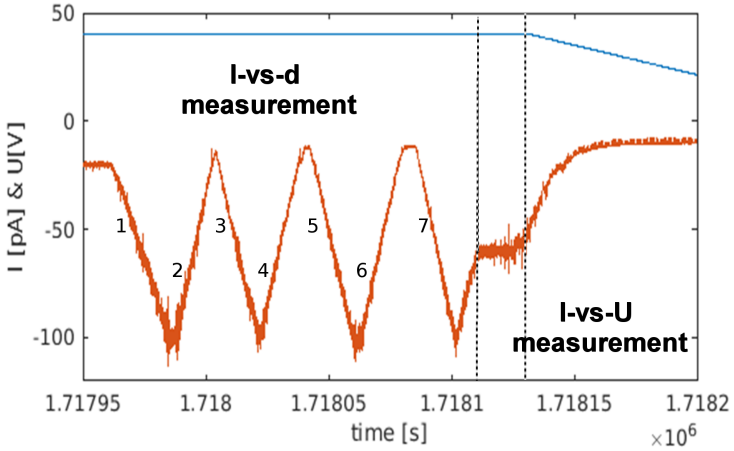

Figure 9.6: Data of total current I (red line) and bias voltage U (blue line) over time using the set-up shown in fig. 9.5 for a single experiment (adapted from [169]). The bias voltage U was kept constant during the variation of tip-sample distance for determination of $I(d)$ ("I-vs-d measurement"). Several cycles of varying d were executed and numbered (here $1-7$). In the 2^{nd} part, $I(U)$ was measured for constant d ("I-vs-U measurement").

navigation structures on the sample are visible as well. In the upper left part of the fig. 9.5 (right), the scanning probe tip can be seen. The tip is in its "off" position far away (several μm) from the sample.
For the field-emission experiments, the following procedure was applied (as seen in fig. 9.6):

1. Tip approach to the sample until current set-point is reached using FE-SPL control algorithm.
2. Measurement of the relative tip-sample distance during variation of the current set-point (several cycles, see fig. 9.7) for constant bias voltage U ("I-vs-d measurement")[2].
3. Turn-off of the FE-SPL control to hold a constant tip-sample distance during the following experiment (assuming negligible drift) at a given current set-point.
4. Fowler-Nordheim measurement, i. e., current strength measurement during variation of the applied bias voltage (at the sample) for constant d ("I-vs-U measurement", see fig.9.6).
5. Imaging of tip and sample without an applied bias voltage directly after the Fowler-Nordheim experiment[3] to define the tip-sample distance.

[2] Here, the current control of the FE-SPL system adjusts the tip-sample distance to achieve the pre-defined current set-points.

[3] It was not possible to achieve an image during the field-emission experiment without image distortions since the applied bias voltage at the tip alters the (primary and secondary) electron trajectories used to generate the SEM image.

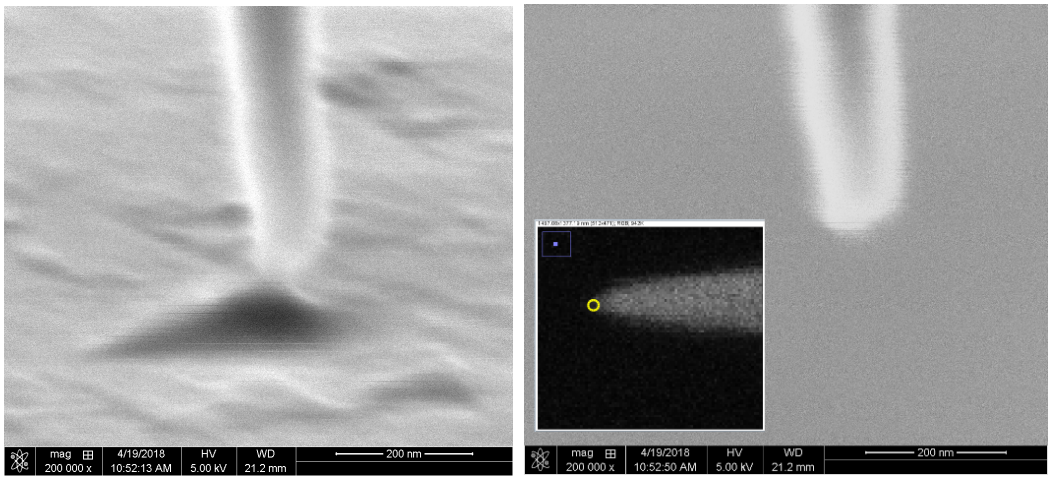

Figure 9.7: SEM images obtained after the field-emission experiments. (*Left*) Image used for the measurement of the tip-sample distance without retracting the tip after application of a bias voltage for the field-emission measurement. It can be seen that during the experiment the surface of the gold layer was modified, which could be due to deposition of material or change of the atomic properties of the layer stack (Au-Cr-Si sample). (*Right*) After the tip is retracted to its stand-by position, a SEM image was taken and used for the tip radius estimation. The grey scale inlet was used to determined the tip radius from a high-resolution SEM measurement. The tip diameter was determined to be around $11\,nm$ using the yellow circle.

6. Retracting the tip to its "off" position and image it to determine the tip radius.

This procedure allowed the estimation of the tip-sample distance and the tip radius directly after the field-emission experiment. Results of the field-emission experiments, the tip-sample and tip radius measurements were recently published by our group [169]. The experiments were repeated several times using three different current set points ($I = 25\,pA, 40\,pA$ and $60\,pA$), i. e., three different tip-sample distances[4]. Therewith, a reliable experimental realization seems to be found to verify the analytical model presented before.
On the left side of fig. 9.7, a SEM image of tip and sample directly after a Fowler-Nordheim experiment is shown. The tip-sample distance d is assumed to be constant, but careful investigations regarding the (horizontal) drift of the system yield a drift velocity of about $1\,nm/s$ after an evacuation time of about $24h$. Therefore, the analysis of the experimental data has to consider the influences of the drift motion.
Unfortunately, it was found that the gold surface was modified during exposure with low-energy electrons as observed on the left side of fig. 9.7. This might be a similar behavior like it was reported for silicon in [170] or maybe the silicon itself, underneath the gold and chromium layer, is modified. Alternat-

[4] These are the so-called off-set values d_{off} since only relative distances could be determined during field-emission experiments.

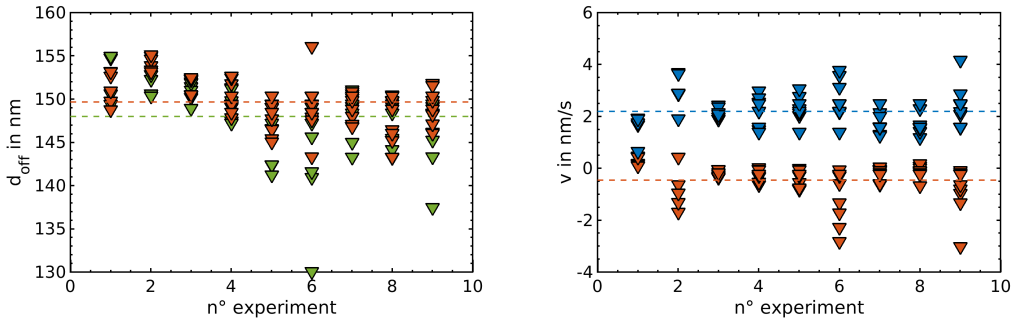

Figure 9.8: Tip-sample distance off-set d_{off} (*left*) and measurement velocity v_M (blue) and fitted drift velocity v_D (red) for all analyzed experiments (*right*). (*Left*) The off-set values d_{off} are obtained by using a fit of the analytical equation (9.1.7) for each cycle of the experiments without considering drift velocity ($v_D = 0$, green $\bigtriangledown$) and with considering drift velocity (eq. (9.2.1), red $\diamondsuit$). The mean values are shown as broken lines.

ively, the surface modifications could be caused by deposition of carbon from residuals in the vacuum chamber [171]. However, an in-depth analysis of the structures was not possible, in particular an in situ material analysis, since the high-resolution SEM mode and an energy-dispersive X-ray analysis unit were not applicable.
On the right side of fig. 9.7, the tip apex is shown after retraction of the tip to its "off" position. The inset shows a zoom of the tip as a grey-scale image used for the determination of the tip apex radius. The tip radius was estimated to be $r_{tip} \approx 5\,nm$ (marked by the yellow circle).
Since the tip-sample distance in this experiment was obtained only by using the signal of the piezoelectric actuators, the off-set value d_{off} is unknown and thus, the current I is given over the relative tip-sample distance d_{rel}. SEM images, like the one shown in fig. 9.7, were used to determine the tip-sample distance but only after the "I-vs-U" measurement of each experiment (see fig. 9.6). Due to drift in the system, a significant difference between the measured value d_{SEM} and d_{off} might occur. By taking the camera's point of view into account, we obtained a distance of about $30\,nm$, but the (unknown) sample tilt was not considered.
Since the experimental determination of d_{off} was not as simple and accurate as expected, the tip-sample distance and the drift velocity were estimated by using a fitting routine. Therefore, the analytical expression (9.1.7) of the current strength was used for the two fitting procedures. The first one considers only the off-set value d_{off} without any drift (i. e., $v_D = 0$) and the second one takes additionally the drift velocity v_D into account using

$$d = d_{rel} + d_{\text{off}} + \frac{v_D}{v_M}\, d_{rel}\,. \tag{9.2.1}$$

Here, v_M is the measurement velocity obtained from linear fits to d_{rel} over the measurement time for the respective cycle (see fig. 9.6).

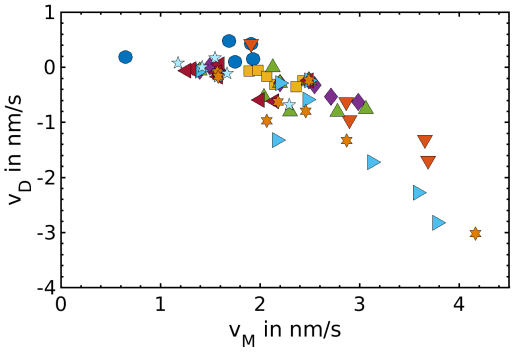

Figure 9.9: Fitted drift velocities v_D over measurement velocity v_M for the all used cycles of the nine I-vs-d experiments.

The resulting d_{off} values for the different cycles of the nine experiments are shown on the left side of fig. 9.8. Most of the obtained off-set values lie between $135\,nm$ and $155\,nm$. The mean values (marked by broken lines in fig. 9.8) were found to be $\overline{d}_{\text{off}} \approx 148.0\,nm$ (green) and $149.6\,nm$ (red) without and with considering v_D, respectively.
On the right-hand side of fig. 9.8, the measurement velocity v_M (blue) and the drift velocity v_D (red) are plotted. Only positive values of v_M are used, since all data sets were transformed to represent increasing tip-sample distances by assuming temporal symmetry during a measurement cycle. The drift v_D is obtained afterwards and found to be smaller than v_M, as it was expected. A constant growth of a structure (as the one seen in fig. 9.7 (left)) should yield a motion of the tip increasing d since the regulation of the system tries to keep the current set-point constant. In the analysis of the experiments, this would not be distinguishable from a drift motion. However, a growth leads always to a positive "drift" in time and the transformation would, thus, yield to an oscillating behavior of v_D. Therefore, the growth rate of the structure seems to be slower than the drift of the system or the growth might be strongly non-linear and limited to the large values of I. Thus, the growth would only influence a small part of the I-vs-d experimental curve, which cannot be captured by the above procedure. Additionally, the almost linear dependency of v_D on v_M (shown in fig. 9.9) suggests that the observed drift might be systemic and not based on an external (random) influence leading to a random drift velocity and direction.
In fig. 9.10, the experimental data of the current strength are plotted as function of the absolute tip-sample distance d given by eq. (9.2.1) using the values v_D, v_M and d_{off} shown in fig. 9.8. Additionally, the results from fitting eq. (9.1.7) to the data are shown neglecting v_D (green line) and taking v_D into account (red line). Here, the analytical results are plotted using the averaged values of d_{off}, v_M and v_D (see broken lines in fig. 9.8). Both analytical results show good overall agreement with the measured data. In this case, it is

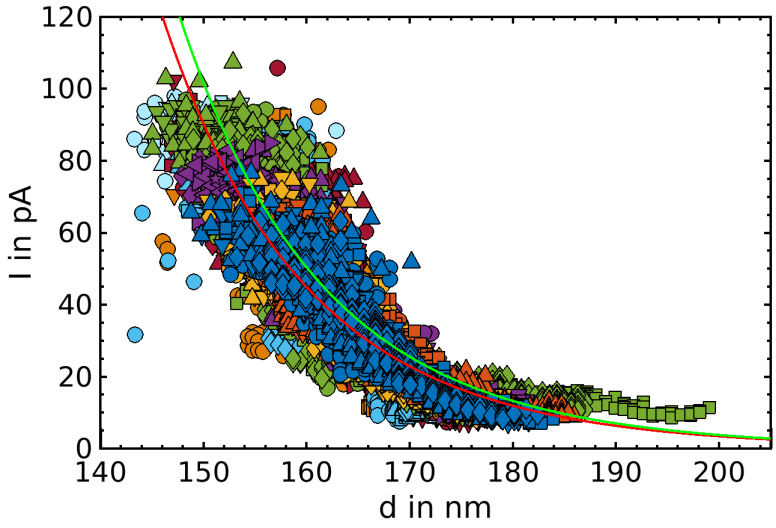

Figure 9.10: Experimental current strength I plotted over the absolute tip-sample distance d (eq. (9.2.1)). The (averaged) analytical results obtained by eq. (9.1.7) without (green) and with considering drift (red) are plotted as well.

obvious that the drift $v_D \approx -0.2\,nm/s$ is almost negligible, in particular, in comparison with the variation of the experimental data.

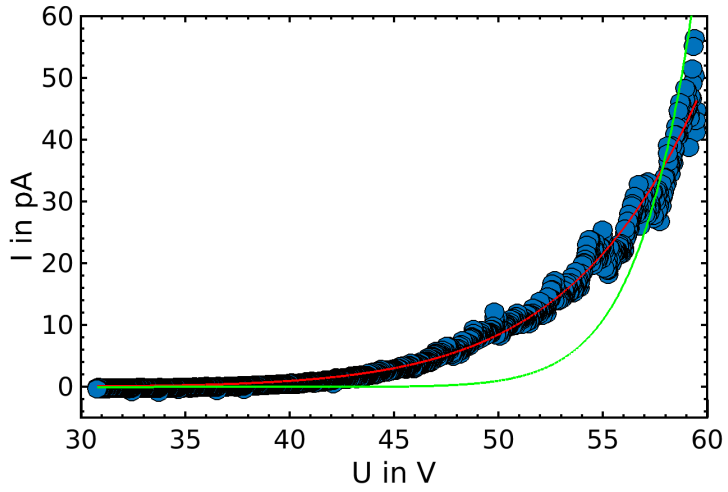

Figure 9.11: Field-emission current I as function of the applied bias voltage for one experiment (n° 1) together with fit with (red) and without (green) considering the experimental drift velocity.

Next, the second part of the experiments is analyzed, i. e., the dependence of

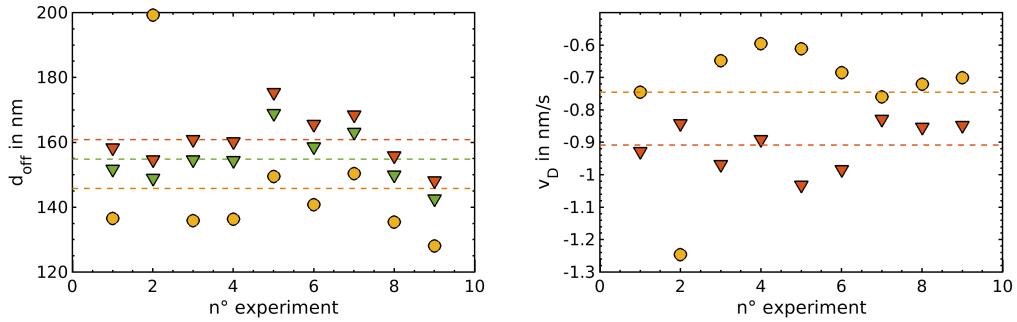

Figure 9.12: Fitted tip-sample off-set values d_{off} (*left*) and drift velocity values v_D (*right*) for the experiments, in which the bias voltage was varied. (*Left*) Off-set values d_{off} are obtained without considering the drift (green). By considering the experimental drift, d_{off} (*left*) and v_D (*right*) are determined, which are marked by red $\bigtriangledown$. From the slope of the (adapted) Fowler-Nordheim plots d_{off} (*left*) and v_D (*right*) are obtained (marked by yellow $\bigcirc$). The respective mean values are shown as broken lines.

the current strength I on the bias voltage U for a constant tip-sample distance as shown for one experiment in fig. 9.11 (exp. $n^\circ 1$). The analytical results are represented by solid lines. Without considering the drift (green curve), the experimental data cannot be described satisfactorily by the Fowler-Nordheim eq. (3.2.18). In contrast, taking a constant v_D into account (red curve in fig. 9.11), the experimentally obtained data could be explained. To include the drift v_D, the following bias-dependent definition of the absolute tip-sample distance was used

$$d = d_{\text{off}} + \frac{v_D}{v_U}\,(U - U_0)\ . \tag{9.2.2}$$

For all experiments, the starting bias U_0 was set to $60\,V$ and it was decreased by an almost constant rate of $v_U \approx 0.3\,V/s$. This was obtained from a linear fit to the $U(t)$ data (see blue curve in fig. 9.6).
The off-set values d_{off} (left) and the drift velocities v_D (right) of all I-vs-U experiments are summarized in fig. 9.12. Neglecting v_D lead to an averaged off-set of approx. $d_{\text{off}} = 154.8\,nm$ and considering v_D to $d_{\text{off}} = 160.8\,nm$, i. e., there is only a difference of $6\,nm$ between them. However, the observed average value of the drift is about $-0.9\,nm/s$, i. e., the tip-sample distance is decreased by almost $90\,nm$ during a single I-vs-U measurement. The drift is, here, much larger than during the first part of the experiment. Since the regulation was turned off, no systemic change of the tip-sample distance should occur in the I-vs-U measurement part. A distinction between a (thermal) drift and a growth of structures at the sample surface is not achievable only by studying the Fowler-Nordheim part. By comparing the drift velocity of both parts, it seems that two different mechanisms are observed, whereby the drift during the measurement of $I(d)$ is much smaller than the one obtained during measuring $I(U)$. As can be seem from SEM images (see fig. 9.7) taken after each experiment, structures were grown on the sample surface. A structure

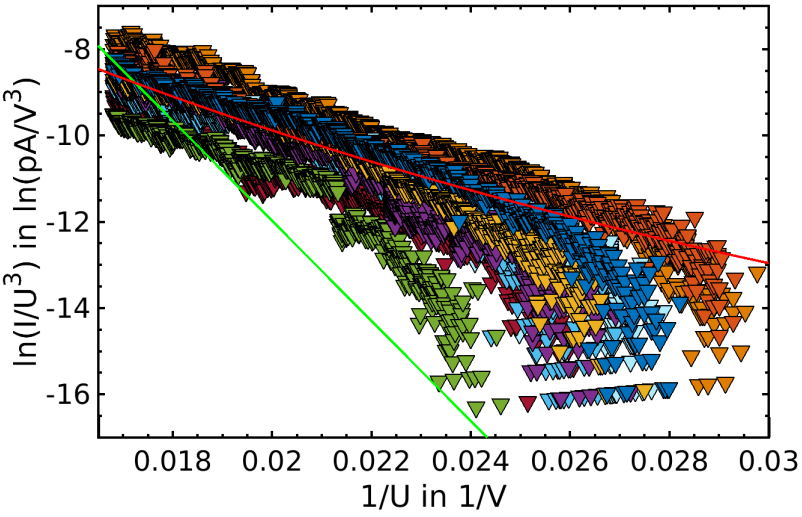

Figure 9.13: Adapted Fowler-Nordheim plots for all nine I-vs-U experiments (colored markers) and averaged results of the fits with (red) and without (green) considering the drift v_D of the FE-SPL system.

growth would yield to a decrease of d, i. e., a negative "drift" v_D. This is observed for all $I(U)$ measurements as seen in fig. 9.12. Therefore, it is proposed that the growth of the features on the sample is mainly responsible for the observed drift in the $I(U)$ experiments. Nevertheless, it is not clear, why the structure growth (treated as a constant drift) is not observed in the I-vs-d curves. For these, the drift depends on the direction of the tip movement during the experiment as shown before. Note, that the experiments differ in regards of the control feedback, i. e., the feedback was adjusting d for I-vs-d measurements whereas the feedback was switched off for the I-vs-U part. This might be another cause for the observed drift behavior.
In fig. 9.13, the adapted Fowler-Nordheim plots are shown for all nine analyzed I-vs-U experiments. The analytical results neglecting (green) and considering v_D (red) are plotted as solid lines. The averaged values of d_{off} and v_D from the analysis of $I(U)$ are used. As already indicated by fig. 9.11 from a single experiment and expected by the large v_D value, the drift needs to be considered to explain the measurement data.
Based on the slope of the adapted Fowler-Nordheim plots (eq. 9.1.10), the values of d_{off} and v_D can be determined by using eq. (9.2.2). The determined data were plotted in fig. 9.12 and marked by yellow ◯. The underestimation of both values, d_{off} and v_D, with regards to the values obtained from the "I-vs-U" analysis, which uses the same experimental data, are clearly visible and explainable by eq. (9.1.9). In equation (9.1.9), the second term on the right side depends on d, which becomes bias-dependent considering a constant drift (eq. (9.2.2)). By neglecting this term and considering only the slope of the

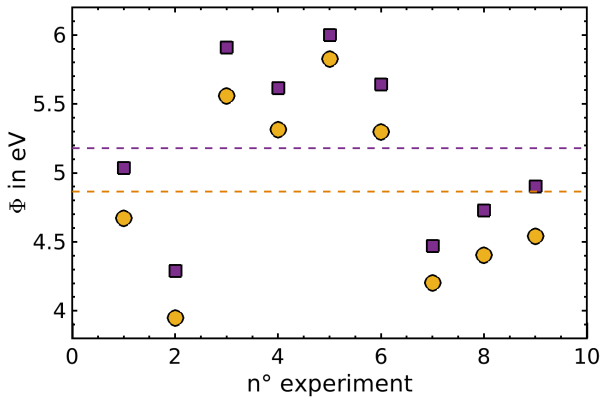

Figure 9.14: Work function Φ obtained from conventional (purple □) and adapted Fowler-Nordheim plots (yellow ◯) for the analyzed experiments using eq. (9.1.10). The data were obtained considering the drift when calculating the slope.

Fowler-Nordheim plot, the values of d_{off} and v_D are underestimated.
In fig. 9.14, the values of the work function Φ determined from the slope of the Fowler-Nordheim plots (conventional (purple □) and adapted (yellow ◯)) of the experimental data are shown[5]. The drift was taken into account and the overestimation of Φ can be explained by the same argument used for determination of d_{off} and v_D. By considering only the slope of eq. (9.1.9), the dependence of the off-set (in the Fowler-Nordheim plot) on Φ is neglected, which leads to the overestimation of Φ.
In summary, the field-emission experiments consisting of "I-vs-d" and "I-vs-U measurements" can be described by the analytical model derived in chapters 8 and 9. It was found that both, off-set value d_{off} and drift velocity v_D, have to be taken into account for describing the experimental data. Two different mechanisms for the drift during $I(d)$ and $I(U)$ are suggested. During the measurement of $I(d)$, a systemic drift (maybe calibration related) of about $-0.2\,nm$ was found. In contrast, an experiment-independent mechanism, most probably related to the growth (or deposition) of structures on the sample surface, is found for $I(U)$ measurements. The deviation of the estimated tip-sample distance $d \approx 30\,nm$ from SEM images taken after the experiment and the off-set values $d_{\text{off}} \approx 150\,nm$ (at the beginning of the $I(U)$ measurement) can be explained using the drift velocity. The "large" drift during the "I-vs-U measurement" of the experiment lead to a tip-sample distance of about $60\,nm$ at the end of the experiment. Taking the unknown tilt between tip and sample, the time between the end of measurement and the time taking the image as well as the measurement tolerances (only low-resolution mode available) into account the deviation between theory and experiment of approx. $30\,nm$ are reasonable.

[5] The work function was set to $\Phi = 4.5\,eV$ for the numerical simulations.

The comparison between experimental and analytical results verifies the derived expression of the current strength I (9.1.7) based on the analytical model of chapter 8. However, it also shows some of the additional influences (drift and surface modifications), which need to be considered even that the experiment was done under highly-controlled (high to ultrahigh vacuum) and highly-stabilized (drift below $1\,nm/s$) conditions.
The next chapter will present results about the application of the field emission from sharp nanotips for lithography using the numerical and the analytical model.

Chapter 10

Theoretical results for field-emission scanning probe lithography

In this chapter, the results of the numerical and analytical model for the lithography application of the field emission from sharp nanotips are summarized. The dependence of the beam diameter d_b and the line width w as indicators for the anticipated resolution of the lithographic process will be presented. Additionally, the ratio of the maximal current density and the threshold current density for a lithographic modification of the resist material is introduced as a measure for the range of application of the analytical model and the lithographic regime. After studying how internal parameters (r, γ, Φ) and external ones (d, U, and lithographic velocity v) affect the lithography, the influence of the resist layer properties (layer thickness d_l, dielectric constant ε, sensitivity and pre-patterned structures) are considered. The lithographic patterning is assumed to be mainly triggered by energy transfer from field-emitted electrons to the resist molecule electrons. This is the subject of section 10.4.5 dealing with the scattering of the electrons inside the resist layer. Note, two approaches will be presented in Appendix B how-to (potentially) improve the lithographic resolution capabilities by increasing the localization of the emitted electrons on the sample surface.

At first, the definitions of the beam diameter and the line width are repeated, which will be used in this chapter. The beam diameter d_b is defined by eq. (5.4.4) as the width, at which the current density distribution J_{sam} at the sample (or resist) surface is decreased to $\frac{1}{e}$ of the maximum of the current density $J_{max} = \max(J_{sam})$. A similar approach was used by Mayer et al. [77]. They used 60% of J_{max} to determine the beam diameter d_b. This yields similar results to our approach or to the use of the full-width half maximum (results are not shown here). However, these definitions neglect the interaction with the resist material. They are applied in electron beam lithography to describe the primary electron distribution. There, the lithographic effect of the high-energy primary electrons can be neglected in comparison with the patterning efficiency of the secondary electrons. The secondary electrons in the

EBL case are mainly electrons backscattered in the bulk of the sample, which have energies up-to $100\,eV$ and can be described by another Gaussian-shaped current density distribution. Typically, the shape of the written lines in EBL experiments are describable by a double Gaussian distribution consisting of a Gaussian distribution of the primary electrons and another one of the secondary electrons [32].
However, in the case of FE-SPL, the energy of the primary electrons is in the range of 10 to $100\,eV$ and, therefore, their patterning capability needs to be considered for the resolution because the binding energies in resist materials are in the same range. To account for this, a second variable, the line width w is introduced. It is determined from a threshold value n_{crit} of the electron number density using eq. 5.4.7. From experiments, a threshold value of approximately 100 electrons per area of $1\,nm^2$ was estimated for a direct removal process of the molecular resist material calixarene [13]. The threshold value depends on the resist material. An analysis of the influence of the resist sensitivity, i. e., different threshold values, on the patterning is given in section 10.4.3 together with a qualitative comparison with FE-SPL experiments.
The beam diameter d_b and the line width w exhibit significantly different characteristics and thus lead to different resolution predictions. In the following, we will compare the values of d_b and w derived from (i) the numerical results, (ii) from the analytical model and (iii) from a Gaussian approximation of the analytical model. For the latter, the derivation of expressions for d_b and w is based on the estimation of the current density distribution J_{sam} using the analytical model of chapter 8 and a Taylor expansion of the exponential function of J_{tip} (eq. (9.1.5)). The Gaussian approximation for the current density distribution at the sample is given by

$$J_{sam}^{GA}(r_{sam}) = \frac{A}{\Phi}\,\kappa_p^2 E_0^2\,\exp\left[\frac{B}{\Phi} - \frac{C\Phi^{3/2}}{\kappa_p E_0}\right]\exp\left[-\frac{r_{sam}^2}{2\tilde{\sigma}^2}\right]\,R_{an}^0\,f^0\,, \qquad (10.0.1)$$

which was derived for $\xi \approx 0$, i. e., for $r_{tip} \approx 0$ and so for $r_{sam} \approx 0$. Consequently, the ratio R_{an} of the emission and exposure area (eq. (8.3.6)) and the weighting factor f (eq. (8.3.7)) at $\xi = 0$ were used, i. e., $R_{an}^0 = R_{an}(\xi = 0) = \frac{r^2}{(d+r)^2}$ and $f^0 = f(\xi = 0) = 4\,f_1\frac{df_2}{rf_3}\left(1 - \exp\left[f_4\frac{U}{d}\right]\right) + 1$, respectively.
In fig. 10.1, examples of J_{sam} are shown, which were obtained from simulations (markers), the analytical model (solid lines) and the Gaussian approxmation (10.0.1). The numerical and analytical data agree relatively well. Deviations occur mainly at the tail of J_{sam}. The Gaussian approximation (10.0.1) describes the analytical expression only for $r_{sam} \approx 0$ and underestimates it for larger r_{sam}.
The beam diameter of J_{sam} can be estimated by the standard deviation of the Gaussian approximation (eq. (10.0.1))

$$d_B^{GA} = 2\,\tilde{\sigma} = 2\,(r+d)\,\sigma = \kappa_p\,(r+d)\,\sqrt{\frac{E_0}{\beta C\,\Phi^{3/2}}}\,, \qquad (10.0.2)$$

where σ, given by eq. (9.1.12), is used.
The line width w is defined by the radial coordinate r_{crit}, which can be estim-

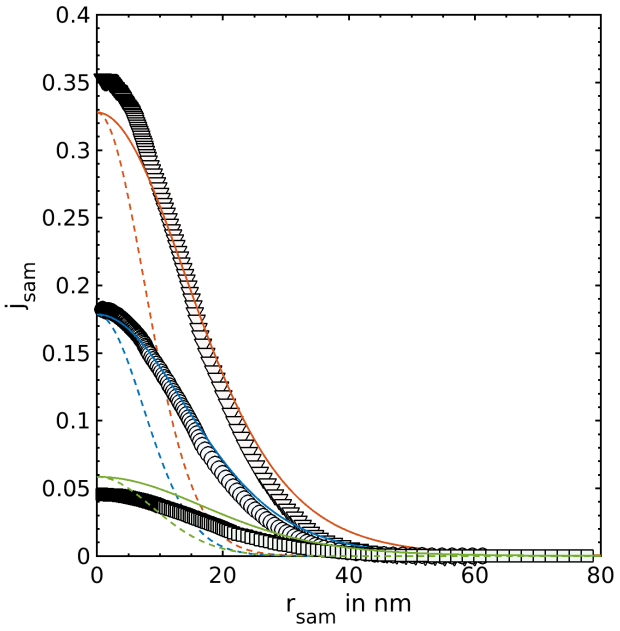

Figure 10.1: Current density distribution J_{sam} over the radial coordinate r_{sam} on the sample surface. The results of the numerical simulation (markers), the analytical model of chapter 8 (solid lines) and the Gaussian approximation (10.0.1) (broken lines) are plotted. The used parameter sets were $r = 8\,nm$, $d = 40\,nm$, $U = 40\,V$ ($\bigtriangledown$ and red), $r = 8.6\,nm$, $d = 40\,nm$, $U = 40\,V$ ($\bigcirc$ and blue), and $r = 12\,nm$, $d = 50\,nm$, $U = 50\,V$ ($\square$ and green).

ated from eq. (10.0.1) using the threshold value[1] $J_{crit} = en_{crit}/\tau$

$$J_{crit} = J_{sam}^{GA}(r_{crit}) = J_{max}\,\exp\left[-\frac{r_{crit}^2}{2\tilde{\sigma}^2}\right]. \tag{10.0.3}$$

This leads to

$$\begin{aligned} w^{GA} &= 2\,r_{crit} = 2\sqrt{-2\,\tilde{\sigma}^2\,\ln\left[\frac{J_{crit}}{J_{max}}\right]} \qquad (10.0.4)\\ &= \sqrt{\frac{2\,\kappa_p^2\,(r+d)^2 E_0}{\beta C\,\Phi^{3/2}}\left\{-\ln\left[\frac{J_{crit}\,\Phi}{A\,\kappa_p^2 E_0^2\,R_{an}^0 f^0}\right]+\frac{B}{\Phi}-\frac{C\Phi^{3/2}}{\kappa_p E_0}\right\}}. \end{aligned}$$

In the following, the results of eqs. (10.0.2) and (10.0.4) will be compared with the results of numerical simulations (see chapter 5) and the analytical model (see chapter 8) for the various parameters. Note, the structure of this chapter is based on the parameters of interest for experiments of FE-SPL.

[1] Here, the more general exposure time τ was used instead of t_{pix} (see eq. (5.4.6)).

10.1 Influence of tip-related parameters

First, dependencies for parameters related to the tip itself are considered. Typically, these tip properties can hardly be modified during FE-SPL experiments but are important to predict the lithography outcome. Additionally, it will be studied if specific requirements for properties of the nanotip exists to enable highest-resolution lithography. Here, tip radius r, tip opening angle γ and tip material in form of its work function Φ will be considered.

10.1.1 Tip radius

In this section, the general assumption that smaller tip radii ("sharper" tips) yield to higher lithographic resolution will be studied.

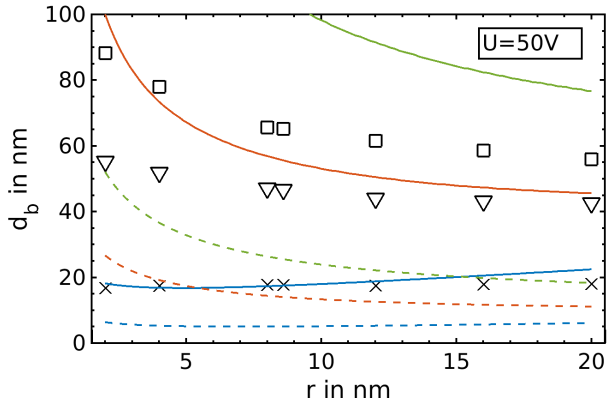

Figure 10.2: Results from the numerical model (symbols), the analytical model (solid lines) and the Gaussian approximation (broken lines, eq. (10.0.2)) of the electron beam diameter d_b as a function of the tip radius r for tip-sample distances $d = 10\,nm$ (X and blue line), $50\,nm$ ($\triangledown$ and red), as well as $100\,V$ ($\square$ and green). The bias voltage between tip and sample was kept constant at $50\,V$ for $\gamma = 20°$ and $\Phi = 4.5\,eV$.

In fig. 10.2, the dependence of the beam diameter d_b on the tip radius r is shown for different tip-sample distances and for a bias voltage of $50\,V$. Variations of r can yield to differences of d_b of up to $40\,nm$ for large tip-sample distances. However, the different dependencies on r can be seen in fig. 10.2. For the smallest tip-sample distance $d = 10\,nm$ (X in fig. 10.2), i. e., for $r \gtrsim d$, a nearly linear increase of d_b with r is observed. In contrast, for $r < d$ ($\triangledown$ and $\square$ in fig. 10.2), the numerically obtained beam diameter d_b decreases non-linearly with increasing r.
The result of the analytical model (solid lines in fig. 10.2) for $d = 10\,nm$, i. e., for $r \gtrsim d$, agrees well with the numerical result but it is visible that d_b increases non-linearly with r in contrast to the linear increase estimated for the numerical result. For $r < d$ (red and green lines in fig. 10.2), d_b obtained from the analytical model shows a non-linear decrease with increasing r similar to

the numerical results. However, the larger the ratio between d and r the larger the deviation between analytical and numerical results for $r < d$.
The results for the beam diameter (10.0.2) obtained from the Gaussian approximation is shown in fig. 10.2 by broken lines. A behavior similar to the results of the numerical and analytical model is visible but d_b is underestimated. Nevertheless, the general dependency from the tip radius can be predicted by eq. (10.0.2). For the case of $r > d$, i. e., $d = 10\,nm$ (X and blue in fig. 10.2), the dependence on r can be estimated by

$$d_b^{GA} \approx r \sqrt{\frac{E_0}{\beta C\, \Phi^{3/2}}} \propto r \tag{10.1.1}$$

using $\kappa_p|_{r<d} \approx 1$. This describes the almost linear increase of d_b with r seen for all models in fig. 10.2.
For $r < d$, i. e., $d = 50\,nm$ (∇ and red) and $100\,nm$ ($\square$ and green) in fig. 10.2, the dependence of d_b on r can be predicted by

$$d_b^{GA} \approx d \sqrt{\frac{\mathcal{A}\, U}{r^{\mathcal{B}}\, \Phi^{3/2}}} \propto \frac{1}{r^{\mathcal{B}/2}} \approx \frac{1}{\sqrt{r}}\,, \tag{10.1.2}$$

which describes the non-linear decrease of d_b with r shown in fig. 10.2. Here, $\kappa_p|_{r<d} \approx \sqrt{\mathcal{A}\, d/r^{\mathcal{B}}}$ was used. Thus, the Gaussian approximation for d_b eq. (10.0.2) reveals that the change of the electric field, described by the field enhancement factor κ_p (eq. (8.3.2)), explains the numerically found dependence of d_b on r.
Therefore, only for tip-sample distances $d \lesssim r$, the assumption that the highest resolution is obtained with the sharpest tips, holds true. However, the requirement $d < r$ causes some difficulties. First, for tip radii below $10\,nm$, a change of the lithography process is expected for $d < 10\,nm$. Under vacuum conditions, tunneling from the tip into the sample might occur whereas under ambient conditions local anodic oxidation mediated by a water meniscus. Second, it is generally more demanding to keep the system stable for small tip-sample distances due to larger electric field changes for tip-sample distance variations, which lead to even larger current density changes. For the more common situation $d > r$ in FE-SPL experiments, tips with larger tip radii yield smaller beam diameters and in this way a higher resolution in contradiction to the above mentioned general assumption. Nevertheless, the influence of the electron number is not included in the beam diameter, which will be investigated in the following using the line width w.
In fig. 10.3, the line width w is shown as function of the tip radius r for different tip-sample distances d. It can be seen that not all parameter sets yield to a value of the line width for two reasons. On one hand, if the maximal current density J_{max} is smaller than the threshold value J_{crit} no lithographic modification is achieved and, thus, no line width can be determined. This can be observed for the numerical simulations but also for the analytical model and its Gaussian approximation. On the other hand, if the current density J_{sam} exceeds J_{crit} over the complete simulation box, w can not be determined.

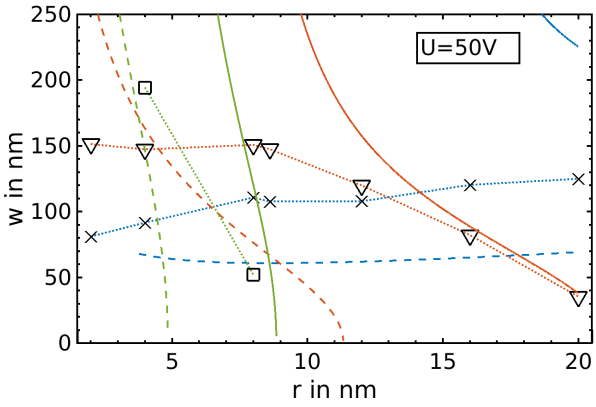

Figure 10.3: Numerically (symbols and dotted lines as guide to the eye) and analytically (solid lines) obtained line width w as a function of the tip radius r for the tip-sample distances $d = 10\,nm$ (X and blue), $50\,nm$ ($\triangledown$ and red) as well as $100\,nm$ ($\square$ and green). The line width obtained from the Gaussian approximation (10.0.4) of the analytical model is shown by broken lines. The applied bias voltage was kept to $50\,V$.

This limit exists only for the numerical simulation. Note, the analytical model (see chapter 8) was derived for $r_{tip} \approx 0$ and its applicability is therefore limited. However, these limitations occur for line widths above $200\,nm$ and are not relevant for high-resolution patterning.
For the numerical result of the smallest tip-sample distance $d = 10\,nm$ (X and blue dotted line as guide to the eye in fig. 10.3), i. e., $r \gtrsim d$, a nearly linear increase is similar to the results for the beam diameter d_b shown in fig. 10.2, but w is much larger than d_b. If $r < d$ ($\triangledown$ and $\square$ in fig. 10.3), the line width w decreases non-linearly for increasing r. The decrease of w increases with r and d and for certain parameter sets $w = 0$ is obtained. This is in contrast to the behavior of d_b, which seems to approach a saturation value as seen in fig. 10.2. The analytical model overestimates w for all parameter sets shown in fig. 10.3. The overestimation of w by the analytical model for parameter sets leading to low-resolution patterning can be explained by the fact that the line width w is determined by the tails of J_{sam} in cases, in which the maximal current density J_{max} significantly exceeds the threshold value J_{crit}. As seen in fig. 10.1, the tails of J_{sam} are not accurately described by the analytical model (solid lines), which was derived for $\xi \approx 0$, i. e., $r_{sam} \approx 0$ (see chapter 8). This yields to the overestimation of w for small d, i. e., large electric fields and so large J_{max}, as shown in fig. 10.3 (for $d = 10\,nm$ (blue solid line)). However, for the smallest line widths, the best agreement between the analytical model and the numerical values occurs. The analytical line width decreases for $r < d$ and for $r > d$ and can therefore not resemble the nearly linear increase of w with r for the case $r > d$. This is caused by the different behavior of the tails of the current density distribution J_{sam} for the analytical model as mentioned above. The line width approaches $w = 0$ for the analytical model because a

finer discretization for r was used in comparison to the numerical simulations. It can be seen, that w hits the x-axis almost perpendicularly, which can be explained by the Gaussian-like shape of the current density distribution since w is almost the inverse function of the current density distribution as seen in eq. (10.0.4).
The results of eq. (10.0.4) from the Gaussian approximation are given by the broken lines in fig. 10.3. For $r > d$, w is nearly constant or even slightly increasing with r, which is in contrast to the result from the analytical model but in agreement with the numerical results. The line width decreases for $r < d$ in agreement with numerical and analytical results but it is underestimated by eq. (10.0.4) for $r < d$. The underestimation of w by the Gaussian approximation can be explained by the current density distribution shown in fig. 10.1, since the width of the Gaussian approximation of J_{sam} (broken lines) is smaller than the widths of the numerically and analytically obtained ones. Since the dependence of w on r is similar to both, numerical and analytical line width, it is worth to extract the dependence on r from eq. (10.0.4) for the both cases $r > d$ and $r < d$. For $r > d$, eq. (10.0.4) yields

$$w^{GA} \approx d_b^{GA}(r > d)\sqrt{\ln\left(\frac{J_{crit}}{J_{max}}\right)} \propto r\sqrt{\text{const} - \ln \text{r}}\,, \tag{10.1.3}$$

which describes the almost linear dependence obtained for the Gaussian approximation but also the numerical line width as seen in fig. 10.3. For $r < d$, the behavior changes to

$$w^{GA} \approx d_b^{GA}(r < d)\sqrt{\ln\left(\frac{J_{crit}}{J_{max}}\right)} \propto \frac{1}{\sqrt{r}}\sqrt{1 - \sqrt{r}}\,, \tag{10.1.4}$$

which describes the dependence of the line width on r for all models in fig. 10.3.

It was found that the ratio of $\frac{J_{crit}}{J_{max}}$ is a measure to predict, for which parameter sets the dependency of $w(r)$ changes in the numerical simulations from the comparison with the Gaussian approximation. Furthermore, it can be used to determine, for which parameter sets the analytical model yields values for w, which are comparable to the numerically obtained ones. In fig. 10.4, this ratio is plotted for an applied bias voltage of $U = 50\,V$. For $\frac{J_{crit}}{J_{max}} > 1$, no patterning can be achieved, since the threshold value is not reached. On the other side, for $\frac{J_{crit}}{J_{max}} \lesssim 10^{-5}$ (see blue curve or X in fig. 10.4), the numerically obtained line width w increases for increasing radius as shown by the symbols X in fig. 10.3 for $d = 10\,nm$. This is similar to the dependency of the beam diameter d_b on r for $d > r$ (shown in fig. 10.2). For $\frac{J_{crit}}{J_{max}} < 10^{-5}$, the maximal current density J_{sam} significantly exceeds the threshold value and the analytical line width w overestimated the numerical results (see blue curve in fig. 10.3) since the tails of J_{sam} are not described well by the analytical model (derived for $r_{sam} \approx 0$). This value is only slightly varied by the bias voltage in the parameter range of FE-SPL experiments. For $10^{-5} \lesssim \frac{J_{crit}}{J_{max}} < 1$, the most interesting region for high-resolution lithography is found since an increase of r yields a decreased

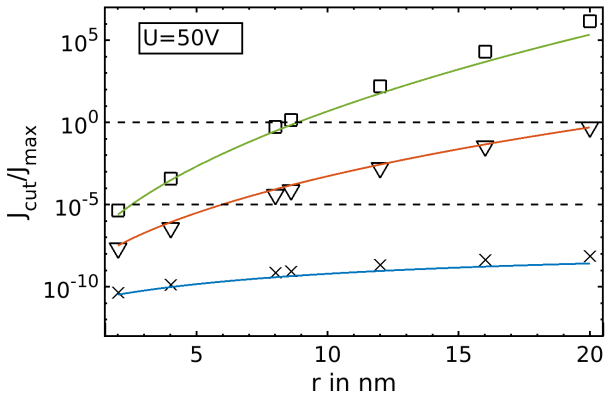

Figure 10.4: Numerical (symbols) and analytical results (lines) of the ratio of the threshold and the maximal current density $\frac{J_{crit}}{J_{max}}$ as a function of the radius r for $U = 50\,V$. The tip-sample distance was set to $d = 10\,nm$ (X and blue), $50\,nm$ ($\triangledown$ and red) and $100\,nm$ ($\square$ and green). The broken lines are guides to the eye representing the crucial region $10^{-5} < \frac{J_{crit}}{J_{max}} < 1$ for lithography.

line width w. Additionally, the results of the analytical model agree reasonably well with the numerical data as seen in fig. 10.3. The highest resolution, i. e., lowest line width w, is found for $\frac{J_{crit}}{J_{max}} = 1$ as expected. Furthermore, the analytical model can describe w in the region, which is most important for achieving the highest lithographic resolution (defined by w).
In summary, the question if the highest resolution can be obtained with the sharpest tips was studied by the beam diameter d_b and the line width w. Thereby, the beam diameter d_b is found to be almost independent on r for $r > d$ whereas for $r < d$, the minimal value of d_b is found for large r in contradiction to the expectation (see fig. 10.2). The (theoretical) line width w decreases with increasing r in the range for high-resolution lithography and reaches even $w = 0$ for certain tip radii as shown by fig. 10.3. However, different tip radii yield to the smallest line width w dependent on the chosen parameter sets. In general, it is possible to achieve a minimal line width $w \to 0$ independent of tip radius r by setting the other parameters appropriately.
In low-resolution mode ($\frac{J_{crit}}{J_{max}} \lesssim 10^{-5}$), the dependence on the tip radius of d_b and w are similar and in this case, the smallest tip radius yields to the smallest patterns which meets the expectation. In contrast, in the high-resolution mode ($10^{-5} \lesssim \frac{J_{crit}}{J_{max}} < 1$), a threshold value for the lithographic process is assumed from experiments and, thus, w is used to describe the size of the lithographic patterns. This leads to the prediction contrary to the expectation, that the highest resolution can be achieved regardless of the tip radius (in the studied range) by adjusting the other parameters.
In the next section, the influence of the tip-angle is shown.

10.1.2 Tip opening angle

As shown before, the influence of the opening angle γ is rather limited, which can be seen for the beam diameter in fig. 10.5 and was neglected in the analytical model (see chapter 8).
However, an increase of γ could lead to a decrease of the line width w and even

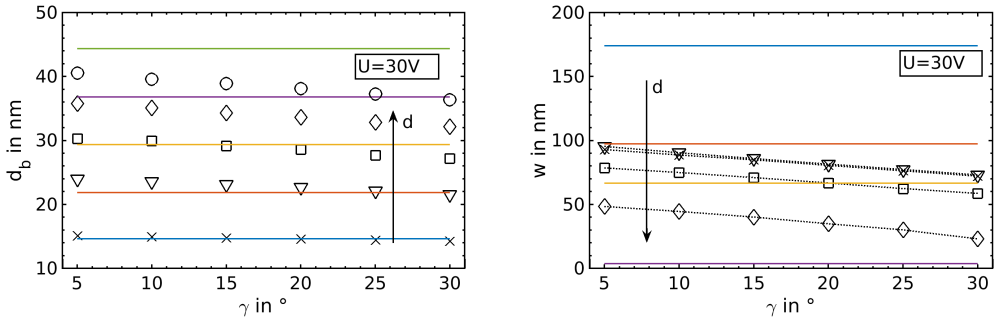

Figure 10.5: Numerically (symbols) and analytically (lines) obtained electron beam diameter d_b (*left*) and line width w (*right*) as a function of the opening angle γ. Beam diameter and line width are shown for tip-sample distances $d = 10\,nm$ (X and blue line), $20\,nm$ ($\bigtriangledown$ and red), $30\,nm$ ($\square$ and yellow), $40\,nm$ ($\diamondsuit$ and purple) as well as $50\,nm$ ($\bigcirc$ and green). The bias voltage was kept to $30\,V$.

a slight decrease is seen for d_b shown on the right-hand side and the left-hand side of fig. 10.5, respectively. Nevertheless, the opening angle γ leads only to a relatively small decrease of w of up to $30\,nm$, which is less than change obtained by the tip radius. Like the tip radius, the tip angle is not crucial for the lithography resolution since it can be compensated by the other adjustable parameters.

10.1.3 Tip work function

In the field-emission theory of Fowler and Nordheim [94, 95], the material properties of the emitter are taken into account only by the material's work function Φ since the theory considers metal emitters. The influence of Φ on the beam diameter d_b and the line width w is presented in the following.
On the left side of fig. 10.6, the beam diameter $d_b(\Phi)$ is shown. A decrease of d_b for increased work function Φ is observed for the numerical and analytical model. The work function influences only the emission probability (Fowler-Nordheim eq. (8.3.5)) and the beam diameter given by the standard deviation (10.0.2) of the Gaussian approximation is proportional to

$$d_b^{GA} \propto \Phi^{-3/4}\,. \tag{10.1.5}$$

As shown in fig. 10.6, d_b^{GA} of the Gaussian approximation describes the dependence of d_b well but the magnitude is underestimated. However, the analytical and numerical results agree well and are comparable with the data published

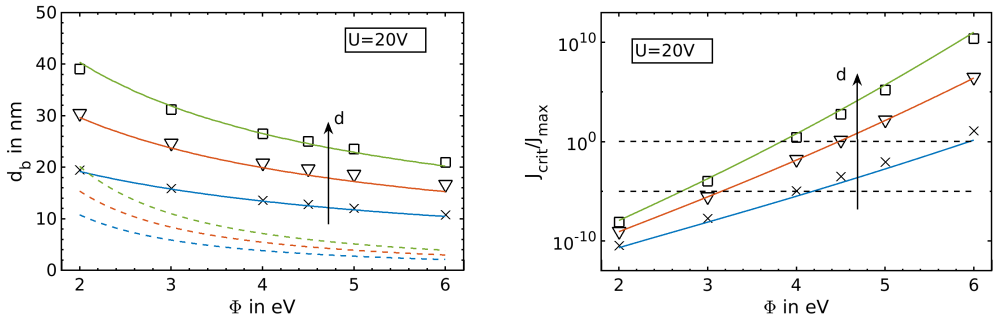

Figure 10.6: Numerical (symbols) and analytical results (solid lines) of the electron beam diameter d_b (*left*) and the ratio of the threshold and the maximal current density $\frac{J_{crit}}{J_{max}}$ (*right*) dependent on the work function Φ. (*Left*) The results of d_b obtained from the Gaussian approximation (10.0.2) are shown by the broken lines. The tip-sample distance d was set to $d = 10\,nm$ (X and blue), $20\,nm$ ($\bigtriangledown$ and red) and $30\,nm$ ($\square$ and green). Here, the bias voltage U was set to $20\,V$.

by Mayer et al. (shown in their fig. 4), where the tip-sample distance was adjusted to keep the current at $1\,nA$ [77].
On the right side of fig. 10.6, the ratio $\frac{J_{crit}}{J_{max}}$ is plotted as function of Φ. For increasing Φ, the ratio is increasing since an increased Φ corresponds to an increased tunneling barrier and, thus, to a decreased emission current probability. This yields a decrease of the line width w for increasing Φ as seen in fig. 10.7 for all models. The analytical model is drawn only in the range $10^{-5} \leq \frac{J_{crit}}{J_{max}} \leq 1$ for high-resolution patterning. In this range, the analytical results agree relatively well with the numerically obtained line width and the best agreement is obtained for smallest w. Dependent on the setting of the other parameters, it is possible to decrease the line width $w \to 0$ by increasing Φ. However, the minimal line width $w = 0$ is obtained for different work function values dependent on the parameter values, which are kept constant. Using eq. (10.0.4), the dependence of w can be approximated with

$$w^{GA} \propto \Phi^{-5/4}\,, \tag{10.1.6}$$

which models the dependence on Φ well but underestimates the value of the line width.
In summary, the work function could lower the line width w for a given parameter set. However, Φ is hardly changeable during FE-SPL experiments and only a limited number of materials can be fabricated leading to ultrasharp nanotips on an active cantilever used in FE-SPL experiments.

10.1.4 Summary of the influence of tip-related parameters

In this section, the influence of the internal parameters tip radius r, tip angle γ and tip work function Φ were investigated. These parameters are hardly changeable during FE-SPL experiments but might be usable for the design

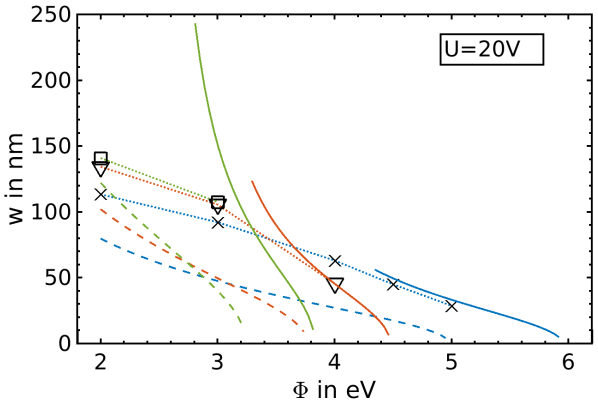

Figure 10.7: Numerical (symbols and dotted lines as guide to the eye), analytical line width w (solid lines) and the line width of the Gaussian approximation (10.0.4) (broken lines) as functions of the work function Φ for $d = 10\,nm$ (X and blue), $20\,nm$ ($\bigtriangledown$ and red) and $30\,nm$ ($\square$ and green). The bias voltage U was set to $20\,V$. The analytical line width was drawn within the range $10^{-5} \leq \frac{J_{crit}}{J_{max}} \leq 1$.

and fabrication of tip emitters. For high-resolution patterning, the following specifications[2] seems to be advantageous: (*i*) large work function Φ; (*ii*) large opening angle γ and (*iii*) large tip radius r. However, these specifications needs to be balanced carefully, since a blunt tip (large r and Φ) fabricated from a material with a high work function might not lead to a sufficient emission probability. Now, the question arises if, how and to which extent the resolution can be optimized by external parameters for a given tip. These external parameters are adjustable during FE-SPL experiments and could help to compensate tip changes caused by tip wear and crashes during usage. This question will be studied in the next sections.

10.2 Influence of external parameters

In this section, the influence of the external parameters (tip-sample distance d, applied bias voltage U and writing velocity v) on the lithographic resolution is investigated. Special interest is given if highest resolution patterns are achievable independently of internal tip parameters (r, γ and Φ).
During FE-SPL experiments, the tip-sample distance d is usually unknown, since the current I is controlled and kept constant (constant-current mode) by varying d (and applying a constant bias voltage) [9–12, 61, 63]. To determine the tip-sample distance, the tip would have to be brought in mechanical contact with the sample (without applying a bias voltage). However, a mechanical contact between tip and sample could lead to a change of the tip shape dependent on the mechanical stability of the tip (not to forget possible damage

[2] Note, these specifications are related to the used parameter ranges, i. e., $\Phi \in [2, 6]\,eV$, $\gamma \in [5, 30]^\circ$ and $r \in [2, 20]\,nm$.

on the sample)[3]. Thus, a contact between tip and sample has to be prevented. Even for another control scheme based on the forces between tip and sample (constant-height mode) [32], in which d is very small (close to contact), the absolute tip-sample distance is not known. Furthermore, for $d < 10\,nm$, tunneling (vacuum) [35,38,39] or local anodic oxidation (ambient conditions) [120] might occur instead of the desired FE-SPL. In both control modii, constant-current and constant-height mode, cantilever bending caused by electric forces might complicate tip-sample distance measurements even more. A possibility to determine d could be in a similar fashion as the FE measurements described in section 9.2. Unfortunately, further experiments based on the ones shown in section 9.2 [169], which include patterning of a resist layer, were not executed so far and, thus, a quantitative comparison with experimental FE-SPL data was not yet possible.
In the constant-current mode, the parameters U and d are interrelated by the control algorithms to ensure a constant current set-point, e. g., an increase of U leads to an increased electric field and to prevent an increased current, d is increased by the control algorithm. In constant-height mode, a variation of the tip-sample distance is rather limited by the force sensitivity of the cantilever bending. A soft cantilever would allow larger distance variations but the lithography becomes more unstable and vice versa.
Despite the difficulties of the experiments, the influence of each external parameter on the lithographic resolution is studied individually in the following. This allows a better understanding of the dependence on the tip-sample distance d, the bias voltage U and the writing velocity v.

10.2.1 Tip-sample distance

The first investigated parameter is the distance d between tip and sample.
In fig. 10.8 (left), the beam diameter d_b in dependence of the distance d is shown for various tip radii r. A nearly linear increase of d_b is obtained for increasing d, which is also predicted by eq. (10.0.2) for $d > r$. For larger d, the electron trajectories are longer. Since these follow approximately rays starting perpendicular at the tip surface as shown in section 8.2, the electron beam is broadened for increasing d. From eq. (10.0.2), d_b^{GA} is given by

$$d_b^{GA} \propto d \tag{10.2.1}$$

for $d > r$ and by

$$d_b^{GA} \propto \sqrt{d} \tag{10.2.2}$$

for $d \approx r$. This is observed in fig. 10.8 for the numerical results of d_b. For $r = 4\,nm$ (symbol X), a nearly linear dependence of d_b on d is seen whereas for $r \geq 8\,nm$ a root-like behavior is observed for small values of d. However, a closer look at the solution of the Gaussian approximation for $r = 20\,nm$ (purple broken line in fig. 10.8) reveals that

$$d_b^{GA} \propto d^2 \tag{10.2.3}$$

[3] A tip crash during lithography might have even more serious consequences since an electrical short cut would lead to a damage of tip and sample due to the electrical current and the corresponding heat.

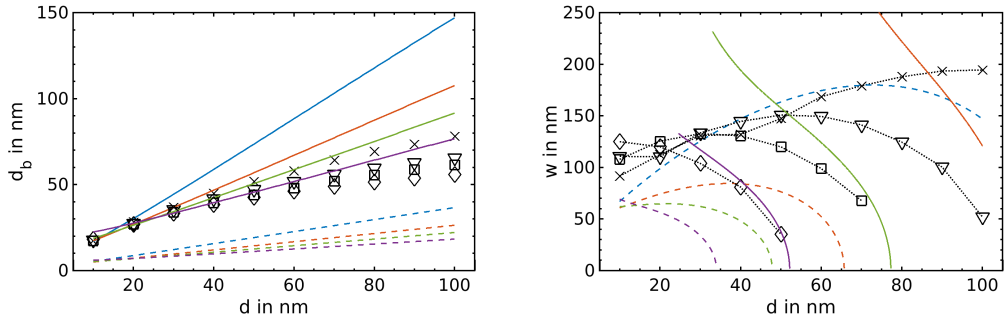

Figure 10.8: Numerical (symbols and dotted lines as guide to the eye) and analytical (colored solid lines) electron beam diameter d_b (*left*) and line width w (*right*) as a function of the tip-sample distance d. The results of the Gaussian approximation are plotted by colored broken lines. The analytical line width is shown for $10^{-5} \leq \frac{J_{crit}}{J_{max}} \leq 1$. $d_b(d)$ and $w(d)$ are drawn for tip radii $r = 4\,nm$ (X and blue), $8\,nm$ ($\triangledown$ and red), $12\,nm$ ($\square$ and green) and $20\,nm$ ($\diamondsuit$ and purple) for $U = 50\,V$.

for $d < r$, which is also seen for the analytical result for $r = 20\,nm$ (purple solid line). This is in contradiction to the numerical results, which do not show this dependency. This can be explained by the increase of the relative error between analytical and numerical result of the maximal enhancement factor κ_p for small $\frac{d}{r}$ as seen in fig. 8.5.
The nearly linear dependence of d_b on d was also found by Mayer et al. [77] but they obtained the smallest value of slope for the smallest radius since they kept the current constant to $1\,nA$ and, thus, changed the bias voltage and the tip-sample distance simultaneously.
The dependence of the line width w on the tip-sample distance d is shown on the right-hand side of fig. 10.8. By changing the tip-sample distance d, two different regimes for w can be obtained for the numerical simulation but also for the analytical models. For small d, the electric field E_0 yields a maximal current densities J_{max} much larger than the threshold value J_{crit}. Here, w is almost linearly increasing with increasing d, i. e., w shows almost the same dependence on d as the beam diameter d_b. In the regime for large d, w is defined by intersection between threshold value and current density distribution, since the ratio $10^{-5} < \frac{J_{crit}}{J_{max}} < 1$ and w decreases for increasing d.
On the right-hand side of fig. 10.8, the results of the analytical model (solid lines) are only plotted for $10^{-5} < \frac{J_{crit}}{J_{max}} < 1$, which agree well for $w \to 0$ (seen for $r = 12\,nm$ ($\square$ and green) and $20\,nm$ ($\diamondsuit$ and purple)), i. e., $J_{max} \approx J_{crit}$. However, the numerical results for small d can not be described.
In contrast, both regimes can be explained by eq. (10.0.4) of the Gaussian approximation for $d > r$ and $d \approx r$, for which

$$w^{GA} \propto \sqrt{d^2 - d^{5/2}} \tag{10.2.4}$$

and

$$w^{GA} \propto \sqrt{d - \text{const}\,\mathrm{d}^2}\,, \tag{10.2.5}$$

was found, respectively. For small d, the first term dominates, whereas for larger d the second term describes $w(d)$, which predicts the observed dependency $w(d)$ for $d \lesssim r$. Nevertheless, it is observed that eq. (10.0.4) underestimates the magnitude of w.

10.2.2 Applied bias voltage

The dependence of the diameter d_b of the electron beam and the line width w on the applied bias voltage is plotted in fig. 10.9 for a tip-sample distance of $d = 40\,nm$. The results are obtained from the numerical simulation (markers), the analytical model (solid lines) and shown as broken lines from eqs. (10.0.2) and (10.0.4), for d_b and w, respectively. As expected, the beam diameter d_b increases with increasing electric field strength, i. e., with increasing the bias voltage U. From eq. (10.0.2) of the Gaussian approximation, the beam diameter

$$d_b^{GA} \propto \sqrt{U}\,, \tag{10.2.6}$$

observable for numerical and analytical results as well in fig. 10.9 (left). An increase of d_b with increasing U was also also observed by Mayer et al. [77] but in contrast to the results here, with an increasing positive slope of $d_b(U)$ especially for the smallest tip radii r. Note, that Mayer et al. adjusted the tip-sample distance d during the variation of U to obtain a constant-current mode, i. e., keeping the emission current constant at $1\,nA$ [77]. However, they only consider voltages up to $50\,V$, where the slope transition might not be clearly observable. In agreement with Mayer's study the largest beam diameter d_b is obtained for the smallest tip radius r due to the highest electric field strength.

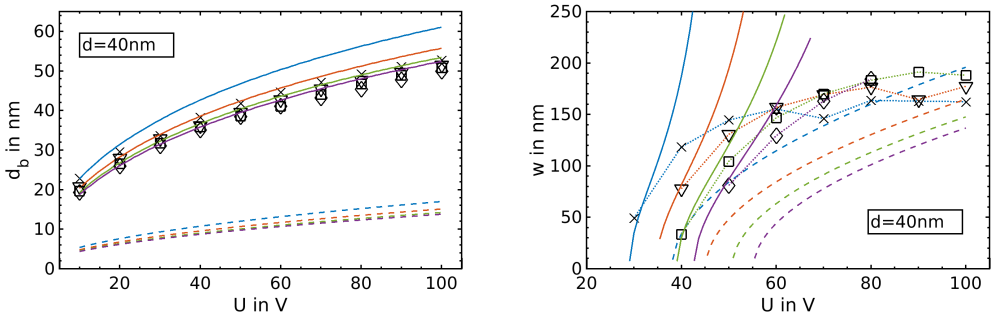

Figure 10.9: Numerical (symbols and dotted lines as guide to the eye) and analytical (solid lines) results of electron beam diameter d_b (*left*) and line width w (*right*) as a function of the bias voltage U. The results of the Gaussian approximation are plotted by broken lines. The analytical results of w are shown for $10^{-5} \leq \frac{J_{crit}}{J_{max}} \leq 1$. The results are drawn for $r = 8\,nm$ (X and blue), $12\,nm$ ($\bigtriangledown$ and red), $16\,nm$ ($\square$ and green), and $20\,nm$ ($\diamondsuit$ and purple). Here, the distance was constant at $40\,nm$.

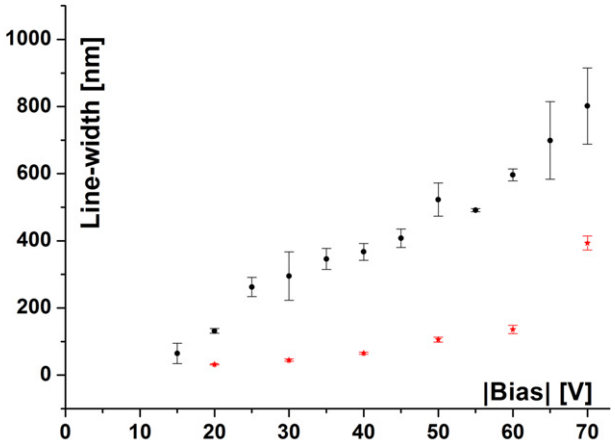

Figure 10.10: Measurement data for line width w as a function of the bias voltage U for two different tips (black and red colored symbols) using an approximately $10\,nm$ thick calixarene resist layer (taken from [9]). The data up to $U = 50\,V$ are shown single-tip results, whereas for higher bias voltages multiple tip emission occurred.

On the right-hand side of fig. 10.9, the line width w exhibits a similar behavior like d_b but the slope of $w(U)$ is more affected by U, i. e., for small U a steep increase of w is observed while for larger U, $w(U)$ seems to approach a saturation value. The theoretical results are similar to the experimental data from [9], shown in fig. 10.10, although the tip-sample distance d was adjusted for a constant-current operation in experiments and in the simulation d was kept constant. However, the magnitude of the experimental data obtained with tips (from which the tip radii were not determined) are larger than obtained from theory. Due to unknown tip radius and the unknown tip-sample distance, a quantitative comparison is not achievable.
The decrease of w with decreasing U is a similar to $d_b(U)$ but with a larger absolute value of the slope as shown in fig. 10.9. The analytical model yields comparable results in this region for $w \to 0$. The beam diameter d_b and the line width w, obtained from the Gaussian estimate, reproduce their dependency on the bias voltage U, but not their magnitude as seen in fig. 10.9. However, the saturation of $w(U)$ observed for the numerical results is not describable by eq. (10.0.4) for the Gaussian approximation, since it yields

$$w^{GA} \propto \sqrt{U + \ln U}\,. \tag{10.2.7}$$

10.2.3 Lithographic velocity

A parameter, not discussed so far, is the velocity v of the tip moving over the sample surface during lithography. This velocity alters the amount of electrons n_e reaching the sample or resist surface described by eq. (5.4.6) by changing the exposure time τ at a certain position (see eq. (5.4.5)[4]). The expression of the line width w eq. (5.4.7) includes, thus, the influence of the velocity w.

[4] In eq. (5.4.6), the exposure time τ is described by a time t_{pix} per pixel.

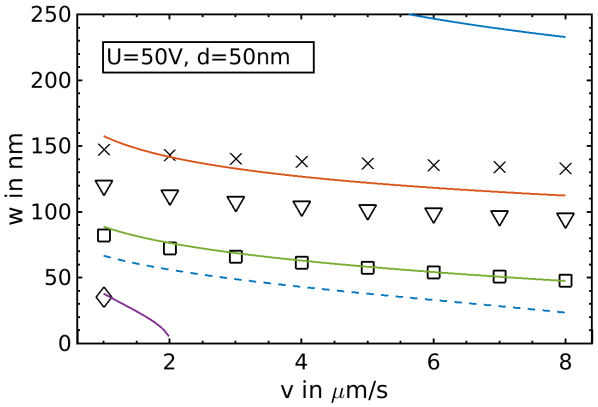

Figure 10.11: Plot of line width w as a function of the writing velocity v computed with the numerical (black symbols) and the analytical model (colored solid lines). The colored broken lines show the results of the Gaussian approximation of the analytical model. $w(v)$ is shown for different tip radii $r = 8.6\,nm$ (X and blue), $12\,nm$ ($\triangledown$ and red), $16\,nm$ ($\square$ and green) and $20\,nm$ ($\diamondsuit$ and purple). The potential difference between tip and sample was kept to $50\,V$ and the distance to $50\,nm$.

In the discussion so far the velocity was set to $v = 1\,\frac{\mu m}{s}$, which is an often used value in experiments. However, since the velocity can be risen up to $8\,\frac{\mu m}{s}$, the range $v \in [1, 8]\,\frac{\mu m}{s}$ is considered in the following consideration. Note, the beam diameter d_b is not affected by the velocity since the (time-independent) current density distribution J_{sam} remains constant.
In fig. 10.11, the dependence of the line width w on the patterning velocity v for different tip radii is plotted. As expected, an increasing velocity v reduces the line width w, which is resembled by the analytical model and eq. (10.0.4). Thereby, the slope increases if $\frac{J_{crit}}{J_{max}}$ approaches 1, caused by the Gaussian-like shape of J_{sam}, which can be seen in fig. 10.11 for $r = 20\,nm$. However, the line width $w(v)$ remains nearly constant when the tail of J_{sam} determines w as seen for small radii in fig. 10.11. Since in experiments, the line width can be decreased by increasing v, the system seems to be typically operated in the range $10^{-5} \leq \frac{J_{crit}}{J_{max}} \leq 1$.
Concluding the studies of the influence of the external parameters on the lithographic resolution, smaller bias voltages and larger tip-sample distances should result in better resolution. Thereby, in many FE-SPL systems, due to the constant-current operation mode, reducing U lead to a decreased d as well. From experiments and the presented theoretical models esp eq. (10.0.1), it is observed that the influence of U on J_{sam} is stronger than the one of d. However, for w, this effects is not observable in the parameter range of FE-SPL experiments as seen by comparing the right-hand sides of figs. 10.8 and 10.9 There, both parameters changes w in a range from $0\,nm$ to $200\,nm$.

10.3 Summary of investigations for resist-less FE-SPL

In this part of chapter 10, the results of the simulations were presented together with the ones of the analytical model and the ones obtained from the estimation of J_{sam} using a Gaussian distribution, for the studies neglecting the resist layer. The physical values necessary to describe the lithography outcome are the beam diameter d_b (as, e. g., reported by Mayer et al. [77]), the ratio $\frac{J_{crit}}{J_{max}}$ and the line width w. The difference between beam diameter d_b and line width w is that d_b does not include the threshold value J_{crit} to trigger a lithographic reaction. The behavior of both values, d_b and w, differs as well as their significance for the patterning process. The beam diameter d_b can yield an estimate for a parameter set in the regime, where the ratio $\frac{J_{crit}}{J_{max}}$ is very small, i. e., below 10^{-5}. This might be relevant for negative tone patterning using calixarene, since very low threshold values were extracted from experimental data [13]. However, in this regime the lithographic process is not achieving its highest resolution. In the highest-resolution regime, $\frac{J_{crit}}{J_{max}}$ is close to unity and the line width w can be used to determine the optimized parameter set. This is the range of the direct ablation and the theoretical predictions show some agreement with the experimental results [9, 13]. However, the experiments were done under ambient conditions and using a resist film, which influence the measured line width. Additionally, the atomic-force microscopy measurements might affected by tip-convolution effects [?, ?].
In the first part of this chapter, the influences of the shape of the tip, i. e., tip radius r and opening angle γ, as well as the tip material in form of the work function Φ on d_b and w were presented. All these internal parameters influence the field emission process and, thus, the lithography. It could be shown that the assumption that smaller tip radii lead to higher lithographic resolution is wrong for $r < d$. In contrast, increasing the tip radius as well as the tip-opening angle can result in smaller line widths due to a decrease of the the field enhancement, i. e., the electric field and finally of the current densities J_{tip} and J_{sam}. The numerical simulation showed for tip-sample distances $d < r$, that a decrease of r increases the resolution. The Gaussian approximation (10.0.4) predicts a change of the behavior for $r \approx d$, which was not numerically observed in the range of the investigated tip radii[5] $r \leq 20\,nm$ and tip-sample distances $d \geq 10\,nm$ (to avoid tunneling or formation of a water meniscus). Furthermore, the resolution can be improved by using tip materials with a high work function Φ. However, the internal parameters do not limit the capability for high-resolution patterning, since the external parameters are able to compensate the effects of the internal parameter.
The external parameters, tip-sample distance d, applied bias voltage U and writing velocity v, were considered thereafter. In the high-resolution limit, an increased d, a decreased U and an increased v lead to a decrease of the line width w, i. e., an increased resolution. Note, only the bias voltage U does not lead to a change of the dependency of d_b and w, because the electric field E_{tip} increases with increasing U. It was not confirmed that the bias voltage U has

[5] For good AFM functionality in experiments.

the most impact on current density J_{tip}. However, it is most convenient in typical (current-controlled) FE-SPL experiments to set U at first. Afterwards, the distance d between sample and tip can be used to reduce the line width. However, already slight changes of d can yield to relatively large changes of w. At last, the line width w can be reduced further by increasing the writing velocity v.

It was found, that the ratio $\frac{J_{crit}}{J_{max}}$ is a measure to characterize the patterning behavior. If the ratio is above unity, a patterning is not possible because the threshold value for a lithographic modification of the resist is not reached by the current density. For ratios below 10^{-5}, beam diameter d_b and w show similar dependencies, while for $10^{-5} < \frac{J_{crit}}{J_{max}} \leq 1$ the dependence of w on the respective parameter changes (except for the bias voltage U). In this range, in particular near $J_{crit} \approx J_{max}$, the highest resolution is observed. The patterning is mainly affected by the field enhancement factor κ_p for ratios below 10^{-5} since the maximal current density is much larger than the threshold value.

In the regime $\frac{J_{crit}}{J_{max}} < 10^{-5}$, the beam diameter can be used to predict the resolution capabilities. The highest resolution is achieved for a ratio close to unity, which is only described by using the line width. Worth to mention is that a lower limit for the line width w was not observed. However, the properties of the resist material influences the lithographic process and its resolution, which will be studied in the next chapter.

The analytical model could not reproduce the numerical results in the regime $\frac{J_{crit}}{J_{max}} < 10^{-5}$, since the resolution is determined by the tails of the the current density distribution. Nevertheless, in the high-resolution region for $\frac{J_{crit}}{J_{max}} \in [10^{-5}, 1]$, the derived physical values, beam diameter d_b and line width w, agreed well with the simulation data. A slight overestimation of the line width w was observed. However, the model can be used to obtain the optimal external parameter for a given tip to conduct highest resolution lithography. Due to the simplicity of the analytical model, it could be implemented into an existing software for a FE-SPL system, which would allow to estimate the parameter range of interest on the basis of a previously done investigation of the tip shape and the knowledge of the work function of the tip.

An even simpler approach using eqs. (10.0.2) and (10.0.4) enables the prediction of the respective behavior of d_b and w but the magnitudes of d_b and w are underestimated.

Although the theoretical models allow to modify each parameter independently, the experimental results ($w(U)$) could be qualitatively reproduced. In the experiments due to the constant-current control mode, a variation of one of the external parameter U and I leads to a modification of the tip-sample distance d. The interrelation of the external parameters and the experimentally inaccessible tip-sample distance complicate the analysis of the experiments. The Gaussian approximation and the analytical model can help to analyze the influence of each external parameter.

10.4 Influence of resist layer on FE-SPL

After studying the influence of internal and external parameters on the field emission based lithography from sharp nanotips, the effect of a resist layer, described by layer thickness d_l and dielectric constant ε, on lithography resolution is considered. Here, the dielectric function is assumed to be isotropic for the amorphous resist material (calixarene), which is a standard resist for FE-SPL (in our group). Additionally, it is assumed that charge effects (like accumulation) are negligible due to biasing the metallic (e. g., gold) or semiconducting sample (e. g., silicon). Note, in the following d refers to the tip-resist distance and d_l to the resist layer thickness. The tip-sample distance d_{tot} is thus the sum of d and d_l. In this study (without loss of generality) only a tip with the following properties is considered: radius $r = 8.6\,nm$, opening angle $\gamma = 20°$ and work function $\Phi = 4.5\,eV$.

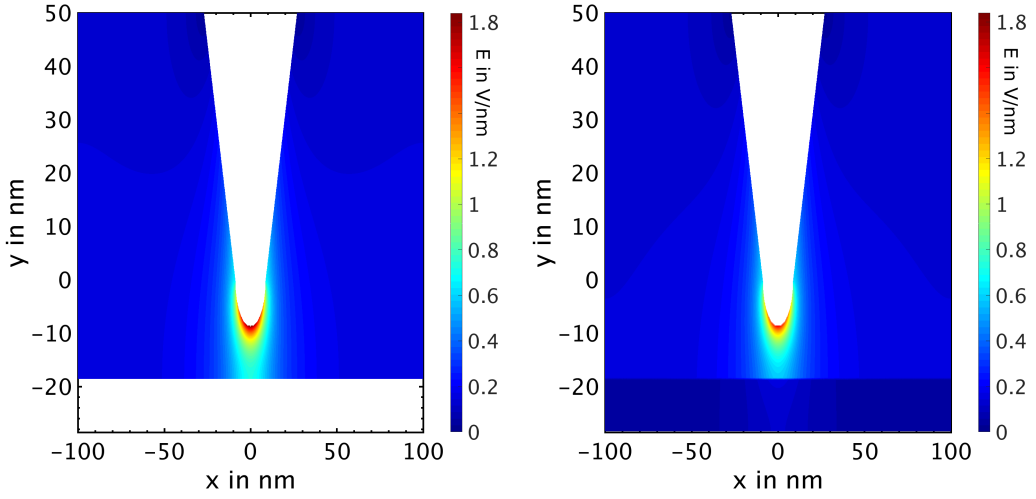

Figure 10.12: Plot of the electric field (as color code) for the situation without (*left*) and with a $10\,nm$-thick resist layer (*right*). For better comparability, the graph on the left is shift upwards by the layer thickness and the same color bars are applied. Here, $U = 10\,V$, $r = 8.6\,nm$ and $d = 10\,nm$.

The electric field computed with and without a resist layer is shown in fig. 10.12. The parameters are chosen that the tip-sample distance without resist (left-hand side) equals the distance between tip and resist (right-hand side of fig. 10.12). Differences between electric field distributions are hardly visible. The electric field maximum is approximately 10% smaller for the case including a resist layer than for the case without one. As it can be observed, the electric field within the resist layer is rather small. This is important for the question of the electric field influence on electron trajectories and scattering cross sections within the resist layer. This effect will be included in section 10.4.5 dealing with the electronic interactions inside the resist.

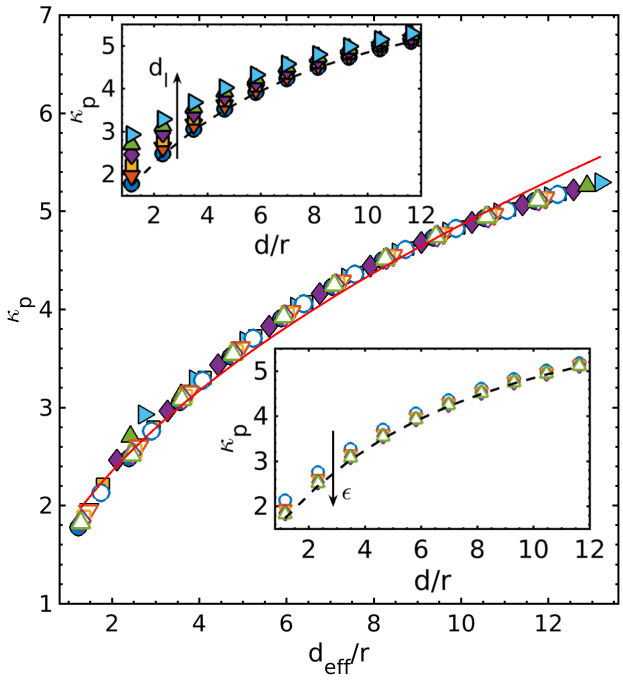

Figure 10.13: Field enhancement factor κ_p as a function of the ratio $\frac{d_{\text{eff}}}{r}$ of the effective tip-sample distance $d_{\text{eff}} = d + \frac{d_l}{\varepsilon}$ and the tip radius r shown for resist layers with different thickness d_l (colored symbols with black frame) and dielectric constant ε (white symbols with colored frame). The influence of d_l on κ_p is shown in the upper inset, in which κ_p over $\frac{d}{r}$ is plotted for $d_l = 2\,nm$ (blue ◯), $10\,nm$ (red ▽), $20\,nm$ (yellow □), $30\,nm$ (purple ♢), $40\,nm$ (green △) and $50\,nm$ (cyan ▷) for $\varepsilon = 3.7$. The effect of ε on κ_p is shown in the lower inset for κ_p vs. $\frac{d}{r}$ for $\varepsilon = 2$ (blue-framed ◯), 4 (red-framed ▽), 6 (yellow-framed □), 8 (purple-framed ♢) and 10 (green-framed △) for $d_l = 10\,nm$. The different values of d_l and ε are plotted together in the main part of the figure. The analytical expression of κ_p (8.3.3) using d_{eff} is plotted as solid red line and κ_p using d is shown as broken black line in the insets.

To include the influence of the resist layer in the analytical model, the plate capacitor case including a resist layer on one electrode is considered. Assuming uniformly distributed charges Q at the electrode surfaces, the surface charge is equal to $\sigma_p = \frac{Q}{A}$, where A is the surface area. The electric field is given by $E(z) = \frac{\sigma_p}{\varepsilon_0\,\varepsilon_r(z)}$ with

$$\varepsilon_r(z) = \begin{cases} 1 & \text{if} \quad 0 \le z < d \\ \varepsilon & \text{if} \quad d \le z < d + d_l \end{cases} . \tag{10.4.1}$$

The bias voltage between the electrodes can be calculated by

$$\begin{aligned} U \;&= \int_0^{d+d_l} E(z)\,dz \;&&= \int_0^{d} E_v\,dz + \int_d^{d+d_l} \frac{E_v}{\varepsilon}\,dz \\ &= E_v\,\left(d + \tfrac{d_l}{\varepsilon}\right) \;&&= E_v\,d_{\text{eff}} \end{aligned} \tag{10.4.2}$$

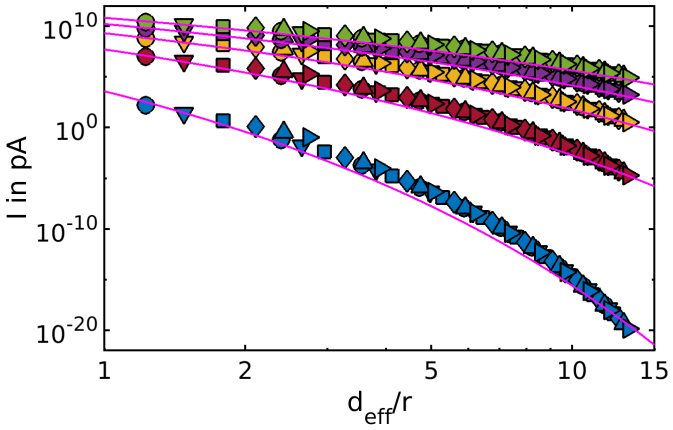

Figure 10.14: Numerical results for the current strength I plotted in dependence of the ratio $\frac{d_{\text{eff}}}{r}$ for bias voltages $U = 20\,V$ (blue), $40\,V$ (red), $60\,V$ (yellow), $80\,V$ (purple) and $100\,V$ (green). Different resist layers were used with $d_l = 2\,nm$ (◯), $10\,nm$ (▽), $20\,nm$ (□), $30\,nm$ (◇), $40\,nm$ (△) and $50\,nm$ (▷). The results of the analytical expression (9.1.7) (using d_{eff} instead of d) are shown as magenta lines.

with the vacuum electric field $E_v = \frac{\sigma_p}{\varepsilon_0}$. The result of the electric field

$$E_v = \frac{U}{d_{\text{eff}}}\,, \tag{10.4.3}$$

can be interpreted as a plate capacitor in vacuum with an effective plate distance d_{eff}. Inserting this into the analytical model of chapter 8 leads to a modified definition of the (maximal) field enhancement factor

$$\kappa_p = \frac{E_{tip}}{E_v}\,. \tag{10.4.4}$$

The results of the analytical eq. (8.3.2) for κ_p using d_{eff} instead of d are plotted in fig. 10.13. The field enhancement κ_p is shown in dependence the ratio of the effective tip-sample distance d_{eff} and the tip radius r. It can be seen that all numerical results (symbols) can be described by the analytical expression (8.3.2) drawn as a solid red line in fig. 10.13. Thus, using $\kappa_p(d_{\text{eff}}, r)$, the enhancement distribution κ (eq. (8.3.3)) and the electric field E_{tip} along the tip surface (eq. (8.3.4)) can be determined. The effect of d_l and ε on κ_p can be seen in the insets showing κ_p vs. $\frac{d}{r}$ for variations of d_l and ε separately. An increase of d_l increases κ_p whereas an increase of ε slightly decreases it. In both cases, the variation of κ_p with d_l or ε is larger for smaller values of $\frac{d}{r}$.
In fig. 10.14, the total current I is plotted in dependence of the ratio $\frac{d\text{eff}}{r}$. It is shown, that the analytical model using d_{eff} instead of d could describe the current strength and so the current density distribution J_{tip} at the tip taking the properties of the dielectric resist layer into account.
The calculation of the current density distribution J_{sam} at the sample from

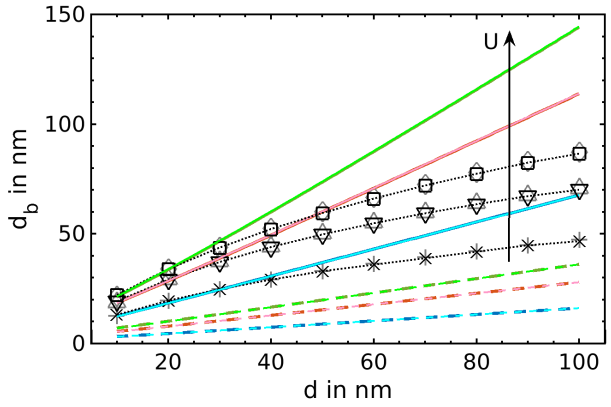

Figure 10.15: Plot of electron beam diameter d_b on the resist surface in dependence on the tip-resist distance d for a resist layer with a thickness of $d_l = 10\,nm$ and a dielectric constant of $\varepsilon = 3.7$ (bright colors and black symbols) in comparison with the resist-less case (darker colors and grey symbols). $d_b(d)$ is shown for the bias voltages $U = 20\,V$ (blue, X and + (resist-less case)), $60\,V$ (red, $\bigtriangledown$ and $\bigtriangleup$), and $100\,V$ (green, $\square$ and $\diamondsuit$). The results of the numerical simulations, the analytical model and of the Gaussian approximation (10.4.6) are shown as symbols, solid lines and broken lines, respectively.

J_{tip} requires $R_{an} = \frac{A_{tip}}{A_{sam}}$ (eq. (8.3.5)) and f (eq. (8.3.6)), which are both distance-dependent. Since only the length of the rays are considered for R_{an}, the geometric length $z \in [d, d+d_l]$ is used and not d_{eff}. In contrast, the weigthing function f expresses the influence of the electric field on the trajectories and so the effective distance d_{eff} is used to calculate f. Therefore, the adapted analytical model can be written as

$$J_{sam}(z, d_{\text{eff}}) = \frac{A}{\Phi}\,\kappa^2(d_{\text{eff}})\,E_v^2(d_{\text{eff}})\exp\left(\frac{B}{\Phi} - \frac{C\Phi^{3/2}}{\kappa(d_{\text{eff}})\,E_v(d_{\text{eff}})}\right) R_{an}(z) f(d_{\text{eff}})\,. \tag{10.4.5}$$

In consequence, from the Gaussian approximation of J_{sam}, the estimates of the beam diameter d_b^{GA} and line width w^{GA} at the resist surface ($z = d$) can be modified to:

$$d_b^{GA} = (d + r)\kappa_p(d_{\text{eff}})\sqrt{\frac{E_v(d_{\text{eff}})}{\beta\, C\Phi^{3/2}}} \tag{10.4.6}$$

and

$$w^{GA} = d_b\sqrt{\ln\left(\frac{J_{crit}\Phi}{A\,\kappa_p^2(d_{\text{eff}})E_v^2(d_{\text{eff}})\,R_{an,0}(d)\,f_0(d_{\text{eff}})}\right) + \frac{B}{\Phi} - \frac{C\Phi^{3/2}}{\kappa_p(d_{\text{eff}})E_v(d_{\text{eff}})}}\,. \tag{10.4.7}$$

Fig. 10.15 shows the beam diameter d_b of the electrons at the resist surface ($z = d$) in dependence of the tip-resist distance d (bright colors and black symbols) together with d_b determined for the resist-less case using d as the tip-sample distance (darker colors and grey symbols). The solid lines repres-

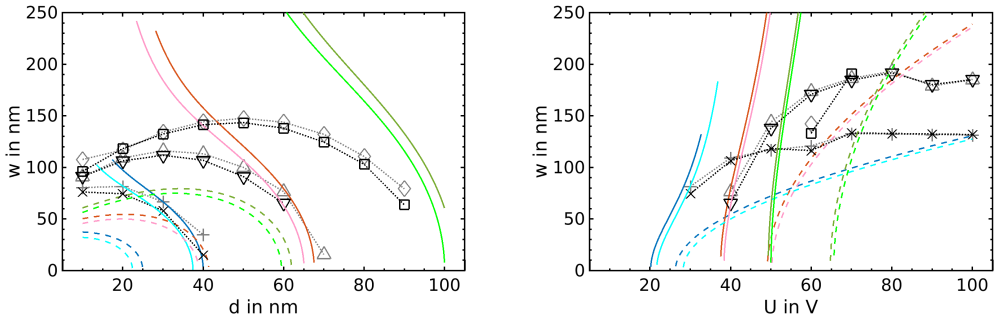

Figure 10.16: Line width w (at the resist surface) is plotted as function of tip-resist distance d (*left*) and of applied bias voltage U (*right*) for a resist layer thickness of $d_l = 10\,nm$ and dielectric constant of $\varepsilon = 3.7$ (bright colors and black symbols) in comparison with the resist-less case (darker colors and grey symbols). (*Left*) $w(d)$ is shown for the bias voltages $U = 30\,V$ (blue, X and + (resist-less case)), $40\,V$ (red, $\bigtriangledown$ and $\bigtriangleup$), $50\,V$ (green, $\square$ and $\diamondsuit$). (*Right*) Plot of $w(U)$ is drawn for tip-resist distances $d = 20\,nm$ (blue, X and +), $60\,nm$ (red, $\bigtriangledown$ and $\bigtriangleup$) and $100\,nm$ (green, $\square$ and $\diamondsuit$). The results of the numerical simulations, the analytical model and of the Gaussian approximation (10.4.7) are shown as symbols, solid lines and broken lines, respectively.

ent the analytical beam diameter whereas the broken lines show the results of eq. (10.4.6). The numerical data are given as symbols. The beam diameter d_b obtained with a resist layer show no visible deviations to d_b of the resist-less case. The nearly linear dependence of d_b on the bias voltage U (for $U > 60\,V$ as seen in fig. 10.9) was already observed by Dobisz et al. [22], which is independent on the resist layer presence as seen in fig. 10.15.

The results of the line width w for a resist layer (bright colors and black symbols) and for the resist-less case (darker colors and grey symbols) dependent on d and U are shown in fig. 10.16. In contrast to the results of d_b, w with and without a resist layer show some deviations for large d and small U, i. e., for high-resolution patterning. Nevertheless, the deviations are rather small and at the resist surface, the results of the resist-less case, calculated with a tip-sample distance identical to the tip-resist distance d, can be used as a good estimate.

The influence of the patterning velocity v on w is shown in fig. 10.17 for tip-resist distances of $d = 40\,nm$ (blue) and $60\,nm$ (green). The line width w was measured at the resist-sample interface (dark colors) and on the resist surface (bright colors). The deviations between the different positions, at which w is determined, are caused be the slightly increased electron spread of trajectories increased by d_l, which lead to a minor increase of w. The difference is larger for smaller ratios of $\frac{J_{crit}}{J_{max}}$, where w depends on the tails of the current density distribution J_{sam}. In this range, electron trajectories for large angles ξ determine w, which spread more with d than the trajectories with small ξ. In fig. 10.17, only the results of the analytical model (10.4.5) are shown, which agree well as expected from previous results. Note, the influence of v is stronger for smaller

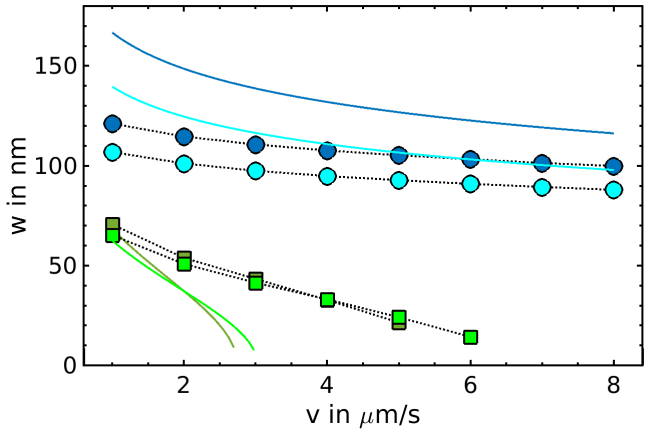

Figure 10.17: Line width w over writing velocity v determined at the resist surface (bright) and at the resist-sample interface (dark). The results are shown for $d = 40\,nm$ (blue and ◯) and $60\,nm$ (green and □). The analytical model results are plotted as solid lines, whereas the dotted lines are guides for the eye for the numerical results.

w, i. e., for $\frac{J_{crit}}{J_{max}} \to 1$.
The kinetic energy of the electrons impinging the resist surface is important for the lithography, since it determines the interactions between electrons and resist molecules. It was briefly studied in the publication of Dobisz et al. [22]. On the left-hand side of fig. 10.18, the radial distribution of the numerically obtained kinetic energy on the resist surface (red lines) and the resist-sample interface (blue lines) are shown together with the kinetic energy distribution in the resist-less case (black broken line). The kinetic energy at the resist-sample interface (and sample surface in resist-less case) is defined by the potential energy $-e\phi$ due to the conservation of energy. Thus, both results (black broken and blue lines) overlap at $\epsilon = 50\,V$ on the left side of fig. 10.18. The kinetic energy at the resist surface (red lines) is increasing with d and the difference between the minimum of ϵ_{kin} at $x = 0$ and the maxima at $|x| \to \infty$ decreases. ϵ_{kin} is determined by the scalar potential, which was studied in section 7.1. Since the scalar potential ϕ is describable by a Gaussian distribution (eq. (7.1.4)) as shown in fig. 7.3, the kinetic energy might be describable by a similar Gaussian distribution with the same standard deviation. The standard deviation σ of ϕ and ϵ_{kin} at the resist surface are plotted in fig. 10.18 (right) in dependence of the resist layer thickness d_l, which were obtained by using a Gaussian fit to the distribution of ϕ and ϵ_{kin}. The agreement of both standard deviations is good and the minor deviations are caused by the automatized fitting routine. For higher tip-resist distances d and smaller d_l, the fitting was not successful because the absolute value of the extremum of the distribution decreases, as can be seen for ϕ and ϵ_{kin} in figs. 7.3 and 10.18 (left), respectively.

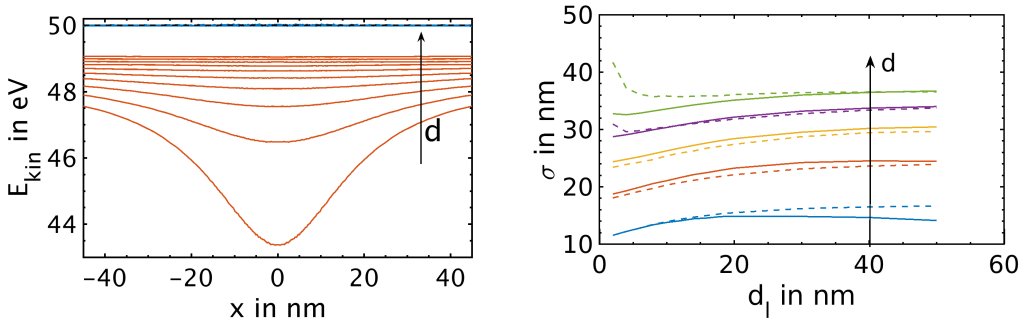

Figure 10.18: (*Left*) Kinetic energy distribution of the electrons ϵ_{kin} at the resist surface (red lines) and the resist-sample interface (blue lines) for different tip-resist distances d. The black broken line represents ϵ_{kin} at the sample surface for the resist-less case. (Note, black broken and blue lines are overlaying each other at $\epsilon_{kin} \approx 50\,eV$). ϵ_{kin} is shown for $d = 10\,nm$ to $100\,nm$ (increase is marked with an arrow). The dielectric constant was $\varepsilon = 3.7$ and the bias voltage $U = 50\,V$. (*Right*) Standard deviation σ of the scalar potential ϕ (solid lines) and the kinetic energy ϵ_{kin} (broken lines) over the resist thickness d_l determined at the resist surface. The tip-resist distance was varied from $d = 10\,nm$ (blue) over $20\,nm$ (red), $30\,nm$ (yellow), $40\,nm$ (purple) to $50\,nm$ (green) for $\varepsilon = 3.7$.

The minimum of the kinetic energy distribution might be helpful for the experimental determination of an energy threshold for the lithography. For this purpose, patterning of dot structures might result in donut structures if the minimal kinetic energy is lower than an energy threshold for lithography. However, the energy threshold is assumed to be in the range of the energy of the molecular bonding of the resist material, which are in the range of $10\,eV$. Thus, such donut structures might be only observable for the bias voltages $U \lesssim 10\,V$. For so small bias voltages, the constant-current control needs to be very sensitive to use a very low current set-point. Otherwise, the tip approaches the sample too much and the lithography process changes to tunneling or local anodic oxidation mediated by a water meniscus. Therefore, the experimental observation of donut structures and thus to determine the energy threshold is demanding and not yet achieved.
The previous results demonstrate that the resist-less case can be used to estimate w and d_b also for a resist layer of $d_l = 10\,nm$ and $\epsilon = 3.7$ but the kinetic energy at the resist surface is not describable. In the following sections, the different influences of the resist layer properties (thickness d_l, dielectric constant ε, structures) on the field-emission scanning probe lithography will be analyzed in detail. In sections 10.4.1-10.4.4, the scattering mechanisms inside the resist layer are neglected. In section 10.4.5, the results of the electronic trajectory calculation inside the resist layer including electron scattering (based on the Monte Carlo algorithm of chapter 6) are presented.

10.4.1 Resist layer thickness

The investigation of the influence of the resist layer thickness d_l is presented in this section. The resist material C-methylcalix[4]resorcinarene ($C_{32}H_{32}O_8$) was used here, since it is a standard resist material for FE-SPL. The dielectric constant of this resist has a value of $\varepsilon = 3.7$ [172].
An assumption on the influence of the dielectric resist layer is, that it will decrease the electric field because the tip-sample distance d_{tot} is increased by the thickness of the resist layer d_l. Thus, also the total current I will decrease for increasing d_l as well as the current density at the sample J_{sam}. This would yield to an decreased line width w (or even to an unsuccessful writing process). This assumption will be studied first.

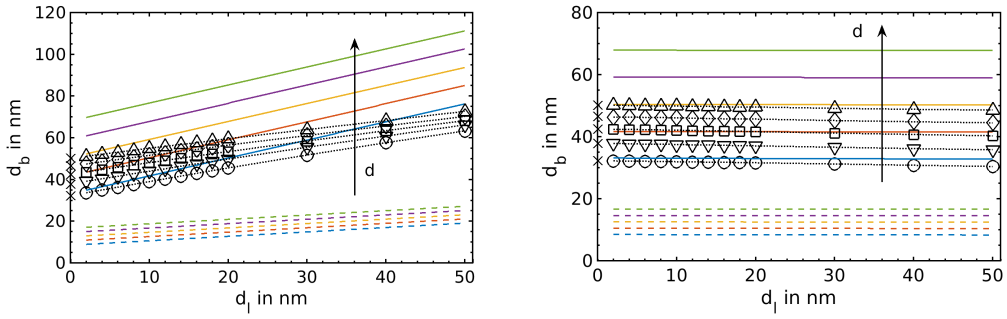

Figure 10.19: Numerical results (symbols), analytical results (solid lines) and results from the Gaussian approximation (broken lines) on the dependence of the beam diameter d_b on the resist thickness d_l determined at the resist-sample interface (*left*) and at the resist surface (*right*) for $U = 40\,V$. The tip-resist distance was varied from $d = 30\,nm$ (blue, ◯) over $40\,nm$ (red, ▽), $50\,nm$ (yellow, □), $60\,nm$ (purple, ◇) to $70\,nm$ (green, △). The black crosses represent the data for $d_l = 0$ (without a resist layer). The dielectric constant was $\varepsilon = 3.7$.

The dependence of the beam diameter d_b on the resist thickness d_l is shown in fig. 10.19 for different tip-resist distances d. Thereby, d_b was determined either at the resist-sample interface (left) or the resist surface (right). The black crosses in fig. 10.19 show the results of the resist-less case ($d_l = 0$). The difference for the two positions is clearly seen, while d_b increases at the resist-sample interface, it remains almost constant at the resist surface (as expected from fig. 10.15) for increasing resist thickness d_l. The increase of d_b at the resist-sample interface (left) can be explained by the increased spread of electrons (neglecting scattering) for increasing tip-sample distance $d_{tot} = d + d_l$ due to an increasing layer thickness d_l. Note, the tip-resist distance is kept constant for each plotted line in fig. 10.19. The eq. (10.4.6) describes the behavior at the resist surface

$$d_b^{GA} = (r + d)\,\kappa_p \sqrt{\frac{E_0}{\beta C \Phi^{3/2}}} \approx \text{const} \tag{10.4.8}$$

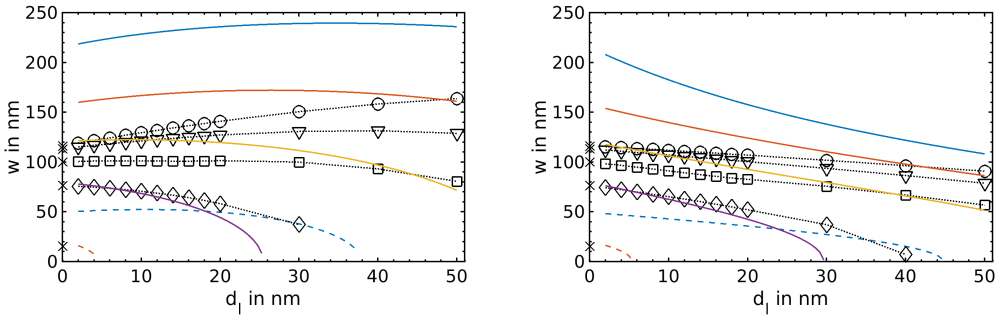

Figure 10.20: Numerical (symbols) and analytical results (solid lines) of the line width w and results from Gaussian approximation (10.4.7) (broken lines) over the resist thickness d_l determined at the resist-sample interface (*left*) and at the resist surface (*right*) for $U = 40\,V$. The tip-resist distance was varied from $d = 30\,nm$ (blue, ◯) over $40\,nm$ (red, ▽), $50\,nm$ (yellow, □) to $60\,nm$ (purple, ◇). The black crosses represents the data for $d_l = 0$ (without a resist layer). The diectric constant was $\varepsilon = 3.7$.

for $d > r$ but also the one at the resist-sample interface

$$d_b = (r + d_{\text{eff}})\,\kappa_p \sqrt{\frac{E_0}{\beta C \Phi^{3/2}}} \propto d_l\,, \tag{10.4.9}$$

since $d = \text{const}$.
In fig. 10.20, w is plotted in dependence of the thickness d_l for a bias voltage of $U = 40\,V$. On the left-hand side of fig. 10.20, w was determined at the resist-sample interface ($z = d + d_l$) and on the right-hand side, w was obtained at the resist surface ($z = d$). For the first case (fig. 10.20), an increase of the tip-sample distance d_{tot} yields to an increased line width w until the maximal current density distribution J_{max} at the sample is in the same range as the threshold value J_{crit}. For $J_{max} \approx J_{crit}$, w decreases with d_l. This is similar to the studies of $w(d)$ without a resist layer only that with a resist layer $J_{max} \approx J_{crit}$ is achieved for larger tip-sample distances $d_{tot} = d + d_l$ (since $d_{\text{resist-less}} = d_{\text{eff}} = d + d_l/\varepsilon$). For w measured on the resist surface (see fig. 10.20 (right)), only a decrease of w can be observed. This is described in good agreement by the Gaussian approximation eq. (10.4.7), which yields

$$w^{GA} \propto \sqrt{\text{const} - \sqrt{\text{d}_\text{l}}} \tag{10.4.10}$$

for $d > r$. The results of the Gaussian approximation are shown by the broken lines in fig. 10.20. The change of w of more than $70\,nm$ is in contrast to the publication of Dobisz et al., who reported that the effects of the resist layer on the spot size (interpreted as line width) are so small that they are only measurable for sub-$10\,nm$ lithography [22].
The dependency of the kinetic energy $\langle \epsilon_{kin} \rangle$ on the resist layer thickness is shown in fig. 10.21 for various bias voltages U (left) and various tip-resist

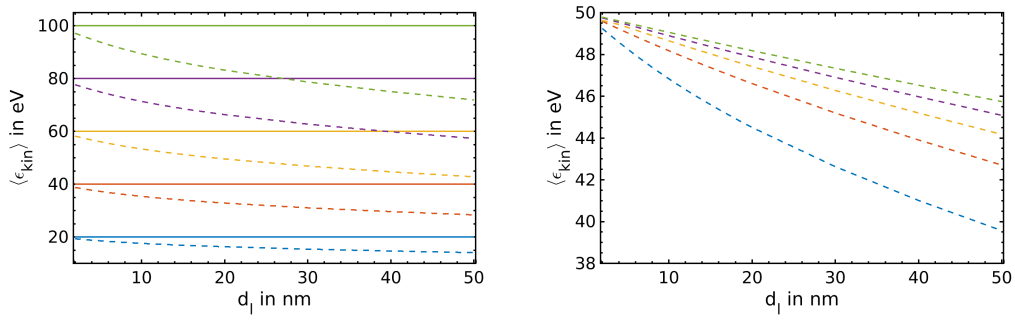

Figure 10.21: (Averaged) kinetic energy of the electrons $\langle \epsilon_{kin} \rangle$ in dependence of the resist thickness d_l for different bias values U (*left*) and different tip-resist distances d (*right*) from numerical simulations. The broken lines represent $\langle \epsilon_{kin} \rangle$ at the resist surface whereas the solid lines represent it at the resist-sample interface. (*Left*) $\langle \epsilon_{kin} \rangle (d_l)$ is shown for $U = 20\,V$ (blue), $40\,V$ (red), $60\,V$ (yellow), $80\,V$ (purple) and $100\,V$ (green) for the tip-resist distance of $d = 10\,nm$. (*Right*) The tip-resist distance d was set to the values $20\,nm$ (blue), $40\,nm$ (red), $60\,nm$ (yellow), $80\,nm$ (purple) and $100\,nm$ (green) for the bias voltage of $U = 50\,V$. The dielectric constant was $\varepsilon = 3.7$.

distances d. Here, the average of the kinetic energy

$$\langle \epsilon_{kin} \rangle = \frac{\int \epsilon_{kin}(\rho)\, n_e(\rho)\, d\rho}{\int n_e(\rho)\, d\rho}\,, \tag{10.4.11}$$

was taken because $\langle \epsilon_{kin} \rangle$ of the electrons depends on ρ, if measured at the resist surface, as shown in fig. 10.18 (left). The increase of the resist layer thickness d_l yields a decrease of ϵ_{kin}, which is similar to the results of Dobisz et al. [22]. As seen in fig. 10.21, the stronger the electric field E_{tip} (i. e., the larger U and the smaller d, respectively) the stronger the difference between kinetic energy on the resist surface and the one on the resist-sample interface $\langle \epsilon_{kin} \rangle (d + d_l) = e|\phi|$. This difference is also increased for increased resist layer thickness d_l. In FE-SPL experiments, the decrease of $\langle \epsilon_{kin} \rangle$ might result in less effective exposure at $\rho \approx 0$ (as shown in fig. 10.18) for large d_l or small d. In this context, thin resist layers are more favorable regarding homogeneity of the exposure and edge roughness of the written patterns.
In the next subsection, the effect of the different resist materials, given by variations of the dielectric constant ε, are considered.

10.4.2 Dielectric function

After the investigation of the influence of the resist layer thickness d_l on line width w and kinetic energy $\langle \epsilon_{kin} \rangle$, the dependency on the dielectric constant ε of the resist is considered. If not stated otherwise, the resist thickness is $d_l = 10\,nm$.
In fig. 10.22, beam diameter d_b (left) and line width w (right) are shown in dependence of ε for different tip-resist distances d. The effect of ε on d_b is

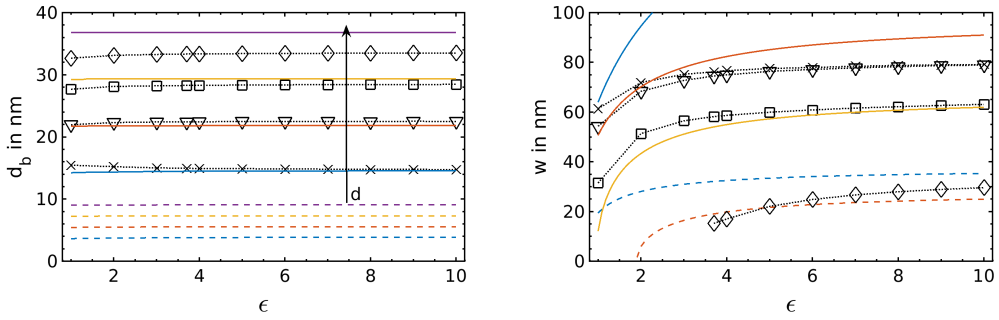

Figure 10.22: Beam diameter d_b (*left*) and line width w (*right*) in dependence of the dielectric constant ε for a bias voltage of $U = 30\,V$ and tip-resist distances $d = 10\,nm$ (blue, X), $20\,nm$ (red, $\bigtriangledown$), $30\,nm$ (yellow, $\square$) and $40\,nm$ (purple, $\diamondsuit$). Numerical results, analytical results and the results of from the Gaussian approximation are plotted as symbols (with dotted lines as guide to the eye), solid lines and broken lines, respectively. All results were determined at the resist surface.

almost negligible, which is observed also for the analytical model and the Gaussian approximation. The influence of ε on w is also relative small, as shown on the right side of fig. 10.22. However, for J_{sam} close to J_{crit}, i. e., larger d, a decrease of w is clearly visible for decreasing ε. The Gaussian approximation leads to

$$d_b^{GA} \propto \text{const} \tag{10.4.12}$$

and

$$w^{GA} \propto \sqrt{\text{const} - \frac{1}{\sqrt{\varepsilon}}} \tag{10.4.13}$$

using the assumption $d > r$.
In fig. 10.23, the kinetic energy $\langle \epsilon_{kin} \rangle$ is plotted in dependence of ε for different U (left) and d (right). Due to the decrease of the effective resist thickness $\frac{d_l}{\varepsilon}$, the kinetic energy at the resist surface approaches $\langle \epsilon_{kin} \rangle$ at the resist-sample interface for an increasing dielectric constant ε. In other words, the voltage drop in the resist becomes smaller and so the acceleration of the electrons inside the resist layer. The decrease of $\langle \epsilon_{kin} \rangle$ with ε and the corresponding increase of the electric field strength is more pronounced for large electric field strengths, i. e., large voltages U (fig. 10.23 (left)) and small tip-resist distances d (fig. 10.23 (right)).

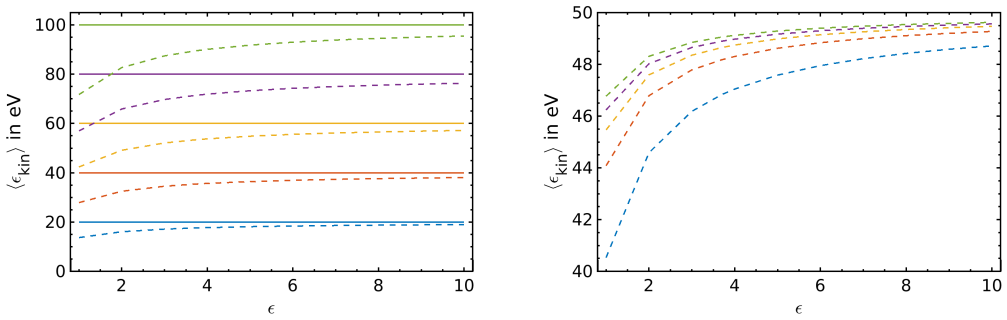

Figure 10.23: (Averaged) kinetic energy of the electrons $\langle \epsilon_{kin} \rangle$ plotted in dependence of the dielectric constant ε for different bias values U (*left*) and different tip-resist distances d (*right*). The broken lines represent $\langle \epsilon_{kin} \rangle$ determined at the resist surface whereas the solid lines represent $\langle \epsilon_{kin} \rangle$ determined at the resist-sample interface. (*Left*) $\langle \epsilon_{kin} \rangle(\varepsilon)$ is shown for $U = 20\,V$ (blue), $40\,V$ (red), $60\,V$ (yellow), $80\,V$ (purple) and $100\,V$ (green) for a tip-resist distance of $d = 10\,nm$. (*Right*) The tip-resist distance d was set to $20\,nm$ (blue), $40\,nm$ (red), $60\,nm$ (yellow), $80\,nm$ (purple) and $100\,nm$ (green) for a bias voltage of $U = 50\,V$ and a resist thickness of $d_l = 10\,nm$.

10.4.3 Resist sensitivity

After investigating parameters mainly influencing the electric field, the resist sensitivity is considered in this section. It describes the efficiency of an electron to trigger a lithographic reaction in the resist layer.
Typically, the pattern size is determined in dependence of the experimentally used exposure dose D, which is defined as $D = I\,t_{pix}$ [13]. Here, t_{pix} is the pixel time, as it was introduced in eq. (5.4.5). Thereby, D is a measure for the number of electrons impinging the resist surface during the lithography process neglecting their energy.
In fig. 10.24, experimental results reported by Kästner [13] are drawn showing the dependence of line width w on exposure dose D. The data were obtained from experiments, in which dot-like patterns were written either in negative-tone or positive-tone lithography. Here, w^{neg} and w^{pos} denote the dot diameter measured either after wet development ("aWD") for the negative-tone case or directly after FE-SPL ("aSPL") for the positive-tone lithography case, instead of aWD and $aSPL$ used in fig. 10.24 taken from [13]. More details about the measurements and about dot patterning technique can be found in [13] and [131]. By fitting these results, M. Kästner [13] obtained the following dependency of $w(D)$ for (i) the negative-tone case:

$$w^{neg}(D) = 12.6\,\frac{nm}{\ln(fC)}\,\ln(D - 0.7\,fC) \tag{10.4.14}$$

and (ii) for the positive-tone case:

$$w^{pos}(D) = 72.6\,\frac{nm}{\ln(pC)}\,\ln(D - 0.19\,pC)\,. \tag{10.4.15}$$

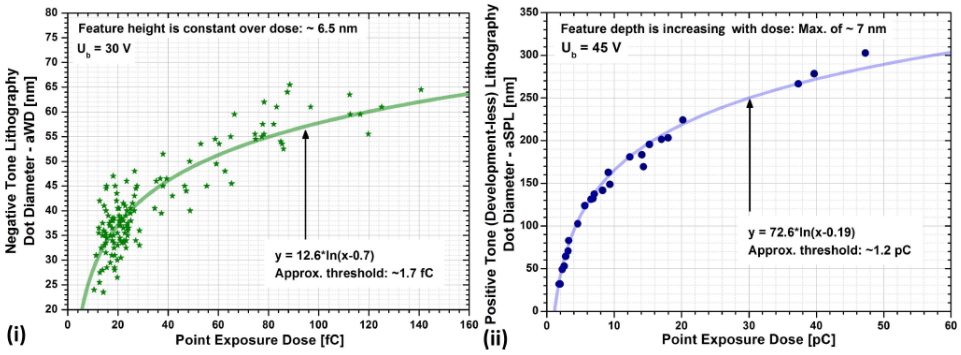

Figure 10.24: Experimental measurements of dot diameter in dependence of the exposure dose for positive-tone (*left*) and negative-tone lithography (*right*) determined either direct after SPL (aSPL, *right*) or after wet development (aWD, *left*). Results are taken from ref. [13].

To enable a comparison with the theoretical results and to predict the dependency for other resists, the critical number of electrons n_{crit}, necessary to induce a lithographic modification of the resist, has to be determined. Since J_{sam} cannot be determined experimentally to obtain an estimation of n_{crit}, one might assume a negligible effect of the shape of the current density distribution and rather assume the exposed area to be equal to the written dot area (defined by the dot diameter "w"), i. e., all electrons take part in the patterning process irrespective of their density and energy distribution. With these assumptions, n_{crit} can be estimated by

$$n^i_{crit}(D) = \frac{D}{e\, A_{dot}(D)} = \frac{D}{e\, \frac{\pi}{4}\, w^i(D)^2}\,. \tag{10.4.16}$$

Here, i can be "*pos*" or "*neg*".

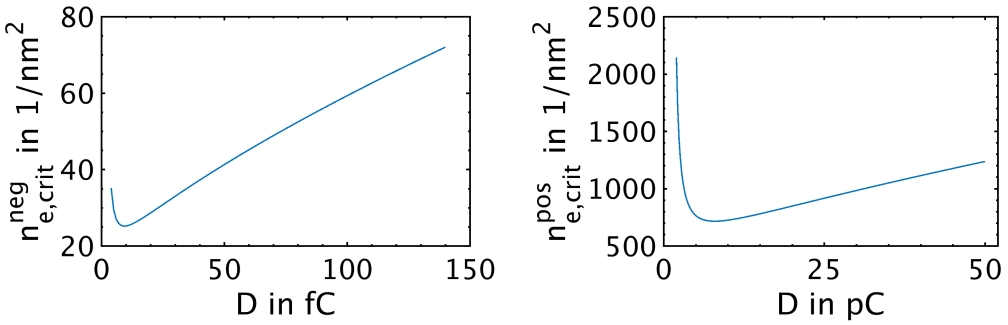

Figure 10.25: Experimental values for electron density threshold based on the experimental data of fig. 10.24.

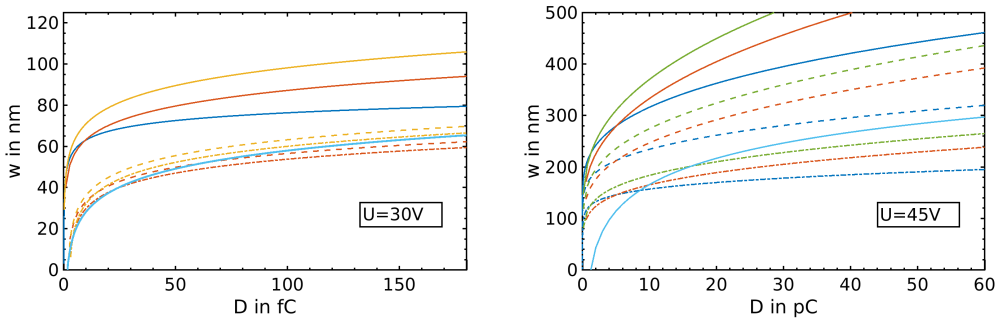

Figure 10.26: Analytical values for dot diameter w in dependence of the exposure dose for negative-tone (*left*) and positive-tone lithography (*right*). (*Left*) The used threshold values for the negative-tone patterning are $n_{crit}^{neg} = 30\,nm^{-2}$ (solid lines), $600\,nm^{-2}$ (broken lines) and $800\,nm^{-2}$ (dash-dotted lines) and (*right*) the ones for positive-tone patterning are $n_{crit}^{pos} = 30\,nm^{-2}$ (solid lines), $100\,nm^{-2}$ (broken lines) and $700\,nm^{-2}$ (dash-dotted lines). The results for the experimentally obtained fit results (eqs. (10.4.14) and (10.4.15)) shown by cyan curves. The blue curves are obtained using a constant exposure time of $\tau = 1\,ms$ and varying the total current by changing the tip-resist distance from $d = 10\,nm$ to $50\,nm$ (*left*) and from $22\,nm$ to $60\,nm$ (*right*). (*Left*) The tip-resist distance was kept constant at $d = 25\,nm$ (red lines) and $30\,nm$ (yellow lines), while the exposure time was varied in the range $\tau \in [0.1, 200]\,ms$. (*Right*) The tip-resist distance was kept constant at $d = 30\,nm$ (red lines) and $35\,nm$ (green lines), while the exposure time was varied in the ranges $\tau \in [0.1, 12]\,ms$ and $\tau \in [0.1 - 50]\,ms$, respectively. The resist thickness value was $d_l = 10\,nm$ and applied bias voltages were $U = 30\,V$ (*left*) and $45\,V$ (*right*).

In fig. 10.25, the electron density thresholds n_{crit}^{pos} and n_{crit}^{neg} extracted from experimental data are shown for positive-tone and negative-tone lithography, respectively. The results were obtained using eq. (10.4.16) with either eqs. (10.4.14) or (10.4.15). As expected, the resulted threshold values n_{crit}^{pos} and n_{crit}^{neg} are not constant since the shape of J_{sam} was neglected. For small D, n_{crit} is overestimated since the exposure area will be larger than the actual dot area A_{dot} because the electron density will be mostly below the threshold value. For large D, the overestimation of n_{crit} is caused by the increasing difference between n_{crit} and $n_{max} = J_{max}\tau/e$. However, the minimal values of n_{crit}^{pos} and n_{crit}^{neg} (seen in fig. 10.25) can be used as estimates for the real threshold values of positive-tone and negative-tone lithography. Therefore, $n_{crit}^{neg} \approx 26\,\frac{1}{nm^2}$ and $n_{crit}^{pos} \approx 715\,\frac{1}{nm^2}$ were found.
In fig. 10.26, the analytical results for the dot diameter w as function of the exposure dose D are shown for negative-tone (left) and positive-tone lithography (right). While in the experiments (see fig. 10.25), the exposure dose was only varied by applying different current set-points and keeping the exposure times nearly constant, the exposure dose in the analytical model (10.4.5) was varied by changing the total current I using the tip-resist distance d (blue lines) and the exposure time τ (red, yellow and green lines). For negative-tone lithography, the analytical results agree relatively well with the experimental ones (cyan) for $n_{crit} = 600\,nm^{-2}$ (broken lines) and $800\,nm^{-2}$ (dash-dotted

lines) for tip-resist distances of $d = 25\,nm$ (red) and $30\,nm$ (yellow), i. e., for constant I. The comparison between the variation of the exposure dose using the exposure time τ or the total current I for $n_{crit} = 30\,nm^{-2}$, reveals different slopes for increasing D. This difference arises from the modified shape of current density distribution for changed tip-resist distance d whereas a modified exposure time τ only changes the current density by a multiplication factor. On the right-hand side of fig. 10.26, the results for positive-tone lithography (direct ablation) are shown consisting of the fit function (10.4.15) obtained from measurements and results from the analytical model (10.4.5). The deviations of the dot diameter w between analytical model and experiment for positive-tone patterning are more prominent than for negative-tone patterning (fig. 10.26 (left)). However, for $n_{crit} = 30\,nm^{-2}$ and variation of d (solid blue line), the analytical model seems to describe the experimental fit result (cyan line) but overestimates them by a constant off-set. In the case of positive-tone patterning, the deviations between variation using τ or I are also observable. Since the tip parameter (r, γ and Φ) are not reported for the actual experimental dataset, it is impossible to refine the analytical model for better agreement. Additionally, the tip-resist distances are unknown since a constant-current control feedback was used for the measurements and the measurements ware done under ambient conditions, which lead to further influences by water, chemical reactions, etc., which were not considered. Nevertheless, the analytical model yields comparable results like the experiments and the usage of threshold values n_{crit}^{pos} and n_{crit}^{neg} seems to explain the experimentally found behavior of the dot diameters w^{pos} and w^{neg} for positive-tone and negative-tone patterning, respectively. This is remarkable since physical scattering and chemical reactions within the resist layer are neglected within the analytical model, which were thought to be crucial for the experiments done under ambient conditions. It might enable the use of the analytical model to predict experimental parameters (U, I and v) to obtain a certain dot diameter after refining the analytical model.
The following two-step procedure might help to refine the analytical model for FE-SPL using different resist materials: (i) Analysis of experimentally obtained "I-vs-d" measurements[6] as shown in section 9.2 to obtain $I(d)$ and, in this way, the exposure dose $D(d)$. Such experiments also determine the necessary tip radius r and (ii) analysis of dot-writing FE-SPL experiments (similar to the ones shown in fig. 10.24) for different exposure doses D modified by τ or I. This procedure might allow to determine the threshold values for different resist materials and to distinguish the materials using threshold values and other chemical parameter.
In section 10.4.5, the physical scattering will be taken into account. Before this, the impact of pre-patterned structures on the lithography process is studied.

[6] In general, measured data for I and d_{rel} from the tip approach could be used as well if the tip radius is known.

10.4.4 Resist structure

In this section, the numerical results using a structured resist layer are presented. The analytical model was not adapted to describe the influence of resist features (trenches or cross-linked resist) and, thus, all results presented in the following are obtained from numerical studies. Here, the different structures taken into account are (*i*) trenches in the resist layer with various widths b and depths h to study possible ablation mechanisms or positive-tone lithography and (*ii*) a local change of the dielectric function of the resist layer as a model for the influence of cross-linked resist due to negative-tone lithography.

Lithography on pre-defined, positive-tone patterns

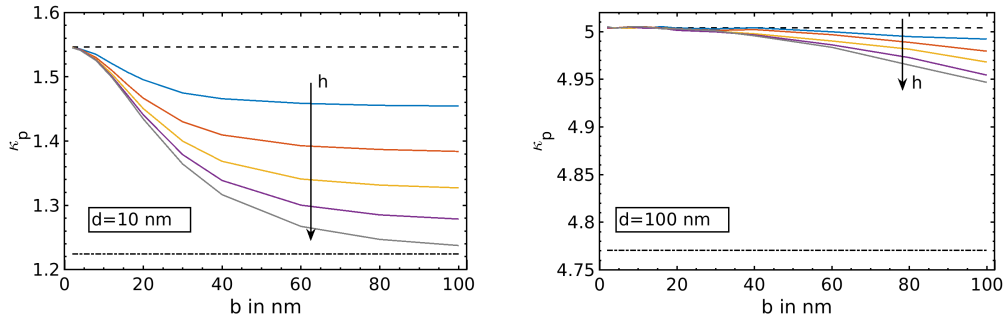

Figure 10.27: Maximal field enhancement factor κ_p as function of the trench width b for tip-resist distances of $d = 10\,nm$ (*left*) and $100\,nm$ (*right*). The broken black lines correspond to the case without a trench, i. e., $b = 0$ and the black dash-dotted lines to results without a resist layer, i. e., $b = \infty$. The trench height was set to $h = 2\,nm$ (blue), $4\,nm$ (red), $6\,nm$ (yellow) and $8\,nm$ (purple). The solid grey line corresponds to a trench throughout the resist layer, i. e., $h = d_l = 10\,nm$.

At first, the effects of a trench in the resist layer are considered. In fig. 10.27, the field enhancement factor κ_p at the tip apex is plotted in dependence of trench width b for two different tip-resist distances d. For comparison, results for the case without a trench (black broken line), i. e., $b = 0$, and for a sample without a resist layer (black dash-dotted line), i. e., $b = \infty$, are shown. As can be seen in fig. 10.27, an increasing width b of the trench yields to a decrease of the field enhancement factor κ_p. For small tip-resist distances $d \lesssim 10\,nm$, i. e., $\frac{d}{r} = 1.2$, κ_p approaches the value of the resist-less case (dash-dotted curve) if the trench is throughout the resist layer (solid grey curve), i. e., $h = d_l$. In this case, the influence of the resist thickness d_l on κ_p is nearly lost for trench widths $b > 100\,nm$ and replaced by an effective resist layer thickness $d_l - h$ as can be seen on the left side of fig. 10.27. In contrast, for a tip-resist distance of $100\,nm$ (right side of fig. 10.27), i. e., $\frac{d}{r} \approx 12$, the influence of the trench is weak, i. e., $\kappa_p \approx \kappa_p(b = 0)$ even for large trench widths. In general, an increasing depth h leads to a decrease of κ_p and this effect is more pronounced

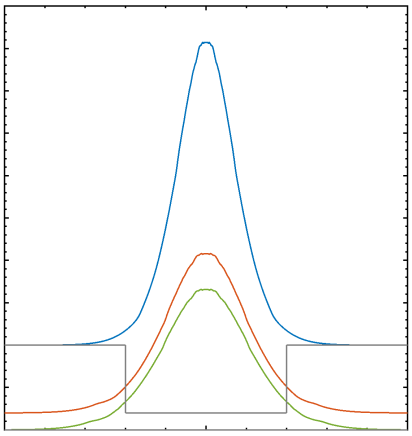

Figure 10.28: Current density distribution determined at the resist surface (blue), at the bottom of the trench (red) and at the resist-sample interface (green) for a tip-resist distance of $d = 10\,nm$, an applied bias voltage of $U = 50\,V$, a resist layer thickness of $d_l = 10\,nm$, a trench width of $b = 20\,nm$ and a trench depth of $h = 8\,nm$.

the larger the trench width b and the smaller the tip-resist distance d, i. e., for larger ratios of b/d.
Since the line width w seems predict the pattern size, its dependence on trench with width b and depth h more realistically, it will be studied and the beam diameter d_b is omitted. Thereby, w will be determined at different positions: (i) at the resist surface, (ii) at the bottom of the trench, and (iii) at the resist-sample interface as shown in fig. 10.28. Considering the three positions, a decrease of the maximum and also an increased width of J can be observed with increasing distance to the tip.
On the left-hand side of fig. 10.29, the line width w, determined at the resist surface, in dependence of the trench width b is plotted for different trench depths h. The results for the trench-less case ($b = 0$) and the resist-less case ($b \to \infty$) are represented by the grey dash-dotted line and the grey dotted line, respectively. It can be seen that even for small trench widths $b < w$, the line width w is smaller than for the trench-less case. This arises from the altered electric field distribution, which affects the trajectories slightly but sufficiently above the resist layer and the trench to yield a notable change of J. The decrease of w is stronger for deeper trenches as shown on the left-side of fig. 10.29.
On the right side of fig. 10.29, w determined at the bottom of the trench in dependence of b for different h. Interestingly, the behavior differs from the one determined at the resist surface. The grey solid line represents $w = b$. For $w > b$, w increases with increasing depth h of the trench. This is expected since the spread of the electrons should increase for increasing distance to the emitter

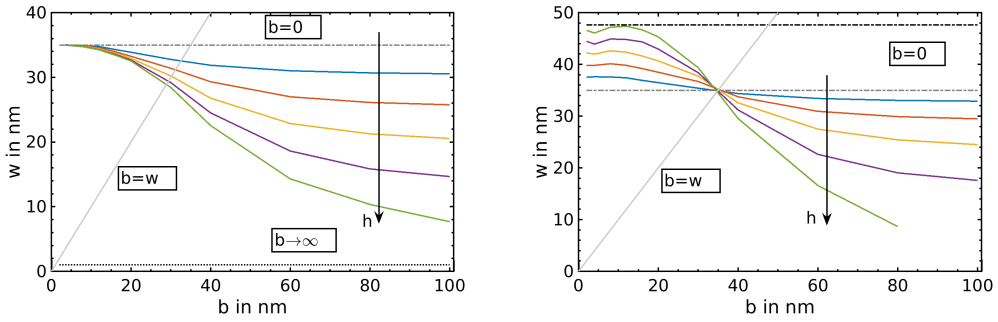

Figure 10.29: Theoretical line width w as function of trench width b for different trench depths h determined at the resist surface (*left*) and at the bottom of the trench (*right*). Trench depth values are $h = 2\,nm$ (blue), $4\,nm$ (red), $6\,nm$ (yellow), $8\,nm$ (purple) and $10\,nm = d_l$ (green). The black dotted line resembles the resist-less result ($b \to \infty$, (*left*) only), the grey dash-dotted lines the trench-less result ($b = 0$) at the resist surface and the black dash-dotted line the trench-less result ($b = 0$) at the sample ((*right*) only). The solid grey lines corresponds $b = w$. Resist thickness was $d_l = 10\,nm$, bias voltage $U = 20\,V$ and tip-resist distance $d = 10\,nm$.

tip (see fig. 10.28) if the trajectories are (nearly) independent on h. This effect would also be observed for increasing tip-resist distances. In other words for $w > b$, the influence of the trench is to increase the effective tip-resist distance. For $w < b$, the contrary is obtained: w decreases for increasing h. Here, the change of the electric field distribution due to the presence of the trench yields a decrease of the current density distribution due to the widening of the trajectories. Thereby, the decrease of w is stronger for increasing h similar to the behavior of w determined at the resist surface (left side of fig. 10.29). The change between both regimes occurs for all h at $w = b$. For the parameters used to obtain fig. 10.29, this point is reached for $w \approx 35\,nm$, which corresponds to the value of w determined at the resist surface for the trench-less case (grey dash-dotted line). To guide the lithography process, one can define a "functional" line width w_f (shown on the left side of fig. 10.30). For $w > b$, w_f is defined by w determined at the resist surface and for $w \leq b$, w_f is equal to w at the bottom of the trench. This yields for pre-defined trenches with $b < w_f$, a line width w_f similar to the value of the trench-less case ($b = 0$) (grey dash-dotted line in fig. 10.30 (left)) independently on h. Thus, trenches with $b < w_f$ have only a very limited influence on w_f. However, for trench widths $b > w_f$, w_f is smaller than the pre-defined trench and even decreases with increasing trench depth h as can be seen on the left side of fig. 10.30. Thereby, a wide and deep pre-defined trench could possibly increase the resolution for a given parameter set and sequential writing procedures can be useful for relatively thick resist layers to decrease w at the sample. A study with a double trench structure could be used to verify this prediction of the model. Note, electron-resist interactions were not considered for this results and could yield to a different behavior. As seen for w_f in fig.10.30 (left), the point $w_f = b$ is found

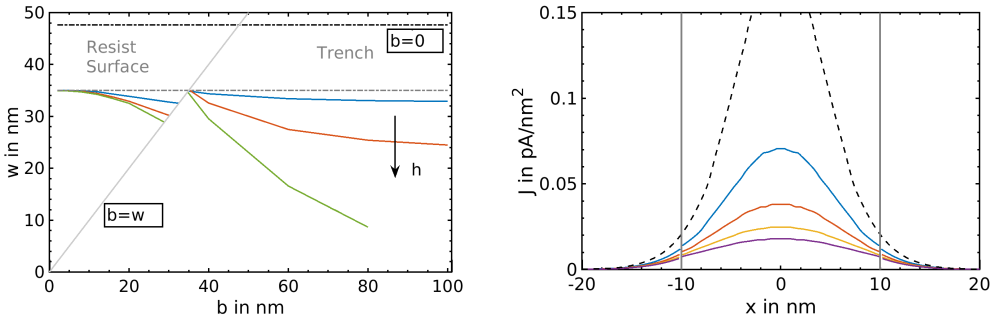

Figure 10.30: (*Left*) "Functional" line width w_f as function of the trench width b. w obtained at the resist surface is drawn as w_f if $w > b$, and $w_f = w$ obtained at the bottom of the trench for $w < b$. The following trench depths are used: $h = 2\,nm$ (blue), $6\,nm$ (red) and $10\,nm$ (green). (*Right*) The current density distribution J determined at the vacuum-material interface for a trench width of $b = 20\,nm$. The black broken line shows the results for the trench-less case ($h = 0\,nm$). The trench depth was set to the following values: $h = 2\,nm$ (blue), $4\,nm$ (red), $6\,nm$ (yellow) and $8\,nm$ (purple). Resist thickness was $d_l = 10\,nm$, bias voltage $U = 20\,V$ and tip-resist distance $d = 10\,nm$.

to be independent on the depth h. Thus, at this point, patterning with vertical sidewalls would be possible since the trench width b is equal to the line width w_f and w_f remains constant even if h increases. Since for all studied parameter sets, the crossing point $w_f = b$ is found to be independent on h, vertical side walls might be obtained independently of the actual parameters.

Finally, the dependence of the current density distribution on a pre-defined trench will be studied. On the right side of fig. 10.30, distributions of the current density J are plotted for a trench width of $b = 20\,nm$ for various trench depths h. Note, these distributions are obtained at the vacuum-material interface. In other words, they are determined at the resist surface for $|x| > \frac{b}{2}$ and at the bottom of the trench inside the trench ($|x| \leq \frac{b}{2}$). The maximum of the current density decreases for increasing trench depth h whereas the tails of the distribution are almost unchanged and no obvious deviation between inside and outside the trench can be observed. One remarkable point of the decrease of the density distributions inside the trench is that it would yield to a self-limitation of the patterning depth of the trench if all parameters are kept constant during the experiment.
For the kinetic energy, it was observed that the energy of the electrons inside the trench is larger than outside the trench. This is expected from fig. 10.21, in which the dependence of the kinetic energy on the resist thickness d_l is shown. However, the variations of the kinetic energy are small and the line-width would be hardly influenced.

Lithography on pre-defined, negative-tone patterns

After investigation of the effects related to previously-written positive-tone features onto the lithographic resolution, the influence of negative-tone (cross-linked) structures is considered by introducing a change of the dielectric function in a part of the resist layer. Note, for negative-tone features, the pre-defined patterns are assumed to be across the complete resist layer, i. e., $h = d_l$. For calixarene resist material, it is assumed that the dielectric constant is increased from $\varepsilon = 3.7$ to 6.6 by cross-linking [13].

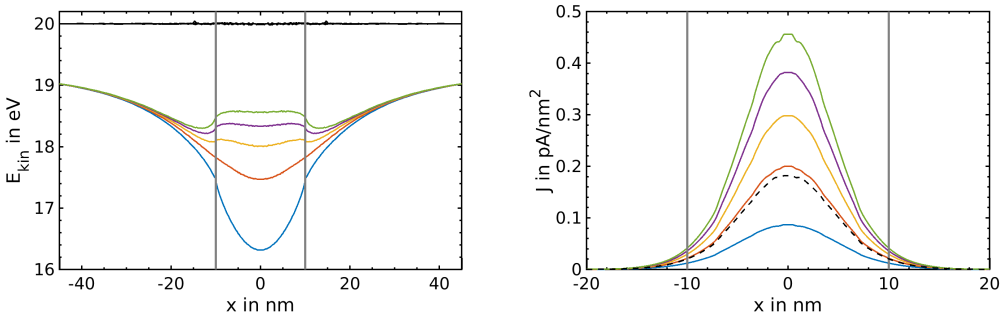

Figure 10.31: Kinetic energy distribution of electrons ϵ_{kin} (*left*) and current density distribution J (*right*) determined at the resist surface for a cross-linked structure with width $b = 20\,nm$ and different dielectric constants $\varepsilon_2 = 2$ (blue), 4 (red), 6 (yellow), 8 (purple) and 10 (green). The black broken lines represent ϵ_{kin} determined at the resist-sample interface (*left*) and J determined at the resist surface (*right*) for the unstructured resist, i. e., $b = 0$. The applied voltage was $U = 20\,V$, the tip-resist distance $d = 10\,nm$ and the thickness of the resist was $d_l = 10\,nm$. The dielectric constant of the unexposed resist was $\varepsilon = 3.7$.

The kinetic energy distributions ϵ_{kin} and the current density distributions J are shown in fig. 10.31 for a cross-linked structure with a width $b = 20\,nm$ and with different values of the dielectric constant ε_2. For an increased dielectric constant ε_2, ϵ_{kin} and J increase. It is caused by the increased electric field E_{tip} at the tip (eq. (10.4.2)) for an increased dielectric constant ε of the resist layer or an increased ε_2 of a part of the resist. This leads to higher kinetic energies ϵ_{kin} of the electrons at the resist surface, which was found to be the reason for the difference of ϵ_{kin} determined at the resist surface and at the resist-sample interface. The emission probability increases for increasing electric field strength leading to the increase of J seen in fig. 10.31 (right). It is observable that for large values of ε_2, the minimum of the kinetic energy ϵ_{kin} is leveled and effects based on an energy threshold can be avoided. The increase of the current density distribution leads to an self-acceleration of the lithographic process (for constant parameters), which is in contrast to the self-limitation for the positive-tone pre-structures.
In fig. 10.32, the line width w in dependence of the pattern width b and the dielectric constant ε_2 for different patterning speeds v as shown. As seen on the left-hand side of fig. 10.32, an increase of the structure width b leads to

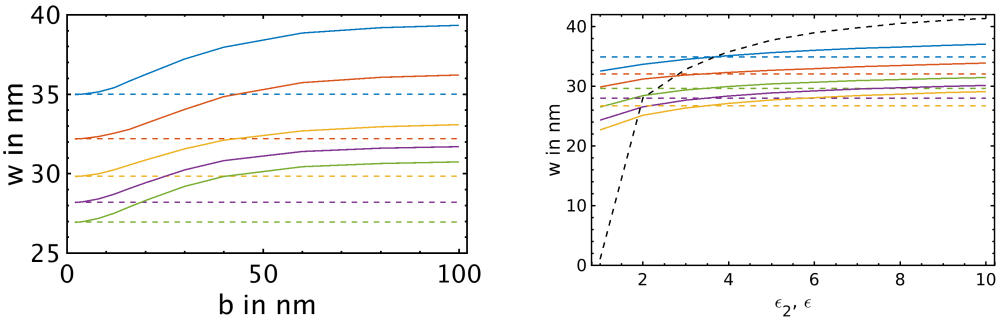

Figure 10.32: Dependence of the w on structure width b (*left*, for $\varepsilon_2 = 6.6$) and its dielectric constant ε_2 (*right*, for $b = 20\,nm$) determined at the resist surface. The used patterning velocities were $v = 1\,\mu m/s$ (blue), $2\,\mu m/s$ (red), $4\,\mu m/s$ (yellow), $6\,\mu m/s$ (purple) and $8\,\mu m/s$ (green). The broken colored lines are the results for an unstructured resist layer, i. e., $b = 0\,nm$ and $\varepsilon_2 = \varepsilon = 3.7$, respectively. The broken black line represents the result of $w(\varepsilon)$ for an unstructured resist layer ($b = 0$). The applied voltage was $U = 20\,V$, the tip-resist distance $d = 10\,nm$ and the thickness of the resist was $d_l = 10\,nm$.

an increase of the line width w. Thus, a previously cross-linked feature (with $\varepsilon_2 > \varepsilon$) widens the pattern to be written as expected from the electric field (eq. (10.4.2)) and J shown in fig. 10.31 (right). From the increase of w for increasing ε for an un-structured resist (observed in fig. 10.22) and the increase of J (shown in fig. 10.31 (right)), it was expected that the change of the locally-defined constant ε_2 also increase w but to a smaller extent (as seen in fig. 10.32 (right)).
To summarize this section, previously patterned structures (ablated or cross-linked) can influence the line width w and so the patterning process whereby the effect of cross-linked structures is smaller than for ablated ones and opposite effects are found. For trenches, a line width reduction can be obtained whereas line width increase occurs for cross-linked structures. Additionally for the ablation process, vertical side walls seem to be obtainable for a specific line width for each parameter set as well as a self-limiting patterning due to the decrease of the current density J within the trench for increasing trench depth. In the range of self-limitation, the achievable writing depth might depend on the applied parameter set and the shape of the trench might vary considerably from an ideal trench with vertical side walls in this case. For negative-tone lithography, a increase of the line width and of the current density distribution is observed, which is opposite to the case of positive-tone patterning.
From experimental FE-SPL studies with calixarene resist, it is concluded that direct ablation patterning consists actually of cross-linking and ablation whereas negative-tone patterning can be achieved without ablation [13]. However, for other resist materials (molecular glasses or polymer films) positive-tone and negative-tone lithography (both including a development afterwards) as well as direct ablation (without development) or a combination of all can be achieved [13, 70, 73]. From studies with polymer resists [70], it might be

possible that the direct ablation is also accompanied by positive-tone patterning for calixarene resist. Thus, both effects found in the numerical simulations presented here, i. e., increase (due to cross-linking) and decrease of the line width (during ablation/positive-tone patterning), might need to be considered. However, the theoretical results might have only limited validity for the lithography experiments, since the electron scattering is not taken into account. The promising results of the comparison between FE-SPL experiments and analytical model (shown in section 10.4.3) reveal that, even by neglecting the electron scattering, valuable predictions seems to be obtainable. However, due to the idealized shape of the trenches used in the model and the neglected electron scattering within the resist, it is unknown to which extent the theoretical predictions are valid. The validity of the predictions (increased and decreased line width for negative-tone and positive-tone lithography, respectively) could be tested by double exposure or mix-and-match experiments [10].
Nevertheless, the calculated energy and current density distributions were initial conditions for a subsequent calculation of scattering processes inside the resist. In this case, the observed increase of the kinetic energy ϵ_{kin} for cross-linked features (see fig. 10.32) will affect the scattering processes, whose probabilities are energy-dependent.
In the next section, the influences of the (physical) scattering on the lithography, i. e., line width w, electron densities n_e/ν_e and the averaged energy distribution $\langle E \rangle$, will be discussed.

10.4.5 Electron interactions within the resist layer

In this section, the influence of the electron scattering within the resist layer onto lithography is presented, which was studied using the Monte Carlo simulation described in section 6.3. Here, only unstructured resist layers are considered. The focus is on the influence of scattering inside the resist on the resolution described by the line width w. The expectation is that the elastic and inelastic scattering will increase the width of the electron distribution and, thus, the line width. Additionally, the electron number should be increasing due to inelastic scattering events, which can yield to ionization of resist molecules[7]. The loss of the kinetic energy of the electrons due to scattering processes might be compensated by the energy gain due to the electric field inside the resist layer as suggested by Wilder et al. [32]. Thus, the line width should be increased and dominated by elastic and inelastic scattering processes [22]. The validity of these expectations will be studied in this section.
First, the place and number of the different types of scattering processes will be presented before studying their influence on the lithographic resolution. In fig. 10.33, selected electron trajectories are shown to visualize the different scattering processes included in the Monte Carlo simulation (see chapter 6). The grey lines represent the trajectories from the nanotip to the resist surface calculated with the nanolithography program (see chapter 5). The trajectories

[7] Ionization processes are characterized by an energy transfer from the scattered electron exceeding a threshold energy ϵ_{co}, which corresponds to the ionization energy of the resist molecules. Here, $\epsilon_{co} = 10\,eV$ is used, if not stated otherwise.

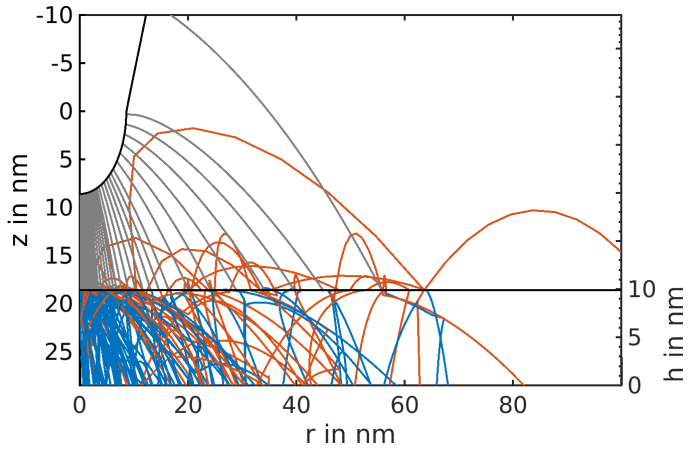

Figure 10.33: Selected trajectories calculated by the nanolithography program and the Monte Carlo simulation of FE-SPL for calixarene resist layer. The trajectories of backscattered electrons are marked in red, the incident electron trajectories from the tip to the resist surface in grey and all other trajectories inside the resist layer in blue. The applied voltage was set to $U = 50\,V$, the tip-resist distance $d = 10\,nm$ and the thickness of the resist was $d_l = 10\,nm$.

of backscattered electrons are drawn in red. Here, the backscattering from the resist into the vacuum is only considered since the probability of backscattering from the sample is vanishingly low as discussed before. These trajectories include subsequent scattering processes after re-entry of the backscattered electrons into the resist layer. The re-entry is caused by the applied electric field attracting the electrons to the sample. It can be seen that also multiple (subsequent) backscattering events occur in accordance with the results from McCord and Pease [6]. The blue lines show trajectories of electrons, which are elastically and/or inelastically scattered within the resist layer, but not backscattered. It is visible that most of the electrons are not backscattered. Nevertheless, re-entering electrons might yield to a significant broadening of the line width if their fraction is sufficiently high.
In fig. 10.33, the electron number per trajectory needed to calculate the number of scattering processes and distribution of electrons are not represented. The number of electrons and scattering processes are shown in fig. 10.34. Thereby, the number N_e of electrons inside the resist layer in a certain depth interval $h + \Delta h$ (see fig. 10.33)[8] is shown in dependence of the depth h. Here, N_{tip} is the number of electrons emitted from the nanotip and N_{tot} the number of all electrons inside a certain depth interval. By comparing N_{tot} (black line) and N_{tip} (orange $\bigtriangledown$) in fig. 10.34, the increase of the number of electrons due to inelastic scattering processes, in particular ionization, is clearly visible. Note, N_{tot} counts all electrons including backscattered ones and electrons re-entering the resist. In this way, some electrons are counted three times. To obtain a net number of electrons without counting certain electrons multiple times, one can

[8] Here, Δh was set to $0.5\,nm$.

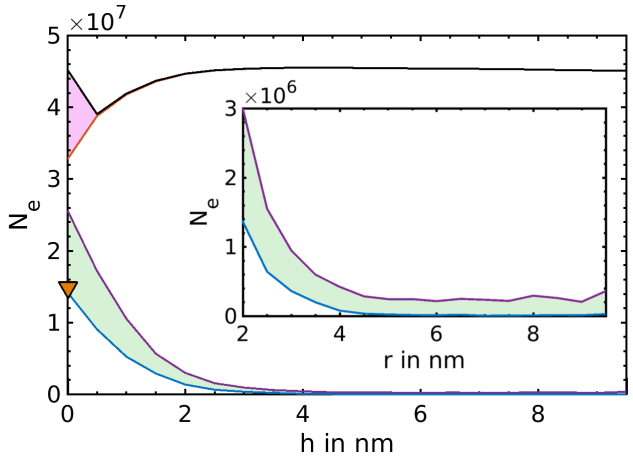

Figure 10.34: The number of electrons in dependence of depth h inside the resist layer. Thereby, N_{tot} (black line) is total number of electrons. N_{dir} (red line) is the net number of electrons and N_{back} the number of backscattered electrons (pink area represents $2\,N_{back}$). The number of inelastically scattered electrons N_{in} is shown by a purple line and the number N_{ion} of electrons ionizing the resist molecules by a blue line. The green area represents the electron number N_{exc} of excitation events. The number N_{tip} of electrons emitted from the tip and exposing the resist surface are given as well (orange $\bigtriangledown$). The bias voltage was $50\,V$, the tip-resist distance $d = 50\,nm$, the resist thickness $d_l = 10\,nm$ and the exposure time $\tau = 1\,ms$.

include the sign of the velocity component in the z direction to the electron number per trajectory. The direction-dependent electron number N_{dir} is given by the red line in fig. 10.34. For N_{dir}, all electrons are counted maximal once since each backscattered electron cancels itself when it re-enters. In the case, that a backscattered electron left the simulation box, it is not counted in N_{dir} at all since the backscattering cancels its primary impact into the resist. This situation is assumed to be negligible due to the small kinetic energies and the high attractive electric field involved esp. for small tip-resist distances. Thus, the number of backscattered electrons can be estimated by $N_{back} \approx \frac{1}{2}\,(N_{tot} - N_{dir})$ (pink area in fig. 10.34). It can be observed that backscattering occurs only in close proximity to the resist surface, i. e., within $h \lesssim 1\,nm$. For $h > 1\,nm$, the probability of backscattering is strongly reduced, indicated by $N_{tot} \approx N_{dir}$. This value of h corresponds to one or two times the inelastic mean free path $\lambda_{in} \approx 0.4\,nm$ for electrons in the energy range $\epsilon_{kin} \in [10, 50]\,eV$. In other words, backscattering occurs mostly in the first (inelastic) scattering events. Note that $h \approx 1\,nm$ is much smaller than expected escape depths used for EBL for energies above $1\,keV$ ($\approx 5 - 15\,nm$) [173]. The difference between N_{dir} and N_{tip} corresponds to the (secondary) electrons generated by ionization of resist molecules. It is indicated by $N_{dir} \gtrsim 2N_{tip}$ that, in average, slightly more than one ionization event per primary electron occurs within the first interval Δh. N_{dir} is increasing until $h \approx 4\,nm$ due to further ionization processes. Saturation of N_{dir}, respective N_{tot}, occurs already at a depth $h \approx 4\,nm$, which

contradicts the expectations that inelastic scattering takes place throughout the complete resist layer. This is due to the small kinetic energy of electrons in FE-SPL and the small potential difference between resist surface and resist-sample interface, which is not large enough to accelerate the electrons within the resist to kinetic energies sufficiently for subsequent ionization events. Thus, lithographic modifications are mainly limited to a resist depth up to $4\,nm$.
The number N_{in} of inelastic scattering events (green line) and the number N_{ion} of ionization processes (blue line) are shown in fig. 10.34 as well. Both numbers N_{in} and N_{ion} decrease rapidly for increasing resist depth h and become constant at approximately $4\,nm$ (see inset of fig. 10.34). In particular, the saturation of N_{dir} is a result of the absence of ionization processes for $h \gtrsim 4\,nm$. Besides ionization also excitation processes (their number is marked by the green area in fig. 10.34), i. e., inelastic scattering without resist molecule ionization, can occur. Inelastic scattering for $h > 4\,nm$ result mostly in excitation of resist molecules. This excitation leads to vibrational and electronic relaxation processes in a certain range around the scattering location. Thereby, it is assumed that excited resist molecules are not influencing the lithographic process since (i) only ionization events yield to breaking of chemical bonds necessary for removal or cross-linking of resist molecules and (ii) the time scale of molecular relaxation processes (ps) [174] is much smaller than the estimated time scale (ns) between two subsequently emitted electrons from the tip. Since ionization events take place mostly within a small depth of the resist layer and thus only there a lithographic reaction is expected for a pristine resist layer, the assumption of a lithographic reaction throughout the complete resist layer cannot be verified. If resist molecules are directly ablated due to the ionization process, a further ablation of deeper molecules can occur leading to fully ablated structures. Thus, direct ablation would be a time-dependent process and the depth of the structures might be controllable by the exposure time τ or exposure dose D as already shown experimentally for calixarene resist materials [13]. For positive-tone lithography only a partial cross-linking might occur in the upper part of the resist layer for short exposure times and only this part will be removable in the subsequent wet development step. This behavior was reported for positive-tone FE-SPL of the polymer resist material PMMA [70]. For negative-tone lithography, the partial cross-linking would lead to unstable patterns, which could also be removed during development. The irregular negative-tone patterns reported for PS resist using the lowest exposure dose [70] could be due to partial cross-linking. Thus, the theoretical description of the dependence on exposure time or exposure dose yield to a similar behavior as reported experimentally.
After considering the number of electrons in dependence of the depth within the resist layer, their radial distribution will be investigated in the following. Therefore, the surface electron densities $\nu_e = \frac{N_i}{A} = \frac{J}{e}$ (figs. 10.35 and 10.36) and the volume electron densities $n_e = \frac{N_e}{V}$ (fig. 10.37) are studied as functions of the radial coordinate r at the resist surface, i. e., $h = 0\,nm$. Note, the surface electron densities are used in this section instead of the current densities, which were used so far, to emphasize that the description considers only the motion

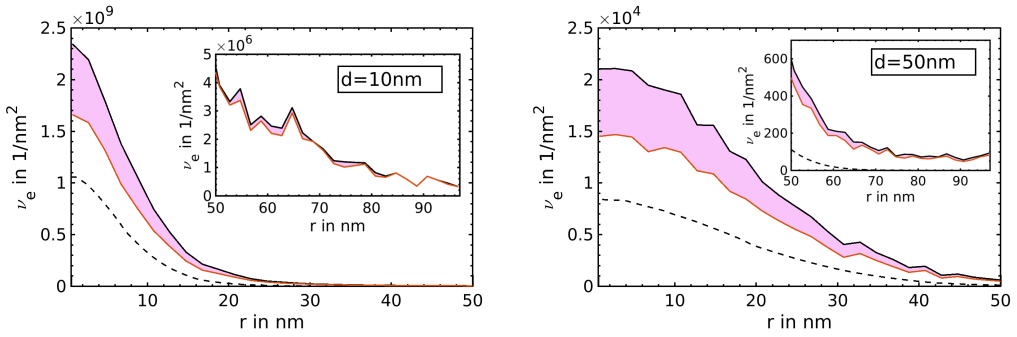

Figure 10.35: Surface electron density distribution ν_e over the radial coordinate r for $h = 0\,nm$. The surface electron density ν_{tot} of all electrons is shown by a black line and the density ν_{dir} of the incident electrons by a red line. The pink area represents the electron density for the backscattered electrons. The surface density ν_{tip} of the field emitted electrons are given by the broken line. The tip-resist distance was set to $d = 10\,nm$ (*left*) and $50\,nm$ (*right*). The bias voltage was set to $50\,V$, the resist thickness to $d_l = 10\,nm$ and the exposure time to $\tau = 1\,ms$.

and scattering of electrons. The surface electron densities ν_e measures the number of electrons at a specific depth h. In contrast, volume electron densities n_e are measured within a certain volume $V = A\Delta h = \pi\,(r^2 - (r - \Delta r)^2)\,\Delta h$. In fig. 10.35, the surface density ν_{tot} of the total amount of electrons (black line) and ν_{dir} of electrons moving only towards the sample (without backscattered electrons; red line) are shown for two tip-resist distances $d = 10\,nm$ (left) and $d = 50\,nm$ (right). Obviously, the maximum of the total density ν_{tot} is more than twice as large as the electron density ν_{tip} of the electrons emitted from the tip and impinging the surface (broken line). This is caused by ionization of resist molecules resulting in secondary electron generation and the backscattering/re-entry of electrons. After subtraction of the backscattered electrons, the electron density ν_{dir} is still considerably larger than the initial electron density ν_{tip} (broken line) not only directly below the tip ($r \approx 0$) but also in the tails of ν_{dir} for $r > 50\,nm$ (see insets of fig. 10.35). This indicates that ionization of resist molecules occurs in a large range of r, which might lead to an increase of the surface roughness, if the number of ionization events is not sufficient and ionization occurs occasionally beside the main pattern. Backscattered electrons (pink area in fig. 10.35) in contrast are mainly measured for $r \leq 40\,nm$ and seem to have only minor influence on the tails ($r > 50\,nm$). Nevertheless, the density ν_{back} exceeds the initial electron density ν_{tip} for $r > 20\,nm$ (left) and $r > 40\,nm$ (right) for $d = 10\,nm$ and $d = 50\,nm$, respectively. This is explainable by multiple backscattering events but also by backscattering after multiple scattering processes within the resist layer. Nevertheless, the value of the distributions ν_{back} but also of ν_{tip} is much less than their maximal values. A similar result, i. e., $\nu_{back} > \nu_{tip}$ for large r, was found by McCord and Pease using a hard boundary approach (neglecting scattering within the resist layer) between vacuum (air) and resist [6].

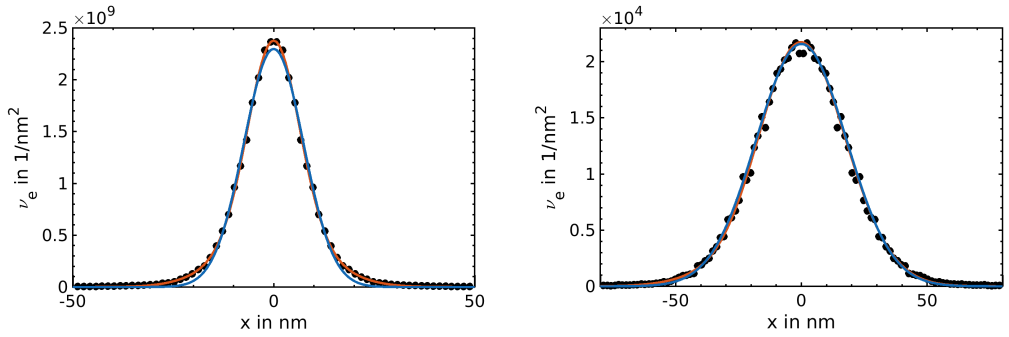

Figure 10.36: Fit to the electron density distribution ν_{tot} (shown as black dots) at the surface for the tip-resist distances $d = 10\,nm$ (*left*) and $50\,nm$ (*right*) and $U = 50\,V$. A single Gaussian function $A\exp[-(x-B)^2/C^2]$ (blue line) and a double Gaussian function $A_1\exp[-(x-B_1)^2/C_1^2] + A_2\exp[-(x-B_2)^2/C_2^2]$ (red) were used to fit ν_{tot}.

Despite the result that backscattering mainly occurs for $r < 50\,nm$, re-entry of backscattered electrons might influence the tails of ν_{tot} more strongly. It could yield to a shape of ν_{tot}, which is describable using a double Gaussian function. Typically, these double Gaussian distributionsare used for the description of EBL due to the large amount of backscattered electrons [32]. This shape of the distribution is considered to be the reason for proximity effects in EBL, i. e., a resolution limit for neighboring features larger than feature sizes from single feature patterning. In experimental studies of FE-SPL, Wilder et al. did not found such double Gaussian shape [32]. However, by comparing the tails of ν_{tot} (black lines) in the insets of fig. 10.35, differences are observed for $d = 10\,nm$ (left) and $d = 50\,nm$ (right), which might indicate a dependence of the shape on the tip-resist distance. This is further investigated by fitting a single (blue line) and a double Gaussian function (red) to ν_{tot}. The results are shown in fig. 10.36. For $d = 10\,nm$, only a double Gaussian function can capture the shape of ν_{tot} whereas ν_{tot} can be described by a single Gaussian function for $d = 50\,nm$. This difference can be explained from the trajectories (shown in fig. 10.33 for $d = 10\,nm$). While for $d = 10\,nm$, re-entry of electrons is observed up to $r \approx 80\,nm$, the situation is different for $d = 50\,nm$ where backscattering and re-entry of electrons is more evenly distributed up to the simulation boundaries at $r = 100\,nm$. Additionally, the number of electrons decreases with increasing d due to the lower electric field strength at the nanotip. The localization of trajectories of re-entering electrons to smaller values of r and the increased number of electrons causes that the influence of backscattered and re-entering electrons is more pronounced and, thus, the observation of a double Gaussian shape, for small d. Hence, a proximity effect (based on backscattering) is present for FE-SPL as well but strongly decreased (compared to EBL) and it can be further decreased by increasing d. Since backscattering is restricted to a small depth interval at the resist surface, this proximity effect is limited to the resist surface, which was not reported so far.

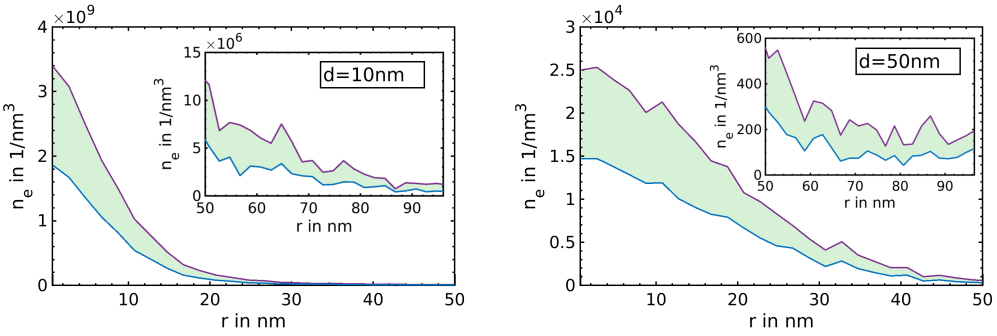

Figure 10.37: Volume densities of inelastic scattering events in the interval $h \in [0, 0.5]\,nm$ plotted over the radial coordinate r. The total density n_{in} of inelastic scattering events is depicted by a purple line. The scattering events involving ionization of resist molecules are given by n_{ion} (blue line). The scattering resulting in an excitation of resist molecules are symbolized by a green area. The insets show the tails of the volume densities for $r > 50\,nm$. The tip-resist distance was set to $d = 10\,nm$ (*left*) and $50\,nm$ (*right*). The bias voltage was $50\,V$, the resist thickness $d_l = 10\,nm$ and the exposure time $\tau = 1\,ms$.

To study the amount of inelastic scattered electrons, the volume density n_{in} of all inelastic scattering events (purple) is shown in fig. 10.37, together with n_{ion} of the electron scatterings leading to secondary electron generation (ionization of resist molecules) (blue) and n_{exc} of those leading to excitation of the resist molecules (green area). The high value of inelastic scattering density n_{in} near $r \approx 0\,nm$ is associated with a spread of the electrons (shown in fig. 10.33) and explains the high surface density ν_{tot} in fig. 10.35. As seen in fig. 10.37, more than half of the inelastic scatterings leads to a molecule ionization with secondary electron generation for $r \approx 0$. These are associated with molecular bond breaking within the resist layer and underlie, thus, lithographic patterning. At the surface, the distributions of n_{ion} and n_{exc} are very similar, however n_{ion} is slightly larger than n_{exc} for $r \approx 0$.
After investigating the radial distribution of inelastic scattering events, the vertical distribution is studied. In fig. 10.38, the volume density of inelastic scattering events causing ionization n_{ion} (left) and excitation n_{exc} (right) of resist molecules are shown. Comparing n_{ion} and n_{exc} in the top row, it is visible that the distributions of n_{ion} and n_{exc} are very similar. For increasing depth h, inelastic scattering, i. e., n_{ion} and n_{exc}, is drastically reduced for $h > 4\,nm$ as already expected from fig. 10.34. In the bottom row of fig. 10.38, the radial distributions of n_{ion} and n_{exc} for various depths h are shown. While for $h \leq 2\,nm$, n_{ion} and n_{exc} are quite similar (as shown for $h = 0$ in fig. 10.37), for $h > 2\,nm$ n_{exc} dominates. Nevertheless, both n_{exc} and n_{ion} are drastically reduced compared to their maximum values observed at the surface ($h = 0$, shown in fig. 10.37). This shows a strong localization of excitations and even more of ionization events to a depth of $h < 4\,nm$ and to a radial distance $r \leq 60\,nm$. This contradicts the expection that ionization occurs throughout the complete resist layer thickness and that the width of the distribution of

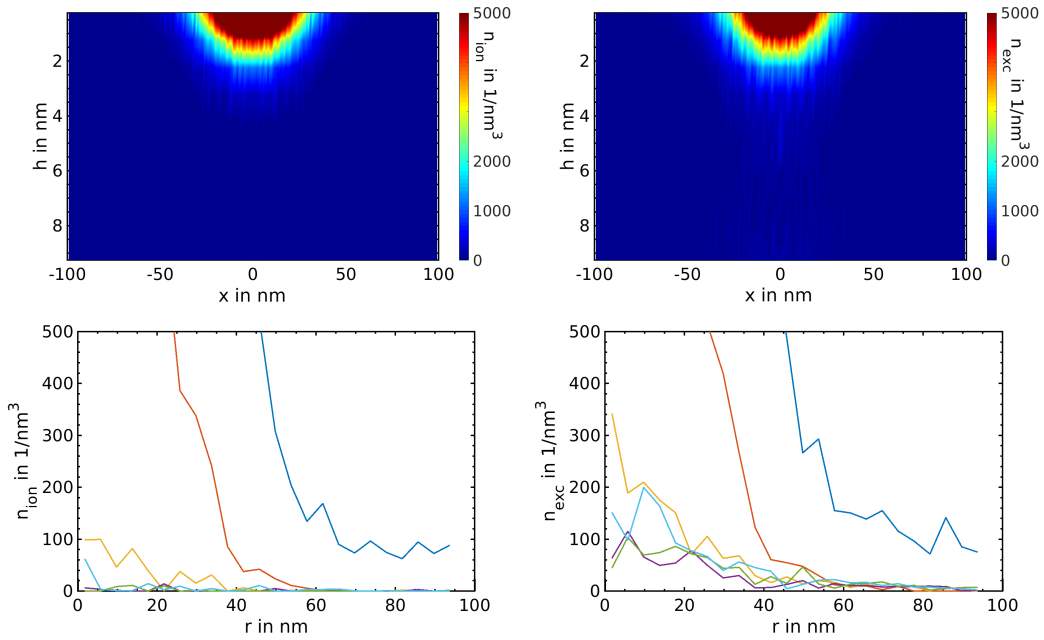

Figure 10.38: Volume density distributions of inelastic scattered electrons causing ionization (*left*) and excitation (*right*) of resist molecules are shown color-coded over x and h (*top*) and over r for cross sections at $h = 0\,nm$ (blue), $2\,nm$ (red), $4\,nm$ (yellow), $6\,nm$ (purple) and $8\,nm$ (green) (*bottom*). The bias voltage was set to $50\,V$, the tip-resist distance to $d = 50\,nm$ and the resist thickness was $d_l = 10\,nm$.

n_{ion} increases with increasing h. However, it is explainable by the transfer of energy from the "primary" electrons to the resist material (excitation and ionization) and to the "secondary" electrons. Due to the energy transfer, the energy of a single electron is decreased and if its value is below the cut-off energy ϵ_{co} no further ionization processes can be triggered by this electron until its energy is sufficiently increased by the electric field.
Despite the decreasing spread of inelastic scattering events, the distributions of the electrons increases due to elastic and inelastic scattering. This can be seen from the total surface density distribution ν_{tot} within the resist, which is shown on the left side of fig. 10.39 for different resist depths h. An enhanced surface density due to the backscattering/re-entry is observed at the resist surface $h = 0\,nm$ (blue curve). Inside the resist, the maximum of ν_{tot} decreases with depth h, while its tails increase since spread of electrons increases due to scattering. Thereby, the total number of electrons is not influenced by the increased spread for $h > 4\,nm$ (as seen in fig. 10.34), i. e., elastic scattering and excitations dominates and ionizations are negligible.
To study, if the electrons can gain enough energy from the electric field within the resist layer to compensate the energy transferred to secondaries and the resist materials and, thus, to enable subsequent ionization scattering events

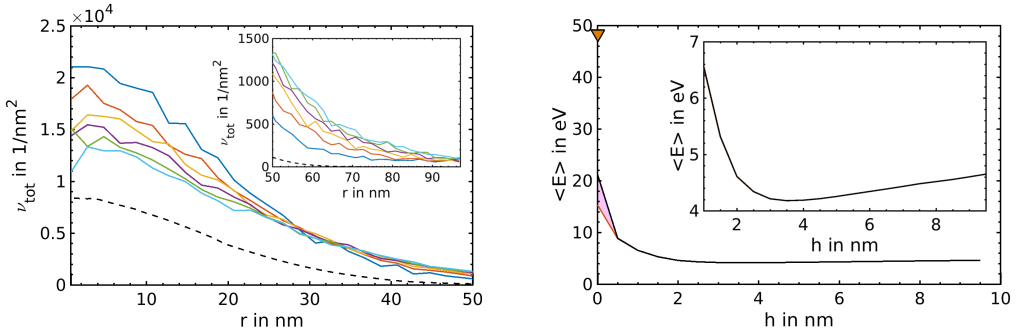

Figure 10.39: (*Left*) Cross sections of surface density ν_{tot} of all electrons for different resist depths $h = 0\,nm$ (blue), $2\,nm$ (red), $4\,nm$ (yellow), $6\,nm$ (purple), $8\,nm$ (green) and $9.5\,nm$ (cyan). Additionally, the density ν_{tip} of the electrons emitted from the tip and impinging the resist surface is plotted as broken line. (*Right*) Averaged energy distribution $\langle\epsilon\rangle$ as function of depth h inside the resist layer. Thereby, $\langle\epsilon_{tot}\rangle$ includes the energy of all electrons (black line) and $\langle\epsilon_{dir}\rangle$ of electrons moving in h direction. The averaged energy distribution $\langle\epsilon_{tip}\rangle$ of electrons emitted from the tip and determined at the resist surface is shown by an orange triangle. $\langle\epsilon_{back}\rangle$ of backscattered and re-entering electrons is visualized by the pink area. The bias voltage was $50\,V$, the tip-resist distance $d = 50\,nm$ and the resist thickness $d_l = 10\,nm$.

(as suggested by Wilder et al. [32]), the averaged kinetic energy distributions are considered. Different averaged energy distributions $\langle\epsilon\rangle = \frac{\sum \epsilon N_e}{\sum N_e}$ are shown on the right side of fig. 10.39: $\langle\epsilon_{tot}\rangle$, which includes the energy of all electrons, $\langle\epsilon_{back}\rangle$ considering only backscattered electrons, $\langle\epsilon_{dir}\rangle$ including only electrons propagating towards the sample surface and $\langle\epsilon_{tip}\rangle$, which takes only the electrons emitted from the tip into account. As expected, the total averaged energy $\langle\epsilon_{tot}\rangle$ (black line) decreases with increasing h due to inelastic scattering events. The part of the energy distribution $\langle\epsilon_{back}\rangle$ associated with backscattering/re-entry is marked by the pink area. It accounts for nearly a third of the averaged energy $\langle\epsilon_{tot}\rangle$ at the resist surface. Furthermore, the average value of the total energy $\langle\epsilon_{tot}\rangle < 22\,eV$, determined at the resist surface, is already strongly reduced compared with the expected one from the applied potential difference of $50\,V$ between tip and sample. This can be explained by two effects. First, field-emitted electrons from the tip are not accelerated to the maximal possible energy of $50\,eV$ since they do not yet reached the sample surface, which was already discussed for figs. 10.18 and 10.21. However, the influence is rather limited. For a tip-resist distance of $50\,nm$, $\langle\epsilon_{tip}\rangle \approx 49\,eV$ (marked by the orange triangle in fig. 10.39 (right)) is determined at the resist surface. The effect even reduces with decreasing tip-resist distance. Second, the effect dominating the reduction of the averaged electron energy is the inelastic scattering and the corresponding energy transfer into the resist material and to secondary electrons as expected. For $h > 3\,nm$, a rise of $\langle\epsilon_{tot}\rangle$ occurs since the inelastic scattering probability is strongly decreased and electrons are accelerated by the electric field inside the resist layer. Nevertheless, the electric field inside

the resist is relatively weak and the energy gain is less then $1\,eV$ for the case considered here ($U = 50\,V$, $d = 50\,nm$ and $d_l = 10\,nm$ yielding $I \approx 2.4\,nA$). Thus, the assumption of Wilder et al. [32] that electrons can gain sufficient energy from the electric field within the resist enabling subsequent ionization processes is not confirmed for the FE-SPL case. The patterning resolution will be investigated in the following by studying the line width in dependence of various parameters. On the left side of fig. 10.40, the line width w_J based on the total electron density (threshold value $100\,\frac{1}{nm^2}$; blue curve), w_E based on the total kinetic energy density distribution (threshold $100\,\frac{1}{nm^2} \cdot 10\,eV$; red curve) and the line width w_{ion} determined from the actual ionization events (green curve) are shown. Both, w_J and w_E, increase with depth h because of the increased electron number (see fig. 10.34) and the increased spread of electrons due to elastic and inelastic scattering (see fig. 10.37). The increase of w_E is similar to the one of w_J, which implies that the electron number density n_{tot} is much larger than the threshold value n_{crit} so that the decrease of kinetic energy with increasing depth h does not affect the line width w_E determined from the total energy density distribution. However, a better estimate for the experimentally obtained line width is w_{ion} determined from the ionization events (green line in fig. 10.40) because it considers the resist modifications (breaking bonds) leading to a lithographic patterning. w_{ion} is calculated using the average value of the ionization events and a threshold value $_{crit}$ of one ionization event per volume of $1\,nm^3$. The number of ionization events $h > 4\,nm$ is strongly reduced (as seen in fig. 10.38) and, thus, the line width w approaches 0.

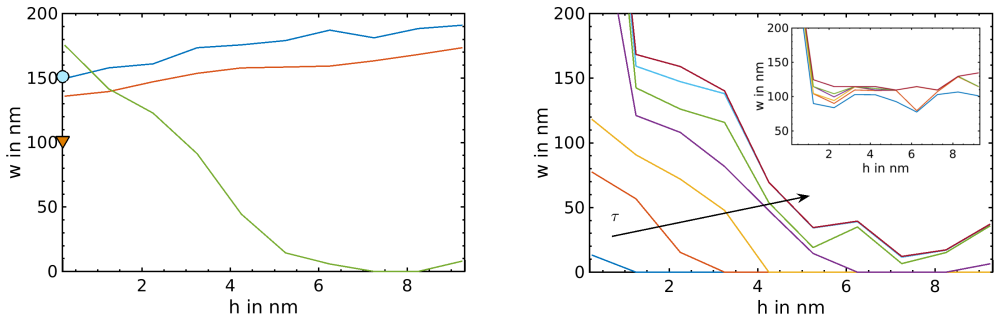

Figure 10.40: Theoretical line width w in dependence of the depth h. w_J based on the electron number is presented by the blue curve, w_E based on the kinetic energy distribution by the red curve and w_{ion} derived from the actual ionization events by the green one (*left*). (*Left*) The line widths w_J^{tip} and w_E^{tip} calculated from the electron beam emitted from the tip, i. e., from their electron number and kinetic energy distribution determined at the resist surface, are represented by the orange triangle and the cyan circle, respectively. (*Right*) Line width w_{ion} in dependence of depth h for different exposure times: $\tau = 0.1\,\mu s$ (blue), $1\,\mu s$ (red), $10\,\mu s$ (yellow), $100\,\mu s$ (purple), $1\,ms$ (green), $10\,ms$ (cyan) and $100\,ms$ (dark red). The bias voltage was set to $50\,V$, the tip-resist distance to $d = 50\,nm$ ($d = 10\,nm$ for the inset (*right*)) and the resist thickness was $d_l = 10\,nm$.

The dependence of w_{ion} on the number of electrons is shown in fig. 10.40 (right). The electron number can be modified by changing the writing velocity v for line patterning or the exposure time τ for dot patterning. As can be seen in fig. 10.40 (right), increasing τ results in an increase of w_{ion}. Thereby, for $\tau \leq 1\,ms$, w_{ion} approaches 0 for $h < d_l$ whereas for $\tau \geq 1\,ms$ an exposure through the complete resist layer depth is obtained for $U = 50\,V$ and $d = 50\,nm$. A direct removal through the complete resist layer can thus be achieved by increasing the exposure time. Furthermore, a sequential ablation process could be possible enabling the exposure through the complete resist layer for small τ. For a sequential ablation process, the experimentally obtained line profile would vary from 0 to the maximal value and effects of the already ablated trench need to be considered to predict the correct pattern shape and line width (see section 10.4.4). However, by tuning the exposure time τ (or writing velocity v) for parameter sets yielding $n_{ion}^{max} \approx n_{crit}$, 3D patterning might be achievable with exposure throughout the complete resist layer.

In contrast, τ has only limited influence on w_{ion} for smaller tip-resist distances as shown in the inset on the right side of fig. 10.40 for $U = 50\,V$ and $d = 10\,nm$. There, after a large drop of w_{ion} in the first part of the resist layer, w remains almost constant with increasing h and τ. As already mentioned, the dominant effect of decreasing d is the strong increase of the amount of electrons n_{tip} emitted from the tip. This leads to an increase of n_{ion} (number of electrons ionizing resist molecules) compared to larger d. Consequently, for a large n_{tip}, n_{ion} can become larger than the threshold value n_{crit} (one electron involved in ionization per $1\,nm^3$) throughout the resist layer. However, the radial distribution of n_{tip} has a Gaussian-like shape and, thus, the shape of $n_{ion}(r)$ can also be assumed to be Gaussian-like due to the limited depth of the resist layer. Therefore, $n_{ion}(r) = n_{crit}$ determining w_{ion}, will be relatively large but not infinity and even slightly increasing with depth h due to the increased spread of electrons. Since the increase of τ only increase the number of electrons but does not affect their distribution, its effect is limited for the case $n_{ion}^{max} \gg n_{crit}$. For a maximal value of n_{ion} close to n_{crit}, an increasing number of electrons by increasing τ leads to a visible effect of w_{ion}. It is a similar behavior than discussed for w without considering the electron interactions within the resist. Since the focus of the implemented model was on the high-resolution limit, the included trajectories were mainly at the tip apex whereas for highest electron numbers emitted from the tip, the number of trajectories at the conical part would need to be increased for more accurate results. However, the found dependencies should not be affected. The largely increased line width w_{ion} determined at the surface might be explained by the backscattered and reentering electrons, which need to be considered for large n_{tip}.

The influence of the bias voltage U (left) and the tip-resist distance d (right) on w_{ion} is shown in fig. 10.41. To extract the influence of U and d without the dominant contribution of the electron number, an adaptive threshold value of $n_{crit} = 1/100\,n_{ion}^{max}$ was used in fig. 10.41. The insets in fig. 10.41 show w_{ion} using a constant threshold value of $n_{crit} = 1\,nm^{-3}$ to include the effect of the

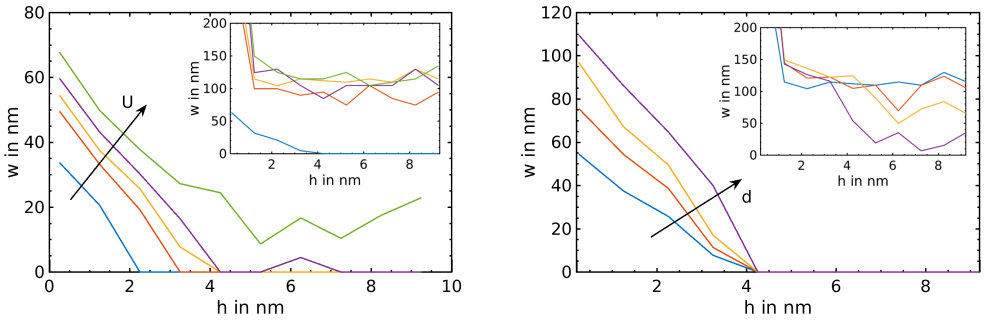

Figure 10.41: Line width w_{ion} in dependence of the depth h for various bias voltages U (*left*) and tip-resist distances d (*right*). An adapted threshold value $n_{crit} = \frac{1}{100}\, n_{ion}^{max}$ was used to extract the effects without the influence of the increased number of electrons. In the insets, the threshold value was kept constant at $1\,nm^{-3}$. (*Left*) The bias voltage was set to $U = 20\,V$ (blue), $40\,V$ (red), $50\,V$ (yellow), $60\,V$ (purple) and $80\,V$ and the tip-sample distance was $d = 10\,nm$. (*Right*) The bias voltage was kept constant at $U = 50\,V$ and the tip-resist distance was varied: $d = 10\,nm$ (blue), $20\,nm$ (red), $30\,nm$ (yellow) and $50\,nm$ (purple). The layer thickness was $d_l = 10\,nm$ and the exposure times were $\tau = 1\,ms$ (*left*) and $\tau = 100\,ns$ (*right*), respectively.

electron number. Increasing U causes an increase of the kinetic energy ϵ_{kin} of the electrons but increases also the electric field E_{tip} at the nanotip and, thus, the emission probability, i. e., n_{tip} and n_{ion}. By using a threshold value n_{crit} related to n_{ion}^{max}, the electric field effects are extracted and only the dependency of ϵ_{kin} on w_{ion} can be observed. On the left-hand side of fig. 10.41, the resulting w_{ion} is plotted and it matches the expectation that an increase of ϵ_{kin} leads to an increased number of ionization events. Thus, the line width w_{ion} and the achievable patterning depth $h|_{w=0}$ increase with increasing $\epsilon_{kin} \propto U$. If a constant threshold of $n_{crit} = 1\,nm^{-3}$ is applied (inset of fig. 10.41), w_{ion} remains constant for increasing w_{ion} because $n_{ion}^{max} \gg n_{crit}$. Only for $U = 20\,V$, w_{ion} is strongly decreased and approaches 0 for increasing h since $n_{ion}^{max} \approx n_{crit}$. On the right-hand side of fig. 10.41, the dependence of w on the distance d between tip and the resist surface is plotted. Without the involved decrease of n_{tip} with d, i. e., using an adaptive threshold value, an increase of w_{ion} is observed without an increase of the patterning depth due to the larger spread of electrons with increased d. However, if n_{tip} is taken into account, an increase of d leads to a decrease of w_{ion} and, thus, the patterning depth. Both values depend on the ratio of n_{crit} and n_{ion}^{max} as discussed at fig. 10.40. The different behavior of $w_{ion}(h)$ shows that a variation of n_{tip} affects w_{ion} more than U and d in the typical range of FE-SPL. Therefore, the behavior of w_{ion} can be explained only by considering the influence of U and d on the number n_{tip} of electrons. The influence of U and d on ϵ_{kin} and electron trajectories can be neglected.

The influence of the resist layer thickness d_l and the cut-off energy ϵ_{co} on the line width w_{ion} is depicted in fig. 10.42. For resist layer thicknesses $d_l < 20\,nm$,

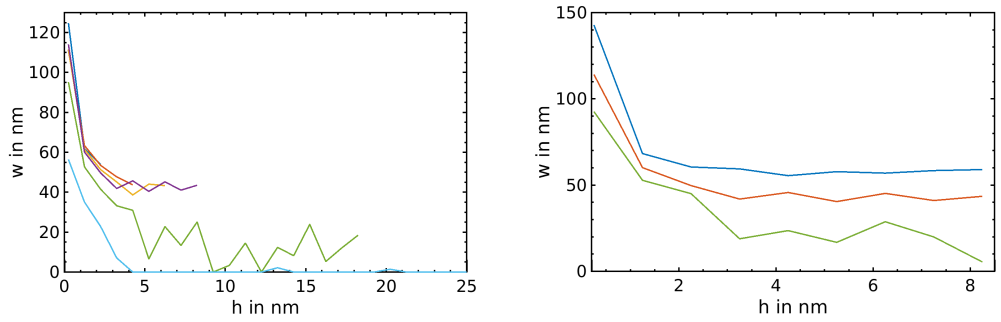

Figure 10.42: Line width w in dependence of depth h for (*left*) various resist layer thickness values: $d_l = 4\,nm$ (blue), $6\,nm$ (red), $8\,nm$ (yellow), $10\,nm$ (purple), $20\,nm$ (green) and $50\,nm$ (cyan) and (*right*) for different cut-off energies $\epsilon_{co} = 5\,eV$ (blue), $10\,eV$ (red) and $15\,eV$ (green). The applied voltage was $U = 50\,V$, the tip-resist distance $d = 10\,nm$ and the exposure time $\tau = 1\,ns$.

the line width w_{ion} distribution is hardly modified by changing d_l. For larger thickness values $d_l \geq 20\,nm$, a rapid decrease of w_{ion} can be observed, which is caused by the reduced electric field E_{tip} at the tip and the reduced kinetic energy ϵ_{kin} at the resist surface (see fig. 10.21). Thereby, the influence of the number n_{tip} of electrons, which depends on the electric field E_{tip}, dominates w_{ion} for increasing resist layer thicknesses.
The cut-off energy ϵ_{co} can be used to differentiate between different molecular bonds (e. g., $C-C$ or $C=C$ in the benzene rings), which are crucial for the ionization process in the resist layer. Thus, ϵ_{co} could be used to simulate different resist materials. However, without including further factors like the distribution of the molecules and their bonds, it only alters the ratio between ionization and excitation events, i. e., $\frac{n_{ion}}{n_{exc}}$. Obviously, a smaller ϵ_{co} yields a higher ionization gain and so w_{ion} increases esp. deep within the resist layer as seen on the right side of fig. 10.42.
As described in section 6.1, two different models for the elastic scattering were used yielding fairly different elastic mean free paths as shown in fig. 10.43 (left). The previously shown results were achieved using the model based on the approximation of the scattering potential as a Wentzel-like potential ("Wentzel model", [126]) with $\lambda < 5\,nm$ for $\epsilon_{kin} \leq 20\,eV$. For the model based on the fitting of different theoretical and experimental data ("fit model"), λ_{el} is in the range from $10\,nm$ to $20\,nm$ (for $\epsilon_{kin} \leq 20\,eV$) (see fig. 10.43 (left)). In this case, no elastic scattering events are expected for $10\,nm$ thick resist layers. In fig. 10.43 (right), the line width obtained by the fit model and the Wentzel model are compared. It is obvious that the differences in w_{ion} from the different elastic scattering models are only minimal (as expected from fig. 10.43 (left)), in agreement to the publication from Seah and Dench, which stated the inelastic scattering is dominant and only a minimal difference should occur if the elastic scattering is completely neglected [133].

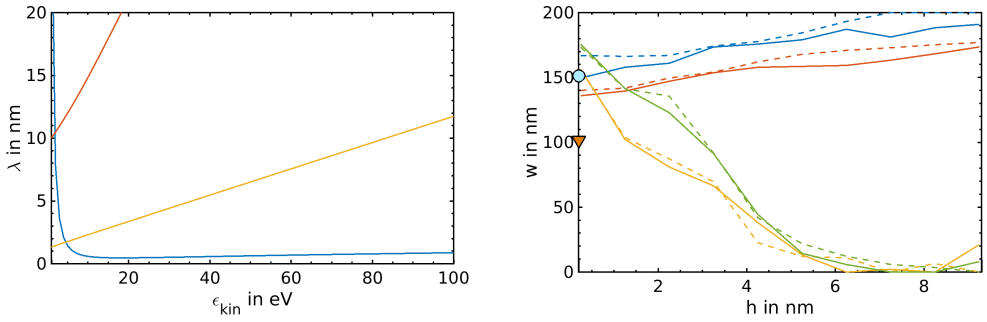

Figure 10.43: (*Left*) Inelastic and elastic mean free paths, λ_{in} (blue curve) and λ_{el} (red and yellow curve) in dependence on the kinetic energy ϵ_{kin} of the electrons. λ_{el} derived from the model using the Wentzel-like potential is plotted as yellow line and from the model using the fitting procedure as red line. (*Right*) Comparison of line width w_J (blue), w_E (red) and w_{ion} (green) determined from the current density, the kinetic energy density inside the resist layer and the ionization event distribution, respectively. The solid lines are used for results obtained with the fit model and the broken ones represent results obtained with the Wentzel model. The applied voltage was $U = 50\,V$, the tip-resist distance $d = 10\,nm$, the exposure time $\tau = 1\,ms$ and the thickness of the resist was $d_l = 10\,nm$.

At the end of this section, some differences related to scattering between electron beam lithogaphy (EBL) and field-emission scanning probe lithography (FE-SPL) will be discussed. These are connected with energy transfer from the primary electrons into the resist layer. In fig. 10.44, electron trajectories for EBL [175] obtained from a Monte Carlo simulation are depicted. Thereby, a $100\,nm$ thick calixarene resist layer on top of a silicon substrate was used [175]. These can be qualitatively compared to the trajectories calculated for the FE-SPL case using a $10\,nm$ thick calixarene resist, shown in fig. 10.33. Obviously, the $30\,keV$ electrons used in the simulation of the EBL case have a very long mean free path and travel far into the silicon substrate. There, only a weak broadening within the $100\,nm$ thick resist layer occurs. In contrast, the low-energy electrons ($\epsilon_{kin} < 50\,eV$ in fig. 10.33) in the FE-SPL case have an inelastic mean free path below $1\,nm$ and are scattered multiple times in the first few nanometers of the resist layer. Hence, the energy dissipation occurs mainly in resist layer and the sample remains nearly free of damages due to the electron exposure in FE-SPL. On the contrary for EBL, where most of the inelastic scattering occurs deep in the sample, which can lead to unintended sample damage. Additionally, backscattering and re-entry of electrons can be seen in the FE-SPL case, which are not included in fig. 10.44 for the EBL case [175]. However, the electrons, which are backscattered in the substrate, contribute strongly to the patterning in EBL, which results in double Gaussian profiles of patterned lines [32]. For EBL, re-entry of electrons is negligible, since there is no attractive electric field for the electrons towards the sample. Thus, in EBL, the beam diameter and backscattering of electrons from the substrate mainly determine the resolutions capabilities while in FE-SPL inelastic

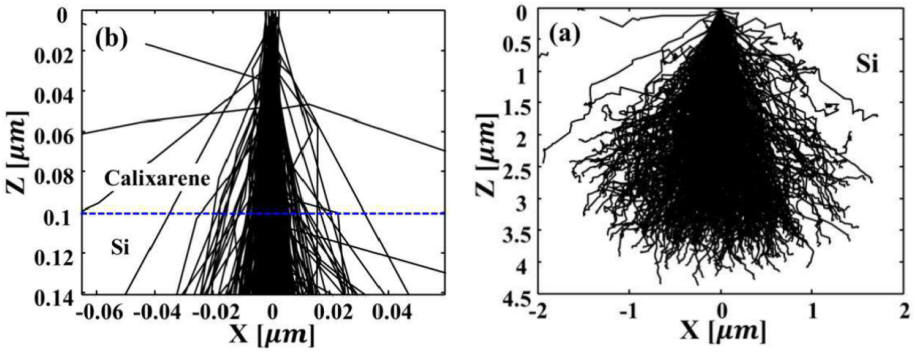

Figure 10.44: Trajectories calculated for EBL for calixarene resist layer, taken from Zhang et al. [175]. The trajectories within the resist layer are shown (*left*) together with the complete trajectories (*right*). An electron beam with $30\,keV$, a Gaussian beam diameter of $2\,nm$ and a resist thickness of $100\,nm$ were used.

scattering within the resist and partly the re-entry of electrons backscattered at the resist surface are the dominant processes. This can be also deduced when considering the average energy loss transfer from electrons to the resist material.

In the left-hand side of fig. 10.45, the averaged electron energy loss density distribution $\langle d\epsilon \rangle$ for ionization events is shown and on the right-hand side, the electron deposition distribution (EDD) for EBL (taken from [175]). It can be seen that the highest energy loss density (plotted on a logarithmic scale) is within $4\,nm$ for FE-SPL with a large decrease in magnitude and a decrease in width for increasing resist depth h. In contrast for EBL, the maximum of EDD remains nearly constant while the horizontal width of EDD increases with h. As a consequence, the patterned features using FE-SPL might have a V-shape whereas the EBL written features might be broader at the bottom of the resist layer. This is caused by the different direction of the patterning, since for EBL the patterning is mostly done by the electrons backscattered from the sample, which have an energy $\epsilon_{kin} \in [10, 100]\,eV$. In FE-SPL, the incident electrons are responsible for the patterning. These have similar energies like the backscattered electrons in the EBL case. The V-shape of lines in FE-SPL can be used also to enhance resolution. Therefore, patterns should be written with parameters for which w_{ion} approaches almost 0 for $h = d_l$. Then, this small resist opening can be used for pattern transfer. It was shown already very thin resist films, as used in FE-SPl, are sufficient to enable pattern transfer into silicon by cryogenic reactive ion etching [69]. Additionally, by using a hard mask, a pattern transfer with even higher aspect ratios can be achieved. The amplitude of the energy loss in FE-SPL is much higher than for the electron deposition distribution in EBL, which should result in more effective patterning, i. e., a smaller exposure dose should yield similar pattern results. However, exposure doses for the same resists are often higher for FE-SPL than for EBL [70]. It was discussed by Wilder et al. [32] that this is probably a

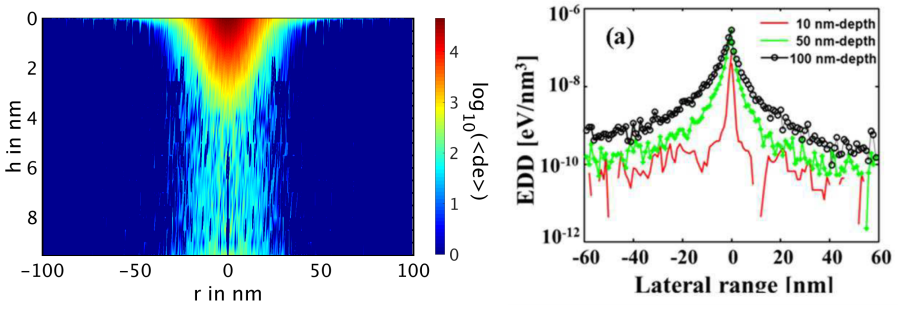

Figure 10.45: Comparison of the averaged electron loss density distribution $\langle de \rangle$ of a $10\,nm$ thick calixarene layer and the electron deposition distribution (EDD) taken from Zhang et al. [175] for a $100\,nm$ thick calixarene layer. For both distributions the logarithm to the basis of 10 are used. (*Left*) The applied voltage was set to $U = 50\,V$, the tip-resist distance $d = 10\,nm$, the exposure time to $\tau = 1\,ns$ and the thickness of the resist was $d_l = 10\,nm$. (*Right*) An electron beam with $30\,keV$, a Gaussian beam diameter of $2\,nm$ and a resist thickness of $100\,nm$ were used.

result of different reaction pathways addressed by FE-SPL compared to EBL. However, in EBL the resist layer is double exposed by the primary electrons and by the backscattered electrons, which involves completely different energy ranges (keV and eV) and due to the large electron densities, excitation events might additionally affect the available ionization processes.
Summarizing this section, the results of the Monte Carlo simulation of electron scattering in ultrathin ($d_l \leq 50\,nm$) resist layers were presented for electron exposure in the FE-SPL case. It was shown, that in contrast to EBL, the inelastic scattering will occur mostly within the first few nanometers of the resist layer and that the number of emitted electrons mainly influence the patterning. However, backscattering and re-entry can affect the patterning at the resist surface and can yield to a broadening of structures, resulting in a V-shape of patterns, which can be used for resolution improvements as discussed above. In dependence of the parameters, i. e., $n_{ion}^{max} \gg n_{crit}$ almost perpendicular side walls can be obtained[9]. Thereby, backscattering and re-entry have a visible effect on the electron distribution at the resist surface for small tip-resist distances d whereas for larger distances this influence becomes negligible. The expected acceleration of the electrons within the resist due to the applied electric field was only approximately $1\,eV$ and could thus not compensate the energy transfer in inelastic scatterings. Despite the localization of the ionization events, excitation occurs throughout the resist layer. This might infuence the cross-linking process if it is associated with excitations rather than ionizations.
The expectation, that the inelastic and elastic scattering increases the width of the electron distribution and, thus, the line width w_{ion} was confirmed at

[9] Neglecting the first part of the resist layer

the resist surface and for $n_{ion}^{max} \gg n_{crit}$. However, w_{ion} depends on the number of ionization events, which are thought to underlie the removal or cross-linking process of molecules. This number can also decrease within the resist if $n_{ion}^{max} \approx n_{crit}$ and thus an decrease of w_{ion} occurs. Nevertheless, the overall electron number should be increasing inside the resist due to inelastic scattering events, associated with ionization of a resist molecules but this larger number of electrons does not result always in larger number of ionizations due to the accompanied energy loss. The line width w_{ion} is dominated by inelastic scattering processes leading to ionization of resist molecules and the influence of elastic scattering events onto the line width is negligible as expected by Dobisz et al. [22].

Chapter 11

Conclusion and summary

The main purpose of the thesis was to derive a model for field-emission scanning probe lithography (FE-SPL), which enables the study of the influence of various parameters on the lithographic process and predict the FE-SPL outcome and optimal parameters. There are a lot of experimental studies demonstrating the successful application of FE-SPL [9–13, 32, 43, 69, 70, 75, 76, 118, 119, 176, 177] ranging from sub-10 nm single line features [2, 10] to single dopant-atom quantum-dot transistors working at room-temperature [178]. However, no comprehensive theoretical model existed describing the dominant influences on field emission and resist patterning. Optimal parameters for patterning with a certain tip had to be deduced from experiments, so-called exposure dose tests, with the potential risk of tip wear and damage. These tests have to be repeated for each new tip.
In this work, a numerical model was developed consisting of the computation of the electric field based on the finite-element method (section 8.1), which was used to obtain the field-emission current density (section 5.2) from the Fowler-Nordheim theory (section 3.2) and the trajectories of the emitted electrons by an one-step Leapfrog algorithm (section 5.3) to determine the distributions of electron number and velocity. This part of the numerical model, called nanolithography program (see section 5), included furthermore the effects of a (structured and unstructured) resist layer. Taking the influence of the resist properties into account (using the nanolithography program) was not reported so far. Previous publications only include the resist influence in certain parts, e. g., Wilder et al. did not calculate the electron's trajectories [75] and Dobisz et al. used the emission only from one emission spot exactly at the tip apex [22, 23] whereas Mayer et al. [77] neglected the resist layer at all. Additionally, a Monte Carlo simulation (chapter 6) was implemented to study interactions between incident electrons and resist molecules (section 10.4.5). This is the first study, which investigates the effects of electron scattering within an ultrathin resist layer ($\leq 50\,nm$) considering the electric field distribution and using the number and energy distributions of field-emitted electrons from sharp nanotips as the initial condition for the computation [2]. Therewith, a comprehensive numerical model for FE-SPL (under vacuum conditions) was developed.

To gain a deeper understanding and to reduce the computational efforts, an analytical model was derived from the numerically obtained results. It includes an expression for the maximal field enhancement factor (section 8.1.2), which could not be described correctly by existing models [78, 80, 83, 85–87, 89, 90, 114, 166] for the parameter range (tip size, tip-sample distance) typically used in FE-SPL. Additionally, the field enhancement distribution was introduced enabling a complete description of the electric field at the sharp emission tip (section 8.1.3). Based on the electric field, the field-emission current density distribution is calculated using the well-known Fowler-Nordheim equation [94, 95] (section 3.2). To obtain the current density distribution at the sample or at the resist surface, the ratio between emission area at the tip and exposure area at the sample/resist was modelled using straight lines starting perpendicular at the tip surface (section 8.2) and a weighting factor (section 8.2.1). It was shown, that the electric field lines are not a good measure for the trajectories of the electrons (see fig. 8.8), in contrast to the assumption of Wilder et al. [75]. The inclusion of the unstructured resist layer into the analytical model was achieved within this thesis (section 10.4) as well.
The results of the analytical model agree well with the results obtained by numerical simulations done with the nanolithography program and, thus, the model can be used to predict the numerical results with a strongly reduced computational effort and time. This might allow an implementation of the analytical model in the FE-SPL software to enable a prediction of the structures to be written and optimal parameters for a certain tip.
Furthermore, the analytical model was experimentally verified by (*i*) field-emission experiments done under vacuum conditions [169] and (*ii*) FE-SPL experiments under ambient conditions. A special set-up of an AFMinSEM tool [60,61] within a dual-beam (SEM and FIB) analysis tool was applied [169] for the first comparison. The experimentally obtained data were fully described using the analytical model and the quantitative comparison yielded a valuable estimate of the tip-resist distance. To enable the quantitative comparison, a correction for the drift of the FE-SPL system and for the growth of structures on the sample surface, respectively, had to be included in the analytical model. Thus, the analytical model can be used to determine the drift of the tip-sample distance in a FE-SPL tool using only the measurement of the current signal and scanner movement during tip approach in lithography mode. Regarding the comparison with FE-SPL experiments, the analytical model can reproduce the dependence of the line width on the applied bias voltage (section 10.2.2) and on the exposure dose, for which the total current was varied.
The analytical and the numerical model can be used to answer the three questions raised in the introduction.
First, existence of a resolution limit:
Based on the results of the numerical and the analytical model for the nanolithography part, there is no resolution limit, if the assumption of a threshold value is used. From the Monte Carlo simulation, it is found that even by including scattering in the resist layer, there exists also no resolution limit since a threshold value exists (at least one primary electron is needed for a successful

ionization process) as well. However, the line width at the resist surface is affected by secondary electron generation and electrons, which are backscattered and re-enter the resist layer. The line width is enlarged at the resist surface due to backscattering/re-entry. Note, that the question of the existence of a resolution limit is only answered within the assumptions of the presented models. However, the size of the molecules, the de Broglie wave length of the electrons and the involved chemical reactions need to be considered as well.

Second, finding optimized parameter sets:

It was shown in chapter 10 that the influence of the intrinsic tip parameters (tip radius, work function and opening angle) can be compensated by adjusting the external parameters (bias voltage, tip-resist distance and writing velocity or exposure time). Thus, fabrication tolerances for tip and resist layers are not limiting the FE-SPL performance. The strongest influence on the current density distribution and, thus, on the line width is caused by the bias voltage and the tip-sample or tip-resist distance. The bias voltage should be set at first in experimental optimization procedures since the tip-sample distance is affected if U is changed in constant-current mode. Afterwards, the tip-resist distance (or the current set point) should be adjusted. In a typical FE-SPL tool, the bias voltage and the current are kept constant. Thus, the tip-sample distance is varied to keep the current constant but its absolute value is not known. With the analytical model, the tip-sample distance can be easily determined using only the $I(d_{rel})$ measurements during the approach of the tip to the sample (section 9.2). At last, the writing velocity or the exposure time can be used to refine the line width. Using this order to set the external parameters, the optimal line width should be obtainable from parameter-testing experiments. However, the procedure can be further simplified if a well-defined tip is used, i. e., tip radius and material are known. By knowing the tip parameters and setting the bias voltage, only the tip-resist distance is undefined, which can be easily found by the analytical model. The pattern properties can be refined experimentally using the writing velocity. Therefore, the experimental procedure to find an optimal parameter set can be simplified using the presented model and if the tip radius is known, the optimal parameter set can be found analytically.

In the appendix B, two different tip designs to increase the resolution of FE-SPL for a certain parameter set, namely volcano-gated tips and partially covered tips, were numerically investigated and the requirements for a successful application were presented.

Third, understanding the physics:

The emission process described by standard Fowler-Nordheim theory does not need to be refined for the FE-SPL case, i. e., no quantum confinement of tip electron states [117] or geometric effects on image charge and Fowler-Nordheim equation [110–112, 115, 116] were necessary to achieve the quantitative agreement with experiments. The relation to describe the dependence of the resist layer on top of the sample on the electric field was not reported previously, which could also be used for thicker resist layers.

Additionally, it was found by the investigations using structured resist layer

that positive-tone lithography and direct ablation seem to be self-limited whereas negative-tone lithography might be self-accelerated. The comparison with the analytical model (for unstructured resist) showed that this behavior is caused by the variations of the field-enhancement factor at the tip surface. Unfortunately, a quantitative comparison with FE-SPL experiments could not be accomplished, since in the experiments some of the tip (e. g., radius) and external parameters (e. g., tip-sample distance) are unknown. Thus, a reliable comparison was not achieved because various parameter sets can yield the same result regarding the line width and resolution. Additional influences like a water film on top of the resist/sample surface might not be negligible in ambient conditions. Despite the result of Dobisz et al. [22, 23] of a negligible effect of an (unchanged) water film on the electrostatic potential, a water film might yield to additional changes. The film might form an (incomplete) water meniscus leading to a different electrostatic potential, water molecules might be ionized during the exposure with electrons affecting the scattering cross sections and the electric field due to a space charge effect. Furthermore, water molecules might enable a variety of chemical reactions due to their reactivity, esp. if they are ionized. The influence of the water molecules might not be limited to the resist surface because the molecules can also penetrate into the resist layer. Nevertheless, the qualitative agreement between experiments under ambient conditions and the analytical model indicates that the influence of the water film might be not important for the resolution.

To enable a quantitative comparison between experiment and theory, FE-SPL experiments under vacuum conditions (combined with the determination of tip radius and tip-resist distance) similar to the field-emission experiments (section 9.2) should be executed to confirm and improve the theoretical model. Dependent on the outcome of the comparison with FE-SPL experiments under vacuum conditions, a subsequent theoretical and experimental investigation should be focused on the influences of the water film, since it is thought to be an important influence (e. g., direct ablation is only observed under ambient conditions) and its effects are not yet completely understood.

The integration of the analytical model into FE-SPL tools will likely increase the reproducibility and resolution capabilities. Additionally, it will reduce the time to find optimal parameters experimentally after tip exchange or even allows the prediction of optimal parameters if the tip radius is known.

The model could be also used for STM tools to access the tip radius, which is not accessible in tunneling mode. The determination of the tip radius is possible by applying the field-emission mode and the analytical model since the tip-sample distance is measurable in STM tools (using sharp wires instead of cantilevers).

Appendix A

Estimation of electronic mean free path in air

Based on the mean free path of air molecules λ_M the electronic mean free path is approximately $\lambda_e \approx 5.6\,\lambda_M$. The collision cross section σ_M for molecules in the hard sphere approximation is $\sigma_M \approx \pi(r_1^2 + r_2^2)$ for molecules with radii r_1 and r_2. For identical molecules ($r = r_1 = r_2$) we get $\sigma_M \approx 4\pi r^2$ and for scattering between an electron and a molecule with $r_e << r$ the cross section is equal to $\sigma_e \approx \pi(r^2 + r_e^2) \approx \pi r^2$. Thus, the ratio between molecular and electronic collision cross section is $\frac{\sigma_M}{\sigma_e} = 4$. The mean free path of molecules is calculated by the distance of a molecule between two scattering events ($d = \overline{v}\,\tau$) divided by product of the interaction volume ($V_i \approx \sigma_M\, d_r = \sigma_M\, \overline{v}_r\, \tau$) times the number of molecules per unit volume n_V, i. e

$$\lambda_M = \frac{\overline{v}\,\tau}{\sigma_M\, \overline{v}_r\, \tau\, n_V}\,. \tag{A.0.1}$$

Here, $\overline{v}$ is the mean velocity of a molecule and $\overline{v}_r = \sqrt{\overline{v}_1^2 + \overline{v}_2^2}$ the mean relative velocity between the molecules. For identical molecules ($\overline{v} = \overline{v}_1 = \overline{v}_2$) it becomes to $\overline{v}_r = \sqrt{2}\,\overline{v}$. The duration between two scattering events is τ. Therefore, the molecular mean free path can be estimated by

$$\lambda_M = \frac{1}{\sqrt{2}\,\sigma_M\, n_V}\,. \tag{A.0.2}$$

For the electrons the molecular velocity can be neglected ($\overline{v}_e >> \overline{v}$) and so the relative velocity is equal to $\overline{v}_r = \overline{v}_e$. This leads to an electronic mean free path of

$$\lambda_e = \frac{\overline{v}_e\,\tau}{\sigma_e\, \overline{v}_e\, \tau\, n_V} = \frac{1}{\sigma_e\, n_V}\,. \tag{A.0.3}$$

The ratio between λ_e and λ_M equals

$$\frac{\lambda_e}{\lambda_M} = \frac{\sqrt{2}\,\sigma_M\, n_V}{\sigma_e\, \tau\, n_V} = 4\sqrt{2} \approx 5.6\,, \tag{A.0.4}$$

which is the value found in the beginning.

Appendix B

Strategies to increase the resolution

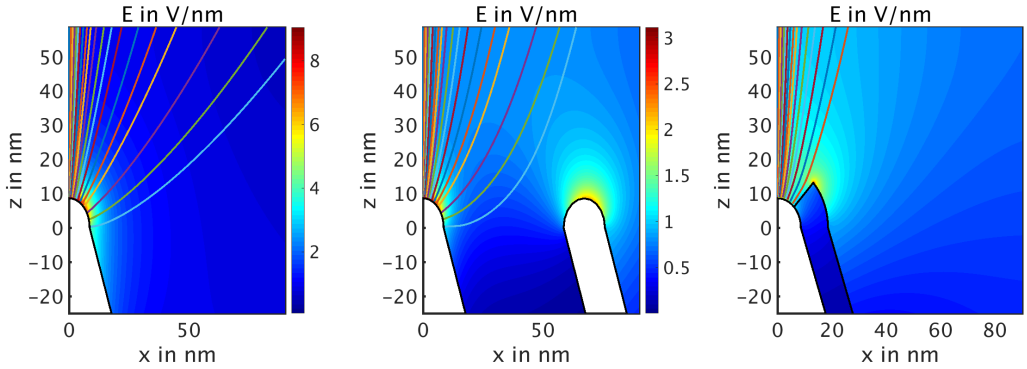

Figure B.1: Comparison of the different tip designs to increase the localisation of the electron density distribution. The electric field strength is shown as color code and the electronic trajectories as colored lines. Black lines are guide for the eyes to distinguish the geometries. On the left side the standard model is shown, in the middle the model including a volcano gate and on the right the partially covered tip.

In this section, the studies about two possible routes to increase the electron density distribution on the sample surface, which are based on changing the tip design are described. On the one hand, nanotips surrounded by a so-called volcano gate are considered. On the other hand, nanotips covered with a thin layer are investigated. Thereby, the material of the layer is expected to have a lower electron emission probability, i. e., a higher work function. It is expected that this partial cover increases the focusing. The two models and the conventional lithography model are shown in fig. B.1. The situation in fig. B.1 is idealized and represents the desired effect of the volcano gate and the partially covered tip. As will be shown in section B.1 and is already visible in fig. B.1, the field emission from the gate is crucial for the successful focusing (increase localisation) of the electron density distribution at the sample surface in the case of the volcano-gated tip. For the partially covered tip, the emission

Table B.1: Simulation parameters, their description and their standard values for the volcano-gate simulations. The values given here are complementary to the ones given in tab. 4.1. The electric potential of the tip, gate and sample are φ_t, φ_v and φ_s, respectively. The standard values given here are used if not explicitely stated.

Parameter	Description	Standard value
d_v	thickness volcano gate	$17\,nm$
h_v	height difference between gate and tip (pos. values for buried tips)	$0\,nm$
l_v	distance between tip and gate	$50\,nm$
Φ_v	Gate work function	$4.8\,eV$
$U = \varphi_s - \varphi_t$	Bias voltage between tip and sample	$50\,V$
$U_v = \varphi_s - \varphi_v$	Bias voltage between gate and sample	$60\,V$

through the layer is not completely prevented, which is described in section B.2. However, possible electron emission from the dielectric layer itself is neglected due to the low-density of free electrons in insulating materials.

B.1 Focusing and defocusing using a volcano gate

The idea behind adding a volcano gate is that by changing the potential at the gate, one can switch between focusing and defocusing of the electron beam due to the modification of the electric field. This would allow to write high-resolution features and to expose large patterns rapidly, respectively. The results shown in this section were published in ref. [20]. The calculation model is depicted in fig. 4.3 and B.1 (middle). The parameter definitions as well as the standard values are given in table B.1. The first part of this study is targeted answering the question, if a focusing / defocusing effect for the electron beam could be achieved. Therefore, we neglect the emission from the volcano gate. Depending on the height difference h_v and the voltage ratio between volcano gate U_v and tip U_t a focusing and defocusing effect of the electron trajectories is obtained, even if the distance between the tip and sample is only tens of nanometers as shown in fig. B.2 (a) and (b), respectively. Thereby, both figures are only differing in the applied volcano gate voltage ((a) $U_v = -20\,V$ and (b) $-100\,V$). In fig. B.2, the tip-gate height was varied from $h_v = -20\,nm$ (protruded tip) to $+20\,nm$ (buried tip). In the case, for which the gate voltage U_v is smaller than the tip voltage U_t, a defocusing occurs since the electrons are affected by the attractive force towards the gate. A focusing occurs if $U_v > U_t$ due to the repulsive gate potential. As can be seen from fig. B.2, the height difference is a crucial parameter. It determines the area, in which the electrons are significantly influenced by the gate potential. For example, in fig. B.2 (left), the smaller the height difference the stronger is the defocusing, i. e., strongest for buried tips. Additionally, the electron emission probability shifts from the tip apex to the tip sides (not shown). In contrast, the larger

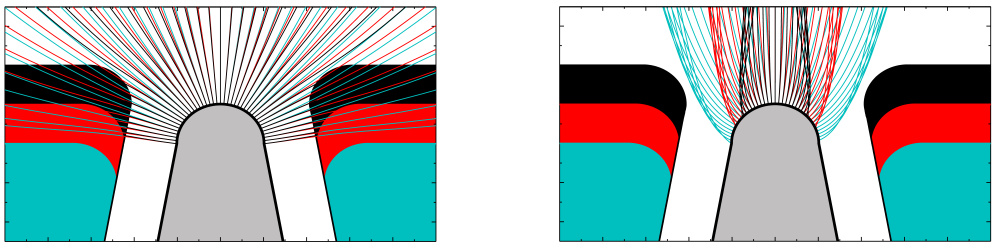

Figure B.2: Calculated electron trajectories for different cases: $U_v < U_t$ (defocusing, *left*), and $U_v > U_t$ (focusing, *right*) for three different height differences $h_v = -20\,nm$ (cyan $\rightarrow$ buried tip), $0\,nm$ (red), $20\,nm$ (black$\rightarrow$protruded tip). The bias voltage was fixed to $U_t = 80\,V$ and the volcano voltages were $U_v = 20\,V$ (*left*) and $100\,V$ (*right*). The tip-gate distance and the tip-sample distance were set to $l_v = 25\,nm$ and $d = 50\,nm$, respectively.

the height difference the stronger is the focusing (see fig. B.2 (right)), i. e., strongest for protruded tips. Thus, different heights h_v for optimal focusing and defocusing are found. To achieve the best of both effects (in order to carry out a focusing as well as defocusing depending on the lithographic application), a tip height of $h_v = 0\,nm$ is favorable. Scattering at the volcano gate would occur for positive height differences in the defocusing case, which is not included in the calculation and would induce a variety of the different scattering scenarios (elastic, inelastic scattering, mechanical damaging, heating, etc.). In this case, the trajectories of the electrons hitting the gate were only computed until they reached the gate surface.

After the proof of a focusing and a defocusing effect, the influence of the volcano gate is quantified and analyzed in order to optimize the design as well as the lithography settings. Considering the electric field, a maximum at the tip was found, which reaches several V/nm. This is expected by the lightning rod effect [80,82] and responsible for the confined electron emission [179]. However, also local maxima of the electric field occur at the gate, which can even exceed the tip field strength for some parameter settings. The emission of electrons from those gate spots is investigated because patterning of wider structures would occur. Since the defocusing is not affected by this parasitic gate emission (attractive potential at the gate), the case of focusing is investigated in more detail. In fig. B.3 (left), the current density distribution J at the sample surface is shown for the focusing regime with parasitic gate emission. Here, the maxima of the gate and the tip emission are nearly identical. It is obvious that a generated line pattern will originate from both emission sites, tip and gate ring. Thus, it is reasonable for high-resolution patterning to define the criteria that the gate emission has to be considerably lower than tip emission. In order to reduce the gate emission, the work function of the volcano material was varied. In fig. B.3 (right), the total emission current I is shown in dependence of the tip-sample distance calculated for different work functions Φ_v of the gate. In case of $\Phi_v < \Phi_t$, the total emission current is strongly enhanced

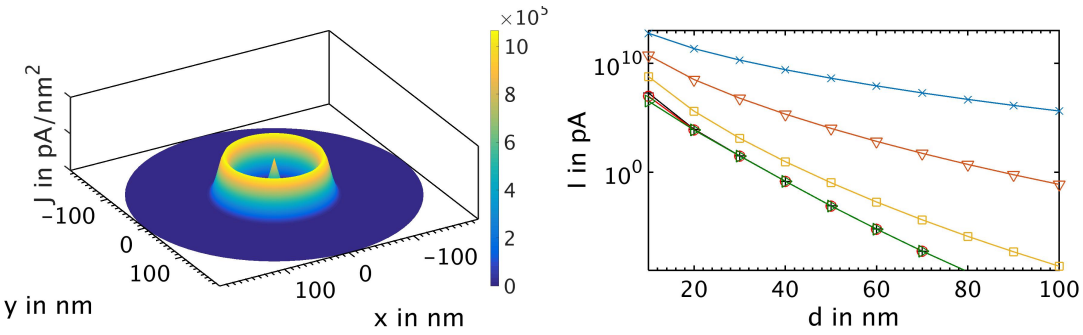

Figure B.3: (a) Example of a current density distribution at the sample surface emitted from a volcano-gated probe. A high emission contribution from the gate for a tip-sample distance $d = 10\,nm$ is present. (b) Total emission current at the sample for different tip-sample distances d and different gate work functions is calculated for $\Phi_v = 2\,eV$ (blue X), $3\,eV$ (brown $\bigtriangledown$), $4\,eV$ (yellow $\square$), $4.8\,eV$ (black $+$), $5\,eV$ (red $\bigcirc$) and $6\,eV$ (green $\triangleright$).

as seen for $\Phi_v = 2\,eV$ to $4\,eV$. Here, the gate emission term dominates the total emission current of the volcano-gated nanotips. In contrast, for $\Phi_v > \Phi_t$ the total emission current is similar for different work functions indicating that the parasitic gate emission is negligible. Only for small tip-sample distances, an unexpected increase of the emission current is observed if the work function of the gate $\Phi_v \rightarrow \Phi_t$. This indicates that the emission coming from the gate increases faster with decreasing tip-sample distance than the tip emission. To summarize, this part shows that the work function Φ_v of the gate needs to be higher than the tip work function Φ_t in order to prevent a parasitic gate emission. Thereby, changing the gate work function alters only the gate emission but not the tip emission probability. The following results were calculated using a gate work function of $\Phi_v = 4.8\,eV$.

Next the influence of the gate height onto the patterning including the parasitic gate emission is studied. As shown in fig. B.2, the gate height h_v changes the focusing or defocusing effect of the gate, respectively. The maxima of the electron emission current density distribution J_{max} as function of the tip-gate height h_v is plotted in fig. B.4 (left) for tip-sample distances of $d = 20\,nm$ (broken lines) and $100\,nm$ (lines). For $d = 20\,nm$ (black broken lines), the tip emission ($\bigcirc$) is not significantly altered by changes of h_v, whereas the gate emission ($\triangle$) increases, if the tip is buried ($h_v > 0$). In contrast, for $d = 100\,nm$ (red solid lines), the tip emission ($\bigcirc$) is strongly affected by h_v due to the change of the electric field at the tip, whereas the gate emission ($\triangle$) is only moderately increased. To conclude, for $h_v \leq 0\,nm$ and for relatively large tip-sample distances ($d \geq 40\,nm$), the tip emission term dominates the total emission current density. However, to enable also a defocusing effect $h_v = 0\,nm$ was chosen for further investigations.

The influence of the bias voltage and the tip-sample distance on the tip ($\bigcirc$) and gate ($\triangle$) emission current maxima J_{max} is shown in fig. B.4 (right). The bias voltage is set to $U_t = 10\,V$ (blue dotted lines), $30\,V$ (magenta broken

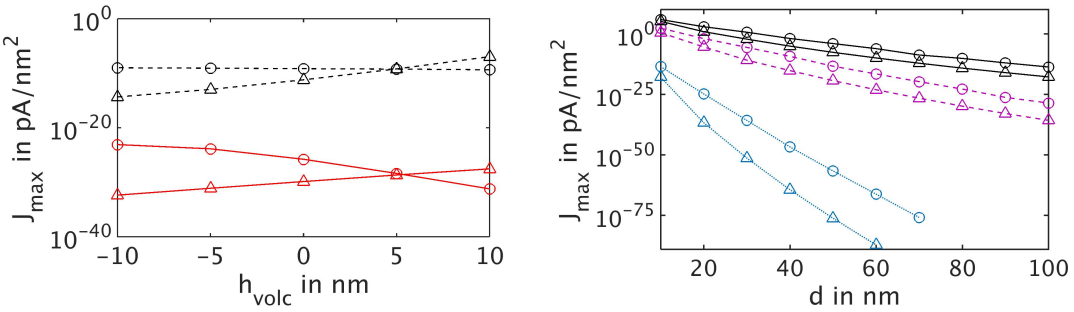

Figure B.4: (*Left*) Maxima of the tip (◯) and the gate (△) current density distribution at the sample surface as function of the gate height h_v related to the tip apex plotted for different tip-sample distances $d = 20\,nm$ (broken lines) and $d = 100\,nm$ (solid lines). (*Right*) Maxima of tip (◯) and gate (△) emission current density at the sample surface for different distances and tip voltages $U_t = 10\,V$ (blue dotted lines), $30\,V$ (magenta broken lines) and $50\,V$ (black solid lines). The bias voltage ratio was set to $U_v/U_t = 1$.

lines) and $50\,V$ (black solid lines), respectively. An enhancement of the lightning rod effect and, thus, higher local electric field strengths are expected for higher voltages. The increase of the maxima of the tip and gate current distribution with increasing bias voltages supports this assumption. Notably, despite the similarity of the dependency of the tip and gate emission on the tip sample distance for large d, in case of smaller d the behavior is slightly changing. Here, the gate emission increases faster than the tip emission with decreasing distances, which proves our interpretation of fig. B.3 (b). Thus for the application of volcano-gated nanotips, they might work better for larger tip-sample distances.
The influence of the volcano-gate voltage on the total current and the line

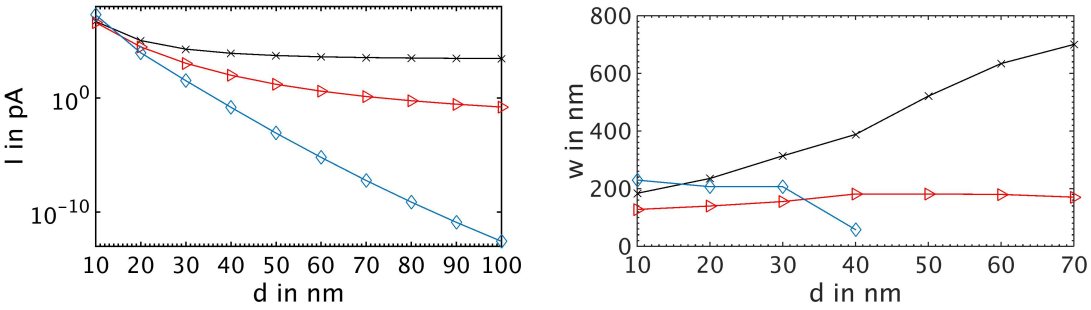

Figure B.5: Dependency of the total current I (*left*) and the line width w (*right*) on the tip-sample distance plotted for different volcano gate voltages of $U_v = 0\,V$ (black X), $25\,V$ (red ▷) and $50\,V$ (blue ♢). The bias gate voltage was set to $50\,V$.

width is depicted in fig. B.5. In both graphs, the same markers and line colors

are used, i. e., $U_v = 0\,V$ (black X), $25\,V$ (red $\triangle$) and $50\,V$ (blue $\diamondsuit$). The emission current is decreased for increasing distances since the electric field is reduced (see fig. B.5 (left)). Furthermore, an increasing gate voltage results in a reduction of the current. This can be explained by an additional decrease of the electric field strength at the tip caused by the potential at the gate for $0 < U_v < U_t$. This effect becomes negligible for small tip-sample distances. The opposite behavior, i. e., increasing current with increasing gate voltage, is obtained for $U_v > U_t$, since the gate contribution becomes dominant (not shown).

The dependence of the line width w on the tip-sample distance and the applied volcano gate voltage is seen in fig. B.5 (right). The tip speed was set to $1\,\mu m/s$, which is a typical value used in experiments. To determine the line width a threshold value of $100\,\text{electrons}/nm^2$ for the direct removal was used. It can be seen in fig. B.5 (right), that the behavior differs from the observations for the total current (Fig B.5 (left)). As seen in fig. B.5 (right), different regimes for the line width w are obtained. For $U_v = 0\,V$ (X), the line width w increases with larger tip-sample distances. This can be explained by the broadening of the current density distribution with increasing distance. For $U_v = 0\,V$ and tip-sample distances above $80\,nm$, the line width estimation is not reasonable due to the limitation of the simulation box ($r = 250\,nm$). For $U_v = 25\,V$, i. e., $U_v/U_t = 1/2$, ($\triangleright$), w increases with increased distance, as for $U_v = 0\,V$ (X), but with a much smaller slope. The decreased slope is caused by the lower electric field at the tip apex due to the changed potential landscape. At $d = 40\,nm$, the behavior changes and a slight decrease of w with d is observed. In this case, the electron density is in the range of the threshold value. Thus, a decrease of the electron density with increasing distance becomes dominant resulting in a decreasing line width. The behavior of the curve ($\diamondsuit$) representing $U_v = 50\,V$, i. e. $U_v/U_t = 1$, can be divided into two regimes. For distances up to $d = 30\,nm$ the line width is determined by the emission from the volcano gate. For $d = 10\,nm$ the linewidth is approximately $50\,nm$ wider in comparison to the obtained values without an applied volcano gate bias (X). The electron density (not shown) drops significantly, but the line width remains nearly constant. Here, the volcano gate emission decreases faster with increasing distance than the tip emission. As a result, the electron density emitted from the volcano gate does not exceed the threshold, for $d > 40\,nm$. In turn, the drop of the line width for a distance of $40\,nm$ is observed. The focusing effect of the volcano gate, combined with the decrease of the electron density, leads to a minimal line width value of $d = 58\,nm$, which is less than a third of the value achieved with $U_v = 0\,V$ at the closest tip-sample distance. This proves that a focusing effect is obtained, even if a gate emission is taken into account.

It has to be noted that the thickness of the gate and the tip-gate distance do not affect the focusing behavior. However, in case of an emission from the gate, as indicated by fig. B.5 (b), the line width is strongly influenced by both parameters.

In summary, a focusing and a defocusing effect can be observed, but the effects

of the parasitic gate emission often dominate.

B.2 Partially covered tips

In this section, the results of partially covered tips to increase the localisation of the electron density distribution are shown. By covering the tip with a dielectric layer, the emission probability from the tip should be decreased. A partially opening of the cover layer might yield to a localisation of the electron emission only to the uncovered part of the tip. In my first attempt presented here, I neglected the emission from the layer itself due to the assumption of a higher work function and the low density of free electrons in an insulator.
The geometrical model is shown in fig. 4.3. The parameter d_{loc} describes the thickness of the layer and ξ the (half) angle of the opening in the cover layer. Additionally, the dielectric constant ε_{loc} is varied from 2 to 10.

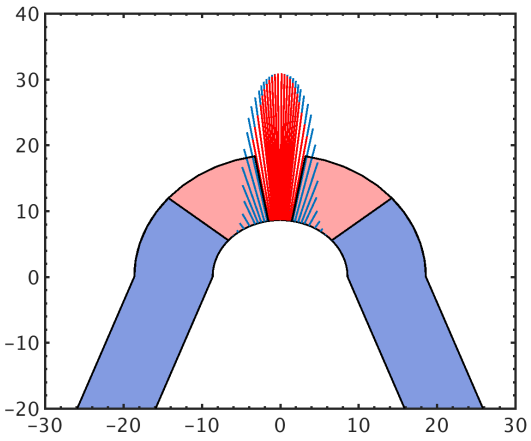

Figure B.6: Focussing of the electron emission density distribution at the tip by different openings in the cover layer. The used parameters are: $U = 90\,V$, $d = 30\,nm$, $d_{loc} = 10\,nm$ and $\varepsilon_{loc} = 3.9$. The blue opening angle ξ is 45° and the red one 5°. The blue and the red colored electron emission density distribution belongs to the blue and red colored cover layers, respectively.

At first, the effects of the cover layer on the current density distribution at the tip and at the sample are investigated and it will be studied if a local decrease of the current density could be achieved. In fig. B.6, the (scaled) electron emission probability distribution is shown for two different openings in the cover layer. These are the two opening angles $\xi = 45°$ (blue) and 5° (red). It can be seen that the emission probability is a little bit narrower for the smaller opening angle, but unfortunately the effect is not as strong as expected.
However, the aim of the partially covered tips is the increase of resolution, i. e., the decrease of the line width at the sample. Therefore, the electron trajectories were computed to estimate the line width using the threshold

value of 100 electrons per $1\,nm^2$ for positive-tone lithography (see section 5.2).

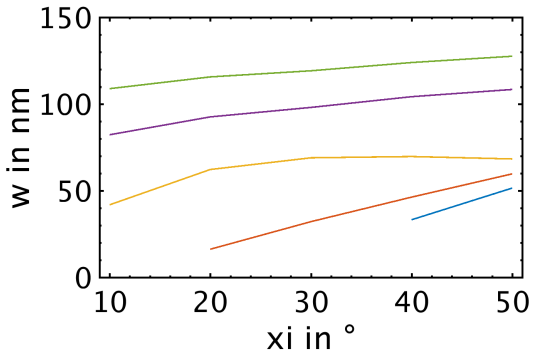

Figure B.7: Line width w dependent on the opening angle ξ of the cover layer. A tip-sample distance of $d = 50\,nm$ was applied and the following applied voltages were used: $U = 60\,V$ (blue), $70\,V$ (red), $80\,V$ (yellow), $90\,V$ (purple) and $100\,V$ (green).

In fig. B.7, the line width w is drawn as function of the cover layer opening angle ξ for different applied bias voltages. The expected behavior is visible, i. e., for increasing size of the opening in the cover layer the line width w is increased as well. In other words, a line width decrease can be induced by decreasing the cover layer opening.

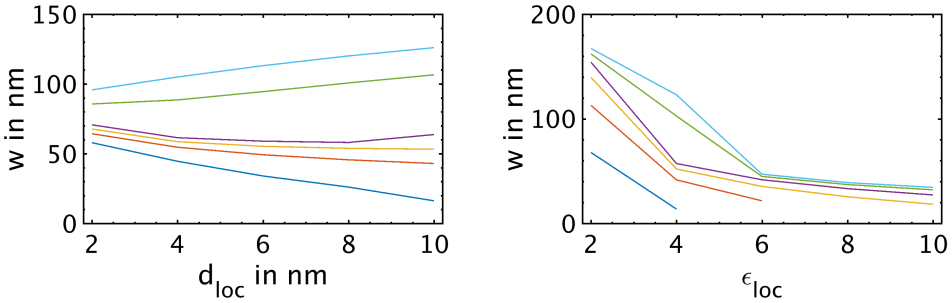

Figure B.8: Line width w dependent on the cover layer thickness d_{loc} (*left*) and its dielectric function ε_{loc} (*right*). A tip-sample distance of $d = 50\,nm$ was applied and the following applied voltages were used: $U = 50\,V$ (blue), $60\,V$ (red), $70\,V$ (yellow), $80\,V$ (purple), $90\,V$ (green) and $100\,V$ (cyan).

The dependence of w on the thickness d_{loc} and on the dielectric constant ε_{loc} is shown in fig. B.8. The line width decrease caused by the increase of d_{loc} and ε_{loc} is partly caused by the reduced field emission due to the cover and partly by a reduced electric field strength at the tip surface, which can be seen in fig. B.1.
Concluding, based on this model, a line width decrease, i. e., a resolution

increase, is observed using an insulating cover upon the tip. Nevertheless, an additional study should verify the results by taking the field emission from the cover into account, which was neglected in this investigation.

Bibliography

[1] G. E. Moore. *Understanding Moore's law: four decades of innovation*, chapter 7: Moore's law at 40, page 67. Chemical Heritage Foundation, 2006.

[2] P. D. Prewett, C. W. Hagen, C. Lenk, S. Lenk, M. Kaestner, T. Ivanov, A. Ahmad, I. W. Rangelow, S. A. Boden, A. P. G. Robinson, D. X. Yang, S. Hari, M. Scotuzzi, and E. Huq. Charged particle single nanometre manufacturing. Beilstein J. Nanotechnol. - under review, 2018.

[3] P. Vettiger, G. Cross, M. Despont, U. Drechsler, U. Dúrig, B. Gotsmann, W. Háberle, M. A. Lantz, H. E. Rothuizen, R. Stutz, and G. K. Binnig. The "millipede"-nanotechnology entering data storage. *IEEE Trans. Nanotechnol.*, 1:39, 2002.

[4] E. Albisetti, D. Petti, M. Madami, S. Tacchi, P. Vavassori, E. Riedo, and R. Bertacco. Nanopatterning spin-textures: A route to reconfigurable magnonics. *AIP Advances*, 7:055601, 2017.

[5] M. A. McCord and R. F. W. Pease. High resolution, low-voltage probes from field emission source close to the target plane. *J. Vac. Sci. Technol. B*, 3:198, 1985.

[6] M. A. McCord and R. F. W. Pease. The effect of reflected and secondary electrons on lithography with the scanning tunneling microscope. *Surf. Sci.*, 181:278, 1987.

[7] S. W. Park, H. T. Soh, C. F. Quate, and S.-I. Park. Nanometer scale lithography at high scanning speeds with the atomic force microscope using spin on glass. *Appl. Phys. Lett.*, 67:2415, 1995.

[8] G. Binnig, C. F. Quate, and C. Gerber. Atomic force microscope. *Phys. Rev. Lett.*, 56:930, 1986.

[9] M. Kaestner and I. W. Rangelow. Scanning probe nanolithography on calixarene. *Microelectron. Eng.*, 97:96, 2012.

[10] M. Kaestner, M. Hofer, and I. W. Rangelow. Nanolithography by scanning probes on calixarene molecular glass resist using mix-and-match lithography. *J. Micro Nanolithogr. MEMS MOEMS*, 12:031111, 2013.

[11] M. Kaestner, T. Ivanov, A. Schuh, A. Ahmad, T. Angelov, Y. Krivoshapkina, M. Budden, M. Hofer, S. Lenk, J.-P. Zoellner, I. W. Rangelow, A. Reum, E. Guliyev, M. Holz, and N. Nikolov. Scanning probes in nanostructure fabrication. *J. Vac. Sci. Technol. B*, 32:06F101, 2014.

[12] M. Kaestner, C. Aydogan, T. Ivanov, A. Ahmad, T. Angelov, A. Reum, V. Ishchuk, Y. Krivoshapkina, M. Hofer, S. Lenk, I. Atanasov, M. Holz, and I. W. Rangelow. Advanced electric-field scanning probe lithography on molecular resist using active cantilever. *J. Micro Nanolithogr. MEMS MOEMS*, 14:0311202, 2015.

[13] M. Kaestner. *Field emission scanning probe lithography on molecular resist*. PhD thesis, Technische Universität Ilmenau, 2016.

[14] I. W. Rangelow, A. Ahmad, T. Ivanov, M. Kaestner, Y. Krivoshapkina, T. Angelov, S. Lenk, C. Lenk, V. Ishchuk, M. Hofmann, D. Nechepurenko, I. Atanasov, B. Volland, E. Guliyev, Z. Durrani, M. Jones, C. Wang, D. Liu, A. Reum, M. Holz, N. Nikolov, W. Majstrzyk, T. Gotszalk, D. Staaks, S. Dallorto, and D.L. Olynick. Pattern-generation and pattern-transfer for single-digit nano devices. *J. Vac. Sci.Technol. B*, 34:06K202, 2016.

[15] T. Michels and I. W. Rangelow. Review of scanning probe micromachining and its applications within nanoscience. *Microelectron. Eng.*, 126:191, 2014.

[16] Z. Durrani, M. Jones, M. Kaestner, M Hofer, E. Guliyev, A. Ahmad, T. Ivanov, J.-P. Zoellner, and I. W. Rangelow. Scanning probe lithography approach for beyond CMOS devices. 8680:8680117, 2013.

[17] I. W. Rangelow and H. Löschner. Reactive ion etching for microelectrical mechanical system fabrication. *J. Vac. Sci.Technol. B*, 13:2394, 1995.

[18] V. Ishchuk, D. L. Olynick, Z. Liu, and I. W. Rangelow. Profile simulation model for sub-50 nm cryogenic etching of silicon using SF_6/O_2 inductively coupled plasma. *J. Appl. Phys.*, 118:053302, 2015.

[19] S. Lenk, M. Kaestner, C. Lenk, T. Angelov, Y. Krivoshapkina, and I. W. Rangelow. 2D Simulation of Fowler- Nordheim Electron Emission in Scanning Probe Lithography. *J. Nanomater. Mol. Nanotechnol.*, 5:6:1000201, 2016.

[20] S. Lenk, M. Kaestner, C. Lenk, and I. W. Rangelow. Simulation of field emission from volcano-gated tips for scanning probe lithography. *Microelectron. Eng.*, 177:19, 2017.

[21] S. Lenk, C. Lenk, and I. W. Rangelow. Simulation of the processes in field emission scanning probe lithography. unpublished.

[22] E. A. Dobisz, H. W. P Koops, F. K. Perkins, C. R. K. Marrian, and S. L. Brandow. Three dimensional electron optical modeling of scanning

tunneling microscope lithography in resists. *J. Vac. Sci. Technol. B*, 14:4148, 1996.

[23] E. A. Dobisz, H. W. P Koops, and F. K. Perkins. Simulation of scanning tunneling microscope interaction with resists. *Appl. Phys. Lett.*, 68:3653, 1996.

[24] I. W. Rangelow, T. Ivanov, Y. Sarov, A. Schuh, A. Frank, H. Hartmann, J.-P. Zöllner, D. L. Olynick, and V. Kalchenko. Nanoprobe maskless lithography. *Proc. SPIE*, 7637:76370V, 2010.

[25] Single nanometer manufacturing for beyond CMOS devices, "SNM" EU-FP7 project (GA 318804). snm-project.eu.

[26] C. Lenk, S. Lenk, and I. W. et al. Rangelow. High-throughput process chain for SET devices based on FE-SPL and SmartNIL^{TM} technology. submitted to J. Vac. Sci. Technol. B.

[27] L. L. Cheong, P. Paul, F. Holzner, M. Despont, D. J. Coady, J. L. Hedrick, A. W. Allen, R. Knoll, and U. Dürig. Thermal probe maskless lithography for 27.5 nm half-pitch Si technology. *Nano Lett.*, 13:4485, 2013.

[28] B. Capella and H. Sturm. Comparison between dynamic plowing lithography and nanoindentation methods. *J. Appl. Phys.*, 91:506, 2002.

[29] A. A. Tseng, J.-I. Shirakashi, S. Nishimura, K. Miyashita, and A. Notargiacomo. Scratching properties of nickel-iron thin film and silicon using atomic force microscopy. *J. Appl. Phys.*, 106:044314, 2009.

[30] Yu Kyoung Ryu, Marco Chiesa, and Ricardo García. Electrical characteristics of silicon nanowire transistors fabricated by scanning probe and electron beam lithographies. *Nanotechnology*, 24:315205, 2013.

[31] F. J. Ruess, L. Oberbeck, M. Y. Simmons, K. E. J. Goh, A. R. Hamilton, T. Hallam, S. R. Schofield, N.J. Curson, and R. G. Clark. Toward atomic-scale device fabrication in silicon using scanning probe microscopy. *Nano Lett.*, 4:1969, 2004.

[32] K. Wilder, C. F. Quate, B. Singh, and D. F. Kyser. Electron beam and scanning probe lithography: a comparison. *J. Vac. Sci. Technol. B*, 16:3864, 1998.

[33] Ricardo García, Armin W. Knoll, and Elisa Riedo. Advanced scanning probe lithography. *Nat. Nanotechnology*, 9:577, 2014.

[34] G. Mesa, J. J. Sáenz, and R. García. Current characteristics in near field emission scanning tunneling microscopes. *J. Vac. Sci. Technol. B*, 14:2403, 1996.

[35] D. M. Eigler and E. I. Schweizer. Positioning single atoms with a scanning tunneling microscope. *Nature*, 344:524, 1990.

[36] I.-W. Lyo and P. Avouris. Field-induced nanometer- to atomic-scale manipulation of silicon surfaces with the STM. *Science*, 253:173, 1991.

[37] M. Aono, A. Kobayashi, F. Grey, H. Uchida, and D.-H. Huang. Tip-sample interactions in the scanning tunneling microscope for atomic-scale structure fabrication. *Jpn. J. Appl. Phys.*, 32, 1993.

[38] J. W. Lyding, T.-C. Shen, J. S. Hubacek, J. R. Tucker, and G. C. Abeln. Nanoscale patterning and oxidation of H-passivated Si(100)-2x1 surfaces with an ultrahigh vacuum scanning tunneling microscope. *Appl. Phys. Lett.*, 64:2010, 1994.

[39] S. R. Schofield, N.J. Curson, M. Y. Simmons, F. J. Ruess, T. Hallam, L. Oberbeck, and R. G. Clark. Atomically Precise Placement of Single Dopants in Si. *Phys. Rev. Lett.*, 91:136104, 2003.

[40] L. Stockman, G. Neuttiens, G. Van Haesendonck, and Y. Bruynseraede. Submicrometer lithographic patterning of thin gold films with a scanning tunneling microscope. *Appl. Phys. Lett.*, 62:2935, 1993.

[41] C. R. K. Marrian, F. K. Perkins, S. L. Brandow, T. S. Koloski, E. A. Dobisz, and J. M. Calvert. Low voltage electron beam lithography in self-assembled ultrathin films with the scanning tunneling microscope. *Appl. Phys. Lett.*, 64:390, 1993.

[42] J. G. Simmons. Generalized formula for electric tunnel effect between similar electrodes separated by a thin insulating film. *J. Appl. Phys.*, 34:1793, 1963.

[43] R. García. Nanometer-scale modification of biological membranes by field emission scanning tunneling microscopy. *Appl. Phys. Lett.*, 64:1162, 1993.

[44] J. J. Sáenz and R. García. Near field emission scanning tunneling microscopy. *Appl. Phys. Lett.*, 65:3022, 1994.

[45] V. R. Manfrinato, L. Zhang, D. Su, H. Duan, R. G. Hoobs, E. A. Stach, and K. K. Berggren. Resolution limits of electron beam lithography toward the atomic scale. *Nano Lett.*, 13:1555, 2013.

[46] W. F. van Dorp and C. W. Hagen. A critical literature review of focused electron beam induced deposition. *J. Appl. Phys.*, 104:081301, 2008.

[47] P. S. Spinney, D. G. Howitt, R. L. Smith, and S. D. Collins. Nanopore formation by low-energy focused electron beam machining. *Nanotechnology*, 21:375301, 2010.

[48] E. Ruska and H. Ruska. Electron microscope. US Patent 2,267,137, 1941.

[49] T. C. Tessner, G. A. Schwind, and L. W. Swanson. Cold field emitter. US Patent US7,888,654A, 2007.

[50] J. B. McGinn, S. G. den Hartog, D. S. Jun, G. G. Magera, and G. A. Schwind. Schottky emitter having extended life. US Patent 6,680,562, 2007.

[51] R. A. Tuck. Thermionic electron emitter. US Patent US4,147,954A, 1979.

[52] I. Sakai and T. Mizuno. Thermal field emission electron gun. US Patent 5,962,961, 1999.

[53] Private communication with Elodie Verzerolie, Sales manager of Orsay Physics.

[54] Raith GmbH. raith.com.

[55] G. Binnig, C. Rohrer, H. Gerber, and E. Weibel. Tunneling through a controllable vacuum gap. *Appl. Phys. Lett.*, 40:178, 1982.

[56] G. Binnig. Atomic force microscope and method for imaging surfaces with atomic resolution. US Patent US4,724,318, 1988.

[57] M. Ringger, H. R. Hidber, R. Schlogl, P. Oelhafen, and H. J. Guntherodt. Nanometer lithography with the scanning tunneling microscope. *Appl. Phys. Lett.*, 46:832, 1985.

[58] Zyvex Labs. zyvexlabs.com.

[59] S. G. Jennings. The mean free path in air. *J. Aerosol Sci*, 19:159, 1988.

[60] I. W. Rangelow, M. Kaestner, T. Ivanov, A. Ahmad, S. Lenk, C. Lenk, E. Guliyev, A. Reum, M. Hofmann, C. Reuter, and M. Holz. Atomic force microscope integrated with a Scanning Electron Microscope for Correlative Nanofabrication and Microscopy. *J. Vac. Sci. Technol. B*, 36:06JL02, 2018.

[61] T. Angelov, A. Ahmad, E. Guliyev, A. Reum, I. Atanasov, T. Ivanov, V. Ishchuk, M. Kaestner, Y. Krivoshapkina, S. Lenk, C. Lenk, I. W. Rangelow, M. Holz, and N. Nikolov. Six-axis AFM in SEM with self-sensing and self-transduced cantilever for high speed analysis and nano-lithography. *J. Vac. Sci. Technol. B*, 34:06KB01, 2016.

[62] T. Angelov, D. Roeser, T. Ivanov, S. Gutschmidt, T. Sattel, and I. W. Rangelow. Thermo-mechanical transduction suitable for high-speed scanning probe imaging and lithography. *Microelectron. Eng.*, 154:1, 2016.

[63] A. Ahmad, N. Nikolov, T. Angelov, T. Ivanov, A. Reum, I. Atanasov, E. Guliyev, V. Ishchuk, M. Kaestner, Y. Krivoshapkina, S. Lenk, C. Lenk, I. W. Rangelow, and M. Holz. Large area fast-AFM scanning with active "quattro" cantilever arrays. *J. Vac. Sci. Technol. B*, 34:06KM03, 2016.

[64] R. Linnemann, T. Gotszalk, I. W. Rangelow, P. Dumania, and E. Oesterschulze. Atomic force microscopy and lateral force microscopy using piezoresistive cantilevers. *J. Vac. Sci. Technol. B*, 14:856, 1996.

[65] T. Ivanov, T. Gotzsalk, T. Sulzbach, and I. W. Rangelow. Quantum size aspects of the piezoresistive effect in ultra thin piezoresistor. *Ultramicroscopy*, 97:377, 2003.

[66] T. Ivanov, T. Gotzsalk, T. Sulzbach, I. Chakarov, and I. W. Rangelow. AFM cantilever with ultra-thin transistor-channel piezoresistor: quantum confinement. *Microelectron. Eng.*, 67-68:534, 2003.

[67] D. Roeser, S. Gutschmidt, T. Sattel, and I. W. Rangelow. Tip Motion-Sensor Signal Relation for a Composite SPM/SPL Cantilever. *J. Microelectronmech. Syst.*, 25:78, 2016.

[68] R. Pedrak, T. Ivanov, K. Ivanova, T. Gotzsalk, N. Abedinov, I. W. Rangelow, K. Edinger, E. Tomerov, T. Schenkel, and P. Hudek. Micromachined atomic force microscopy sensor with integrated piezoresistive sensor and thermal bimorph actuator for high-speed tapping-mode atomic force microscopy phase-imaging in higher eigenmodes. *J. Vac. Sci. Technol. B*, 21:3102, 2003.

[69] M. Hofmann, C. Aydogan, C. Lenk, Y. Krivoshapkina, S. Lenk, B. Volland, M. Kaestner, B. E. Alaca, E. Manske, and I. W. Rangelow. Selective pattern transfer of nano-scale features generated by FE-SPL in 10 nm thick resist layers. *Am. J. Nano Res. Appl.*, 6:11, 2018.

[70] Y. Krivoshapkina, M. Kaestner, C. Lenk, S. Lenk, and I. W. Rangelow. Low-energy electron exposure of ultrathin polymer films with scanning probe lithography. *Microelectron. Eng.*, 177:78, 2017.

[71] I. W. Rangelow, R. Pedrak, and T. Ivanov. Patent Method for the electrostatic structuring of a substrate surface and raster probe. EU Patent EP1,759,247, 2007.

[72] C. Neuber, A. Ringk, T. Kolb, F. Wieberger, P. Strohriegl, H.-W. Schmidt, V. Fokkema, M. Cooke, C. Rawlings, U. Duerig, A. Knoll, J.-F. de Marneffe, P. de Schepper, M. Kaestner, Y. Krivoshapkina, M. Budden, and I. W. Rangelow. Molecular glass resists for scanning probe lithography. *Proc. SPIE*, 9049:9049V, 2014.

[73] C. Neuber, H. W. Schmidt, P. Strohriegl, A. Ringk, T. Kolb, V. Fokkema, M. G. A. van Veghel, M. Cooke, C. Rawlings, U. Duerig, A. Knoll, J.-F. de Marneffe, Z. el Otell, M. Kaestner, Y. Krivoshapkina, M. Budden, and I. W. Rangelow. Tailored molecular glass resists for scanning probe lithography. *Proc. SPIE*, 9425:94250E–2, 2015.

[74] E. A. Dobisz and C. R. K. Marrian. Scanning tunneling microscope lithography: A solution to electron scattering. *J. Vac. Sci. Technol. B*, 9:3024, 1991.

[75] H. T. Soh, K. Wilder, T. Guarini, and C. F. Quate. Scanning probe lithography. In A. J. Ricco R. T. Howe, editor, *Microsystems*, volume 7. Springer US, New York, 1 edition, 2001.

[76] K. Wilder, H. T. Soh, A. Atalar, and C. F. Quate. Hybrid atomic force/scanning tunneling lithography. *J. Vac. Sci. Technol. B*, 15:1811, 1997.

[77] T. M. Mayer, D. P. Adams, and B. M. Marder. Field emission characteristics of the scanning tunneling microscope for nanolithography. *J. Vac. Sci. Technol. B*, 14:2438, 1996.

[78] S. Podenok, M. Sveningsson, K. Hansen, and E. E. B. Campbell. Electric field enhancement factors around a metallic, end-capped cylinder. *Nano*, 1:87, 2006.

[79] A. J. le Febre, L. Abelmann, and J. C. Lodder. Field emission at nanometer distances for high-resolution positioning. *J. Vac. Sci. Technol. B*, 26:724, 2008.

[80] G. Mesa, E. Dobado-Fuentes, and J. J. Sáenz. Image charge method for electrostatic calculations in field-emission diodes. *J. Appl. Phys.*, 79:39, 1996.

[81] G. C. Kokkorakis, A. Modinos, and J. P. Xanthakis. Local electric field at the emitting surface of a carbon nanotube. *J. Appl. Phys.*, 91:4580, 2002.

[82] M. W. Jernegan. Benjamin Franklin's "Electrical Kite" and lightning rod. *New Engl. Q.*, 1:180, 1928.

[83] H. Craig Miller. Change in field intensification factor β of an electrode projection (Whisker) at short gap lengths. *J. Appl. Phys.*, 38:4501, 1967.

[84] X. Q. Wang, M. Wang, P. M. He, and Y. B. Xu. Model calculation for the field enhancement factor of carbon nantube. *J. Appl. Phys.*, 96:6752, 2004.

[85] C. J. Edgcombe and U. Valdrè. Microscopy and computational modelling to elucidate the enhancement factor for field electron emitters. *J. Microsc.*, 203:188, 2001.

[86] C. J. Edgcombe and U. Valdrè. The enhancement factor and the characterization of amorphous carbon field emitters. *Solid-State Electron.*, 45:857, 2001.

[87] C. J. Edgcombe and U. Valdrè. Experimental and computational study of field emission characteristics from amorphous carbon single nanotips grown by carbon contamination i. experiments and computation. *Phil. Mag. B*, 82:987, 2002.

[88] Jean-Marc Bonard, Kenneth A. Dean, Bernard F. Coll, and Christian Klinke. Field emission of individual carbon nanotubes in the scanning electron microscope. *Phys. Rev. Lett.*, 89:197602, 2002.

[89] Henry G. Kosmahl. Analytic evaluation of field emission enhancement factors for ellipsoidal cones and elliptic cross-section wedges. *IEEE Trans. Electron Devices*, 38:1534, 1991.

[90] Richard G Forbes, C.J Edgcombe, and U Valdrè. Some comments on models for field enhancement. *Ultramicroscopy*, 95:57, 2003.

[91] R. C. Smith, D. C. Cox, and S. R P Silva. Electron field emission from a single carbon nanotube: Effects of anode location. *Appl. Phys. Lett.*, 87:1, 2005.

[92] Zhi Xu, X. D. Bai, and E. G. Wang. Geometrical enhancement of field emission of individual nanotubes studied by in situ transmission electron microscopy. *Appl. Phys. Lett.*, 88(13), 2006.

[93] W.P. Dyke and W.W. Dolan. Field Emission. *Adv. Electron. El. Phys.*, 8:89, 1956.

[94] R. H. Fowler and L. Nordheim. Electron Emission in Intense Electric Fields. *Proc. R. Soc. Lond. A*, 119:173, 1928.

[95] L W Nordheim. The effect of the image force on the emission and reflexion of electrons by metals. *Proc. R. Soc. Lond.*, A121:626, 1928.

[96] Timothy Groves. *Charged particle optics theory.* CRC Press, Boca Raton, 2015.

[97] A. Sommerfeld. Zur Elektronentheorie der Metalle auf Grund der Fermischen Statistik. *Z. Phys.*, 47:1, 1928.

[98] A Modinos. *Field, thermionic, and secondary electron emission spectroscopy.* Plenum Press, New York, 1984.

[99] Robert Gomer. *Field emission and field ionization.* Havard University Press, Cambridge, 1961.

[100] W. Schottky. Über den Einfluss von Strukturwirkungen, besonders der Thomsonschen Bildkraft, auf die Elektronenemission der Metalle. *Phys. Zeitschr.*, 15:872, 1914.

[101] W. Schottky. Über kalte und warme Elektronenentladungen. *Z. Phys.*, 14:63, 1923.

[102] R Gomer. Work Function in Field Emission - Chemisorption. *Journal of Chemical Physics*, 21:1869, 1953.

[103] S. C. Miller Jr. and R. H. Good Jr. A WKB-type approximation to the Schrödinger equation. *Phys. Rev.*, 91:174, 1953.

[104] E. L. Murphy and R. H. Good Jr. Thermionic Emission, Field Emission, and the Transistion Region. *Phys. Rev.*, 102:1464, 1956.

[105] J. H. B. Deane and R. G. Forbes. The formal derivation of an exact series expansion for principal Schottky-Nordheim barrier function v, using the Gauss hypergeometric differential equation. *J. Phys. A: Math Theor.*, 41:395301, 2008.

[106] C. A. Spindt, I. Brodie, L. Humphrey, and E. R. Westerberg. Physical properties of thin-film field emission cathodes with molybdenum cones. *J. Appl. Phys.*, 47:5248, 1976.

[107] W. W. Dolan. Current density tables for field emission theory. *Phys. Rev*, 91:510, 1953.

[108] D. R. Whaley, B. M. Gannon, C. R. Smith, C. M. Armstrong, and C. A. Spindt. Application of Field Emitter Arrays to Microwave Power Amplifiers. *IEEE Trans. Plasm. Sci.*, 28:727, 2000.

[109] P. A. Serena, L. Escapa, J. J. Sáenz, García, and H. Rohrer. Coherent electron emission from point sources. *J. Microsc.*, 152:43, 1988.

[110] J. He, P. H. Cutler, and N. M. Miskovsky. Generalization of Fowler-Nordheim fiel emission theory to nonplanar metal emitters. *Appl. Phys. Lett.*, 59:1644, 1991.

[111] J. He, P. H. Cutler, N. M. Miskovsky, T. E. Feuchtwang, T. E. Sullivan, and M. Chung. Derivation of the image interaction for non-planar pointed emitter geometries: application to field emission I-V characteristics. *Surf. Sci.*, 246:348, 1991.

[112] P. H. Cutler, J. He, N. M. Miskovsky, T. E. Sullivan, and B. Weiss. Theory of electron emission in high fields from atomically sharp emitters: Validity of the Fowler-Nordheim equation. *J. Vac. Sci. Technol. B*, 11:387, 1993.

[113] T. L. Kirk, O. Scholder, L. G. De Pietro, U. Ramsperger, and D. Pescia. Evidence of nonplanar field emission via secondary electron detection in near field emission scanning electron microscopy. *Appl. Phys. Lett.*, 94:153502, 2009.

[114] C. J. Edgcombe and N. de Jonge. Deduction of work function of carbon nanotube field emitter by use of curved-surface theory. *J. Phys. D: Appl. Phys.*, 40:4123, 2007.

[115] A. Kyritsakis and J. P. Xanthakis. Derivation of a generalized Fowler-Nordheim equation for nanoscopic field-emitters. *Proc. R. Soc. A*, 471:20140811, 2015.

[116] A. Kyritsakis and J. P. Xanthakis. Extension of the general thermal field equation for nanosized emitters. *J. Appl. Phys.*, 119:045303, 2016.

[117] A. A. Patterson and A. I. Akinwande. Elementary framework for cold field emission from quantum-confined, non-planar emitters. *J. Appl. Phys.*, 117:174311, 2015.

[118] K. Wilder, C. F. Quate, D. Adderton, R. Bernstein, and V. Elings. Non-contact nanolithography using the atomic force microscope. *Appl. Phys. Lett.*, 73:2527, 1998.

[119] K. Wilder, H. T. Soh, A. Atalar, and C. F. Quate. Electron beam and scanning probe lithography: a comparison. *Rev. Sci. Instrum.*, 70:2822, 1999.

[120] A. García-Martin and R. García. Formation of nanoscale liquid menisci in electric fields. *Appl. Phys. Lett.*, 88:123115, 2006.

[121] Private communication with Prof Ricardo García (CSIC Madrid) at the SNM project Kick-off meeting, 2013.

[122] Zyvex Labs, LLC. *ZyVector^{T}M - User Manual for SCANZ 1.5*, 10 2015. zyvexlabs.com.

[123] K. Jensen, D. A. Shiffler, I. M. Rittersdorf, J. L. Lebowitz, J. R. Harris, Y.Y. Lau, J. J. Petillo, W. Tang, and J. W. Luginsland. Discrete space charge affected field emission: Flat and hemisphere emitters. *J. Appl. Phys.*, 117:194902, 2015.

[124] D. A. Shiffler, W. Tang, K. L. Jensen, K. Golby, M. LaCour, J. J. Petillo, and J. R. Harris. Effective field enhancement factor and the influence of emitted space charge. *J. Appl. Phys.*, 118:083302, 2015.

[125] The MathWorks, Inc. *Matlab Partial Differential Equation Toolbox*, 2016b edition, 2016.

[126] Maurizio Dapor. *Electron-beam interactions with solids: Application of the Monte Carlo method to electron scattering problems.* Springer, Berlin, 2003.

[127] L. de Broglie. *The wave nature of the electron.* Nobel Prize Lecture, 1929.

[128] J. D. Jackson. *Klassische Elektrodynamik.* De Gruyter, Berlin, 1983.

[129] W. Nolting. *Grundkurs Theoretische Physik 3 Elektrodynamik.* Springer, Berlin, 2007.

[130] I. N. Bronstein, K. A. Semendjajew, G. Musiol, and H. Mühlig. *Taschenbuch der Mathematik.* Harri Deutsch, Frankfurt am Main, 2000.

[131] M. Budden. Nanofabrication by electron emission scanning probe lithography. Master's thesis, Technische Universität Ilmenau, 2015.

[132] Erik Kieft and Eric Bosch. Refinement of Monte Carlo simulations of electron-specimen interaction in low-voltage SEM. *J. Phys. D: Appl. Phys.*, 41:215310, 2008.

[133] M.P. Seah and W.A. Dench. Quantitative electron spectroscopy of surfaces. *Surf. Interf. Anal.*, 1:2, 1979.

[134] I. Adesida, R. Shimizu, and T. E. Everhart. A study of electron penetration in solids using a direct Monte Carlo approach. *Journal of Applied Physics*, 51:5962, 1980.

[135] Wei Mao-xin, Wang Jian-kun, and Qiao Yi-zeg. A novel Monte Carlo simulation in electron beam exposure. *Microelectronic Engineering*, 3:99, 1985.

[136] Zhenyu Tan, Yueyuan Xia, Xiangdong Liu, and Minwen Zhao. Monte-Carlo simulation of low-energy electron scattering in PMMA - Using stopping powers from dielectric formalism. *Microelectron. Eng.*, 77:285, 2005.

[137] H.-J. Fitting, E. Schreiber, J.-Ch. Kuhr, and A. von Czarnowski. Attenuation and escape depths of low-energy electron emission. *Journal of Electron Spectroscopy and Related Phenomena*, 119:35, 2001.

[138] Appendix c. quantum theory of scattering by a central potential. *Journal of the International Commission on Radiation Units and Measurements*, 7:131, 2007.

[139] A. Jablonski, F. Salvat, and Cedric J. Powell. *NIST Electron Elastic-Scattering Cross-Section Database Version 3.2 SRD64*. National Institute of Standards and Technology (NIST), Gaithersburg, MD, 2010.

[140] A. Jablonski, F. Salvat, and C. J. Powell. Comparison of electron elastic-scattering cross sections calculated from two commonly used atomic potentials. *Journal of Physical and Chemical Reference Data*, 33:409, 2004.

[141] Francesc Salvat, A. Jablonski, and C. J. Powell. Elastic scattering of electrons and positrons by atoms. Positive Ions and Molecules. *Comput. Phys. Commun.*, 165:1571, 2005.

[142] M. Blaha and J Davis. Elastic scattering of electrons by oxygen and nitrogen at intermediate energies. *Phys. Rev. A*, 12:2319, 1975.

[143] Gabriel Sunshine, Bertrand B Aubrey, and Benjamin Bederson. Absolute Measurements of Total Cross Sections for the Scattering of Low-Energy Electrons by Atomic and Molecular Oxygen. *Phys. Rev.*, 154:1, 1967.

[144] A. Jain and K. L. Baluja. Total (elastic plus inelastic) cross sections for electron scattering from diatomic and polyatomic molecules at 10-5000 eV: H_2, Li_2, HF, CH_4, N_2, CO, C_2H_2, HCN, O_2, HCl, H_2S, PH_3, SiH_4 and CO_2. *Phys. Rev. A*, 45:202, 1992.

[145] Yukikazu Itikawa. Cross sections for electron collisions with oxygen molecules. *Journal of Physical and Chemical Reference Data*, 38:1, 2009.

[146] J. C. Gibson, M. A. Green, K. W. Trantham, S. J. Buckman, P. J. O. Teubner, and M. J. Brunger. Elastic electron scattering from co_2. *J. Phys. B: At. Mol. Opt. Phys.*, 32:213, 1999.

[147] H. Tanaka, T. Okada, L. Boesten, T. Suzuki, T. Yamamoto, and M. Kubo. Differential cross sections for elastic scattering of electrons by CH4 in the energy range of 3 to 20 eV. *J. Phys. B: Atom. Molecul. Phys.*, 15:3305, 1982.

[148] H. Tanaka, T. Ishikawa, T. Masai, T. Sagara, L. Boesten, M. Takekawa, Y. Itikawa, and M. Kimura. Elastic collisions of low- to intermediate-energy electrons from carbon dioxide: Experimental and theoretical differential cross sections. *Phys. Rev. A*, 57:1798, 1998.

[149] Santosh K. Srivastava, a. Chutjian, and S. Trajmar. Absolute elastic differential electron scattering cross sections in the intermediate energy region. I. H2. *J. Chem. Phys.*, 63:2659, 1975.

[150] Joseph Callaway and J. F. Williams. Scattering of electrons by hydrogen atoms at intermediate energies: Elastic differential cross sections from 10 to 30 eV. *Phys. Rev. A*, 12:2312, 1975.

[151] T. W. Shyn and W. E. Sharp. Angular distribution of electrons elastically scattered from 02: 2.0-200 eV impact energy. *Phys. Rev. A*, 26:1369, 1982.

[152] H. Tanaka, Santosh K. Srivastava, and A. Chutjian. Absolute elastic differential electron scattering cross sections in the intermediate energy region. IV. CO. *J. Chem. Phys.*, 69:5329, 1978.

[153] E. Schreiber and H.-J. Fitting. Monte Carlo simulation of secondary electron emission from the insulator SiO2. *Journal of Electron Spectroscopy and Related Phenomena*, 124:25, 2002.

[154] Sven Tougaard. Universality Classes of Inelastic Electron Scattering Cross-sections. *Surf. Interf. Anal.*, 25:137, 1997.

[155] S. M. Sze, J. L. Moll, and T. Sugano. Range-Energy Relation of Hot Electrons in Au. *Solid-state electronics*, 7:509, 1964.

[156] John J. Quinn. Range of Excited Electrons in Metals. *Phys. Rev.*, 126:1453, 1962.

[157] Private communication with Prof Thomas Hotz, TU Ilmenau.

[158] Prof Martin Neumann. *Notes of lecture "Computational Physics I".*

[159] T. N. Todd, C. J. amd Rhodin. Work function in field emission - the (110) plane of tungsten. *Surf. Sci.*, 36:353, 1973.

[160] J. Kollar. Calculation of the Fermi velocity in tungsten. *Sol. State Commun.*, 27:1313, 1978.

[161] P. J. Feenan, A. Myers, and D. Sang. De Hass-Van Alphen measurements of the electron cyclotron mass in W. *Sol. State Commun.*, 16:35, 1975.

[162] Russell Young, John Ward, and Fredric Scire. The topografiner: An instrument for measuring surface microtopography. *Rev. Sci. Inst.*, 43:999, 1972.

[163] K. A. Nikiforov, N. V. Egorov, and M. N. Lunkovskiy. Modelling of field emitter surface structure. *J. Phys.: Conf. Ser.*, 643:012010, 2015.

[164] S. Sun and L. K. Ang. Onset of space charge limited current for field emission from a single sharp tip. *Phys. Plasmas*, 19:033107, 2012.

[165] S. Sun and L. K. Ang. Analysis of nonuniform field emission from sharp tip emiiter of Lorentzian or hyperboloid shape. *J. Appl. Phys.*, 113:144902, 2013.

[166] J. D. Zuber, K. L. Jensen, and T. E. Sullivan. An analytical solution for microtip field emission current and effective emission area. *J. Appl. Phys.*, 91:9379, 2002.

[167] L.-H. Pan, T. E. Sullivan, V. J. Peridier, P. H. Cutler, and N. M. Miskovsky. Three-dimensional electrostatic potential, and potential-energy barrier, near a tip-base junction. *Appl. Phys. Lett.*, 65:2151, 1994.

[168] F. R. Blom, S. Bouwstra, M. Elwenspoek, and J. H. J. Fluitman. Dependence of quality factor of micromachined silicon beam resonators on pressure and geometry. *J. Vac. Sci. Technol. B*, 10:19, 1992.

[169] C. Lenk, S. Lenk, and I. W. Rangelow. Experimental study of field emission from ultrasharp silicon, diamond, GaN and tungsten tips. *J. Vac. Sci. Technol. B*, 36:06JL03, 2018.

[170] Y. Huang, Z. Deng, Win Wang, C. Liang, J. She, S. Deng, and N. Xu. Field-induced crystalline-to-amorphous phase transformation on Si nano-apex and the achieving of highly reliable nano-cathodes. *Sci. Rep.*, 5:10631, 2015.

[171] A. J. V. Griffiths and T. Walther. Quantification of carbon contamination under electron beam irradiation in a scanning transmission electron microscope and its suppression by plasma cleaning. *J. Phys: Conf. Series*, 241:012017, 2010.

[172] M. Fleischer, F. Panteleit, and D. A. Wharam. Fabrication of nanostructures using a C-methylcalix[4]resorcinarene dielectric spacer. *J. Vac. Sci. Technol. B*, 25:877, 2007.

[173] D. Cohen-Tanugi and N. Yao. Superior imaging resolution in scanning helium-ion microscopy: a look at beam-sample interactions. *J. Appl. Phys.*, 104:063504, 2008.

[174] D. Brinks, R. Hildner, E. M. H. P. van Dijk, F. D. Stefani, J. B. Nieder, J. Hernando, and N. F. van Hulst. Ultrafast dynamics of single molecules. *Chem. Soc. Rev.*, 43:2476, 2014.

[175] H. Zhang, Y. Zhang, S. Hosaka, and Y. Yin. Dependence of Electron Beam Diameter, Electron Energy, Resist Thickness and Resist Type for Forming Nano-sized Dot Arrays in EB Lithography by Using Monte Carlo Simulation. *American Journal of Nano Research and Applications*, 1:11, 2013.

[176] M. Kaestner and I. W. Rangelow. Scanning proximal probe lithography for sub-10 nm resolution on calix[4]resorcinarene. *J. Vac. Sci. Technol. B*, 29:06FD02, 2011.

[177] M. Hofmann, T. Ivanov, A. Ahmad, S. Lenk, I. W. Rangelow, A. Reum, C. Reuter, and M. Holz. Diamond field emitter on active cantilevers for Scanning Probe Lithography. submitted to J. Vac. Sci. Technol. B.

[178] Z. Durrani, M. Jones, F. Abualnaja, C. Wang, M. Kaestner, S Lenk, C. Lenk, I. W. Rangelow, and A. Andreev. Room-temperature single dopant atom quantum dot transistors in silicon, formed by field-emission scanning probe lithgraphy. 124:144502, 2018.

[179] A Modinos. Field emission from surface states in semiconductors. *Surface Science*, 42:205, 1974.

Danksagung

Als Erstes möchte ich mich bei meiner Frau Dr. Claudia Lenk und meinen Töchtern Helena und Rosalie bedanken. Ihre Unterstützung, ihr Verständnis und ihre Liebe haben mir die Kraft für meine Doktorarbeit gegeben. Außerdem danke ich meiner Frau für die wissenschaftlichen Diskussionen und Anregungen sowie die Durchführung der Feldemissionsexperimenten.

Mein besonderer Dank gilt meinem Doktorvater Prof. Ivo W. Rangelow für die Möglichkeit der Durchführung und der Betreuung meiner Arbeit in seinem Fachgebiet und die Möglichkeit das Projektmanagement des SNM-Projektes zu übernehmen. Außerdem bedanke ich mich für die kontroversen Diskussionen, seinen Enthusiasmus und sein Vertrauen in meine Fähigkeiten im Bezug auf meine Doktorarbeit.

Den Gutachtern Prof. Timothy Groves und Prof. Dirk Lützenkirchen-Hecht danke ich für die Bereitschaft die vorgelegten Dissertation zu begutachten.

Mein weiterer Dank gilt Prof. Erich Runge für die kritische Auseinandersetzung mit den theoretischen Ergebnissen der Dissertation und den dazugehörigen wissenschaftlichen Anregungen.

Prof. Thomas Hotz möchte ich für die Unterstützung bei der Herleitung des Abbruchkriterium für die Monte Carlo Simulation danken.

Bei Dr. Marcus Kästner und Dr. Burkhard Volland bedanke ich mich für die Diskussionen zur Feldemissionsrastersondenlithographie und zur Auswertung der Feldemissionsexperimente.

Für die Unterstützung bei der Nutzung des MaPaCC (Massive Parallel Compute Cluster), für seine Ratschläge und seine freundschaftliche Art möchte ich mich bei Henning Schwanbeck bedanken.

Ich möchte mich bei meinen Kollegen in den Fachgebieten Mikro- und Nanoelektronische Systeme und Theoretische Physik I für die gute Arbeitsatmosphäre mit diversen Kaffeerunden und vielfältigen Diskussionen bedanken. Dabei seien besonders Dr. Martin Körner, Dr. Thomas Hänsel, Felix Schwarz, Mathias Holz, und Steve Durstewitz erwähnt.

Weiterhin gebührt vorallem meinen Kollegen Mathias Holz, Christoph Reuter und Alexander Reum großer Dank für den Auf- und Einbau des AFMinSEM Systems in das SEM/FIB System zur Durchführung der Feldemissionsexperimenten.
Für ihren unermütlichen Einsatz in allen Belangen möchte ich unserer "guten Fee" im Fachgebiet Mikro- und Nanoelektronische Systeme, Frau Gaby Winkler, danken genauso wie Dagmar Böhme aus dem Fachgebiet Theoretische Physik I.

Für ihre Unterstützung und ihre Ratschläge zur Arbeit und für ihre Freundschaft danke ich Dr. Anja Himmerlich, Dr. Marcel Himmerlich und Chirag Saraswati.

Weiterhin bedanke ich mich bei meiner ganzen Familie, meinen Freunden und allen ungenannten Personen, die mich zu dem Menschen gemacht haben, der ich heute bin.

Erklärung

Ich versichere, dass ich die vorliegende Arbeit ohne unzulässige Hilfe Dritter und ohne Benutzung anderer als der angegebenen Hilfsmittel angefertigt habe. Die aus anderen Quellen direkt oder indirekt übernommenen Daten und Konzepte sind unter Angabe der Quelle gekennzeichnet.

Bei der Auswahl und Auswertung folgenden Materials haben mir keine Personen in der jeweils beschriebenen Weise weder entgeltlich noch unentgeltlich.

Weitere Personen waren an der inhaltlich-materiellen Erstellung der vorliegenden Arbeit nicht beteiligt. Insbesondere habe ich hierfür nicht die entgeltliche Hilfe von Vermittlungs- bzw. Beratungsdiensten (Promotionsberater oder anderer Personen) in Anspruch genommen. Niemand hat von mir unmittelbar oder mittelbar geldwerte Leistungen für Arbeiten erhalten, die im Zusammenhang mit dem Inhalt der vorgelegten Dissertation stehen.

Die Arbeit wurde bisher weder im In- noch im Ausland in gleicher oder ähnlicher Form einer Prüfungsbehörde vorgelegt.

Ich bin darauf hingewiesen worden, dass die Unrichtigkeit der vorstehenden Erklärung als Täuschungsversuch bewertet wird und gemäß § 7 Abs. 10 der Promotionsordnung den Abbruch der Promotionsverfahrens zur Folge hat.

Ilmenau, den 27.10.2019